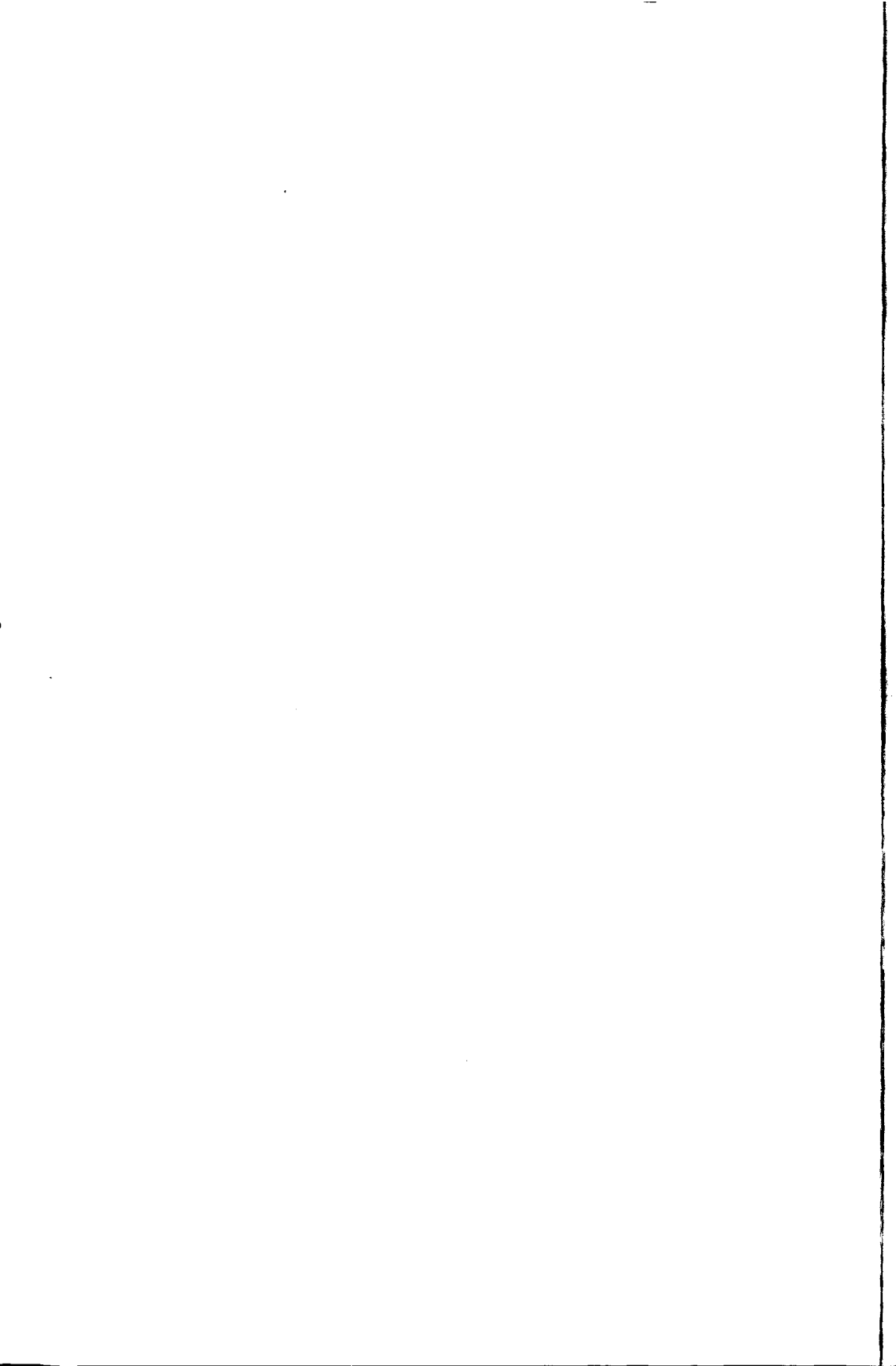# Stress Analysis of the Scapula
Design Considerations of Glenoid Prostheses

Sanjay Gupta

Propositions (Stellingen)

belonging to the Ph.D. thesis

Stress Analysis of the Scapula: Design Considerations of Glenoid Prostheses

Sanjay Gupta

(1) The submodelling technique has practical advantages regarding realistic finite element predictions for an implanted glenoid structure.

(2) A part of the subchondral bone along the longitudinal axis of the glenoid cavity should be preserved to strengthen the glenoid structure, since removal of bone and replacing it by cement means a substantial loss in the strength of the glenoid and an increase in stresses in the cement.

(3) The cement-bone interface adjacent to the tip of the prosthesis keel appears most likely to fail.

(4) Based on the structure and loading conditions, the shell-solid modelling approach is well suited for a finite element representation of the scapula.

(5) Since the interfaces are often the mechanically most critical zones in a bone-prosthesis configuration, the distribution of normal and shear stresses at the interfaces are of crucial importance when evaluating the implant design.

(6) The use of local interface strength data in the Hoffman's failure criterion is an attempt to account for the microstructure of bone, and therefore an effective method to predict local interface failure; inclusion of the trabecular microstructure in the failure criterion would be a major step forward towards the estimation of interface debonding.

(7) The principal stresses are more relevant for evaluating stress distribution in a bone, as compared to the Von Mises stresses.

(8) It is easier to figure out the defects in an implant-bone structure rather than to suggest concrete measures for its improvement.

(9) During the last decade, research on mechanical engineering has shifted more towards numeric computations only, sometimes without understanding the physical significance of a problem.

(10) Intense nationalistic feeling often gives birth to fundamentalism.

(11) A religion is a way of life rather than a set of beliefs.

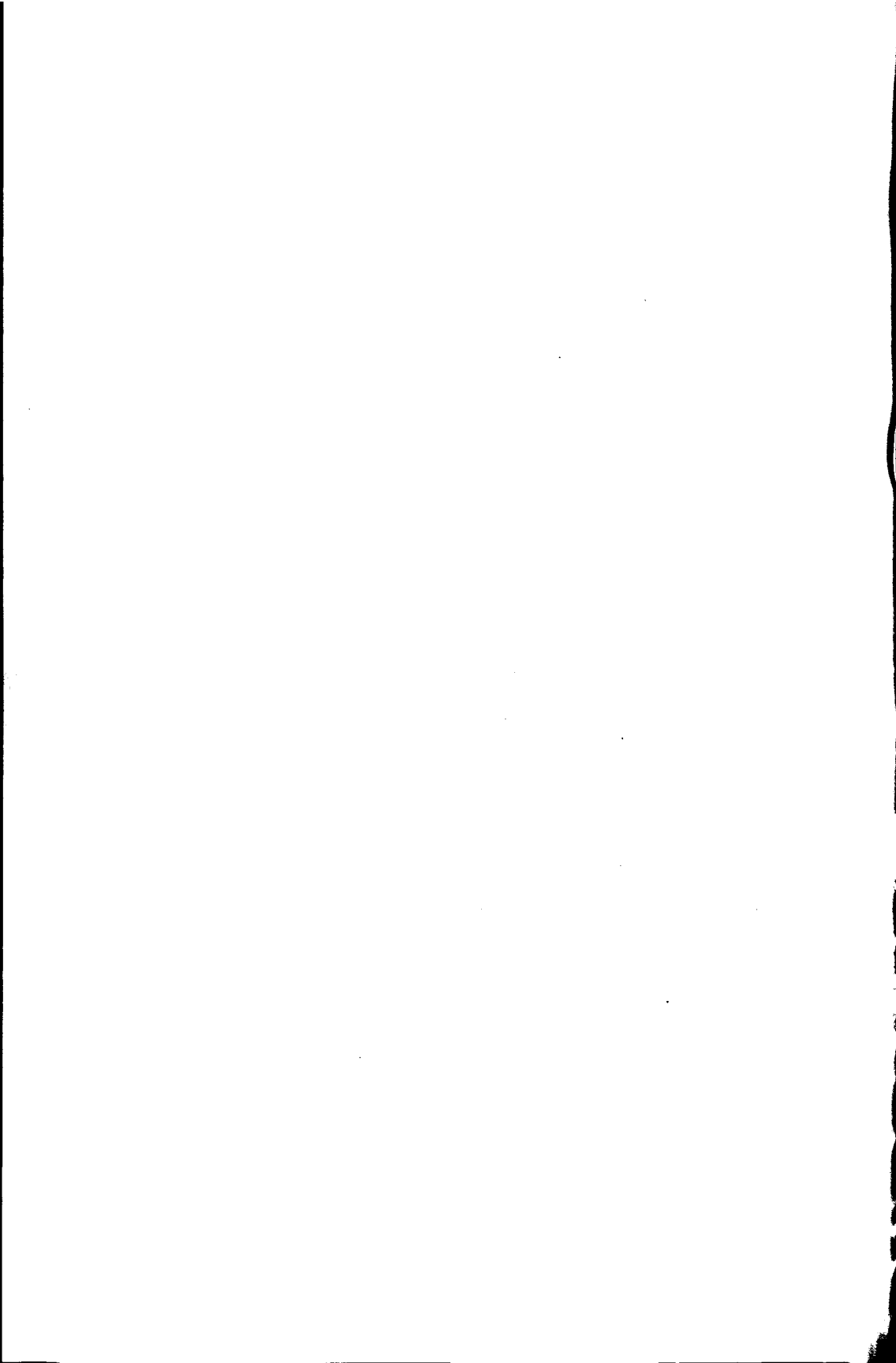(12) Ph.D. is something more than a degree; it is an experience.

3834

270767

TR 3832

Stress Analysis of the Scapula:
Design Considerations of Glenoid Prostheses

Doctoral Thesis

Man-Machine Systems and Control Group
Department of Mechanical Engineering and Marine Technology
Faculty of Design, Engineering and Production
Delft University of Technology

Sanjay Gupta

Dedicated to
my parents

Stress Analysis of the Scapula:
Design Considerations of Glenoid Prostheses

Proefschrift

ter verkrijging van de graad van doctor
aan de Technische Universiteit Delft,
op gezag van de Rector Magnificus Prof. Dr. Ir. J. T. Fokkema,
voorzitter van het College voor Promoties,
in het openbaar te verdedigen op dinsdag 5 Maart 2002 om 16.00 uur
door

Sanjay Gupta
Werktuigkundig ingenieur,
Geboren te Calcutta, India.

Dit proefschrift is goedgekeurd door de promotor:
Prof. Dr. Ir. H.G. Stassen
Prof. Dr. F.C.T. van der Helm
Prof. Dr. Ir. A. van Keulen

Samenstelling promotiecommissie:

Rector Magnificus	Technische Universiteit Delft, voorzitter
Prof. Dr. Ir. H.G. Stassen	Technische Universiteit Delft, promotor
Prof. Dr. F.C.T. van der Helm	Technische Universiteit Delft, promotor
Prof. Dr. Ir. A. van Keulen	Technische Universiteit Delft, promotor
Prof. Dr. P.M. Rozing	Rijksuniversiteit Leiden
Prof. Dr. Ir. R. Huiskes	Technische Universiteit Eindhoven
Prof. Dr. Ir. R. de Borst	Technische Universiteit Delft
Dr. Ir. J.R. de Wijn	Rijksuniversiteit Leiden, Biomaterials Research Group

Contents

Chapter 1

General Introduction

1.1 Introduction

During the last two decades, research on Total Shoulder Replacement may be considered as scarce, as compared to the comprehensive literature on Total Hip and Knee Replacements. The reason behind this scarcity may be attributed to the high demand for Total Hip Arthroplasty (THA) and Total Knee Arthroplasty (TKA) in recent times, as compared to the Total Shoulder Arthroplasty (TSA). According to the American Academy of Orthopaedic Surgeons, during 1990 – 1995, a total number of 1,060,000 TKA and 746,000 THA was performed compared to only 26,000 TSA (Source: National Centre for Health Statistics, 1990-1995; data extracted and analysed by American Academy of Orthopaedic Surgeons, Department of Research and Scientific Affairs). However, with the increasing number of shoulder complications in normal as well as prosthetic joints and the demand for improved shoulder prostheses, in particular the glenoid prostheses, research on TSA is increasing rapidly. As compared to other commonly performed arthroplasties, like the hip and the knee, the TSA involves a far more complicated procedure with a greater potential for errors and complications in fulfilling the objective to restore the large range of motions.

Research in the shoulder region is mainly focused on the glenohumeral joint. The terms shoulder and shoulder joint are commonly used to denote the glenohumeral joint. The shoulder is a multifunctional joint with an infinite number of functions ranging from manipulating objects, throwing a ball and rising from a chair to lifting a heavy load. The shoulder girdle (Fig. 1) consists of the clavicle (collarbone) and the scapula (shoulder blade). The scapula is not only connected to the thorax (rib cage) via the clavicle, but also slides at the backside over the thorax. Motions of the shoulder girdle are closely related to the motions of the humerus. The combined motion of the scapula and the humerus is referred to as the scapulohumeral rhythm. The normal motions of the shoulder are: abduction and adduction, flexion and extension, horizontal flexion and extension, exorotation and endorotation.

1.2 The shoulder mechanism

The shoulder mechanism is an example of a very complex musculoskeletal structure consisting of a chain of bones connecting the upper extremity to the trunk. The shoulder girdle consists of a scapula and a clavicle and functions as a movable but stable base for the motions of the humerus (Fig. 1). The shoulder comprises of three synovial joints which interconnect the bones:

- The sternoclavicular (SC-) joint, connecting the sternum part of the thorax to the clavicle.
- The acromioclavicular (AC-) joint, connecting the clavicle to the acromion of the scapula.
- The glenohumeral (GH-) joint, usually represented by a ball-and-socket joint between the glenoid cavity of the scapula and the head of the humerus (Fig. 2).

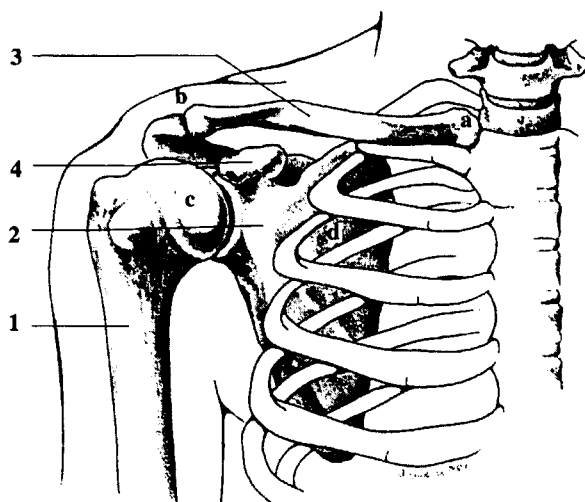**Figure 1.** The bony structure and joints of the shoulder girdle (Stenvers, 1994).
1. Humerus; 2. Scapula; 3. Clavicle; 4. Coracoid Process; a. SternoClavicular
(SC) joint; b. AcromioClavicular (AC) joint; c. GlenoHumeral (GH) joint;
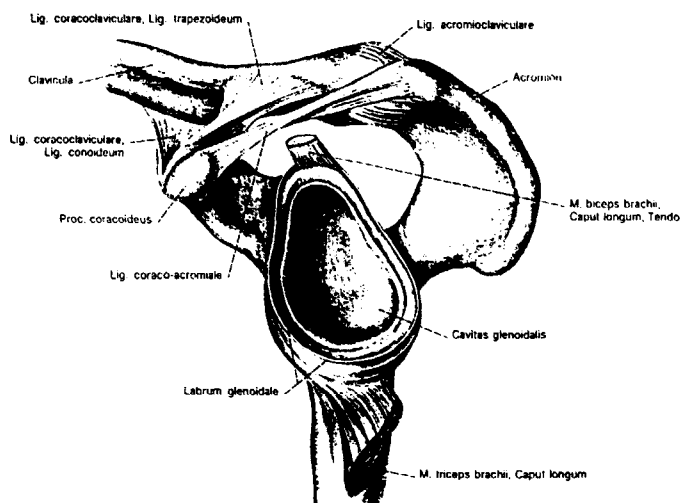d. ScapuloThoracic Gliding Plane (STGP).

Figure 2. A view of the glenoid cavity, in which the humeral head articulates,
with the surrounding anatomical structure (adapted from Sobotta, 1988).

Table 1. The seventeen muscles of the shoulder mechanism with subdivision of the muscles in 20 functional parts and ninety-five muscle lines of action (Van der Helm, 1991). The abbreviation m. stands for muscles (Fig. 3).

Muscle	Part	Origin	Insertion	Number of muscle lines of action
m. trapezius	pars clavicularis	thorax	clavicle	6
	pars scapularis	thorax	scapula	6
m. levator scapulae		thorax	scapula	3
m. rhomboideus		thorax	scapula	3
m. pectoralis minor		thorax	scapula	4
m. subclavius		thorax	clavicle	-
m. serratus anterior		thorax	scapula	6
m. latissimus dorsi		thorax	humerus	5
m. pectoralis major	pars clavicularis	clavicle	humerus	5
	pars thoracalis	thorax	humerus	5
m. deltoideus	pars clavicularis	clavicle	humerus	6
	pars scapularis	scapula	humerus	6
m. coracobrachialis		scapula	humerus	6
m. teres major		scapula	humerus	6
m. teres minor		scapula	humerus	6
m. infraspinatus		scapula	humerus	6
m. supraspinatus		scapula	humerus	6
m. subscapularis		scapula	humerus	6
m. triceps	caput longum	scapula	ulna	2
m. biceps	caput longum	scapula	radius	1
	caput breve	scapula	radius	1

The articulating geometry of these synovial joints is complex. For many purposes they can be regarded as ball joints, neglecting the possibility of small translations. During movement of the arm, the medial border of the scapula slides over the dorsal side of the thoracic cage, pressed onto it by the combined action of muscles. This connection gives rise to a fourth joint, the Scapulo-Thoracic Gliding Plane (STGP). The double connection between the scapula and the thorax, one via the clavicle and the other by the STGP makes the system a closed chain mechanism. There are three extracapsular ligaments in the shoulder girdle: the costoclavicular ligament limiting the range of motion of the SC-joint and the conoid and trapezoid ligament acting at the AC-joint. Seventeen muscles are crossing the joints of the shoulder mechanism; most of them are polyarticular, fan-shaped and have large attachment sites. The locations of the muscles are shown in two views in Figures 3a and 3b. The muscles were divided into twenty different muscle parts based on the joints that each muscle part crossed. Based on the muscle fibre distribution within a muscle, each of these muscles was represented by 1 to 6 muscle lines of action of force between origin and insertion (Van der Helm and Veenbaas, 1991). A classification of the muscles and muscle parts for the shoulder mechanism is presented in Table 1.
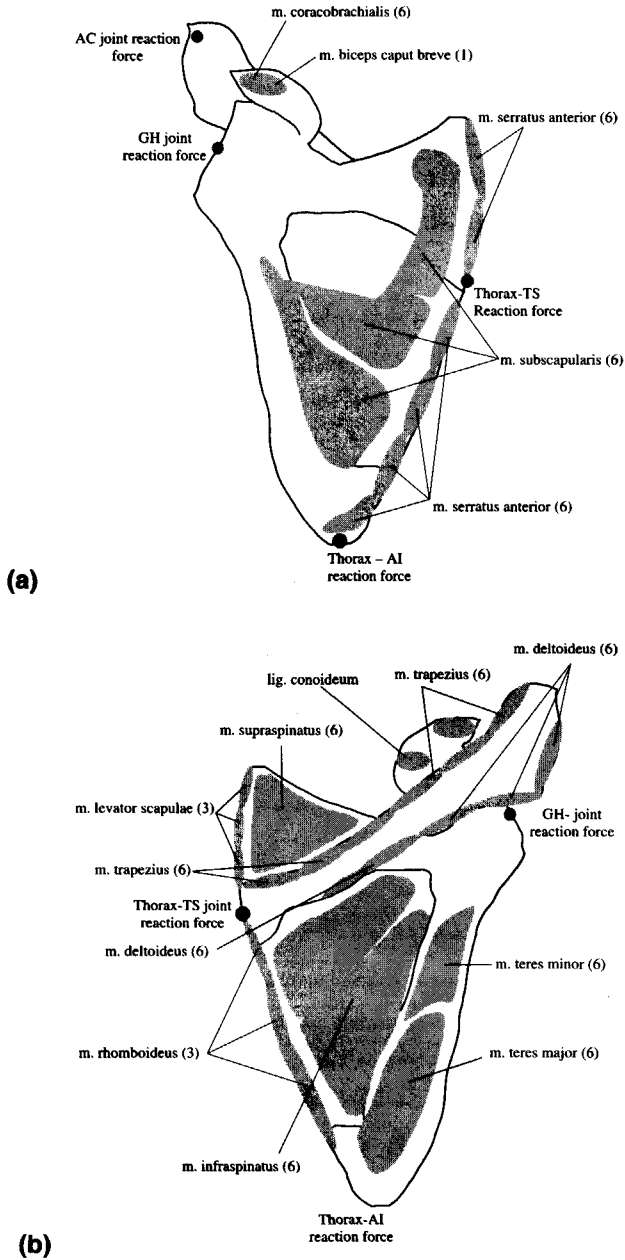
(a)

(b)

Figure 3. The locations of the muscles (m.) and the joint reaction forces in the scapula. Numbers within bracket indicate the number of muscle lines of action. (a) ventral view; (b) dorsal view.

In contrast to the pelvic girdle, a considerable range of motion is achieved by the shoulder girdle. Although the motions of the scapula are severely constrained, the large range of motion of the humerus is due to the simultaneous motions at the SC-, AC- and GH- joints.

1.2.1 The scapula

The scapula is a large, flat, triangular bone consisting of five solid bony ridges (glenoid, scapular spine, lateral border, medial border and coracoid process) and two thin, hard laminated structures (infraspinous and supraspinous fossa). The infraspinous fossa is surrounded by the glenoid, the scapular spine, the medial border, and the lateral border. The structure of the scapula, in two views (ventral and dorsal) is shown in Figures 4a and 4b. It is subject to a number of muscle forces, ligament and joint reaction forces during motions of the arm. The quantitative and qualitative estimates of all the muscle, ligament and joint reaction forces acting on the scapula, during activities like unloaded humeral abduction, unloaded anteflexion, loaded abduction and loaded anteflexion was investigated extensively by Van der Helm (1994[a,b]). It seems, from the location, magnitude and direction of these forces that the scapula is loaded all over its structure. The primary function of the scapula is two-fold. On the one hand it offers an additional joint, so that the total rotation of the humerus with respect to the thorax can increase. On the other, it is a large bone, where the muscles have large lever arms with respect to the SC- and AC- joint. Hence, smaller muscles are sufficient to provide the necessary moments, which are in general larger than the moments around the GH- joint. The shape of the scapula provides large moment about SC- and AC-joint. This function is more important for the particular shape of the scapula.

1.3 Gleno-humeral arthroplasty: state-of-the-art

In 1893, Jules Emile Pean (1830 – 1898), a French surgeon, performed the shoulder replacement in a patient with arthritis of the shoulder for the first time (Lungi, 1978). He used a prosthesis made of platinum and rubber, which lasted for approximately two years after implantation and was removed because of uncontrollable inflammation. Despite this complication, the short-term benefits were encouraging and the advent of shoulder arthroplasty was realised.

Shoulder arthroplasty can be classified into two types: the hemi-arthroplasty and the total shoulder arthroplasty. In the former, a humeral component is inserted into the humerus while the scapula remains intact causing a direct metal-bone contact. In the TSA, in addition to the humeral component, a glenoid component is inserted into the glenoid part of the scapula. Hemi-arthroplasty of the shoulder has given excellent results for glenohumeral arthritis in patients with massive irreparable rotator cuff tears (Wirth and Rockwood, 1996). It has the advantage of avoiding a relatively complicated procedure of the insertion of glenoid prosthesis, which requires high technical skill of the surgeon. However, because of the imperfect fit of humeral head in the glenoid cavity, TSA is more widely used.

The TSA involves the reconstruction of GH-joint (Fig. 2), when it is affected by osteoarthritis, rheumatoid arthritis and fractures or dislocations with traumatic arthritis. It was born with the introduction of new total polyethylene glenoid component by Neer (1974). The Neer I prosthesis has been used extensively for the past twenty years and is still widely used. In 1984, Neer introduced the metal-backed polyethylene component as the Neer II prosthesis.

Aseptic glenoid loosening is the most-frequently-encountered complication threatening the TSA (Cofield, 1984; Barrett et al., 1989; Berms, 1993; Sneppen et al., 1996; Torchia et al., 1997;

Sperling et al., 1998; Wallace et al., 1999). Loosening is defined as the progression of radiolucent lines exceeding 1.5 mm in width or any definite change in the position of the component (Stewart and Kelly, 1997; Torchia et al., 1997; Wallace et al., 1999). It is hastened by conforming prostheses, incorrect positioning, rotator cuff tears, and capsular contractures, but it can be protected by secure glenoid fixation. Loosening may occur shortly after surgery, probably due to excessive stresses in the cement, or at the interfaces of cement-bone, implant-cement and implant-bone. Medium (3 to 10 years) and long term (10 years or more) follow-up observations show radiographic changes that indicated loosening (McCullagh, 1995; Berms, 1993; Sneppen et al., 1996; Torchia et al., 1997; Sperling et al., 1998; Skirving, 1999; Wallace et al., 1999). This may be due to bone remodelling, which is caused by TSA induced changes in the stress distributions.

Although cement has been most widely used to achieve almost immediate fixation of the implant with bone, it has been susceptible to failure within itself and at the interfaces with other materials. The uncemented glenoid prosthesis with bone-ingrowth surface emerged as an alternative possibility to the cemented designs. However, variations in the design of uncemented glenoid component were few and the use was limited to patients having a relatively good quality bone stock. Clinical and radiographic feedbacks on uncemented glenoid prosthesis were encouraging as compared to the cemented prostheses (Cofield, 1994; Wallace et al., 1999). The major variable of the study, by Wallace et al., 1999, was the method of fixation of the glenoid component. The results of this study revealed that fixation without cement provided an outcome that was comparable to that fixed with cement, in terms of relief of pain, subjective functional capacity, range of motion, and effect on general health. These findings were consistent with other studies on TSA performed with cement (Barrett et al., 1987; Cofield, 1984; Hawkins et al., 1989; Matsen et al., 1996) or without cement (Franklin et al., 1988; Cofield and Daly, 1992). The overall rate of complications was also similar to those in previous reports (Cofield and Edgerton, 1990; Cofield, 1994; Wirth and Rockwood, 1996). However, the overall prevalence of radiolucent lines associated with the cemented implants was higher than that in case of the uncemented implants (Wallace et al., 1999).

TSA is a technically difficult procedure, with perhaps a greater potential for errors and complications as compared to other commonly performed arthroplasties, like the hip and the knee. In general, the restoration of functional capabilities and the patient satisfaction are considered to be far from normal. For example, a long-term study by Sperling et al. (1998) reported that the results of TSA were considered to be satisfactory if the patient had no or slight pain or moderate pain only with vigorous activity, had external rotation of at least 20 degrees, had active abduction of at least 90 degrees, and was satisfied with the procedure. The likelihood of mechanical failure depends on the stresses induced within the implant material and at the material interfaces as compared to the strength of the material and the interfaces (Huiskes, 1993[a]). Together with the higher stresses evoked in the polyethylene cup, the risk of wear and wear debris formation in these areas might be accelerated in a few cases (Wirth and Rockwood, 1994). From anatomic point of view, a small volume of bone, available for fixation of the glenoid component, is a major limitation in the TSA (Cofield, 1984). CT-scans of the glenoid of a normal healthy person reveal that the cancellous bone has a higher density anteriorly and posteriorly than centrally (Anglin et al., 1996; Müller-Gerbl et al., 1992).

In the biomechanical study on stability and fixation of glenoid components, Fukuda et al. (1988) remarked that the fixation strength of glenoid component was lowest for the Neer I prosthesis (total polyethylene design). The study focuses on comparisons between the types of glenoid prostheses – the metal-backed polyethylene and the non-backed polyethylene.

Table 2. Investigation with cemented glenoid prosthesis (without revision surgery).
PE - PolyEthylene; MB – Metal-Backed polyethylene; N.R. – data Not Recorded.

Author, year	Design	Follow-up period (years)	No. of shoulders	Percentage of defective glenoid component	
				Radio-lucency	*Loosen-ing*
Amstutz et al., 1981	DANA	2 – 10	56	94	4
Neer et al., 1982	Neer I (PE, MB)	2 – 8.25	194	30	0
Cofield, 1984	Neer I	2 – 6.5	73	82	21
Barrett et al., 1987	Neer I	2 – 7.5	50	74	18
Barrett et al., 1989	Neer I (PE) & Neer II (MB)	2 – 11	129	82	10
Hawkins et al., 1989	Neer I	2 – 8.6	70	Nearly all	7
Boyd et al., 1990	Neer I	2 – 10.3	131	N.R.	12
Sneppen et al., 1996	Neer II	4.3 – 11.6	62	21	40
Torchia et al., 1997	Neer I	5 – 17	89	84	82
Stewart and Kelly, 1997	Neer II	7 – 13	37	62	24
Sperling et al., 1998	Neer I	5 – 20	32	59	28
Wallace et al., 1999	Neer II (PE and MB), Cofield (PE), Global (PE)	3.8 – 7.5	32	41	25

In general, all metal backed glenoid components appeared to have sufficient fixation strength against normal shoulder joint forces. The strength of highly porous spongy bone is low, which adds to the complications of fixation of the prosthesis in the glenoid (Frich et al., 1997). Hence, it becomes a real challenge to design a glenoid prosthesis that can maintain secure fixation during the normal movements of the arm.

1.4 The cemented and the uncemented glenoid prostheses

Since the introduction of Neer I prosthesis in the 1970s, several designs closely resembling the Neer I and II prostheses, were developed (Amstutz et al., 1981; Amstutz et al., 1988; Cofield, 1984). The glenoid prosthesis consists of a polyethylene cup with a keel to anchor inside the scapula.

Table 3. Investigation with uncemented glenoid prosthesis (upgraded from Cofield, 1994).

Author, year	Design	Fixation	No. of shoulders	Number of defective glenoid component	
				Radio-lucency	*Loosen-ing*
Bayley and Kessel, 1982	Kessel	Pressfit	33	0	0
McElwain and English, 1987	English-Macnab	Tissue-ingrowth	13	1	1
Copeland, 1990		Pressfit	20	0	0
Roper et al., 1990	Roper-Day	Pressfit	13	1	1
Weiss et al., 1990	English-Macnab	Tissue-ingrowth	9	1	0
Brostrom et al., 1992	Kessel	Pressfit	23	13	2
Cofield and Daly, 1992	Cofield	Tissue-ingrowth	31	3	1
Cofield, 1994	Cofield	Tissue-ingrowth	180	6	4
Wallace et al., 1999	Cofield	Tissue-ingrowth	26	6	2

The designs of these components differ mainly in the radius of the curvature of the cup and the shape of the keel. A larger radius of curvature of the glenoid as compared to the humeral head would allow translation during movement. However, it would lead to an increase in the contact stresses, resulting due to nonconformity of the surfaces in contact. Metal-backed polyethylene component and the use of bone-ingrowth surface (only for metal-backed) are also available.

Clinical and radiographic investigations, mostly with the Neer I (total polyethylene glenoid), and the Neer II (all-polyethylene and metal backed polyethylene glenoid) prostheses, have revealed potential complications with possible revisions and recommendations. Post-operative complications are important in the light of the increasing number of patients who receive shoulder replacements. Component loosening has been identified as the most frequently (33%) occurring complication apart from instability of the rotator cuff, rotator cuff tear, periprosthetic fracture, nerve injury, infection, size of implant and dysfunction of the deltoid muscle (Wirth and Rockwood, 1996). A summary of the radiographic and clinical studies on the cemented glenoid prosthesis is presented in Table 2.

The use of polymethylmethacrylate (PMMA) for fixation of the glenoid prosthesis has been one of the most-frequently-occurring problems in TSA. It has been widely used and preferred, because the fixation of the implant in the bone can be achieved almost immediately. But the use of PMMA has been reported to be less reliable, particularly in the presence of instability or massive tear of the rotator cuff (Barrett et al., 1987; Franklin et al., 1988; Weiss et al., 1990). In some reports, both the total-polyethylene and the metal-backed components fixed with cement

demonstrated radiographic lucent lines at the cement-bone interface of the glenoid component (Amstutz et al., 1988; Cofield and Daly, 1992). Even with modern cementing techniques the progression of radiolucent lines was observed in at least 20 percent of the cases and it was associated with pain and decreased functional capabilities (Cofield, 1983; Cofield, 1984; Norris and Lachiewicz, 1996).

The problem of progressive radiographic changes, the long term efficacy of the cement, and the need for revision of cemented glenoid components have prompted the development of implants with porous surfaces having capabilities of bone-ingrowth to achieve secure fixation with bone. Insertion without cement, of a glenoid component with tissue-ingrowth capability, is not a new concept. But the technique is yet to gain wide acceptance. Cofield (1994) and Wallace et al. (1999) retrospectively reviewed clinically evident loosening of glenoid components, inserted with and without cement. Both these studies remarked that despite the number of complications, the results of uncemented glenoid component were very similar to those reported for TSA using the cemented glenoid component. One of the several features observed in the merit analysis of TSA, was the striking lack of radiographic changes at the implant-bone interface. As compared to the cemented version, slightly increased frequency of high-density polyethylene wears and displacement of the polyethylene from the metal tray, were observed for the uncemented design. A summary of the radiographic and clinical investigation with uncemented glenoid prosthesis is presented in Table 3.

Design variations in the uncemented glenoid prosthesis are few. Most of them consist of, in principle, a polyethylene cup with a metal-backing with tissue-ingrowth capability. Interestingly, one of the earliest forms of TSA possessed tissue-ingrowth at the glenoid and the humeral components (McElwain and English, 1987). The Kessel prosthesis with press fit design, the Cofield metal-backed design with tissue-ingrowth capability, and the Bio-modular porous coated glenoid components (Biomet Inc., Warsaw, Indiana) were developed and continued to be used. Only selected patients, having good bone stock were recommended for the use of these porous coated uncemented prostheses. Some biomechanical studies on uncemented glenoid prostheses, however, were inadequate to draw significant conclusions on the design of the implant (Orr et al., 1988; Stone et al., 1999).

1.4.1 Failure scenarios

The failure scenarios for total hip arthoplasty, introduced by Huiskes (1993[a]) are also useful, more or less, to analyse failure mechanisms of other reconstructed joints like the TSA. Although the failure of an implant is mainly due to biological causes, the initiation of the failure process may be due to mechanical events. Two dominant failure scenarios of the cemented reconstruction can be identified (Huiskes, 1993[a]).

(1) According to the *accumulated-damage failure scenario*, the materials or interfaces are too weak to sustain the effect of long-term, dynamic loads applied on the implants. The likelihood of mechanical failure depends on the stress induced in a material versus the strength of that material. The repetitive nature of the external loads generates high dynamic stresses in the materials and at the interfaces. As a result, mechanical damage, typically micro-cracks, is gradually accumulated in the cement. These micro-cracks reduce the strength of the cement and its bonds at the layer of interface between implant and bone, eventually causing failure. In case of uncemented prostheses, loosening may occur due to the failure of the implant-bone interface as well as the polyethylene-metal interface. The polyethylene cup may be dissociated from the metal-backing, which may still maintain a secure fixation with bone, thus resulting in failure of the prosthesis. The eventual gross

loosening of the implant may be due to the cement-bone interface loosening, failure (cracking) of the cement due to excessive stresses, and relative motions between the materials.

(2) According to the *particulate-reaction failure scenarios*, the cement-bone interface gradually disintegrates due to the migration of wear particles. These tiny particles may be polyethylene debris, abraded from the cup of glenoid prosthesis, cement particles abraded from the cement mantle, or metal debris burnished from the implant. The polyethylene wear debris, in particular, is considered to be a major threat to any arthroplasty. These wear debris cause particulate reactions by macrophages, osteolysis, soft tissue interposition and finally gross loosening.

In this study, particle generation was not really used. Only, mechanical damage due to stresses has been studied. However, the effect due to progressive damage accumulation in different material has not been studied. The initial stress distribution in the implant-bone structure has been critically examined with regard to the strength of the material. The multi-axial stresses at the interface of the different material have been evaluated. The comparisons and evaluations of the study were based on (1) fixation technique – cemented and uncemented, (2) type of the implant – metal-backed or non-backed. The study is considered to be a first major step towards understanding the load transfer mechanism in the glenoid prostheses and to identify the mechanical factors responsible for the loosening of the implant, postoperatively.

1.5 Finite element model of the scapula

Stress analysis is required for evaluations on implant-bone configuration. It helps in design, failure prediction and improvement of an implant. The introduction of computer modelling techniques, in particular, the finite element method, offers the possibility to test and to validate certain clinical hypotheses rigorously (Huiskes et al., 1987; Huiskes et al., 1989; Huiskes et al., 1992; Huiskes, 1993[a]; Huiskes, 1993[b]; Dalstra et al., 1995; Huiskes, 1997; Kerner et al., 1999). The basic tool used in this thesis is the Finite Element Method (FEM), which has emerged as an important tool in orthopaedic research to determine stresses and strains in bone and in various components concerning the fixation of artificial joints and the effect of adaptive bone remodelling. It is a fast and efficient pre-clinical testing method to visualise biomechanical problems as compared to the clinical follow-up procedure.

Studies related to FE analysis of the scapula were mostly restricted to two-dimensional (2-D) models of the glenoid with or without a prosthesis (Orr et al., 1988; Friedman et al., 1992; Lacroix and Prendergast, 1997; Stone et al., 1999). The geometry, material properties and loading conditions of these models appeared to be far from real. The 2-D models can indicate certain trends in the stress distributions, but for more detailed evaluations, 3-D models are indispensable.

The 3-D model of Lacroix et al. (1997) and Lacroix et al. (2000) using CT-scan data was an effort in that direction. The errors involved in the FE modelling, however, were not discussed in these studies, thus making it difficult to assess the accuracy of FE representation. A number of investigators have reported 3-D FE modelling of bone (Keyak et al., 1990; Harrigan and Harris, 1991; Weinans et al., 1991; Keyak and Skinner, 1992; Keyak et al., 1993; Dalstra et al., 1995) using CT-scan data for various biomechanical studies. Unfortunately, until now, there has been hardly any report on the load transfer mechanism across a normal scapula, using a realistic 3-D FE model.
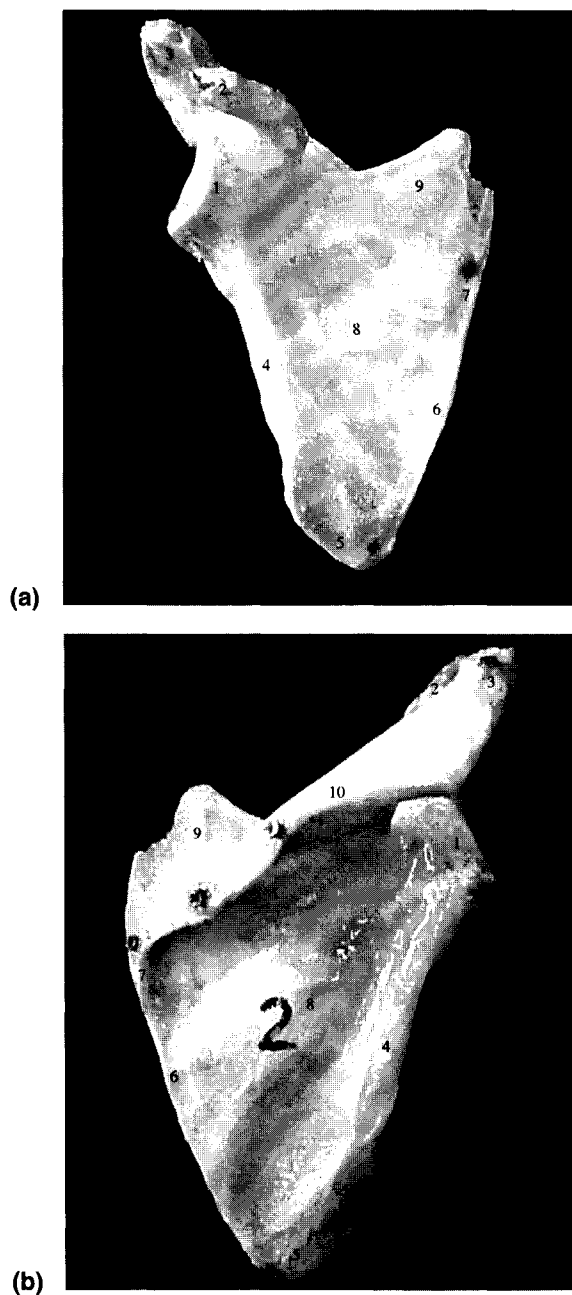
(a)

(b)

Figure 4. The scapula. (a) ventral view; (b) dorsal view.
1. Glenoid; 2. Coracoid Process; 3. Acromion; 4. Lateral border; 5. Angulus Inferior;
6. Medial border; 7. Trigonum Spinae; 8. Infraspinous fossa; 9. Supraspinous fossa;
10. Scapular spine.

The quality of a FE model and the accuracy of the results depend on the model itself, as compared to the actual conditions (normal bone or a bone with implant). The accuracy is highly dependent on the correct estimation and distribution of the elastic moduli of elements, constituting the FE model of the scapula. The anisotropy of cancellous bone has considerable effect on the mechanical properties. The type and size of finite elements is an important factor in the correct representation of the structure of bone, with or without implants. The convergence test has often been used to estimate the quality of the FE model. But a thorough experimental validation, though a very difficult and tedious procedure, has always been considered as the best tool to judge the quality of the numerical predictions. The FE models of femur (Keyak et al., 1993) and pelvic bone (Dalstra et al., 1995) were experimentally validated using strain gage technique. Therefore, an experimental validation of the FE model of the scapula using strain gage measurements is considered to be a major investigation. A new experimental set-up was required to test a fresh specimen of cadaveric scapula with strain gages attached all over its surface.

1.6 Motivation of the study

Although the mechanisms of glenoid loosening are not clearly defined, they have been associated with anatomical and biomechanical factors. The precise relationship between the cause and the effect, regarding aseptic loosening of the glenoid prostheses and the extent to which the mechanical factors play a role in this process, however, are not clearly understood yet. In order to analyse these biomechanical factors a detailed 3-D FE model of the glenoid prosthesis is required. These 2-D FE models accounted for several design parameters such as implant material, implant shape, method of fixation by screws or pegs and the use of metal backing (Orr et al., 1988; Friedman et al., 1992; Lacroix and Prendergast, 1997; Stone et al., 1999). But they excluded the detailed 3-D geometry and material properties of the glenoid. The complex shape of the scapula and the varying forces acting on it certainly requires a new approach using a detailed 3-D FE model.

Clinical and radiographic follow-up studies, though a few, reported encouraging results on the prospects of uncemented glenoid prosthesis. But, in order to reveal the biomechanical factors involved in the design of uncemented prosthesis and to develop a better understanding of the load transfer with regard to the potential failure mechanisms, a detailed 3-D FE analysis of the uncemented glenoid prosthesis is necessary. The 2-D FE studies (Orr et al., 1988; Stone et al., 1999), on several designs of uncemented glenoid prosthesis were inadequate to evaluate the implant design.

A realistic three-dimensional (3-D) FE model, using on Computed Tomography (CT) scan data, can reveal the function of constituent parts of a bone and can be useful in understanding the load transfer mechanism due to muscles, ligaments and joint reaction forces. This FE model can be further used for developing a submodel with fine mesh size in the domain of inclusion of the prosthesis to calculate stresses and strains in the different components and at the respective interfaces. These results may be useful in analysing some failure criteria and in recommending measures for improvement of the prostheses design.

1.7 Goal of the study

The primary goal of the study is to develop a better glenoid prosthesis. Therefore, the present study is aimed at investigating the glenoid load transfer mechanism with regard to probable failure scenarios of glenoid prostheses. Analysis of the failure criteria may suggest measures for improved glenoid prostheses. In order to achieve the primary goal, 3-D FE models of two fundamental designs

of cemented glenoid prostheses, one total polyethylene and the other, metal backed polyethylene, are certainly required. The possibilities of the uncemented glenoid prosthesis as compared to the cemented designs are also investigated, using FE stress analysis.

Before analysing an artificial (prosthetic) joint, it is advised to analyse a healthy functioning joint and to understand the basic mechanics of load transfer on a scapula, due to the action of muscles, ligaments, and joint reaction forces. A realistic 3-D FE model of the whole scapula along with the loading conditions taken from the static shoulder model (Van der Helm, 1994[a,b]), are required for assessing the stress distribution in various parts of a scapula during normal physiological movements of the arm. The effect of the load transfer on individual parts of the scapula can be useful in understanding the basic mechanics of the scapula and can serve as the reference solution for comparing deviations in stress distribution, due to insertion of prosthesis. The overall reference model of the natural scapula is also useful in developing a submodel with glenoid prosthesis. Therefore, the development and stress analysis of the 3-D FE model of a normal scapula is an important sub-goal. Although both the computer models and the experimental validation have been used, the emphasis of this study lies on the development, validation and use of the 3-D FE model of the scapula. The later part of the thesis deals with stress analyses of cemented and uncemented glenoid prostheses, in order to understand the load transfer mechanism and to investigate the mechanical factors responsible for potential failure scenarios.

1.8 Structure of the thesis

The present study deals with a biomechanical analysis of stresses and strain in the scapula and the effect of application of glenoid prostheses with or without cement. In view of the complicated 3-D structure of the scapula, the FE method has been used as the basic tool for analysing stresses and strain. Experimental strain gage measurements on fresh scapulae were undertaken in order to validate the FE model of the scapula. The scope of each chapter of the thesis, which collectively contributes towards achieving the primary goal of this study, is presented in the following order.

Chapter 2 describes a study on the bone density and stiffness of scapula trabecular and compact bone from CT-scan measurement. In order to supply the FE model with realistic input data on density and elastic modulus, relationships between the CT gray values in Hounsfield Units, the apparent density and the elastic modulus were determined. Formulation of these relationships is based on experimental data of Frich (1994) and on the analytical structure of the trabecular and compact bone.

An elaborate description on the development of a 3-D FE model of the scapula is presented in Chapter 3. Quantitative CT-scan data have been used for realistic representation of geometry and material properties of the whole scapula. The musculoskeletal shoulder model of forces has been used as applied loading conditions for estimation of stresses in the scapula.

Chapter 4 deals with the experimental strain gage validation of the FE model of a fresh scapula, obtained from a donated cadaver. Eighteen strain gages were glued on the surface of the scapula, which was loaded on a mechanical testing machine. The measured strains and numerical FE strains for all the eighteen strain gages were compared for different load cases in order to obtain a thorough validation of the FE model of the scapula.

The FE model, developed in Chapter 3, has been used in Chapter 5 to study the load transfer in a natural scapula when it is subject to muscle, ligament and joint reaction forces. Using the static

musculoskeletal shoulder model, which includes all muscles, ligaments and joint reaction forces, during humeral abduction, stress distributions in the individual parts of the scapula were analysed.

In Chapter 6, sub-models of two fundamental cemented glenoid component designs (total polyethylene and metal-backed polyethylene) have been developed. These submodels were based on the overall reference solution of the natural scapula (Chapter 5). Using these 3-D FE models of the cemented glenoid prostheses, stress distributions in the individual components and at the material interfaces were obtained for the purpose of analysing design features and failure criteria.

Chapter 7 deals in another 3-D FE submodel model of the glenoid inserted with an uncemented metal-backed prosthesis. Similar to Chapter 6, the stress analysis of its individual components and the respective material interfaces were obtained for analysing failure criteria and exploring the possibilities of uncemented glenoid prostheses as compared to the cemented designs.

Finally, in Chapter 8, the significance and conclusions of the study, as a whole, is presented. Based on the results of each chapter, conclusions are drawn with regard to the motivation and goal of the study, as discussed in the preceding section. A retrospective review and recommendations for future research on improved of glenoid prostheses have been presented.

References

Amstutz, H.C., Sew Hoy, A.L. and Clarke, I.C. (1981). UCLA Anatomic total shoulder arthroplasty. Clin. Orthop. Rel. Res., 155, 7-20.

Amstutz, H.C., Thomas, B.J., Kabo, M.J., Jinnah, R.H. and Dorey, F.J. (1988). The DANA total shoulder arthroplasty. J. Bone Joint Surg. 70A, 1174-1182.

Anglin, C., Tolhurst, P., Wyss, U.P. and Pichora, D.R. (1996). Mechanical properties of glenoid cancellous bone. Proc. 1st Conf. of the International Shoulder Group, Delft University of Technology, Delft, 13-18.

Bayley, J.I.L. and Kessel, L. (1982). The Kessel Total Shoulder Replacement. In Bayley I, Kessel L (eds), Shoulder Surgery. Springer-Verlag, New York, 160-164.

Barrett, W.P., Franklin, J.L., Jackins, S.E., Wyss, C.R. and Matsen, F.A. III (1987). Total shoulder arthroplasty. J. Bone Joint Surg. 69-A (6), 865-872.

Barrett, W.P., Thornhill, T.S., Thomas, W.H., Gebhart, E.M. and Sledge, C.B. (1989). Non-constrained total shoulder arthroplasty for patients with polyarticular rheumatoid arthritis. J. Arthroplasty 4 (1), 91-96.

Berms, J. (1993). The glenoid component in total shoulder arthroplasty. J. Shoulder Elbow Surg. 2, 47-54.

Boyd, A.D., Thomas, W.H., Scott, R.D., Sledge, C.D. and Thornhill, T.S. (1990). Total shoulder arthroplasty versus hemiarthroplasty. J. Arthroplasty 5 (4), 329-336.

Brostrom, L-A., Wallensten, R., Olsson, E. and Anderson, D. (1992). The Kessel prosthesis in total shoulder arthroplasty. Clin. Orthop. Rel. Res. 277, 155.

Cofield, R.H. (1983). Unconstrained total shoulder prosthesis. Clin. Orthop. Rel. Res. 173, 97-108.

Cofield, R.H. (1984). Total shoulder arthroplasty with Neer prosthesis. J. Bone Joint Surg. 66-A(6), 899-906.

Cofield, R.H. and Edgerton, B.C. (1990) Total shoulder arthroplasty: complications and revision surgery. In Instructional Course Lectures, American Academy of Orthopaedic Surgeons 39, 449-462. Park Ridge, Illinois.

Cofield, R.H. and Daly, P.J (1992). Total shoulder arthroplasty with a tissue-ingrowth glenoid component. J. Shoulder Elbow Surg. 1, 77-85.

Cofield, R.H. (1994). Uncemented total shoulder arthroplasty. Clin. Orthop. Rel. Res. 307, 86-93.

Copeland, S. (1990). Cementless total shoulder replacement. In Post. M, Morrey, B.F., Hawkins, R.J. (eds). Survey of the shoulder. St. Louis, Mosby Year Book, 289-297.

Dalstra, M., Huiskes, R. and van Erning, L. (1995). Development and validation of a three-dimensional finite element model of the pelvic bone. J. Biomech. Eng. 117, 272-278.

Frich, L.H. (1994). Glenoid Knoglestyrke og knoglestruktur. Doctoral thesis, University of Aarhus, Denmark.

Frich, L.H., Jensen, N.C., Odgaard, A., Pedersen, C.M., Søjbjerg, J.O. and Dalstra, M, (1997). Bone strength and material properties of the glenoid. J. Shoulder Elbow Surg. 6: 97-104.

Friedman, J.R., LaBerge, M., Dooley, R.L. and O'Hara, A.L. (1992). Finite element modelling of the glenoid component: Effect of design parameters on stress distribution. J. Shoulder Elbow Surg 1, 261-270.

Franklin, J.L., Barrett, W.P., Jackins, S.E. and Matsen, F.A. (1988). Glenoid loosening in total shoulder arthroplasty. Association with rotator cuff deficiency. J. Arthroplasty 3, 39-46.

Fukuda, K., Chen, C.M., Cofield, R.H. and Chao, E.Y. (1988). Biomechanical analysis of stability and fixation strength of total shoulder prostheses. Orthopaedics 11(1), 141-149.

Gibson, L.J. (1985). The mechanical behaviour of cancellous bone. J. Biomechanics 18, 317-328.

Harrigan, T.P. and Harris, W.H. (1991). A three-dimensional non-linear finite element study of the effect cement prosthesis debonding in cemented femoral total hip components. J. Biomechanics 24, 1047-1058.

Hawkins, R.J., Bell, R.H. and Jallay, B. (1989). Total shoulder arthroplasty. Clin. Orthop. Rel. Res. 242, 188-194.

Huiskes, R., Weinans, H., Grootenboer, H.J., Dalstra, M., Fudala, B. and Slooff, T.J. (1987). Adaptive bone-remodelling theory applied to prosthetic-design analysis. J. Biomechanics 20, 1135-1150.

Huiskes, R., Weinans, H. and Dalstra, M. (1989). Adaptive bone-remodelling and biomechanical design considerations for non-cemented total hip arthroplasty. Orthopaedics 12, 1255-1267.

Huiskes, R., Weinans, H. and van Rietbergen, B. (1992). The relationship between stress shielding and bone resorption around total hip stems and the effect of flexible materials. Clin. Orthop. Rel. Res. 274, 124-134.

Huiskes, R. (1993[a]). Failed innovation in total hip replacement. Acta Orthop. Scand. 64, 699-716.

Huiskes, R. (1993[b]). Stress shielding and bone resorption in THA: clinical versus computer-simulation studies. Acta Orthopaedica Belgica 59 (Suppl. 1), 118-129.

Huiskes, R. (1997). Validation of the adaptive-bone remodelling simulation models. In: Lowet, G. et al. (Eds). Bone Research in Biomechanics. IOS Press, Amsterdam, 33-48.

Kerner, J., Huiskes, R., van Lenthe, G.H., Weinans, H., van Rietbergen, B., Engh, C.A. and Amis, A.A. (1999). Correlation between pre-operative periprosthetic bone density and post-operative bone loss in THA can be explained by strain-adaptive remodelling. J. Biomechanics 32, 695-703.

Keyak J.H., Meagher J.M., Skinner H.B. and Mote C.D. Jr. (1990). Automated three-dimensional finite element modelling of bone: a new method. J. Biomed. Eng., 12, 389-397.

Keyak, J.H and Skinner, H.B. (1992). Three-dimensional finite element modelling of bone: effects of element size. J. Biomed Eng. 14, 483-489.

Keyak J.H., Fourkas, M.G., Meagher J.M. and Skinner H.B. (1993). Validation of an automated method of three-dimensional finite element modelling of bone. J. Biomed. Eng., 15, 505-509.

Lacroix, D., Prendergast, P.J., Murray, R., McAlinden, S. and D'Arcy, E. (1997). The use of Quantitative Computed Tomography to generate a finite element model of the scapula. Proc. of the 14th Conf. Irish Manufacturing Committee. Eds. J. Monaghan & C.G. Lyons, 257-262.

Lacroix, D. and Prendergast, P.J. (1997). Stress analysis of glenoid component designs for shoulder arthroplasty. Proc. Inst. Mech. Engrs, Part H 211, 467-474.

Lungli, T. (1978). Artificial shoulder joint by Pean (1893). The facts of an exceptional intervention and the prosthetic method. Clin. Orthop. Rel. Res. 277, 142-154.

Matsen, F.A. III (1996) Early effectiveness of shoulder arthroplasty for patients who have primary glenohumeral degenartive joint diseases. J. Bone Joint Surg. 78-A, 260-264.

McCullagh, P.J.J. (1995). Biomechanics and design of shoulder arthroplasty. Proc. Instn. Mech. Engrs, Part H 209, 207-213.

McElwain, J.P. and English, E. (1987). The early results of porous-coated total shoulder arthroplasty. Clin. Orthop. Rel. Res. 218, 217-224.

Müller-Gerbl, M., Putz, R. and Kenn, R. (1992). Demonstration of subchondral bone density patterns by three-dimensional CT Osteoabsorptiometry as a nonevasive method for in vivo assessment of individual long-term stresses in joints. J. Bone and Mineral Res. 7, Supl. 2, S411 - S418.

Neer, C.S. II (1974). Replacement arthroplasty for glenohumeral osteoarthritis. J. Bone Joint Surg. 56A, 1-13.

Neer, C.S. II, Watson, K.C., Stanton, F.J. (1982). Recent experiences in total shoulder replacement. J. Bone Joint Surg. 64A. 319-337.

Norris, B.L. and Lachiewicz, P.F. (1996). Modern cement technique and the survivorship of total shoulder arthroplasty. Clin. Orthop. Rel. Res. 328, 76-85.

Orr, T.E., Carter, D.R. and Schurman, D.J. (1988). Stress analyses of glenoid component designs, Clin. Orthop. Rel. Res. 212, 217-224.

Roper, B.A., Paterson, J.M.H. and Day, W.H. (1990). The Roper-Day total shoulder replacement. J. Bone Joint Surg. 72-B, 694.

Skirving, A.P. (1999). Total shoulder arthroplasty – current problems and possible solutions. J. Orthop. Sc. 4(1), 42-53.

Sneppen, O., Fruensgaard, S., Johannsen, H.V., Olsen, B.S., Sojbjerg, J.O. and Andersen, N.H. (1996). Total shoulder replacement in rheumatoid arthritis: proximal migration and loosening. J. Shoulder Elbow Surg. 5(1), 47-52.

Sobotta, J. (1988). Atlas of human anatomy. Volume 1: Head, neck upper limbs, skins. Ed. J. Staubesand. Urban & Schwarzenberg, Munich.

Sperling, J.W., Cofield, R.H. and Rowland, C.M. (1998). Neer hemiarthroplasty and Neer total shoulder arthroplasty in patients fifty years old or less. Long-term results. J. Bone Joint Surg. 80-A (4), 464-473.

Stenvers, J.D. (1994). De primaire frozen shoulder, Doctoral thesis, State University of Groningen, The Netherlands.

Stewart, M.P. and Kelly, I.G. (1997). Total shoulder replacement in rheumatoid disease: 7-to 13-year follow-up of 37 joints. J. Bone Joint Surg. 79-B (1), 68-72.

Stone, K.D., Grabowski, J.J., Cofield, R.H., Morrey, B.F. and An, K.N. (1999). Stress analysis of glenoid components in total shoulder arthroplasty. J. Shoulder Elbow Surg. 8(2), 151-158.

Torchia, M.E., Cofield, R.H. and Settergren, C.R. (1997). Total shoulder arthroplasty with Neer prosthesis: long-term results. J. Shoulder Elbow Surg. 6(6), 495-505.

Van der Helm, F.C.T. (1991). The shoulder mechanism, a dynamic approach. Doctoral Thesis, Delft University of Technology. The Netherlands.

Van der Helm, F.C.T. and Veenbaas, R. (1991). Modelling the mechanical effect of muscles with large attachment sites: application to the shoulder mechanism. J. Biomechanics 24(12), 1151-63.

Van der Helm, F.C.T. (1994[a]). Analysis of the kinematic and dynamic behaviour of the shoulder mechanism. J. Biomechanics 27, 527-550.

Van der Helm, F.C.T. (1994[b]). A finite element musculoskeletal model of the shoulder mechanism. J. Biomechanics 27, 551-569.

Wallace, A.L., Phillips, R.L., MacDougal, G.A., Walsh, W.R. and Sonnabend, D.H. (1999). Resurfacing of the glenoid in total shoulder arthroplasty. A comparison, at a mean of five years, of prostheses inserted with and without cement. J. Bone Joint Surg. 81-A (4), 510-518.

Weinans, H., Huiskes, R. and Grootenboer, H.J. (1991). Trends of mechanical consequences and modelling of a fibrous around femoral hip prostheses. J. Biomechanics 23, 991-1000.

Weiss, A.-P.C., Adams, M.A., Moore, J.R. and Weiland, A.J. (1990). Unconstrained shoulder arthroplasty. A five-year follow-up study. Clin. Orthop. Rel. Res. 257, 86-90.

Wirth, M.A. and Rockwood, C.A. (1994). Complications of shoulder arthroplasty. Clin. Orthop. Rel. Res. 307, 47-69.

Wirth, M.A. and Rockwood, C.A. (1996). Current concepts review: complications of total shoulder-replacement arthroplasty. J. Bone Joint Surg. 78A, 603-616.

Chapter 2

Relationships between Computed Tomography Gray Values, Apparent Bone Density and Bone Stiffness for the Human Scapula

Abstract

Mechanical properties of scapular trabecular bone are assumed to be similar to those of other trabecular bone of different anatomical regions, like tibia, femur, humerus. In this paper an attempt has been made to relate quantitatively Computed Tomography (CT) gray values with apparent density, and apparent density with elastic modulus. A linear regression, generalised for all CT-scan slices defining the whole scapula, is derived from two reference points (one no-bone condition, i.e. air, another cortical bone). Based on structural and analytical models of trabecular bone, power law relations are fitted for two ranges of apparent density. Powers of 2 and 3 ($E \sim \rho^2$, $E \sim \rho^3$) have been used for open cell rod-like structure and closed cell plate-like structure, respectively. The transition from open to closed structure is assumed to occur at an apparent density of 350 kg m^{-3}. The theoretical relationships are fitted to experimental data of glenoid cancellous bone specimens. The above-mentioned relationships for scapular trabecular bone are meant to be used for a finite element model of a scapula, with or without an implant, based on CT-scan images.

Keywords: Glenoid, computed tomography, apparent density, elastic modulus, finite element model.

2.1 Introduction

Characterisation of mechanical properties of trabecular bone of human scapulae is essential for glenoid arthroplasty design. From an engineering point of view, bone is a non-homogeneous, anisotropic, and viscoelastic material. Bone has the ability to adapt its structure, by apposition and resorption, according to changes in mechanical loading. This phenomenon of change of internal structure and external geometry is termed as bone remodelling. One of the major problems of shoulder joint replacement is loosening of the glenoid prosthesis. In more than 12% of all Total Shoulder Arthroplasty (TSA), complications due to loosening of the glenoid component were reported by Boyd et al. (1990). The causes of loosening may be either due to localised peak stresses in the different materials of the implant or due to the effect of bone remodelling. Both the effects are caused by the insertion of the implant, which induces changes in the stress distribution as compared to the normal condition. These changes in the stress distribution may trigger bone remodelling process and may cause eventual failure of the implant. Finite Element (FE) models of glenoid component were mostly based on assumptions that the material properties of the glenoid were similar to those of the tibial plateau (Orr et al., 1988; Friedman et al., 1992). Research directed towards investigating the causes of mechanical loosening of the glenoid component and its improvement in design, calls for reliable data on mechanical properties of scapular trabecular bone.

A unique quantitative relationship between the apparent density and the elastic modulus is required to assign material properties to each element of the FE model of the scapula. A relation between quantitative Computed Tomography (CT) gray values (H) of pixels in Hounsfield units and the apparent density (ρ) of bone is of prime importance to start with. McBroom et al. (1985) found a good correlation ($R^2 = 0.89$, $p < 0.0001$) and established a linear relationship between the CT gray values and apparent density (ρ, g/cm^3) of vertebral trabecular bone ($\rho = 0.01317 + 0.00098$ H). Hvid et al. (1989) reported good correlation (R=0.935) and a linear relationship between CT gray values and apparent density of tibial trabecular bone ($\rho = 0.103 + 0.00130$ H). A statistically significant ($R^2 = 0.82$) linear relation between CT gray values and apparent density was observed by Ciarelli et al. (1991) for human trabecular bone from major metaphyseal regions, like tibia, femur, radius and humerus ($\rho = 0.11837 + 0.001141$ H).

Although none of the existing reports predicts a relation between CT gray value and apparent density for scapular trabecular bone, a similar linear relationship can be expected for scapula trabecular bone. Many authors have reported mechanical properties of trabecular bone and relationships between the apparent density and bone stiffness (Carter and Hayes, 1977; Ashman et al., 1987; Ashman and Rho, 1988; Ashman et al., 1989; Choi and Goldstein, 1992; Rho et al., 1993; Keaveny and Hayes, 1993; Van Reitbergen et al., 1995). The results of these studies predicted linear as well as power law relationships. The variation was large and was primarily due to differences in anatomic location, anisotropy of material properties, direction of testing and testing protocol (Rho et al., 1993; Ciarelli et al., 1991; Goldstein, 1987; Carter and Hayes, 1977). Currey (1986), while criticising Hvid et al. (1985), preferred power law models ($E = a\,\rho^{\,b}$, where a and b can be determined) to linear regression models for the mechanical properties of cancellous bone. He argued that there are three advantages:
(1)   theoretically, a power law relation is predicted, which was confirmed by experiments;
(2)   the equation will produce marked improvements towards extrapolation to compact bone on one side and non-bone on the other;
(3)   the distribution of the residuals will be improved for power law model as compared to linear model.

Carter and Hayes (1977) reported a power exponent of 3 to relate apparent density and elastic modulus. However, their study utilised specimens from human tibial plateau and bovine femoral condyles with a significantly different geometry. Turner et al. (1990) formulated relationships between the orthotropic elastic constants of cancellous bone and the fabric tensor, a tensorial measure of anisotropy as well as tissue apparent density. They concluded that relationships between the elastic constants and power (square or cubed) functions of apparent density have better predicted value as compared to linear functions over the entire physiological range.

Gibson (1985), on theoretical considerations, suggested relationships of powers 2 and 3 depending on cancellous bone architecture. An experimental study by Frich (1994) reported densities, elastic moduli, and other mechanical properties of scapula trabecular bone samples. Frich & Odgaard (1995) studied the trabecular bone volume fraction (V_v) in eight zones of six normal glenoids and six rheumatoid arthritis (RA) glenoids. They noted that bone density was lower in RA than normal. The ratio of posterior to anterior V_v was 2:1. They further reported that graphical three-dimensional (3-D) reconstruction and multiplaner image analysis of the normal glenoid specimens showed that a cancellous structure mainly composed of thick platelike trabeculae interconnected by thin rods. Müller-Gerbl et al. (1992) found a greater glenoid subchondral density anteriorly and posteriorly in young people whereas the greatest density was central in elderly people. Batte et al. (1996) conducted an indentation study on five normal cadaveric glenoids. They found the superior regions to be the strongest with anterior-posterior trends varying at three different depths. Mansat et al. (1998) presented data on regional variation of elastic modulus and degree of anisotropy for glenoid cancellous bone. Their data might be useful for FE modelling of the glenoid region only. However, mechanical properties throughout the scapula is required for an overall FE analysis of the scapula and for further prediction of stresses and strain in a glenoid prostheses model using the submodelling technique. Therefore, mathematical relationships between CT-gray value, apparent density and elastic modulus are certainly required, in order to ascribe mechanical properties to each and every element of a detailed FE model of the scapula using CT measurements.

Using the experimental data of density and elastic modulus for scapular bone (Frich, 1994), the purpose of this study is to formulate a quantitative relationship between CT gray value (H) in Hounsfield Units and apparent density (ρ), and between apparent density (ρ) and elastic modulus (E), by regression analyses.

2.2 Materials and Methods

A cadaveric scapula was treated with hydrogen peroxide to remove soft tissues, cleaned with compressed air and water to remove bone marrow and allowed to dry. CT-scans of the dried scapula were made at the Department of Radiology, Leiden University Medical Centre, on a Philips CT scanner (SR7000, scanning energy 120kVp). The CT-images of the scapula were stored in 320X320 pixels, with a pixel size of 0.5 mm X 0.5 mm and slice thickness of 3.0 mm. A total number of 69 slices was obtained to define the whole scapula. The CT images in digitised form were used for subsequent image processing and analysis. CT gray values in Hounsfield units corresponding to specific positions within the scanned image were obtained. The range of the CT gray value of bone (trabecular and compact) was between –1200 (i.e. non-bone) and 2895 (i.e. cortical bone). However, this particular dry scapula could not be further used for preparation of bone samples for measurement of apparent density and elastic modulus. Hence, it was decided to use the data reported by Frich (1994) to establish generalised relationship between apparent density and elastic modulus.

The study by Frich (1994) reported experimental data on apparent density and elastic modulus of trabecular bone samples taken from twenty-five fresh human scapulae. The bone samples, one from each scapula, had all been taken between 3 and 11 mm from the articular surface at the "bare areas" (i.e. approximately in the middle of the articular surface). The cylindrical bone samples 8 mm long and 6.5 mm in diameter were taken from an area, just below the subchondral plate of the glenoid. They were subjected to compression test in order to obtain stress-strain curves. The elastic modulus is determined as the maximum slope of the stress-strain curve in compression up to 1.5% strain. The strain rate of the bone cylinder compression test was 0.1% per second. After these tests the bone samples were cleaned with compressed air to remove bone marrow, degreased in alcohol and acetone, again cleaned with compressed air, and allowed to dry. Apparent densities of the samples were calculated by dividing the weight of the bone mineralised tissue by bulk volume of the specimen.

2.2.1 Statistical analysis

Regression curves are fitted to observations in order to reduce the relationship to a parametric equation. The correlation coefficient (R) and the standard errors (SE) quantify the "goodness of fit" of the dependent variable. The regression curves $f(x)$, with p as the number of parameters and n data points (x_i, y_i) we have,

$$SE = \sqrt{\frac{1}{n - n_p} \sum_{i=1}^{n} (y_i - f(x_i))^2} \tag{2.1}$$

where the denominator $(n - n_p)$ is the number of degrees of freedom.

The correlation coefficient is given by

$$R = \sqrt{\sum_{i=1}^{n} (f(x_i) - \bar{y})^2 \left\{ \sum_{i=1}^{n} (y_i - \bar{y})^2 \right\}^{-1}} \tag{2.2}$$

where $\bar{y}$ is the average of the n data points.

The power law relationship, given by

$$E = a \rho^b, \tag{2.3}$$

with parameters a and b, is fitted to experimental data points of ρ and E by means of least square linear regression method. However, in some cases, only the exponent b were predefined and values of a were calculated. Results are estimates of the parameters (a and b) of the fitted equation, the correlation coefficient and the standard error. The correlation coefficient indicates the extent of agreement in the data. The SE of an estimate is the sum of the residuals, which is related to multiple correlation coefficient squared (r^2). It is a measure of the scatter in the data about the regression line and hence, reflects a component of uncertainty in the data.

2.3 Results and Discussion

2.3.1 Relation between CT gray values *(H)* and apparent density *(ρ)*

The apparent density (ρ) is computed from the CT gray values (H), in Hounsfield units, using a linear calibration derived from two reference points in one of the CT-scan slices. The first point is the CT gray value of air, i.e. -1200, which represents non-bone condition (0 kg m⁻³). The second point is the CT gray value of cortical bone, i.e. 2895, which is assumed to have an apparent density of 1800 kg m⁻³ (Carter and Hayes, 1977; Gibson, 1985; Keyak et al., 1990). The apparent density at any point in the bone can be predicted by linear interpolation of CT gray values. This linear relationship, generalised for all CT-scan slices and based on these two sets of values is:

$$\rho = c + d\,H \tag{2.4}$$

where, $c = 527$ and $d = 0.44$

It may further be added that in case of moist (with marrow *in situ*) bone samples, the first point in the linear calibration should be the CT gray value of water, i.e. 0, which corresponds to non-bone (0 kg m⁻³) condition. The second point can be the CT gray value of compact bone with an apparent density of 1800 kg m⁻³.

2.3.2 Relation between apparent density *(ρ)* and elastic modulus (E)

Apart from twenty-five experimental data points, two additional sets of values of compact bone have been considered for the power law regression analysis. The apparent density of compact bone was about 1800 kg m⁻³ (Galante et al., 1970; Carter and Hayes, 1977), whereas the elastic modulus varied between 15 GPa and 20 GPa (Choi et al., 1990; Rho et al., 1993).

It has been established, both theoretically (Gibson, 1985) and experimentally (Carter and Hayes, 1977; William and Lewis, 1982; Bensusan et al., 1983, Dalstra et al., 1993), that the Young's modulus of cancellous bone was strongly dependent on the bone's apparent density. It was concluded that the power law model was better suited than the linear model for mechanical properties of cancellous bone (Gibson, 1985, Currey, 1986; Turner et al., 1990). A statistical analysis of the power law relationships between apparent density and elastic modulus is presented in Table 1. Considering twenty-seven data points (twenty-five cancellous bone + two assumed compact bone) and fitting regression models, the parameters (*a* and *b* of $E = a\,\rho^{b}$), the SE and the R, were calculated (Table 1); resulting in

$$E = 9.354 \cdot 10^{-7}\, \rho^{3.15}$$

Fitting models with predetermined powers of 2 and 3 results in

$$E = 5.288 \cdot 10^{-3}\, \rho^{2}$$

and
$$E = 2.998 \cdot 10^{-6}\, \rho^{3}$$

Results indicate that the cubic relations are better suited to fit the data as compared to the squared relations (Table 1). The predefined exponent value of 3 fits the data slightly better than the exponent value of 3.15, since the SE is marginally higher in case of the latter (Table 1). However, the high correlation coefficient, ranging between 0.979 and 0.988, for all the three models are considered to be artificially high, since these relations are mainly guided by a cloud of data points located mostly at

the lower and the upper extreme values in the entire range of apparent density. Hence, these relations do not represent the model structure, correctly. To obtain more meaningful relations, the two data points of cortical bone (assumed) were omitted and new regression analyses were performed.

The mechanical behaviour of cancellous bone, consisting of an interconnected network of rod and plate like trabeculae, is similar to that of other cellular solids, such as polymeric foam (Pugh et al., 1973; Gibson, 1985; Rajan, 1985; Gibson and Ashby, 1988). Figure 1, redrawn from Gibson (1985) shows the relationship between Young's modulus and density for cancellous bone with asymmetric structure, fitted to experimental data of Carter and Hayes (1977).
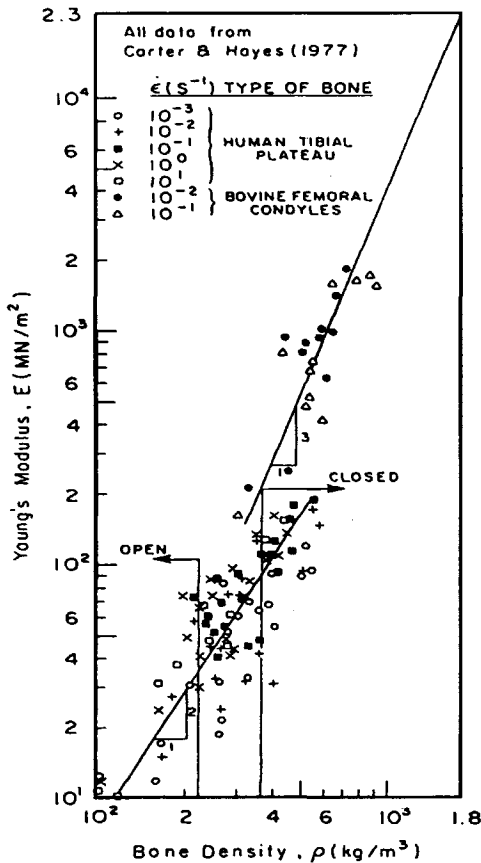

Figure 1. Young's modulus plotted against density for cancellous bone with asymmetric structure, adapted from Gibson (1985). All data from Carter & Hayes (1977).

Table 1. Statistical analysis of power law relationships between apparent density (ρ) and elastic modulus (E). Total number of data points: 27 (experimental data points: 25, and additional cortical bone data points: 2). The coefficients a and b correspond to $E = a\,\rho^{\,b}$.
* excluding two compact bone data points. ‡ for $\rho \leq 350$ kg m^{-3};
† for $350 \leq \rho \leq 1800$ kg m^{-3}; + predefined.

Power fit	Number of data points (n)	a	b	Standard error (SE) (*eqn. 2.1*)	Correlation coefficient (r) (*eqn. 2.2*)
$E = a\,\rho^{b}$	27	9.35×10^{-7}	3.15	714.14	0.988
$E = a\,\rho^{b}$	27	3.00×10^{-6}	3^{+}	703.70	0.987
$E = a\,\rho^{b}$	27	5.30×10^{-3}	2^{+}	953.37	0.979
$E = a\,\rho^{b}$	25^{*}	27.21×10^{-3}	1.41	75.40	0.524
$E = a\,\rho^{b}$	25^{*}	779.87×10^{-6}	2^{+}	75.65	0.488
$E = a\,\rho^{b}$	25^{*}	1.626×10^{-6}	3^{+}	83.81	0.256
$E = a\,\rho^{b}$	$15^{\ddagger}$	1049.25×10^{-6}	2^{+}	43.31	0.403
$E = a\,\rho^{b}$	$13^{\dagger}$	3.00×10^{-6}	3^{+}	1034.63	0.987

The relative density, ρ/ρ_s, can be calculated from the density of cancellous bone, ρ, and that of the trabeculae (or solid cell wall) ρ_s. This is equivalent to the volume fraction of solids in the cancellous bone. At low relative densities, it has rods connecting to form open cells. At higher relative densities, more material is accumulated in the cell walls and the structure transforms into a more closed network of plates. Gibson's analysis showed that the Young's modulus should vary with the square of the density for an open cell structure, and with the cube of density for a closed cell structure. Results of Carter and Hayes (1977) agreed with this prediction and suggested a transition from rod-like to plate-like elements at a density of about 350 kg m^{-3}, or a relative density of 0.20.

Whitehouse (1975) in his scanning electron micrograph study indicated that the cancellous bone structure of the human sternum becomes plate-like for relative densities over 0.20. Following these information, we divide the set of data into two parts as shown in Figure 2. The first set consists of data in the range of 170 – 350 kg m^{-3} (n = 15). The second set ranges from 350 kg m^{-3} to 1800 kg m^{-3} (n = 13). The apparent density value of 350 kg m^{-3} was common to both the sets, and was assumed to be the transition point from open cell structure to closed cell structure. Based on theoretical analysis (Gibson, 1985), powers of 2 and 3 were fitted to the range of data that corresponds to the open cell and the closed cell structure of cancellous bone, respectively.

Considering the set of only twenty-five experimental data points, the power law regression analysis results in,

$$E = 0.0272\ \rho^{1.41}$$

Models with predefined exponent values,

$$E = 780 \cdot 10^{-6}\ \rho^{2}$$

and
$$E = 1.63 \cdot 10^{-6}\ \rho^{3}$$

suggest even weaker correlation (Table 1). A low correlation implies that incorrect model structure has been used, and/or a parameter (e.g. anisotropy) causing the scatter in experimental data could not be estimated. Since the microstructure of bone varies with density, it appears from these results that the data may not belong to a single type of bone.

In this study, a power law model for open cell structure,

$$E = 1049.25 \cdot 10^{-6} \rho^2, \qquad for\ \rho \leq 350\ kg\ m^{-3} \qquad (2.5)$$

was fitted to the data (n=15) in the lower range of apparent density (Fig. 2).
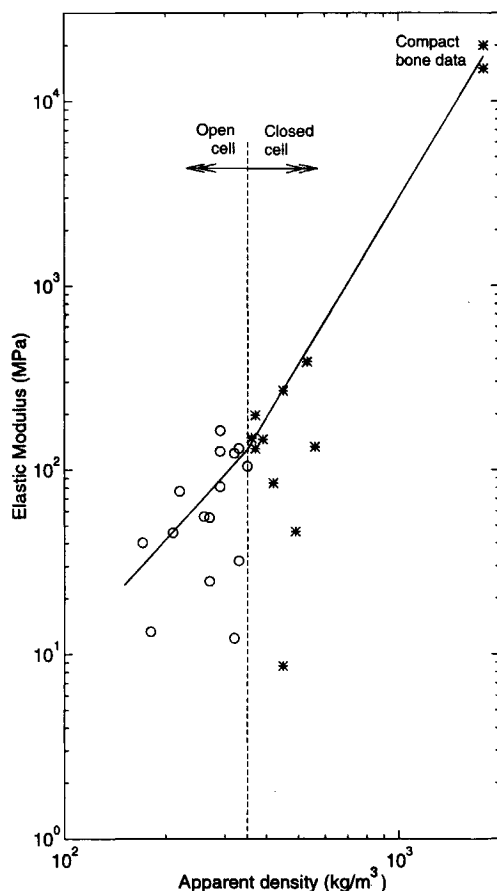
Figure 2. Elastic modulus (MPa) plotted against apparent density (kg/m³);
O experimental data points less than apparent density, 350 kg m⁻³.
* experimental data points for apparent density range from 350 to 1800 kg m⁻³.

The available number of data above 350 kg m^{-3} density (n=13) was limited to a short range. For closed cell structure, a power law model,

$$E = 3.00 \cdot 10^{-6} \rho^3 \qquad for\ 350 \leq \rho \leq 1800\ kg\ m^{-3} \qquad (2.6)$$

was fitted to the higher range of apparent density (Fig. 2). Although in real bone some interval of densities between cancellous and compact bone may never occur, one should expect intermediate values as a result of averaging over CT voxel. In order to ascribe matching mechanical properties to finite elements, elastic modulus should be defined for the whole range of densities.

It is important to know the factors responsible for the considerable scatter in the measured elastic moduli, which causes the low value of the correlation coefficient. In the lower apparent density range, the cancellous bone is an open network of rod-like structures. The variation of trabecular orientation and anisotropy of cancellous bone; from location to location and from specimen to specimen has a considerable effect on the mechanical properties. Hence, anisotropy of cancellous bone is a major factor responsible for the scatter. The data provided by Frich et al. (1997) revealed that the glenoid consists of medium-density, highly anisotropic cancellous bone with a pronounced variation in topographic strength. Non-destructive tests performed on eight cubic specimens taken from glenoid subchondral region, with an average apparent density of 380 kg m^{-3}, indicate large variations in measured elastic modulus (MPa) in three perpendicular directions (Frich et al., 1997). The average elastic modulus values of 410.8 MPa (E_1), 157.1 MPa (E_2) and 78.3 MPa (E_3) were measured in the direction perpendicular to joint surface, anterior-posterior direction and superior-inferior direction, respectively. They found an average anisotropy ratio of 5.2, which indicated strong anisotropy.

Mansat et al. (1998) also presented data on anisotropic material properties for glenoid cancellous bone with ratios $E_1/E_2 = 1.72$, $E_1/E_3 = 1.95$ and $E_2/E_3 = 1.22$, which represented the degree of anisotropy. Their data was based on seventy-four cancellous bone specimens, taken from different regions of the glenoid. These specimens were obtained from six different scapulae. The average values of data indicate lateromedial elastic modulus ($E_1 = 372$ MPa) had the highest value, whereas anteroposterior modulus ($E_2 = 222$ MPa) had an intermediate value, and superoinferior modulus ($E_3 = 193$ MPa) had the lowest value.

The effect of anisotropy is evident in the experimental data of Frich (1994) due to the presence of high (E_{max}) and low (E_{min}) values of elastic modulus corresponding to a value of apparent density ($\rho = 270, 290, 330, 370$ kg m^{-3}). It is also observed that within a very small range of apparent density, an increase in density is associated with a decrease in value of elastic modulus. The other cause that leads to scatter in the measured data is the presence of pores and other forms of inhomogeneity. This is evident in the experimental data; corresponding to a value of apparent density there is a very high and a very low value of elastic modulus. The ratio of a set of high and low values of elastic modulus was found to abnormally high (greater than 10), which is no way comparable to the values of degree of anisotropy presented in earlier studies (Frich et al., 1997; Mansat et al, 1998). Moreover, the degree of anisotropy could not be quantitatively determined, since information on the trabecular orientation of bone specimens was not known. Hence, it is difficult to formulate relations between orthotropic elastic constants and apparent density based on fabric dependence. For practical purposes, relations between the effective isotropic tissue modulus and the apparent density has been formed that might be useful for the FE model of the scapula and the glenoid prostheses.

Table 2. Comparison of power law models for cancellous bone stiffness.
E = elastic modulus; ρ = apparent density; a = constant; b = constant; s.r.= strain rate;
C.L.= confidence level.

Reference	Type of bone	Power law model $E = a\,\rho^{b}$ Exponent, b	Testing protocol
Carter and Hayes (1977)	General	3	$0.001 \leq$ s.r.≤ 10 s^{-1}
Gibson (1985)	Open cell	2	Theoretical consideration
	Closed cell	3	*(Ref.: data from*
			Carter & Hayes, 1977)
Lang et al. (1988)	Vertebra	1.21	Not reported
Rice et al. (1988)	General	2	s.r.= 0.001 s^{-1}
Hvid et al. (1989)	Proximal tibia	1.33	s.r.= 0.01 s^{-1}
Ciarelli et al. (1991)	Proximal femur	1.80	s.r.= 0.01 s^{-1}
	Distal femur	1.45	
	Proximal tibia	2.05	
	Proximal humerus	2.06	
	Distal radius	1.80	
	Overall population	1.87	
Dalstra et al. (1993)	Pelvic bone	2.46 (C.L. 90%)	s.r.= 0.001 s^{-1}
		2.32 (C.L. 95%)	
		2.33 (C.L. 99%)	
Anglin et al. (1996)	Scapula	0.76	Not reported
Our model	Scapula		s.r. = 0.001 s^{-1}
	Overall	3	*(based on data from*
	Open cell	2	*Frich, 1994)*
	Closed cell	3	

The basic question about the quality of the suggested models (ρ and E) is still unanswered. It should be noted that the Root Mean Square Error (RMSE) values are almost 50% of the actual values of the elastic modulus in the lower density range (open cell structure). The results of the experimental study by Kabel et al. (1999), however, supported the hypothesis that for practical purposes, tissue anisotropy has negligible – if any – impact on the apparent elastic properties of human cancellous bone. Without providing any experimental evidence, earlier studies had often implicitly assumed the hypothesis to be valid (Cowin, 1985; Turner et al., 1990; Goulet et al., 1994). The experimental study, challenging the hypothesis, was based on twenty-nine trabecular bone specimens taken from different parts of the vertebral body of a whale (Kabel et al., 1999). Good

agreement was found between the elastic constants determined from experiments and those determined from micromechanical FE analyses in which a unique 'effective isotropic tissue modulus' was used (Kabel et al., 1999). They suggested that for practical purpose, the concept of an 'effective isotropic tissue modulus' was a viable one. They also remarked that the value of such a modulus was independent of volume fraction but dependent on the average tissue density, hence the bone mineral content (BMC). Considering the experimental errors, it seems reasonable to accept the relations of powers 2 and 3 from Gibson (1985) between apparent density and elastic modulus for the purpose of finite element modelling and stress analysis. Table 2 summarises the comparison of our model with similar studies on trabecular bone of different anatomical locations.

2.4 Conclusion

A linear relation between computed tomography (CT) gray values and apparent density of scapula trabecular bone is formed. A power law relationship between apparent density and elastic modulus has been formulated for two different ranges of apparent density. For the lower range ($\rho \leq$ 350 kg m^{-3}), a power of 2, and for the upper range ($350 \leq \rho \leq 1800$ kg m^{-3}), a power of 3 was fitted to experimental data of Frich (1994). It may be argued that the power law relations not only take into account a combination of cancellous, trabecular and cortical bone but also the mechanically implicit data point of zero bone mineral content, with associated zero values of elastic modulus. The considerable scatter in the experimental data is mainly due to the anisotropy of glenoid cancellous bone. The relationships obtained from experimental data of Frich (1994) regarding the apparent density and elastic modulus of human scapula cancellous bone, are consistent with the predictions of Gibson (1985) and can be useful in finite element modelling of scapula from CT-scan images.

Acknowledgements

References

Anglin, C., Tolhurst, P., Wyss, U.P. and Pichora, D.R. (1996). Mechanical properties of glenoid cancellous bone. Proc. 1st Conf. of the International Shoulder Group, Delft University of Technology, Delft, 13-18.

Ashman, R.B., Corin, J.D., and Turner, C.H. (1987). Elastic properties of cancellous bone: measurement by an ultrasonic technique. J. Biomechanics 20, 979-986.

Ashman, R.B., and Rho, J.Y. (1988). Elastic modulus of trabecular bone material. J. Biomechanics 21, 177-181.

Ashman, R.B., Rho, J.Y., and Turner, C.H. (1989). Anatomical variation of orthotropic elastic modulii of the proximal human tibia. J. Biomechanics 22, 895-900.

Batte, S.W.P., Cordy, M.E., Lee, T.Y., King, G.J.W., Johnson, J.A., and Chess, D.G. (1996). Cancellous bone properties of the glenoid: correlation of quantitative CT and mechanical strength. Trans. Orthop. Res. Soc. 21, 707.

Bentzen, S.M, Hvid, I., and Jorgensen, J. (1987). Mechanical strength of tibial trabecular bone evaluated by X-ray computed tomography. J. Biomechanics 20, 743-752.

Bensusan, J.S., Davy, D.T., Heiple, K.G. and Verdin, P.J. (1983). Tensile, compressive and torsional testing of cancellous bone. Trans. Ortho. Res. Soc. 29th Meeting, 132.

Boyd, A.D., Thomas, W.H., Sledge, and C.D., Thornhill, T.S. (1990). Failed shoulder arthroplasty (Abstract), Orthop. Trans. 14, 255.

Carter, D.R., and Hayes, W.C. (1977). The compressive behaviour of bone as a two-phase porous structure. J. Bone Joint Surg. 59-A, 954-962.

Choi, K. and Goldstein, S.A. (1992). A comparison of the fatigue behaviour of human trabecular and cortical tissue. J. Biomechanics 25, 1371-1381.

Ciarelli, M.J., Goldstein, S.A., Kuhn, J.L., Cody, D.D., and Brown, M.B. (1991). Evaluation of orthogonal mechanical properties and density of human trabecular bone from major metaphyseal regions with material testing and computer tomography. J. Orthop. Res. 9, 674-682.

Cowin, S.C. (1985). The relationship between the elasticity tensor and the fabric tensor. Mechanics Mater. 4, 137-147.

Currey, J.D. (1986). Power law models for the mechanical properties of cancellous bone. J. Engineering in Medicine 15, No. 3, 153-154.

Dalstra, M., Huiskes, R., Odgaard, A., and Erning, L. van (1993). Mechanical and textural properties of pelvic trabecular bone. J. Biomechanics 26, 523-535.

Frich, L.H. (1994). Glenoid Knoglestyrke og knoglestruktur. Doctoral thesis, University of Aarhus, Denmark.

Frich, L.H. and Odgaard A. (1995). Bone architecture of the normal and rheumatoid arthritic glenoid. Trans. Orthop. Res. Soc. 20, 683.

Frich, L.H., Jensen, N.C., Odgaard, A., Pedersen, C.M., Søjbjerg, J.O. and Dalstra, M, (1997). Bone strength and material properties of the glenoid. J. Shoulder Elbow Surg.; 6: 97-104.

Friedman, J.R., LaBerge, M., Dooley, R.L. and O'Hara, A.L. (1992). Finite element modelling of the glenoid component: Effect of design parameters on stress distribution. J Shoulder Elbow Surg. 1, 261-270.

Galante, J., Rostoker, W., and Ray, R.D. (1970). Physical properties of trabecular bone. Calcif Tissue Res. 5, 236-246.

Gibson, L.J. (1985). The mechanical behaviour of cancellous bone. J. Biomechanics 18, 317-328.

Gibson, L.J. and Ashby, M.F. (1988). Cellular solids: structure & properties, Pergamon Press, Oxford, UK.

Goldstein, S.A. (1987). The mechanical properties of trabecular bone: dependence on anatomical location and fixation. J. Biomechanics 20, 1055-1061.

Goulet, R.W., Goldstein, S.A., Ciarelli, M.J., Kuhn, J.L., Brown, M.B. and Feldkamp, L.A. (1994). The relationship between the structural and orthogonal compressive properties of trabecular bone. J. Biomechanics 27, 375-389.

Hvid, I., Jensen, N.C., Bünger, C., Sølund, K., and Djurhuus, J.C. (1985). Bone mineral assay: its relation to the mechanical strength of cancellous bone, Engng Med., 14, 79-83.

Hvid, I., Bentzen, S.M., Linde, F., Mosekilde, L., and Pongsoipetch, B. (1989). X-ray quantitative computer tomography: the relations to physical properties of proximal tibial trabecular bone specimens. J. Biomechanics 22, 837-844.

Kabel, J., van Rietbergen, B., Dalstra, M., Odgaard, A., and Huiskes, R. (1999). The role of an effective isotropic tissue modulus in the elastic properties of cancellous bone. J. Biomechanics 32, 673-680.

Keaveny, T.M., and Hayes, W.C. (1993). A 20-year perspective on the mechanical properties of trabecular bone. J. Biomechanical Eng. 115, 534-542.

Keyak, J.H., Meagher, J.M., Skinner, H.B., and Mote, C.D. (1990). Automated three-dimensional finite element modelling of bone: a new method. J. Biomed. Eng. 12, 389-397.

Lang, S.M., Moyle, D.D., Berg, E.W., Gilpin, A.T., Pappas, N.J., Renolds, J.C., Tkacik, M, and Waldron, R.L. (1988). Correlation of mechanical properties of vertebral trabecular bone with equivalent mineral density as measured by computer tomography. J. Bone Joint Surg. 70-A, 1531-1538.

Mansat, P., Barea, C., Hobatho, M-C., Darmana, R. and Mansat, M. (1998). Anatomic variation of the mechanical properties of the glenoid. J. Shoulder Elbow Surg. 7, 109-115.

McBroom, R.J., Hayes, W.C., Edwards, W.T., Goldberg, R.P., and White, A.A. (1985). Prediction of vertebral body compressive fractures using quantitative computer tomography. J. Bone Joint Surg. 67A, 1206-1214.

Müller-Gerbl, M., Putz, R. and Kenn, R. (1992). Demonstration of subchondral bone density patterns by three-dimensional CT Osteoabsorptiometry as a nonevasive method for in vivo assessment of individual long-term stresses in joints. J. Bone and Mineral Research 7, Supl. 2, S411-S418.

Orr, T.E., Carter, D.R. and Schurman, D.J. (1988). Stress analyses of glenoid component designs, Clin. Orthop. Rel. Res. 212, 217-224.

Pugh, J.W., Rose, R.M., and Radin, E.L. (1973). A structural model for the mechanical behaviour of trabecular bone. J. Biomechanics 6, 657-670.

Rajan, K. (1985). Linear elastic properties of trabecular bone: a cellular solid approach. J. Mat. Sc., Letters 4, 609-611.

Rho, J.H., Ashman, R.B., and Turner, C.H. (1993). Young's modulus of trabecular and cortical bone material: ultrasonic and microtensile measurements. J. Biomechanics 26, 111-119.

Rice, J.C., Cowin, S.C., and Bowman, J.A. (1988). On the dependence of the elasticity and strength of cancellous bone on apparent density. J. Biomechanics 21, 155-168.

Turner, C.H., Cowin, S.C., Rho, J.Y., Ashman, R.B. and Rice, J.C. (1990). The fabric dependence of the orthotropic elastic constants of cancellous bone. J. Biomechanics 23, 549-561.

Van Rietbergen, B., Weinans, H., Huiskes, R., and Odgaard, A. (1995). A new method to determine trabecular bone elastic properties and loading using micromechanical finite element models. J. Biomechanics 28, 69-81.

Whitehouse, W.J. (1975). Scanning electron micrographs of cancellous bone from the human sternum. J. Pathol. 116, 213-223.

William, J.L and Lewis, J.L. (1982). Properties and an anisotropic model of cancellous bone from the proximal tibial epiphysis. J. Biomech. Engng 104, 50-56

Chapter 3

Three-dimensional Finite Element Modelling of the Human Scapula using Computed Tomography

Abstract

The scapula is one of the most complex bones of the human body due to its irregular geometry and loading conditions. In some Finite Element (FE) models, mostly two-dimensional (2-D) and restricted to the glenoid area, these aspects have been simplified to a great extent resulting in evaluations of stress patterns that are far from real. The objective of this study is to develop a detailed 3-D FE model of the scapula that can predict stresses and strains realistically. A combination of shell and solid elements has been used to model the structure of the scapula. Shell elements were used to represent a part of the compact bone layer (i.e. the outer cortical bone layer) and the thin and flat part of the scapula - infraspinous fossa and supraspinous fossa, respectively. Solid elements were used to model the remaining part of the compact bone and the trabecular bone. The geometry of the model, material properties throughout the scapula, and thickness of the shell elements, were obtained from Computed Tomography (CT) scan data. The FE model results in proper element shapes without distortion. The applied loading conditions, corresponding to 90-degree abduction of the arm, were obtained from a static shoulder model of forces. High stresses (tensile and compressive) in the range of 40 – 60 MPa, are generated in the lateral border, scapular spine, and at the connection of spine-glenoid-fossa. Relatively low stresses (0.06 – 15 MPa) are observed in the infraspinous and supraspinous fossa. The stresses in the low-density trabecular bone are observed macroscopically. Microscopically, these stresses in the open cell trabecular structure will differ, significantly. Stresses in the outer cortical layer, represented by shell elements are higher (25 – 40%) than stresses induced in the underlying compact bone layer of solid elements. Based on the structure and loading conditions, the combination of shell and solid elements is appropriate for scapula modelling since bending and membrane capabilities can be included in the model, while reduction of the number of elements is an important advantage.

Keywords: Finite element analysis, bone, shoulder, scapula, computed tomography.

3.1 Introduction

The Finite Element (FE) method has become an indispensable tool in orthopaedics research to estimate stresses and strain in bones and endoprosthetic constructions. Three-dimensional (3-D) FE analysis is required to access the total stress field in the bone. It helps in design, failure prediction and improvement of the total joint replacement.

The shoulder mechanism is an example of a very complex musculoskeletal system. Four joints articulating in the shoulder (Fig. 1) are, (1) the GlenoHumeral (GH) joint; (2) the AcromioClavicular (AC) joint; (3) the SternoClavicular (SC) joint; and (4) the ScapuloThoracic Gliding Plane (STGP). One of the most important joints in the shoulder girdle is the GH joint connecting the scapula to the humerus. Replacement of the joint is necessary when it is affected by osteoarthritis or rheumatoid arthritis. This causes pain and immobility. Initiation of loosening in the implant is probably due to excessive stresses, (1) in the implant material and (2) at the interfaces of bone and cement or implant, with regard to the strength of the material and the interface. Boyd et al. (1990) reported that in more than 12 percent of the total shoulder arthroplasties (TSA), complications due to loosening of the glenoid component have occurred. Berms (1993) presented data on the failure percentage of different types of shoulder prostheses used in TSA. He reported that the overall percentage of total shoulders with radiolucent lines was 38.6. Before analysing the artificial (prosthetic) joint, it is advised to analyse a healthy functioning joint and to understand the mechanics of load transfer on the scapula. This study would lead to prediction of stresses and strain due to physiological loading conditions, during unloaded humeral abduction. The overall FE model of the scapula would serve as a reference solution, which is necessary for developing FE models of glenoid prostheses using the submodelling technique.

Studies related to FE modelling and stress analysis of the scapula have been mostly restricted to two-dimensional (2-D) models of the glenoid with or without a prosthesis (Orr et al., 1988; Friedman et al., 1992; Lacroix and Prendergast, 1997, Stone et al., 1999). The geometry, material properties and loading conditions of these models appear to be far from realistic condition. The 2-D models can indicate certain trends in stress pattern, but for more detailed evaluations, 3-D models are indispensable. The 3-D model of Lacroix et al. (1997) and Lacroix et al. (2000) using Computed Tomography (CT) data was an effort in this direction. But the accuracy of the FE representation, in particular the errors involved in the FE reconstruction from CT-scan data and in the numerical analysis are not clearly indicated. A number of investigators have reported 3-D FE modelling of bone using CT-scan data for various biomechanical studies (Keyak et al., 1990, Keyak and Skinner, 1992, Weinans et al., 1993, Keyak et al., 1993, Dalstra et al., 1995). A 3-D model of femur was generated from CT-scans to investigate adaptive bone remodelling in THA (Huiskes et al., 1987, Huiskes et al., 1989, Van Rietbergen et al., 1993; Weinans et al., 1993). Pelvic bone models in 3-D were developed and analysed by Oonishi et al. (1983) and Dalstra et al. (1995). In this paper the development of a realistic 3-D FE model of a normal healthy scapula is described.

Reliable data on mechanical properties of scapular trabecular and cortical bone are required for the FE model. The properties can be estimated from CT-scan data using relations between the CT gray values (H), the apparent density (ρ) and the elastic modulus (E). Such relations have already been estimated for a variety of long bones (Carter and Hayes, 1977; Gibson, 1985; Rice et al., 1988; Hvid et al., 1989; Ciarelli et al., 1991; Dalstra et al., 1993). Data on glenoid trabecular bone samples subjected to compression tests have been taken from Frich (1994). Relations between CT gray value, apparent density and elastic modulus were developed using these data (Chapter 2).

It is difficult to obtain proper loading conditions for the upper extremity since many different tasks can be performed. The shoulder girdle consists of scapula and clavicle and functions as a movable and stable base for the articulation of the humerus. The SC joint connects the clavicle to the sternum, and the scapula in its turn is connected to the clavicle by the AC joint. Another connection between scapula and thorax is the scapulothoracic gliding plane, which constrains possible movements with two Degrees-Of-Freedom (DOF) and makes the system a closed chain. The humerus articulates with the scapula at the GH joint, a ball-and-socket joint. The extracapsular ligaments in the shoulder are the costoclavicular ligaments, limiting the range of motions of the SC joint and the conoid and trapezoid ligaments limiting motions at the AC joint. Some seventeen muscles are crossing the joints of the shoulder mechanism. Many of them are polyarticular, fan-shaped and have large attachment areas. The musculoskeletal shoulder model of forces (Van der Helm, 1994[a,b]) was a significant contribution towards quantitative evaluation of muscles, ligament and joint reaction forces acting on the scapula during movements of the arm.

The objective of this study is to develop a detailed 3-D FE model of the scapula that may resemble its peculiar structure and material properties accurately. The geometry and material properties of the FE model are obtained from CT-scan data, whereas the forces calculated with the musculoskeletal shoulder model (Van der Helm, 1994[a,b]) have been applied as loading conditions to evaluate the nature of stresses in the scapula.
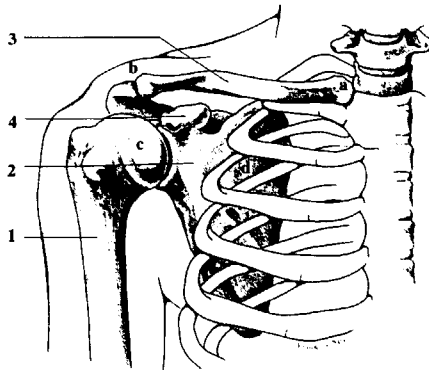

Figure 1. The bony structure and joints of the shoulder girdle (Stenvers, 1994).
1. Humerus; 2. Scapula; 3. Clavicle; 4. Coracoid Process;
a. SternoClavicular (SC) joint; b. AcromioClavicular (AC) joint;
c. GlenoHumeral (GH) joint; d. ScapuloThoracic Gliding Plane (STGP).

3.2 Materials and Methods

3.2.1 Deriving bone geometry from CT-scan data

A cadaveric scapula was treated with hydrogen peroxide to remove soft tissues. CT-scans of the dried scapula were made at the Department of Radiology, Leiden University Medical Centre, on a Philips CT scanner (Type SR7000). Images were contained in 320X320 pixels of size 0.5X0.5

mm; the slice thickness was 3 mm. A total number of 69 slices were obtained to cover the entire scapula. A semiautomatic contour detection algorithm, based on a mathematical optimisation procedure, was used to find the closed contours in each CT-slice (Martelli, 1976; Dumay et al., 1994). This procedure requires an initial approximate contour (about 10 points per slice) generated manually. The contour detection algorithm optimises the contour by connecting the points with high derivatives of CT gray value on lines perpendicular to the initial contour (Dumay et al., 1994). The procedure was repeated for all the consecutive CT slices. This algorithm was developed to make the procedure more efficient and accurate. The number of points in a contour was reduced automatically by selecting the keypoints, so that the error between the modified contour and the original points defining the contour remained less than 0.5 mm.

The keypoints defining contour data, transferred into ANSYS FE software, were connected by cubic B-splines. The splines were connected to form areas within one slice. A skin-like area was generated by connecting the corresponding approximated contours of two consecutive slices. Volume between two slices was enclosed by connecting the upper and lower contour areas, and the skin-like area between them.

3.2.2 Element selection and generation

The scapula geometry is complex and irregular. There are some solid, thick regions (e.g. glenoid, scapular spine, lateral border and to a lesser degree the medial border) and two extremely thin regions (infraspinous fossa and supraspinous fossa). The scapula consists of an outer hard, dense cortical shell and an inner cancellous bone region. Ten-node tetrahedral solid element, with three translational DOF per node, was chosen to mesh the solid thick regions. The conventional pure solid modelling approach, if applied to both the cortical shell and the inner cancellous bone, would lead to the following problem. The dimension of the cortical bone is so thin that it is difficult to use brick elements, since the aspect ratio (ratio of the maximum and minimum dimensions of an element) of the elements would be small. This would require the need of applying many more elements to avoid this problem of excessive distortions and abnormal aspect ratios; eventually increasing the computational time, significantly. An alternative technique, using membrane elements, was adapted to represent the cortical layer in the FE model of pelvic bone (Dalstra et al., 1995). Although this approach of combining solid and membrane elements is indeed an elegant idea, it has certain limitations. Such limitations and a comparison on the use of membrane and shell elements with relevance to our problem are presented in the following discussion.

The membrane element, with three translational DOF, can be viewed as a three-dimensional plane stress element. The element has membrane (in-plane) stiffness, but no bending (out-of-plane) stiffness. It should be noted, however, that a membrane element does not necessarily lie in a plane (say, x-y plane), which is the case for a two-dimensional plane stress element. A simple flat shell element is obtained by superimposing a plate bending element and a plane stress membrane element. The basic proposition in plate bending and shell analyses is that the structure is thin in one dimension and therefore, the following assumptions can be made:

(1)   The stress through the thickness (i.e. normal to the mid-surface) of the plate/shell is zero.
(2)   Material particles that are originally on a straight line normal to the mid-surface of the plate/shell remain on a straight line during deformation.

The primary difference between plates and shells is that shells have curvature. As a consequence a shell is capable of resisting transverse loads not only with bending but also with membrane action. The stresses in the shell element are composed of a membrane component and a bending component. A shell can carry a large load if membrane action dominates over bending, just as a thin wire can carry a large load in tension but only a small load in bending. Practically, it is not

possible to have only membrane action in a shell. Bending action is also present if concentrated loads are applied, if supports apply moments or transverse forces, or if a radius of curvature changes abruptly. Typically, the bending action can be quite localised; the bending stresses are large only near the load or discontinuity (boundary conditions) that produces them. Classical shell theory is concerned with thin shells, in which the transverse shear deformation is considered negligible. The thickness (t) of a thin shell element should be very small as compared to the smallest principal radius of curvature (R) and the smallest characteristic length of the deformation pattern (l) of the model (i.e. $(t/R) << 1$ and $(t/l)^2 << 1$). A shell structure is classified as thin if the ratio of its thickness to the radius of curvature is equal to or less than 1/10. In practice one may encounter thick shell, which accounts for transverse shear deformation, and perhaps also for the effects of thickness-direction normal stress. Based on these observations and their relevance to the structure and loading conditions of the scapula, the shell elements are preferred to the membrane elements to develop a FE model of the scapula and to study the effect of applied loading conditions during movements of the arm. Higher order eight-node quadrilateral layered-shell elements (elements may be reduced to triangular shape) with six DOF (three translational and three rotational) per node have been used to model the outer cortex of 0.5 mm thickness. The shell element consists of two layers, one layer stacked over the other, each with a thickness of 0.5 mm.

The purpose of using a first layer, embedded in the solid element zone, is to keep the reference plane along the interface of the outer cortical shell and the underlying compact bone (Fig. 2). All other nodes except those located along the interface, will be lost (Fig. 2b). Ideally, the modulus of elasticity (E) of this overlapping shell layer should be zero, in order to minimise it's contribution in the FE stress analysis. But a non-zero value of E is required according to the numerical requirement of ANSYS. Therefore, a very low value of 0.0001 MPa was allocated. The solid elements were overlaid with the shell elements so that they share common nodes. We assume linear isotropic material properties. Difficulties were faced during mesh generation in those regions where thick bone tapers to an extremely thin curved bone. In this transition zone, there are a few (17) shell elements with excessive curvature.
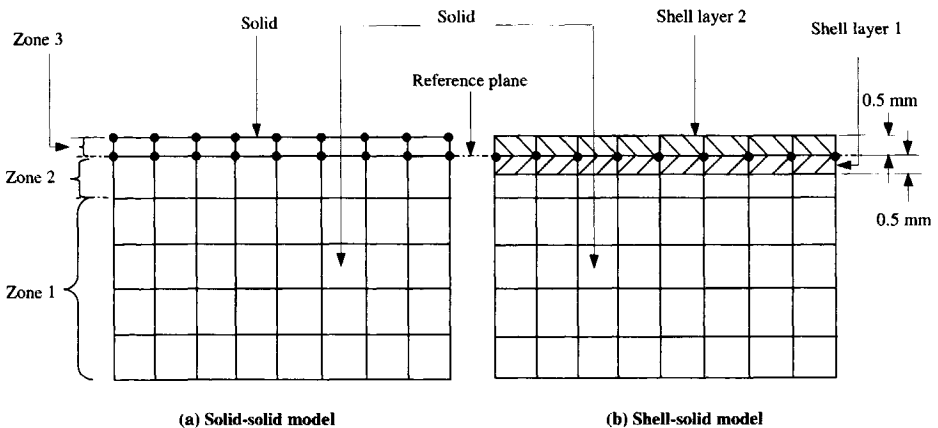

Figure 2. The proposed FE model of scapula. Zone 1: trabecular bone; zone 2: compact bone; zone 3: outer cortical bone.

Table 1. Number of nodes, elements, and Degrees-Of-Freedom (DOF) in the FE model of scapula.

Item	DOF per node	Number
Solid elements (10-node tetrahedral)	3	7412
Shell elements (8-node quadrilateral)	6	357
Layered-shell elements	6	3152
Total elements		10921
Total nodes		14086
Active DOF		63435

The selection of the size of element is, primarily, problem dependent. The element size has considerable influence on the results of stresses and strain. When the size of the element is increased, regions of high and low density are combined within an element. Hence, the variations in the modulus are accurately reflected, and it has a smoothing effect on the stress fields. Consequently, the magnitudes of peak stresses are reduced, and the relatively lower stresses near these peaks are elevated. The effect of element size is more critical to regions where large loads are transmitted through bone that has sharp variation in mechanical properties and in geometry. In both the situations high stress gradients are generated.

Stress gradients call for mesh refinement. Keeping in view the complexity in the scapular structure and the effect of the applied loading conditions that might generate regions of high and low stresses, variable element sizes are considered to be most relevant for the FE model of the scapula. Although the solid model of the scapula was initially meshed with element sizes varying between 4 – 5 mm on a side using ANSYS FE software, the mesh was refined in selected regions. The element sizes were reduced to 3 – 4 mm on a side or smaller, in regions where stress gradients were present. These areas include the lateral border, the scapular spine, the acromion and the coracoid process. Relatively smaller element sizes, varying between 2 – 3 mm on a side, were chosen where solid bony structures originated from the thin infraspinous fossa. These areas include the lateral border, the scapular spine, the angulus inferior and the medial border near the thorax-TS. The curved wedge shaped geometry requires a finer mesh to avoid the problem of element distortion. Though this procedure generates many more elements, it is essential to avoid excessive distortion in the elements, and subsequently maintain accuracy of the numerical analysis. Only in areas (e.g. infraspinous and supraspinous fossa), where the stresses are expected to be low and the variation in properties of bone is less, element sizes varying between 4 – 5 mm on a side had been chosen for modelling. None of the generated elements were distorted or poorly shaped, thus resulting in a detailed FE representation of scapula that would facilitate realistic prediction of stresses and strain. The number of nodes, elements and DOF is listed in Table 1. The accuracy of the results has been checked, using some comparison, discussed later in Section (3.4). A sequence of successively refined meshes produces convergence towards correct results. The deviations in results of the convergence study remained less than 1%, which indicate that the element sizes used in this model are "sufficiently" accurate to predict stresses and strain in the scapula.

3.2.3 Quantitative computed tomography information and material properties of bone

In this study, bone was assumed to be a linear isotropic material. The material properties such as density and elastic modulus of each solid and shell element were calculated and assigned to each element. CT images of a dry scapula, scanned with respect to air, were used to extract material

properties. Apart from the generation of bone contours, these images are used to obtain the following quantities:

(1) CT gray value (H) of pixels and (2) thickness of the shell elements in the fossa areas.

3.2.3.1 Solid elements

After mesh generation co-ordinates (x, y, z) of the centroid of each element and corresponding volume were stored in a file. Since the FE model was based on CT-scan data, the relationship between the FE co-ordinate system and the CT-scan co-ordinate system was already defined. The location of the centroid of each element was retrieved back to the CT-scan image from the FE co-ordinate system through geometric transformation. A cube was constructed with this point as the centroid and sides equal to the cubic root of a tetrahedral volume element. The FE model was based on layer reconstruction procedure using unidirectional (inferior-superior) CT-scan images. Considering the complex geometry of the scapula, in particular the branching out of the scapular spine normal to the plane of the scapula, unidirectional CT-scan for the entire scapula leads to few inaccuracies in FE modelling of this region using layer reconstruction procedure. While locating the position of the elements back to the CT-scan image it was observed that some elements in the scapular spine region were located outside the contours of the scapula. The pixel gray values of these elements were approximated to the nearest element located within the contours of the scapula. The average CT gray value of all the pixels contained in the cubic volume and within the contours of the scapula was calculated and was related to material properties. The mechanical properties of scapular cortical and trabecular bone were assumed to be similar to other bones, like humerus, tibia, femur and pelvis.

The apparent density (ρ) was computed from CT-scan data. A linear relationship was derived between apparent density (ρ) and CT gray value (H) using the CT numbers for air i.e. 0 corresponding to bone density, 0 kg m^{-3} and the CT numbers for compact bone i.e. 2895 corresponding to bone density, 1800 kg m^{-3}. Based on the proposed analytical model of cancellous bone (Gibson, 1985) and regression analysis of experimental data of Frich (1994), power law relations between apparent density and elastic modulus were formulated for two different ranges of apparent density. Powers of 2 and 3 were used for apparent density range, $\rho \leq 350$ kg m^{-3} and apparent density range, $350 \leq \rho \leq 1800$ kg m^{-3}, respectively (Chapter 2). The following relationships were used to define the material properties of each element in the FE model.

(i) Apparent density, ρ (kg m^{-3}) and CT gray value, H (Hounsfield Units)

$$\rho = 527.47 + 0.44 \ H$$

(ii) Elastic modulus, E (MPa) and apparent density, ρ (kg m^{-3})

$$E = 0.00105 \ \rho^2 \qquad \text{for} \quad \rho \leq 350 \text{ kg m}^{-3}$$
$$E = 3. \ 10^{-6} \rho^3 \qquad \text{for} \quad 350 \leq \rho \leq 1800 \text{ kg m}^{-3}$$

The Poisson's ratio of the trabecular bone was assumed to be 0.3 (Dalstra et al., 1995).

This method of estimating mechanical properties of bone involves certain assumptions. Very few testing data (n = 25) were available regarding scapular trabecular bone (Frich, 1994). There were hardly any relationships between CT gray value, apparent density and elastic modulus that could be used to ascribe mechanical properties to FE model of the entire scapula. An 'effective isotropic tissue modulus' has been used at this level of study, since detailed information on the effect of anisotropy was still missing.
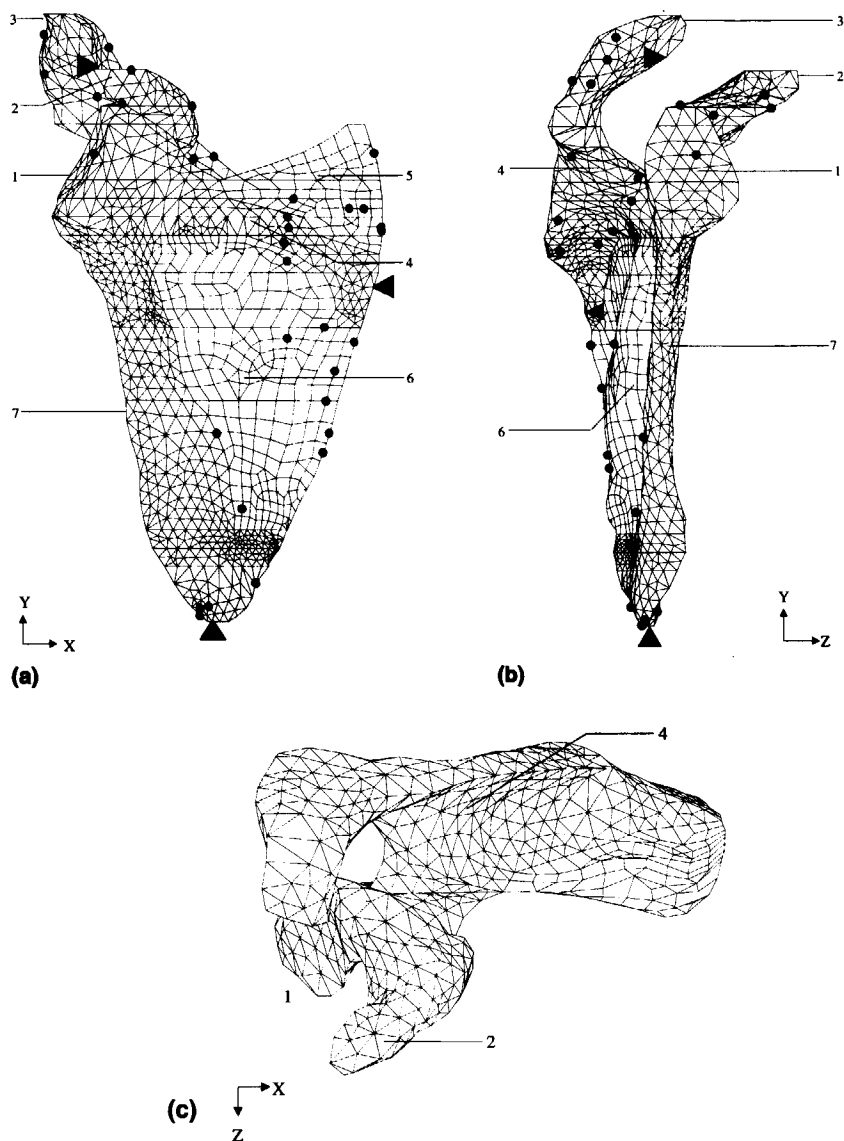
Figure 3. Finite element model of the scapula. 1. Glenoid; 2. Coracoid Process; 3. Acromion; 4. Scapular Spine; 5. Supraspinous fossa; 6. Infraspinous fossa; 7. Lateral border. (a) Ventral view; (b) Lateral view; (c) Superior view. ● point of application of force; ▲ node restraint to translate in all directions ($U_x = U_y = U_z = 0$); ◀ node restraint to translate in x- and z-directions ($U_x = U_z = 0$); ▶ node restraint to translate in x-direction ($U_x = 0$).

3.2.3.2 Shell elements – infraspinous fossa and supraspinous fossa

A similar procedure was applied to calculate the CT gray value of shell elements. The location of the centroid of an element was transformed back to the CT image. A square area was constructed with this point as the centroid and sides equal to the square root of a shell element. The centroid points that were located between two consecutive slices or slightly outside the extent of a bone contour were approximated to the nearest bone contour. The pixel gray values, located within the area, were averaged and allocated to each element as individual gray value. This procedure was repeated for all the shell elements. The Poisson's ratio was assumed to be 0.3 (Dalstra et al., 1995).

The next objective was to find the nodal thickness of the shell elements. Since the planes of the infraspinous and supraspinous fossa are almost perpendicular to the CT slices, bone contours were used to calculate the nodal thickness. The thickness of a node was calculated as the shortest distance between two points located on two opposite sides of a bone contour. Nodal co-ordinates were subsequently mapped back to the CT-scan image from the FE model through geometric transformations. Nodes located between two consecutive slices were approximated to the nearest bone contour. The points that were located on the same side as the nodal point are excluded from the search to detect the nearest point on the opposite side of the contour. The procedure was repeated for all the nodes defining the shell elements. Within an element, the thickness varies from one node to the other. The thickness of the nodes in the fossa area, mostly, varies between 1 – 3 mm, except a few locations along the medial border where it ranges between 3 – 4 mm. This may suggest sharp local variations. The calculated thickness was assigned to each node in an element.

3.2.3.3 Layered shell elements – outer cortical bone

The elastic modulus and Poisson's ratio of the topmost (outermost) cortical shell layer of 0.5 mm thickness were assumed to be 17500 MPa (Chapter 2) and 0.3 (Dalstra et al., 1995), respectively. In order to satisfy the numerical requirements of ANSYS FE software, a non-zero positive value of elastic modulus is required for the shell elements embedded in the solid element zone. Hence, a very low non-zero value of 0.0001 MPa, was allocated for the lower shell layer with 0.5 mm thickness, so as to minimise its contribution in the FE analysis.

3.2.4 Applied loading conditions

The static shoulder model for forces (Van der Helm, 1994[a,b]) and the CT images were based on the same scapula. Screws were driven into the scapula to serve as markers to relate the CT-image to the morphological measurements of the muscle attachments. After removal of the screws, their voids were detectable on the CT images. Presence of these voids allowed calculations of geometric transformations to relate the force model to the CT image. The origin of the global co-ordinate system was located on the lateral side and at the lowest slice defining the scapula (Fig. 3). The x-axis is pointing from lateral to medial, y-axis is pointing from caudal to cranial and the z-axis is pointing from dorsal to ventral (Fig. 3). Van der Helm and Veenbaas (1991) reported that generally more than one muscle line of force is necessary to adequately represent the mechanical effect of muscles with large attachment sites. Each muscle was represented by one to six elements where each element can be considered as a single independent muscle line of force. During humeral abduction, the muscle elements representing a muscle, changes their length as well as orientation with respect to each other. A total number of 95 muscle elements were used to define all the shoulder muscles in the model. Forces calculated with this shoulder model during 0-180 degree abduction (Van der Helm, 1994[a]) were used as applied loading conditions for the FE model as seven load cases.
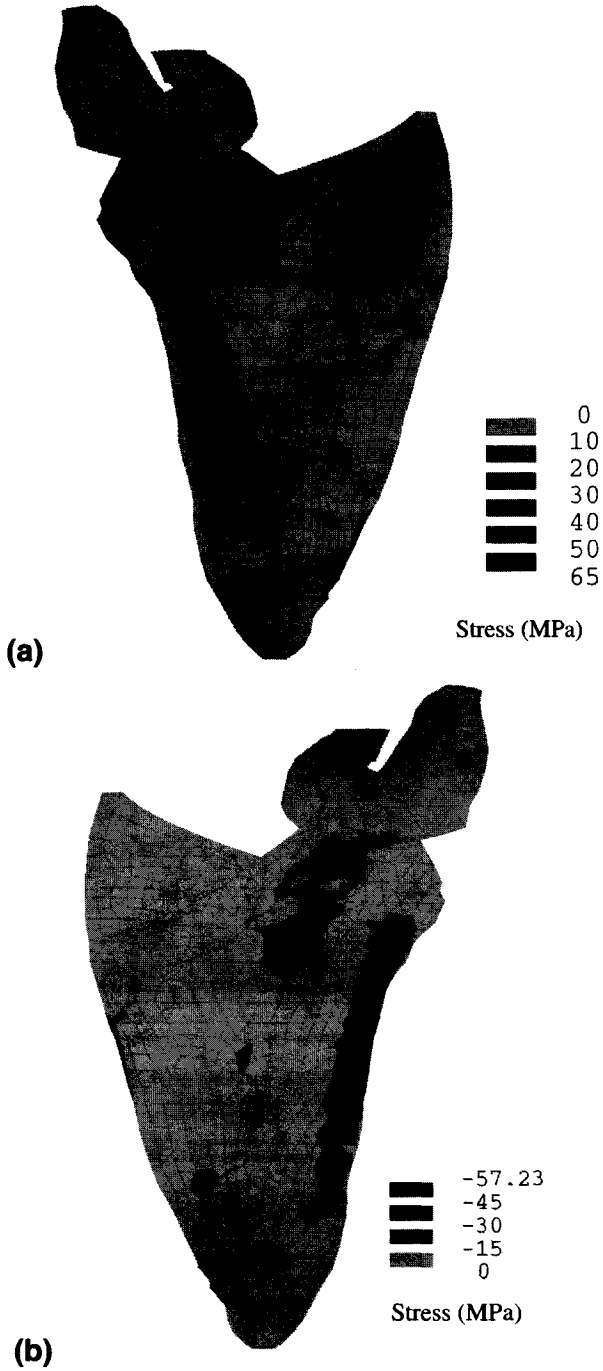
(a)

(b)

Figure 4. Principal normal stress distribution (MPa) during 90-degree humeral abduction; (a) tensile (ventral view); (b) compressive (dorsal view).

Table 2. Reaction forces (in Newton) acting on the scapula (after transformation to the global co-ordinate system) during 90-degree humeral abduction. GH- GlenoHumeral, AC-AcromioClavicular, STGP- ScapuloThoracic Gliding Plane, TS- Trigonum Spinae, AI- Angulus Inferior. The forces – F_x, F_y, and F_z corresponds to x, y, and z directions, respectively (Fig. 3).

Reaction force	F_x	F_y	F_z
GH-joint	383.71	-77.28	34.62
AC-joint	-102.55	-96.56	-66.14
STGP:			
(1) Thorax-TS	0	0	0
(2) Thorax-AI	-53.68	1.11	-102.48
Ligament:			
(1) Conoideum	27.96	102.75	4.80
(2) Trapexoidem	0	0	0

Forces acting on the scapula, during 90-degree humeral abduction were chosen for more detailed evaluation, since the magnitude of the set of forces for this load case was maximum. These forces are of two types, active and passive. Active forces are the muscle forces. The passive ones are the joint reaction forces at GH, AC, ScapuloThoracic Gliding Plane (STGP) and the reaction forces due to the conoid ligament. Typical values are presented in Table 2. The force components, F_x, F_y and F_z correspond to x, y and z directions, respectively (Fig. 3). The nearest node, on the surface of the FE model, for each transformed point of application of force is located. This procedure resulted in a small shift of the point of application as compared to the shoulder model (Van der Helm, 1994[a]), thereby introducing an error in the form of residual moment. The effect of the residual moment might result in some high stresses around the constraints. All the active and passive forces were applied as concentrated forces on these nodes. Six constraints are applied at three nodes, located farthest from each other to avoid rigid body motion (Fig. 3). The residual forces at the constraints were negligibly small and therefore, had minimum effect on the stress distribution of the scapula.

3.3 Results

The FE model of the scapula is represented in three views in Figures 3a, 3b, and 3c. The distribution of principal stresses (tensile, compressive) is shown in two views (ventral and dorsal) in Figures 4a and 4b. A comparison of the principal stresses (tensile, compressive) generated in the shell and the solid elements are presented in Figures 5 and 6. It appears that the structure of the scapula is characterised as a partial sandwich construction, in which the bulk of the load is carried by the outer layer of high-density compact bone, whereas the inner core of low-density trabecular bone acts more as a spacer. The stresses in the outer cortical shell (40 – 65 MPa) are higher as compared to that in the underlying compact bone (30 – 40 MPa). This implies predominantly high bending effect in the structure of the scapula. Horizontal sectional views, as shown in Figures 7a, 7b, and 7c reveals that the Von Mises stresses in the inner core, i.e. in the trabecular bone, is low (0.07 – 5 MPa) as compared to higher stresses (20 – 50 MPa) in the compact bone along the periphery.
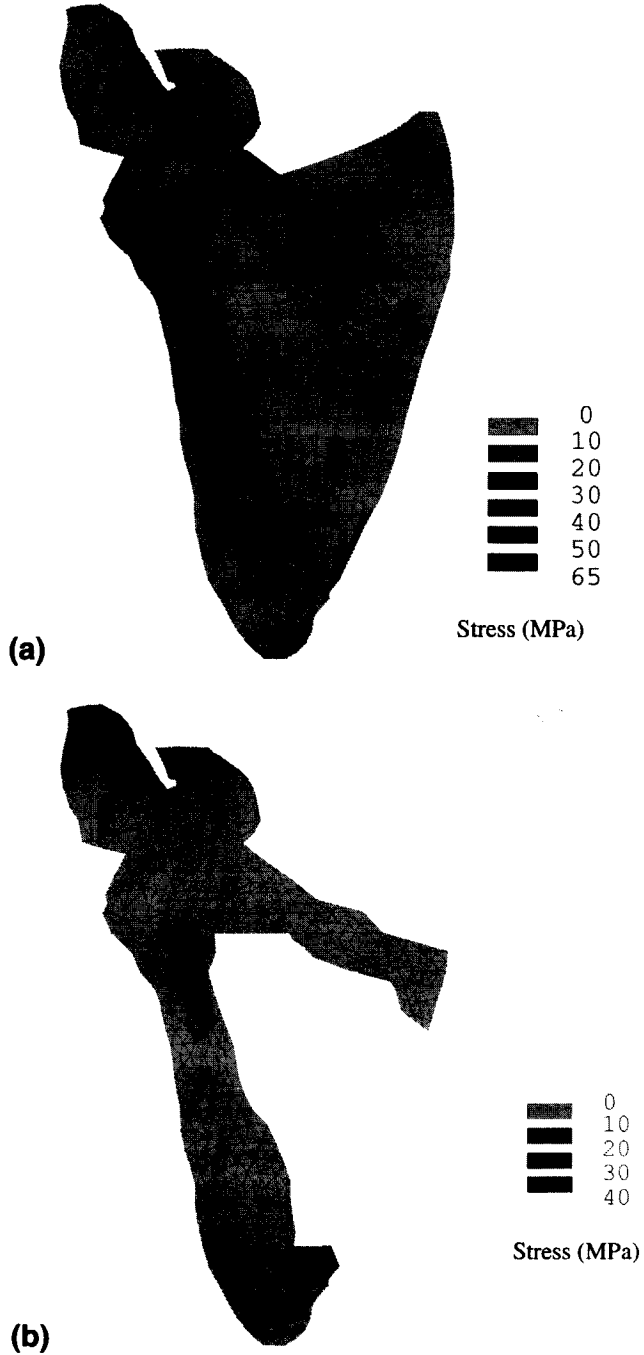
(a)

Stress (MPa)

(b)

Stress (MPa)

Figure 5. Principal normal (tensile) stress distribution (MPa) during 90-degree humeral abduction (ventral view); (a) shell elements; (b) solid elements.

(a)

```
■     -57.23
≡     -45
■     -30
▨     -15
       0
```
Stress (MPa)

```
■     -36
≡     -30
■     -20
▨     -10
       0
```
Stress (MPa)

(b)

Figure 6. Principal normal (compressive) stress distribution (MPa) during 90-degree humeral abduction (dorsal view); (a) shell elements; (b) solid elements.

During 90-degree humeral abduction, high stresses are mostly generated in the solid bony ridges of the scapula. The resultant force due to the action of m. trapezius and m. deltoideus generates high stresses (tensile and compressive), varying between 30 – 60 MPa, at the cranial (upper) and caudal (lower) part of the scapular spine, indicating bending (Figs 4a and 4b). The bending effect caused by the AC-joint reaction force and the m. deltoid also contributes to the high stresses in the spine. The bulk of the GH-joint reaction force is carried by the glenoid and to a lesser degree by the lateral border. Stresses within the glenoid are largely compressive (10 – 60 MPa) in nature. During 90-degree abduction, the highest compressive stress of 58 MPa is generated at the junction of glenoid, infraspinous fossa and spine (Fig. 4b).

During 90-degree abduction, high tensile (20 – 60 MPa) and compressive (20 – 60 MPa) stresses are generated in the ventral and dorsal part of the lateral border, respectively, indicating bending of the lateral border (Figs 4a and 4b). The action of the muscles in this region being negligibly small, it may be concluded that the high GH-joint reaction force, a part of the thorax-AI reaction force and the m. serratus anterior inserting at the AI is transmitted along the lateral border. The combined effect of two large forces exerted by the m. serratus anterior, inserting at the AI and the m. deltoid inserting at the lateral end of spine, generates high compressive stresses (40 – 58 MPa) in the TS. The location of the TS is at the medial border, where the scapular spine attaches to the thin infraspinous fossa. This stress concentration may be also due to the structure of bone in that location. The wedge shaped solid elements in this region taper to an extremely thin bone, the infraspinous fossa.

The distribution of principal stresses (tensile and compressive) in the infraspinous fossa ranges between 0.05 and 15 MPa, except a few locations adjacent to the medial border and the connection with spine-glenoid, where it varies between 15 – 30 MPa (Fig. 4). The stresses in the supraspinous fossa remain less than 5 MPa. These results indicate that the fossa areas act more as attachment sites of large muscles rather than sharing of load.

A few words must be said about the residual moments and their effect on the stress distribution. It may be recalled that the procedure of locating the nearest node number in the FE model, for each transformed point of application of force, resulted in a small shift of the point of application as compared to the shoulder model (Van der Helm, 1994[a]). This procedure introduces an error in the form of residual moments. Consequently, these shifts result in moment non-equilibrium. The residual moments and the reactive forces at the constraints are presented in Table 3. These moments increase with humeral abduction, from 30- to 90-degree, reducing thereafter. The contribution of the GH-, the AC- and the Thorax-AI reaction forces (in descending order of magnitude) are estimated to have predominant influence in the residual moments as compared to the state of moment equilibrium in the shoulder model (Van der Helm, 1994[a]). As a result, some localised high stresses around the three constraints are generated. However, the reactive forces induced at the constraints being negligibly small (either 0, or very close to 0), the effect on the stress distribution of the scapula would be minimal (Table 3).

3.4 Discussion

FE modelling and stress analyses of the human scapula has been described only in a few publications and were mostly restricted to 2-D models of the glenoid with or without a prosthesis (Orr et al., 1988; Friedman et al., 1992; Lacroix and Prendergast, 1997, Stone et al., 1999).
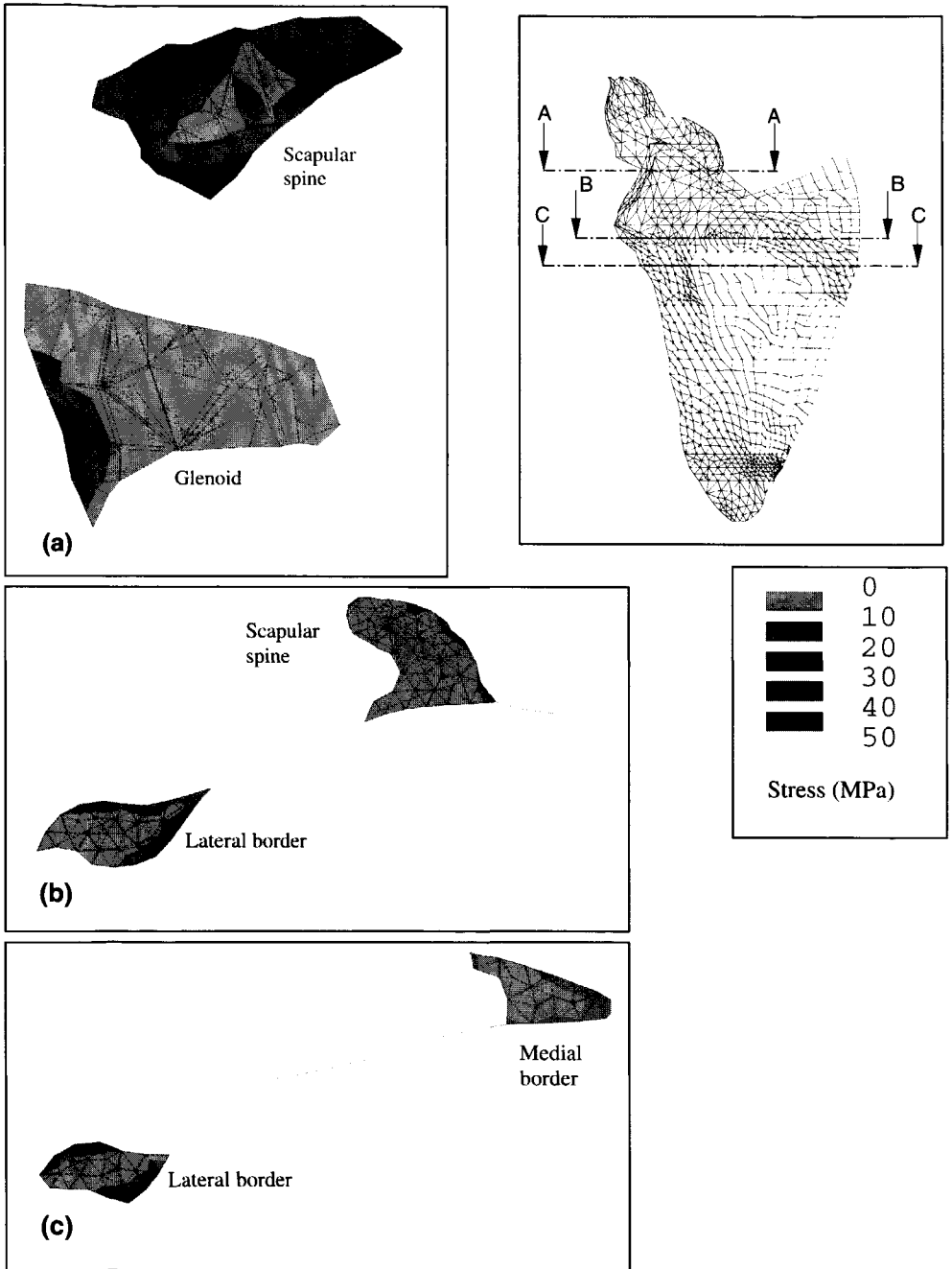
Figure 7. Von Mises stress (MPa) distribution on horizontal sections. (a) Section through A-A; (b) Section through B-B; (c) Section through C-C.

Table 3. Residual moments (M_x, M_y, M_z) in *N-m* during 0 - 180 degree humeral abduction at the thorax-TS constraint, around x-, y- and z-axis, respectively. The Reactive forces (Rf_x, Rf_y, Rf_z) in *N*, along x-, y- and z-axis induced at the three constraints located at Thorax-AI (Th-AI), Thorax-TS (Th-TS) and acromion (AC) (Fig. 3).

Load case	M_x	M_y	M_z	Rf_x	Rf_y	Rf_z
1	-0.0531	-0.2737	-0.2617	Th-AI: 2.3894 Th-TS: -2.3895 AC: Total: -0.0001	Th-AI: 0.0001 Th-TS: AC: Total: 0.0001	Th-AI: 1.0037 Th-TS: -2.9080 AC: 1.9043 Total: 0.0000
2	0.1396	-0.0178	0.4658	Th-AI: -5.2426 Th-TS: 5.2426 AC: Total: 0.0000	Th-AI: -0.0003 Th-TS: AC: Total: -0.0003	Th-AI: 1.3095 Th-TS: -0.6874 AC: -0.6219 Total: 0.0002
3	-0.0461	1.0318	0.3772	Th-AI: -7.1288 Th-TS: 7.1290 AC: Total: 0.0002	Th-AI: 0.00 Th-TS: AC: Total: 0.00	Th-AI: -5.1852 Th-TS: 11.1760 AC: -5.9912 Total: 0.0000
4	-0.1474	1.0096	0.4082	Th-AI: -7.4805 Th-TS: 7.4804 AC: Total: -0.0001	Th-AI: 0.0002 Th-TS: AC: Total: 0.0002	Th-AI: -5.7233 Th-TS: 11.088 AC: -5.3649 Total: 0.0000
5	-0.2236	0.4411	0.4107	Th-AI: -7.2108 Th-TS: 7.2106 AC: Total: 0.0002	Th-AI: 0.00 Th-TS: AC: Total: 0.00	Th-AI: -2.9422 Th-TS: 3.3701 AC: -0.42797 Total: 0.0000
6	0.034.2	0.2914	-0.2233	Th-AI: -0.1923 Th-TS: 0.1951 AC: Total: -0.0028	Th-AI: 0.0003 Th-TS: AC: Total: 0.0003	Th-AI: -1.4462 Th-TS: 2.4622 AC: -1.0160 Total: 0.0000
7	0.2711	0.1866	-0.2982	Th-AI: 1.8134 Th-TS: -1.8135 AC: Total: -0.0001	Th-AI: 0.00 Th-TS: AC: Total: 0.00	Th-AI: 0.25662 Th-TS: 1.5406 AC: -1.7974 Total: -0.0001

These models also fail to include the influence of the 3-D complicated geometry of other important bony structures (e.g. scapula spine, medial border, lateral border, infraspinous and supraspinous fossa), joints (e.g. AC, STGP). Another serious shortcoming of these 2-D models is that the loading is restricted to the plane of modelling, which does not include the effect of all muscles, ligaments and joint reaction forces. Although a 3-D FE model of the scapula has been developed and analysed using CT-scan data by Lacroix et al. (1997) and Lacroix et al. (2000), the geometry and the applied forces were based on two different scapulae, giving rise to non-equilibrium of forces.

Four nodes in the middle of the fossa were constrained to avoid rigid body motion. A total reactive force of 118 N was induced at the constraints, indicating a substantial non-equilibrium in applied forces (Lacroix et al. 2000). Moreover, the errors involved in the FE representation were not clearly indicated, which makes it difficult to assess the accuracy of the FE model. The use of only solid elements for modelling the fossa, as well as the solid bony ridges, is considered to be an inappropriate modelling approach. In fact, it is virtually impossible to model the complicated geometry of scapula by the use of brick elements unless simplifications are made in the structure. The quality of mesh generation (total elements: 7251; total DOF: 29415), compared to our model (total elements: 10921; nodes: 14086, total DOF: 63435) is considered to be coarse. The 3-D model of Lacroix et al. (1997) and Lacroix et al. (2000), therefore, might predict a general trend, but lacks the ability to thoroughly understand the biomechanical stresses induced in the individual parts of the scapula due to action of muscle, ligaments and joint reaction forces. We have aimed at accurate representation of the geometry of scapula using a 3-D mesh, a combination of solid and shell elements with material properties and thickness taken from CT-scan data. The applied loading conditions include the effect of all muscles, ligaments, and joint reaction forces, obtained from the static shoulder model of forces (Van der Helm, 1994[a,b]), which would be useful in understanding the load transfer mechanism across the scapula. However, the forces were applied as concentrated loads; representation of trapezius muscle action, for example, is by six lines of force. But in reality, the forces should be distributed on the surfaces of those elements that are located in the respective physiological areas of insertion, which are yet to be investigated.

The accuracy of the FE model is highly dependent on the quality of estimation of bone elastic modulus from the CT image. The relations between CT gray value and apparent density, apparent density and elastic modulus were based on very few testing data that were available regarding scapular trabecular bone (Frich, 1994). This method of obtaining bone elastic modulus involves certain assumptions. For practical necessity, bone was assumed to be isotropic, linearly elastic material and its elastic modulus was related to the density only. Whereas, in reality, bone is anisotropic and is subject to continuous remodelling. These assumptions are obviously idealisations of reality. Hence, the study is conceptual in nature and the results predict certain qualitative trends.

The higher order shell elements are particularly well suited to model the outer curved geometry of the scapula as well as the infraspinous and the supraspinous fossa, thus resulting in a partial sandwich structure. While checking the quality of element shapes and sizes, it appears that the radius of curvature of some shell elements (only seventeen) in the curved supraspinous fossa area were very small. The geometry and the thickness of nodes of these shell elements were based on the CT-scan data. These elements belonged to the thicker supraspinous fossa, as compared to the infraspinous fossa, and did not satisfy the requirements of thin shell elements and therefore, might lead to inadequate results. For thin shell elements, the principal radius of curvature to thickness ratio must be greater than 10. The effect of the residual moment arising due the shift in point of application of force generates localised stresses, primarily around the constraint at the Thorax-TS connection at the medial border. This stress concentration may be also due to the structure of bone in that location. The wedge shaped solid elements (scapular spine) in this region taper to a thin bone (infraspinous fossa). Probably, at this particular area the present model generates rather inadequate results of stresses and strain.

The stresses (tensile, compressive) in the cortical shell of the scapula vary between 10 to 60 MPa, whereas for low-density trabecular bone it ranges between 0.07 to 5 MPa, indicating that the cortical shell and the underlying compact bone, carries majority of the load. The inner core of trabecular bone acts as a spacer (Jacob et al., 1976; Dalstra and Huiskes, 1990). In this, the scapula represents a 'sandwich structure' and its behaviour is similar to pelvic bone. It is interesting to note

that stresses in the outer cortical layer, represented by shell elements, is higher (25 – 40%) than stresses induced the underlying compact bone. The stresses induced in the low-density open cell trabecular bone, however, are observed macroscopically. These stresses will, however, differ from the microscopically calculated stresses in the individual trabeculae (Van Rietbergen et al., 1995).

In developing the present 3-D model of the scapula, the priorities have been proper element selection, computational time and ease of model generation with the consideration of moderate quality of mesh size (3-4 mm or less on a side), discussed earlier in Section (3.2.2). The selection of type and size of element, largely, comply with the recommendations of Ulrich et al. (1998) and Keyak and Skinner (1992), respectively. The complex bone structure of the scapula requires a tetrahedron meshing technique. Ulrich et al. (1998) suggested that the tetrahedral elements are better suited to model the original geometry of a bone structure as compared to the commonly used voxel conversion technique, providing meshes with brick (hexahedron) elements. The results of their FE analyses were based on micro-CT images (resolution, 168 μm) of three cube-shaped human trabecular bone specimens, one taken the femoral head, one from the iliac crest and one from the lumber spine. Keyak and Skinner (1992) analysed three models of a human proximal femur using linear cube-shaped hexahedral elements, each with a different element size (3.1 mm, 3.8 mm and 4.8 mm). Convergence of the models had been verified (Keyak et al., 1990) and the qualitative results of all the three models were in agreement. Although the mesh refinement from 4.8 mm to 3.8 mm and further to 3.1mm can be hardly called a major refinement, the quantitative results (stresses and strain) of the FE analyses were highly sensitive to these variations of element size (Keyak and Skinner, 1992). They concluded that regions with high stress gradients could only be modelled with an element size of 3 mm or smaller on a side to obtain precise numerical predictions in this region. Use of larger elements (even 3.8 mm on a side) decreased the predicted peak stresses/strain and increased the uncertainty in the data (Keyak and Skinner, 1992). Although these recommendations are based on a different bone (human proximal femur), using linear cube-shaped hexahedral elements, they are assumed to be, more or less, useful for similar situations of stress gradient that may arise for other bones. The accuracy of the results of the 3-D FE model, however, can be assessed using a convergence study.

In order to calculate the stresses with "sufficient" accuracy, a convergence study based on stresses in the areas of interest is required. Choosing any node near a concentrated load was avoided, since stresses close to concentrated loads can be artificially increased with mesh refinement. The first coarse model consists of 6253 elements, 8000 nodes and a total number of 37164 DOF. The second case corresponds to the present FE model with mesh refinement; consisting of 10921 elements, 14086 nodes, and a total number of 63435 DOF. In the present problem (a blend of 3-D and 2-D elements), a uniform mesh refinement with factor 2 would lead to 4 – 8 times DOF. The solution of such a large size FE model is hindered by computer resources and software limitations. Hence, local mesh refinement has been performed judiciously on areas with stress gradients. In the third case, mesh refinement with element size less than 3mm, has been performed in the solid bony regions, resulting in 14582 elements (solid: 10181; shell: 357; layered-shell: 4044), 18720 nodes and a total number of 82701 DOF. Comparison of results between the first and the second case indicate differences of stresses (principal normal and Von Mises) in the order of 11 – 13%. Whereas, these deviations are significantly reduced (0.6 – 1%) when results are compared between the second (present) and the third model. It may therefore, be concluded that the present FE model (10921 elements, 14086 nodes, 63435 DOF) would be sufficient to calculate the stresses and strain in the scapula, macroscopically. Moreover, a comparison of measured and numerically obtained strain using strain gage measurements would be a better means to assess the accuracy of FE results.

Considering all the assumptions and the contributing factors responsible for the deviations in predicted results, it appears as a whole, that the quality of numerically predicted results are significant and realistic.

3.5 Conclusion

The proposed method of generating a 3-D FE model of scapula, using CT-scan data and the combination of shell and solid elements is appropriate for the complex structure of the scapula. The use of shell elements induces bending and membrane capabilities in the model, while the reduction of the number of elements is an important advantage. This modelling approach, therefore, would lead to a realistic model of the scapula and at the same time reduces computational time and complexity, significantly. This model is reasonably detailed in the description of scapula geometry and material properties and results in good element shapes with no distortion. The FE model, using a static shoulder model of forces would be useful in understanding the mechanics of load transfer across the scapula during movements of the arm.

Acknowledgements

References

Berms, J. (1993). The glenoid component in total shoulder arthroplasty. J. Shoulder Elbow Surg. 2, 47-54.

Boyd, A.D., Thomas, W.H., Scott, R.D., Sledge, C.D. and Thornhill, T.S. (1990). Total shoulder arthroplasty versus hemiarthroplasty. J. Arthroplasty 5, 329-336.

Carter, D.R., and Hayes, W.C. (1977). The compressive behaviour of bone as a two-phase porous structure. J. Bone Joint Surg. 59-A, 954-962.

Ciarelli, M.J., Goldstein, S.A., Kuhn, J.L., Cody, D.D. and Brown, M.B. (1991). Evaluation of orthogonal mechanical properties and density of human trabecular bone from major metaphyseal regions with material testing and computer tomography. J. Orthop. Res. 9, 674-682.

Dalstra, M. and Huiskes, R. (1990). The pelvic bone as a sandwich construction; a three dimensional finite element study. In Proc. Europ. Soc. Biomech. 7, B32.

Dalstra M., Huiskes R., Odgaard A. and Erning, L. van (1993). Mechanical and textural properties of pelvic trabecular bone. J. Biomechanics 26, 523-535.

Dalstra, M., Huiskes, R. and van Erning, L. (1995). Development and validation of a three-dimensional finite element model of the pelvic bone. J. Biomech Eng. 117, 272-278.

Dumay A.C.M., Gerbrands J.J. and Reiber J.H.C. (1994). Automated extraction, labelling and analysis of the coronary vascular from arteriograms. Int. J. Cardiac Imaging 10, 205-215.

Frich L.H. (1994). Glenoid Knoglestyrke og knoglestruktur, Doctoral thesis, University of Aarhus, Denmark.

Friedman, J.R., LaBerge, M., Dooley, R.L. and O'Hara, A.L. (1992). Finite element modelling of the glenoid component: Effect of design parameters on stress distribution. J. Shoulder Elbow Surg. 1, 261-270.

Gibson, L.J. (1985). The mechanical behaviour of cancellous bone. J. Biomechanics 18, 317-328.

Hvid, I., Bentzen, S.M., Linde, F., Mosekilde, L. and Pongsoipetch, B. (1989). X-ray quantitative computer tomography: the relations to physical properties of proximal tibial trabecular bone specimens. J. Biomechanics 22, 837-844.

Huiskes, R, Weinans, H., Grootenboer, H.J., Dalstra, M., Fudala, B., and Slooff, T.J. (1987). Adaptive bone-remodelling theory applied to prosthetic-design analysis. J. Biomechanics, 20, 1135-1150.

Huiskes, R, Weinans, H. and Dalstra, M. (1989). Adaptive bone remodelling and biomechanical design considerations for non-cemented total hip arthroplasty. Orthopaedics 12, 1255.

Jacob, H.A.C., Huggler, A.H., Dietschi, C. and Schreiber, A. (1976). Mechanical function of subchondral bone as experimentally determined on the acetabulum of the human pelvis. J. Biomechanics, 9, 625-627.

Keyak, J.H., Meagher, J.M., Skinner, H.B. and Mote, C.D. Jr. (1990). Automated three-dimensional finite element modelling of bone: a new method. J. Biomed. Eng., 12, 389-397.

Keyak, J.H and Skinner, H.B. (1992). Three-dimensional finite element modelling of bone: effects of element size. J. Biomed. Eng., 14, 483-489.

Keyak, J.H., Fourkas, M.G., Meagher, J.M. and Skinner, H.B. (1993). Validation of an automated method of three-dimensional finite element modelling of bone. J. Biomed. Eng., 15, 505-509.

Lacroix, D. and Prendergast, P.J. (1997). Stress analysis of glenoid component designs for shoulder arthroplasty. Proc. Inst. Mech. Engrs, Part H 211, 467-474.

Lacroix, D., Prendergast, P.J., Murray, R., McAlinden, S. and D'Arcy, E. (1997). The use of Quantitative Computed Tomography to generate a finite element model of the scapula. Proc. of the 14th Conf. Irish Manufacturing Committee. Ed J. Monaghan & C.G. Lyons, 257-262.

Lacriox, D., Murphy, L.A. and Prendergast, P.J. (2000). Three-dimensional finite element analysis of glenoid replacement prosthesis; a comparison of keeled and pegged anchorage systems. J. Biomech Engg. 122, 430-436.

Martelli, A. (1976). An application of heuristic search methods to edge and contour detection. Communications of the ACM, 19, 73-83.

Oonishi, H., Isha, H. and Hasegawa, T. (1983). Mechanical analysis of human pelvis and its application to the articular hip joint - by means of the three dimensional finite element method. J. Biomechanics 16, 427-444.

Orr, T.E., Carter, D.R. and Schurman D.J. (1988). Stress analyses of glenoid component designs, Clin Orthop. Rel. Res. 232, 217-224.

Rice, J.C., Cowin, S.C. and Bowman, J.A. (1988). On the dependence of the elasticity and strength of cancellous bone on apparent density. J. Biomechanics 21, 155-168.

Stenvers, J.D. (1994). De primaire frozen shoulder, Doctoral thesis, State University of Groningen, The Netherlands.

Stone, K.D., Grabowski, J.J., Cofield, R.H., Morrey, B.F. and An, K.N. (1999). Stress analysis of glenoid components in total shoulder arthroplasty. J. Shoulder Elbow Surg. 8(2), 151-158.

Ulrich, D., Van Reitbergen, B., Weinans, H. and Rüegsegger, P. (1998). Finite element analysis of trabecular bone structure: a comparison of image-based meshing techniques. J. Biomechanics 31, 1187-1192.

Van der Helm, F.C.T. and Veenbaas, R. (1991). Modelling the mechanical effect of muscles with large attachment sites: application to the shoulder mechanism. J. Biomechanics 24(12), 1151-63.

Van der Helm, F.C.T. (1994[a]). Analysis of the kinematic and dynamic behaviour of the shoulder mechanism. J. Biomechanics 27, 527-550.

Van der Helm, F.C.T. (1994[b]). A finite element musculoskeletal model of the shoulder mechanism. J. Biomechanics 27, 551-569.

Van Rietbergen, B., Huiskes, R., Weinans, H., Sumner, D.R., Turner, T.M., and Galante, J.O. (1993). The mechanism of bone remodelling and resorption around press-fitted THA stems. J. Biomechanics, 26, 369-382.

Van Rietbergen, B., Weinans, H., Huiskes, R., and Odgaard, A. (1995). A new method to determine trabecular bone elastic properties and loading using micromechanical finite element models. J. Biomechanics 28, 69-81.

Weinans, H., Huiskes, R., Van Rietbergen, B., Sumner, D.R., Turner, T.M., and Galante, J.O. (1993) Adaptive bone remodelling around bonded noncemented THA: a comparison between animal experiments and computer simulation. J. Orthop. Res., 11, 500-513.

Chapter 4

Experimental Validation of Three-dimensional Finite Element Modelling of the Scapula

Abstract

Three-dimensional (3-D) Finite Element (FE) modelling and stress analysis of the human scapula has hardly been reported in literature. In most cases, simplified approaches in geometry and loading conditions of FE models were used to obtain some idea about the mechanics involved in the scapula bone. A thorough experimental validation with strain gage measurement on a fresh bone has always been considered as a better tool to assess the quality of FE predictions. The present study provides a new approach in mechanical testing of bone for the purpose of validating a FE model. In this study, a fresh cadaveric scapula with eighteen strain gages attached at various locations and orientations, was loaded in a mechanical testing machine and supported at three locations by linkage mechanisms interconnected by ball joints. The objective of these constraint conditions was to unambiguously impose bending and deflection of the scapula in all directions, in response to applied loads at various locations. A detailed FE model of the tested scapula has been developed by using 3-D mesh, combination of solid and shell elements, with material properties and thickness taken from quantitative Computed Tomography (CT) measurements. The loading and the support conditions of the experiment are simulated and applied on this FE model. The measured strains (experimental) are compared with the numerical (FE) strains, corresponding to several load cases, in order to validate the proposed FE modelling technique. Linear regression analysis was used to assess the accuracy of this FE model of scapula. The percentage error in the regression slope varies between 9 – 23%. It appears, as a whole, that the two variables (measured and numerical strain) strongly depend on each other with a confidence level more than 95%. High correlation coefficient (0.89 – 0.97) and low standard error (29 – 105 $\mu\varepsilon$) were observed between the measured and predicted strain, except a single case where the standard error was calculated as 198 $\mu\varepsilon$. Considering the complicated testing procedure on a fresh sample of scapula, the high correlation coefficients and the relatively low standard errors and percentage errors in regression slope, strongly suggest that the numerical strains calculated by the FE model can be used as a valid predictor of the actual measured strain.

Keywords: Finite element method, biomechanics, scapula, strain gage, computed tomography.

4.1 Introduction

The Finite Element Method (FEM) has emerged as an important tool to analyse and predict stresses and strain in bone. With the development of precision imaging techniques, three-dimensional (3-D) Finite Element (FE) modelling and analyses of bone, using Computed Tomography (CT) data, are more frequently used to test and validate certain clinical hypotheses, rigorously (Huiskes et al., 1987; Huiskes et al., 1989; Keyak et al., 1990; Huiskes et al., 1992; Huiskes, 1993; Dalstra et al., 1995; Huiskes, 1997; Kerner et al., 1999). However, the quality of the predicted results is dependent on the quality of the FE model.

The quality of a FE model and its accuracy of predicted stresses and strains depend on the quality of representation of the FE model as compared to the actual conditions (normal bone or a bone with implant). The accuracy is highly dependent on the correct estimation and distribution of the material properties of elements constituting the FE model of the scapula. Material properties, such as, elastic modulus are based on CT-scan data using density-CT gray value and elastic modulus-density relationships. The type and size of element is an important factor in the correct representation of the structure of bone with or without implants. A thorough experimental validation, though a very difficult and tedious procedure, is a better tool to assess the quality of FE predictions (Keyak et al., 1993; Dalstra et al., 1995). Experimental strain gage measurements were used for stress analysis of bone, and sometimes, for the purpose of validation of the FE models (Jacob et al., 1976; Lionberger et al., 1985; Finlay et al., 1986; Ries et al., 1989; Dalstra et al., 1995, Keyak et al., 1993). The studies of Keyak et al. (1993) and Dalstra et al. (1995), based on the femur and the pelvic bone, respectively, are significant contributions towards strain gage validations of FE modelling of bone. The purpose of these studies was to validate a realistic FE modelling of bone using CT-scan data, with the help of comparisons of stresses and strain predicted by this method with those measured on a bone, *in vitro*. However, in both the studies, a part of the bone was fixed in a bed of cement, which seems to be a simplified method of constraining the bone in the experiment.

Stress analysis of the scapula, numerically and experimentally, has hardly been reported. The structure of the scapula, as compared to other bones, is far more complicated and irregular. The scapula is subject to complex loading conditions. A realistic 3-D FE model of a scapula would be useful in assessing the total stress field in the bone. It helps in design, failure prediction and improvement of total joint replacements. A thorough experimental validation, using strain gage measurements, of the proposed FE model of scapula is considered to be a major investigation.

The purpose of this study is to experimentally validate a 3-D FE model of scapula. The present model is aimed at more realistic representation of the scapula, by using a 3-D mesh and a combination of shell-solid modelling approach. Material properties and thickness are taken from quantitative CT-scan measurement. The loading and the support conditions of the experiment were most closely represented in this FE model. A new experimental set-up was developed, in order to test a fresh specimen of cadaveric scapula with strain gages fixed all over its surface. The experimental method involves a precise measurement technique, with specially designed fixtures and load application mechanism, which can effectively impose bending and deflection of the tested scapula, almost in any direction. The measured strains of the experiment and the numerically predicted strains of the FE model were compared to obtain an estimate of the quality of FE model.

4.2 Materials and Methods

4.2.1 Preparation of the tested scapula

A fresh scapula (C521a) of an 87-year old woman, who died of pancreatic cancer, was retrieved from a donated body. Soft tissues were scrapped and removed from the bone surfaces as far as possible. Six steel markers, 1 mm diameter by 10 mm length, were prepared and inserted in six holes (diameter 1 mm), drilled in the bone at several locations (Figs 1a and 1b). The objective of using these markers was to obtain transformations in order to relate the coordinate system of the experimental scapula to that of the CT-scan coordinate system. Two more holes of 5 mm diameter, one in supraspinous fossa and the other in Angulus Inferior, were drilled to fix the scapula to the supporting linkage mechanism.

4.2.2 Computed Tomography (CT) scan

The prepared scapula, fresh before freezing, with six markers and two holes, was placed in a polyethylene container to hold the bone in position. The scapula was CT scanned at the Department of Radiology, Leiden State University Medical Centre, on a Philips Tomoscan (120kVp, MAS: 175) of Type SR7000. Images of the scapula were stored in 512 X 512 pixels, with a pixel size of 0.5 mm, slice thickness of 3.0 mm. The CT gray value (H) has been linearly calibrated in terms of apparent density (ρ) by using the CT numbers of water, i.e. 0, corresponding to bone density of 0 kg m^{-3} and the CT numbers of compact bone i.e. 2808 corresponding to bone density, 1800 kg m^{-3}, resulting in ρ = 0.6410 H. After CT-scanning, the scapula was preserved in a freezer at $-35°$ C.

4.2.3 Strain gage fixation and measurement

The bone was thawed and the remaining soft tissue, except the cartilage on the face of glenoid, was scrapped and removed using a surgical knife. The surface of the bone where strain gages were to be fixed was cleaned with isopropyl alcohol followed by repeated scrapping and degreasing with acetone and 220 and 340 grit emery paper. The method of surface preparation was similar to those suggested by Wright and Hayes (1979) and Keyak et al. (1993). General purpose strain gages (KFG-5-120-C1-11L1M2R, KYOWA, Japan) with gage length of 5 mm, gage width of 1.4 mm, gage factor of 2.1, and resistance of 120 Ω, were used. They were glued on the scapula, using a single-component cyanocrylate (CC-33A, KYOWA, Japan). A coating of air-drying silicone rubber (M-coat C KIT, Micro-measurement division, USA) was applied on the gage surface and on the gage-wire junctions, in order to prevent short-circuiting. Following this procedure, a total number of eighteen strain gages were fixed on the surface of the scapula at a variety of locations and orientations as shown in Figure 1. Dummy strain gages were fixed on another fresh scapula, earlier used for a pilot study, for the purpose of temperature compensation. Nine strain gages at a time were connected to a strain amplifier (KWS 3073 TF-mess verstarker, Hottinger Boldwin Messtechnik, Germany) in a half-bridge circuit, via an analog-to-digital (AD) converter (12 bits, Frequency: 50 Hz). In a second execution of the experiment, the other nine strain gages were connected. A lowest possible voltage, one Volt, of the amplifier was chosen, so that the development of heat was minimised, since bone samples have low heat conductivity.
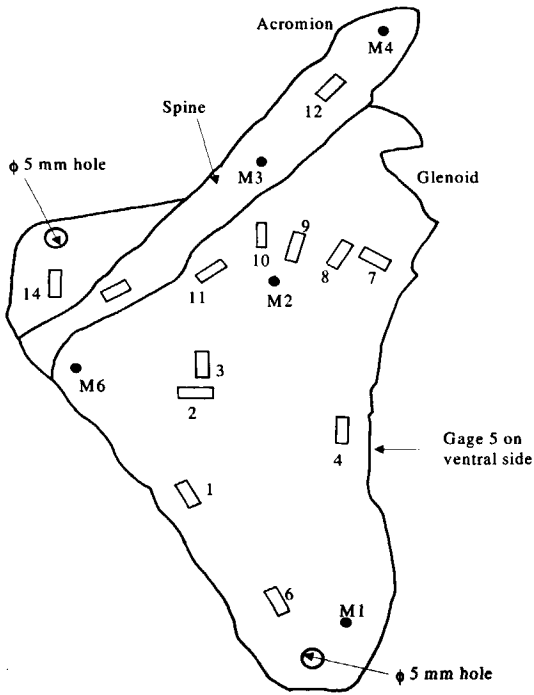
Figure 1a. A dorsal view of the experimental scapula with strain gage location and orientation, positions of markers (M1 to M6; except M5) and drilled holes.
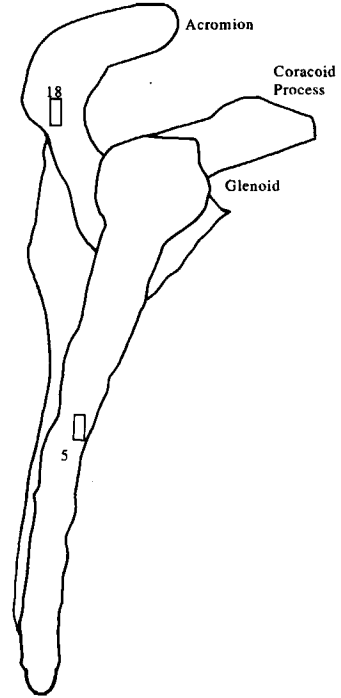
Figure 1b. A lateral view of the experimental scapula with strain gage location and orientation and position of marker, M5.
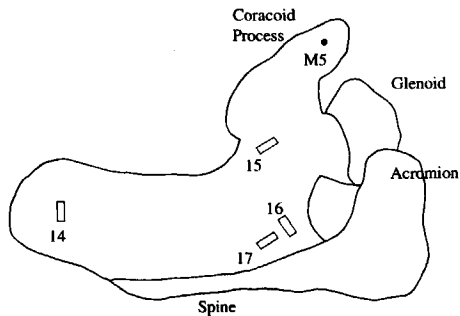

Figure 1c. A superior view of the experimental scapula with the location and orientation of strain gages 14 to 18.

4.2.4 Experimental set-up; fixation and loading of the scapula

The fresh scapula with eighteen strain gages fixed all over its surface, was supported on a mechanical testing machine (Zwick 1484, Germany) at three different locations, namely, Angulus Inferior (constraint 1), lateral border (constraint 2) and supraspinous fossa (constraint 3), as shown in Figure 2. These constraint systems consisted of links, interconnected by ball joints. The objective of using these supports was to allow for bending and deflection of the scapula in all directions, in response to applied loads at several locations. Six Degrees Of Freedom (DOF) were fixed, so that the reactions forces at the constraints were well defined and no statically indeterminate loading case could result.

4.2.4.1 Constraints

Constraint 1 consisted of a link, one end of which was completely fixed to a plate and the other held a ball joint, as shown in Figure 2. The ball joint was fixed in position, but was free to rotate in any direction. Thus, three translational DOF's were constrained at the ball joint. A second link connected the first ball joint to the bone through a bolt. The second constraint, Constraint 2, consisted of two ball joints connected to each other by a link. The first ball joint was connected to a fixture mounted on a plate (Fig. 2). Thus, one translational DOF of the second ball joint was constrained. The second ball joint was in turn connected to a second link, which had a fork type arrangement for fixation with bone (Fig. 2). The third constraint, Constraint 3, was comprised of a combination of a hinge joint and a ball joint. A link of length 63 mm, connected the hinge joint to the ball joint (Fig. 2). Thus two translational DOF's of the ball joint were constrained. A second link, similar to the Constraint 1, connected the ball joint to the bone through a bolt. In total six translational DOF's at the centres of the ball joints were constrained.
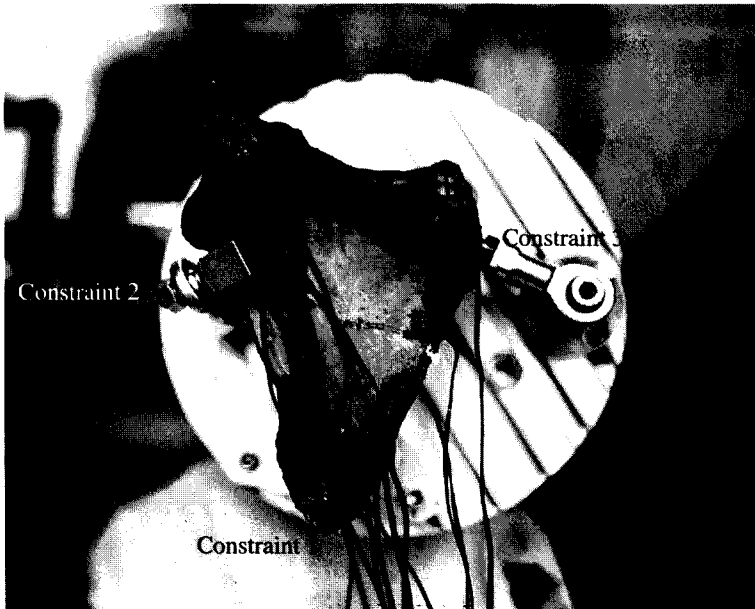

Figure 2. The experimental set-up for strain gage measurement on fresh scapula.

Table 1. Applied load cases on the scapula. F_x, F_y, F_z (in Newton) represents forces in x, y and z directions, respectively, with the area of location and the point of application of force with respect to the global co-ordinate system of the FE model (Figs 3, 4 and 5).

Load case	Location Area	x	y	z	F_x	F_y	F_z
1	Glenoid cavity	45.17	93.09	-52.77	65.88	15.07	13.90
2	Spine	115.14	110.79	-81.00	-0.20	-32.38	-55.34
3	Acromion	49.57	97.43	-9.56	-30.01	-49.95	-139.17
4	Glenoid cavity	47.02	91.94	-51.00	73.00	15.32	10.34
5	Glenoid cavity	40.07	92.25	-60.00	58.65	7.95	13.78
6	Acromion	53.89	98.61	-12.70	-19.30	-30.15	-73.30
7	Glenoid cavity	43.543	91.06	-56.16	71.34	15.74	14.32
8	Glenoid cavity	45.62	86.42	-55.94	175.45	2.88	-13.05
9	Glenoid cavity	41.07	90.53	-60.00	146.20	15.52	-26.65
10	Glenoid cavity	45.707	88.35	-54.48	97.70	9.51	8.42

4.2.4.2 Loading of the scapula

The force on the scapula surface was applied by a 5 mm diameter steel ball attached to a specially designed fixture in the mechanical testing machine (Zwick 1484, Germany). The components of the applied force (F_x, F_y and F_z) were recorded from the testing machine. These load cases, which were applied at the glenoid, scapular spine, and acromion, are presented in Table 1.

4.2.5 Three-dimensional model of the experimental scapula

An extensive description of the general procedure of generation of FE model of scapula, using CT-scan data, has been discussed in Chapter 3. A brief outline is presented here. A semi-automatic contour detection algorithm, based on a mathematical optimisation procedure, was used to find the closed contours in each CT-scan slice. Keypoints were generated from the contour data within ANSYS and were connected by cubic B-splines. Splines were connected to form areas, which were in-turn connected to form volumes. A combination of shell and solid model was used for the FE model of the scapula. Ten-node tetrahedral solid elements were used to model the solid, thick regions of the scapula (e.g. glenoid, spine, lateral border, and partial medial border), whereas eight-node shell elements were used to represent the infraspinous and supraspinous fossa. Shell-elements with 2-layers (0.5 mm thickness of each layer) were overlaid with solid elements to model a part of the compact bone, which represents the outer cortical layer. Each link in the supporting structure of the test apparatus was modelled as rigid beam element, with six DOF per node. The type and number of elements in the model are presented in Table 2. The material properties of cancellous and cortical bone of the FE model were based on CT-scan data and the relationships formulated in Section (4.2.2) and in Chapter 2.
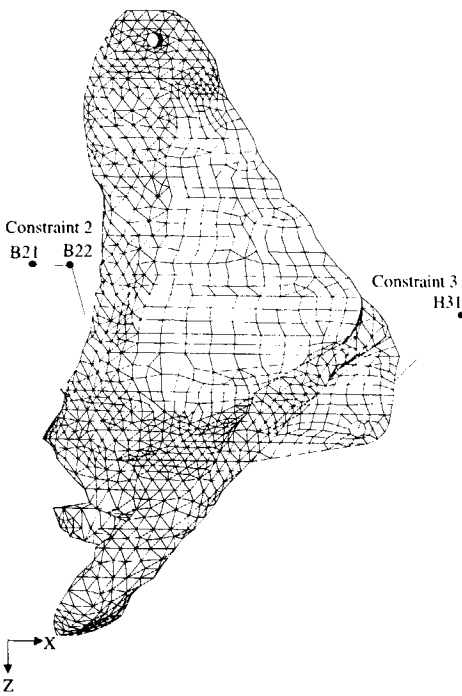
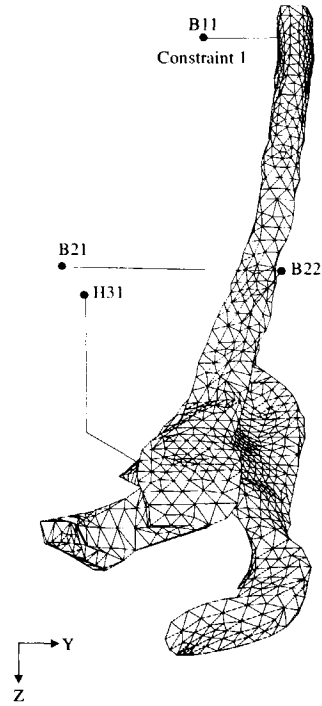**Figure 3.** A dorsal view of the FE model of scapula with constraints 2 and 3. B = Ball joint; H = Hinge joint.

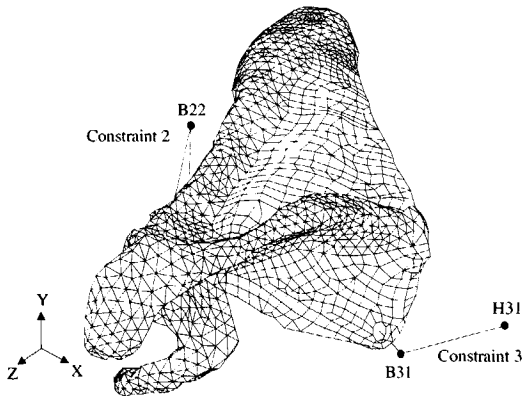**Figure 4.** A lateral view of the FE model of scapula with constraints 1, 2 and 3. B = Ball joint; H = Hinge joint.

Figure 5. An oblique view of the FE model of scapula with constraints 2 and 3. B = Ball joint; H = Hinge joint.

Table 2. Type and number of elements used in the FE model of scapula. DOF: degrees of freedom.

Type of element	DOF per node	Number of elements in the FE model
Solid (3-D, 10-Node tetrahedral)	3	9934
Shell (2-layered; 8-Node quadrilateral)	6	3450
Shell (8-Node quadrilateral)	6	464
Beam elements (3-D elastic)	6	5
Total number of elements		13853

4.2.5.1 Loading of the FE model

The force components in three mutually perpendicular directions (x, y and z) as measured in the experiment were used as applied loading conditions for the FE model of scapula (Table 1). The point of application of the 3-D forces (F_x, F_y, and F_z) corresponds most closely to the point of force application in the experiment. The applied load cases with major areas of applications have been presented in Table 1.

4.2.5.2 Constraint conditions in the FE model

The FE model of the scapula was supported at three regions, namely, the angulus inferior (Constraint 1), the lateral border (Constraint 2) and the supraspinous fossa (Constraint 3), resembling the constraint condition in the experimental set-up (Fig. 2). The supporting system consisted of several links, where each link was modelled as rigid beam element. Based on the position and orientation of the supporting linkage system in the experiment, local coordinate systems were defined at nodes. The x-axis of these local coordinate systems was orientated along the axis of the beam elements. All constraints were defined based on these local coordinate systems. The FE representations of the applied constraints are shown in three views in Figures 3, 4 and 5.

Constraint 1

This constraint consisted of a link (beam element), one end of which was completely fixed to a plate and the other holding a ball joint (B11) as shown in Figure 6. The ball joint (B11) of this constraint was represented by a node that was fixed in position (i.e. $U_x = U_y = U_z = 0$), but was free to rotate. The second beam element connected the first node (B11) to the bone through a bolt. The end-point of this link was regarded as the 'master' node, which was in-turn rigidly connected to the 'slaves' nodes (with 3 DOF per node) located on the periphery of the 5 mm hole in the Angulus Inferior (Fig. 6). The 'slaves' nodes move similar to the 'master' node due to rigid coupling between them. This constraint restrains 3 DOF (i.e. $U_x = U_y = U_z = 0$). Three reaction forces (R_x, R_y, and R_z) can be calculated. Moments are zero ($M_x = M_y = M_z = 0$), which was used as a check of the internal consistency of the model.

Constraint 2

This constraint represented two ball joints connected by a link (Figs 3 and 7). The first node, representing the first ball joint B21, was connected to the second node (ball joint: B22) by the first beam element. Axial translation of the first link being negligibly small as compared to the deflection of the scapula, the translational DOF ($U_x = 0$) at second node (B22) was restrained. A second ball joint is in-turn connected to a second beam element, which has a fork type arrangement for fixation with bone. This link connects the second node (B22) to an end-point node, which was regarded as the 'master'. The 'slaves' nodes those were located on the bone move similar to the 'master' node, since rigid coupling was specified between them. Hence, the reactive force at the bone-link interface (R_x) can be calculated from the FE analysis, since only one DOF was fixed (i.e. $U_x = 0$).

Constraint 3

In the experiment this constraint consisted of a hinge joint (H31) with axis of rotation in the y-direction as shown in Figures 5 and 8. As a result, the node at the hinge was allowed to rotate about the y-axis (resulting in $U_x = U_y = U_z = Rot_x = Rot_z = 0$). A beam element of length 63 mm connected that node (H31) to a node representing the ball joint (B31). Axial translation of this first link being negligibly small as compared to the deflection of the scapula, the translational DOF ($U_x = 0$) at the second node (B31) was restrained. A second beam element connected the ball joint (B31) to the bone through a bolt. The end-point of this link was regarded as the 'master' node, which was in-turn rigidly connected to the 'slaves' nodes located in the periphery of the 5 mm hole in the supraspinous fossa (Fig. 8). This ball node (B31) was constrained to move in z-direction, which implies an additional restraint on the translational DOF ($U_z = 0$). Therefore, two DOF ($U_x = U_z = 0$) was fixed, and R_x and R_y can be calculated from the FE analysis.

4.2.5 Transformations: experiment to FE model

In order to find a relation between the CT-scan coordinate system and the experiment coordinate system, six markers were used. The strain gage positions, the load application points, direction of loading and constraint positions in the experiment were transformed relative to the coordinate system of the FE model. Calculations were based on two sets of position coordinate of markers, one set measured relative to the experiment coordinate system and the other measured relative to the CT-scan coordinate system. The position of the six markers in the scapula, were measured with respect to four fixed points on the experimental set-up with the help of 3-D coordinate measuring system, the palpator (Pronk and Van der Helm, 1991). The precision of the palpator is estimated as 0.96 mm standard deviation per coordinate and 1.43 mm per reconstructed point (Pronk and Van der Helm, 1991). The position of a marker can be recorded by pressing the end point of the palpator (radius, 1.5 mm) to the palpated landmark. The markers in the scapula defined the position of the scapula in the experimental reference frame. Rotational matrix and translation vectors that are required for transformation of coordinate system were calculated according to Veldpaus et al. (1988). The coordinate systems of the CT-scan images and the FE model were identical. In the experiment the position of the scapula, for different load cases, can be recorded by remeasuring the six marker positions using the palpator. The position of the FE model of the scapula being fixed with respect to the global coordinate system (equivalent to the CT-scan coordinate system), it was decided to rotate and translate the forces instead of the rotating and translating the scapula. The position and orientation of a strain gage, defined by two endpoints of the gage in the longitudinal direction was measured relative to the six markers. The orientation of a strain gage was required for the calculation of strain from the FE model. Similar measurements were performed to trace the positions of the constraint mechanisms in the FE model.
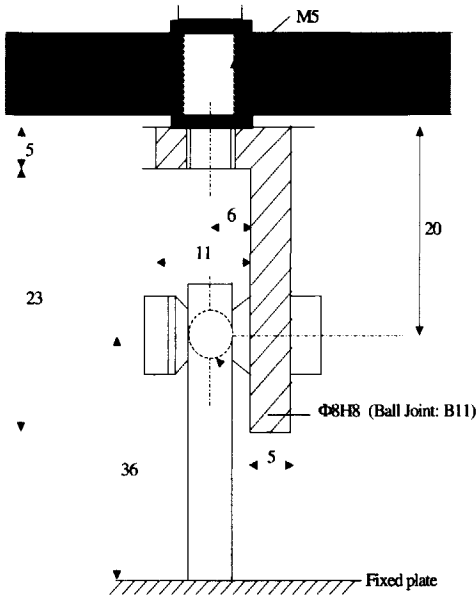
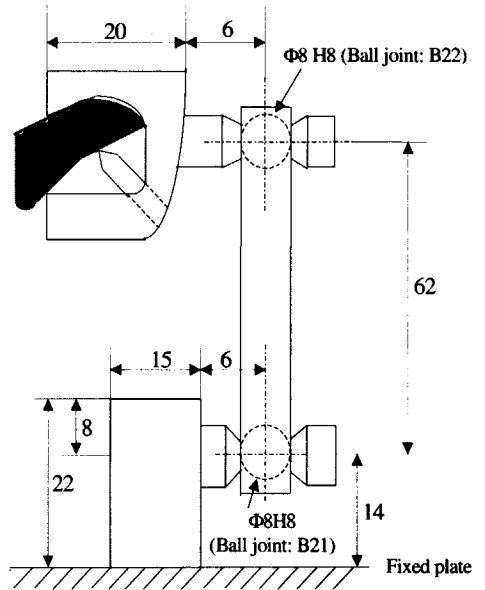**Figure 6.** Constraint 1, with one ball joint and links.

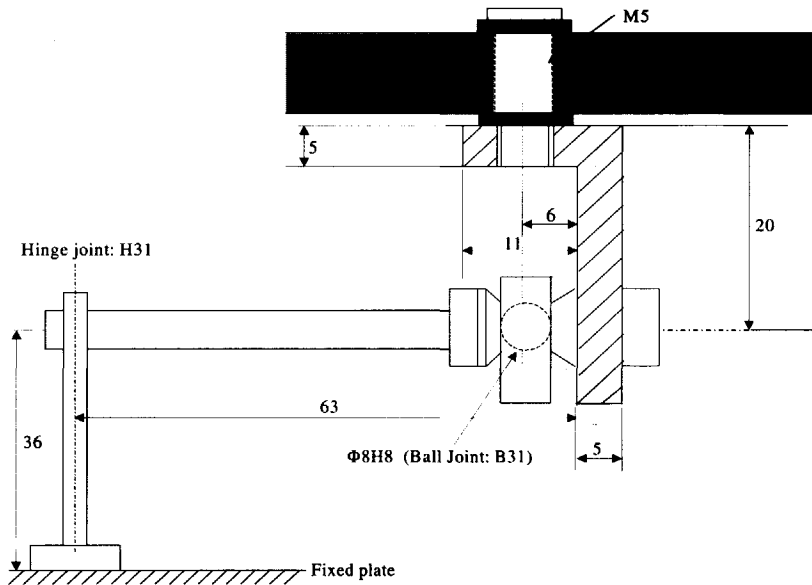**Figure 7.** Constraint 2, with two ball joints interconnected by links

Figure 8. Constraint 3, with hinge joint and ball joint interconnected by links.

Table 3. Measured (expt.) and numerical (FE) strains (με) for load cases 1 to 7. Strain gages (1 – 9) are active for these load cases.

Strain gage number	Load case 1 (glenoid)		Load case 2 (spine)		Load case 3 (acromion)		Load case 4 (glenoid)		Load case 5 (glenoid)		Load case 6 (acromion)		Load case 7 (glenoid)	
	Expt. Strain	FE strain	Expt. Strain	FE strain	Expt. strain	FE strain	Expt. strain	FE strain	Expt. strain	FE strain	Expt. strain	FE strain	Expt. strain	FE strain
1	-12	-58	-44	-31	-100	-836	-24	-37	-16	-149	-96	-423	-18	-40
2	-46	-54	-38	-52	106	369	-36	-37	-40	-47	80	209	-44	-56
3	65	199	22	120	-124	-107	58	111	62	102	-90	-277	70	209
4	-428	-407	-314	-209	774	1074	-433	-446	-312	-323	503	641	-460	-433
5	436	577	228	214	-993	-994	438	631	325	493	-634	-762	465	620
6	-11	-22	-102	-69	66	135	-42	-48	-20	-31	57	75	-15	-23
7	-68	-109	47	-34	316	379	-75	-123	-31	-92	177	244	-75	-119
8	60	-11	-9	-18	-62	-381	62	-37	42	26	-33	-213	64	-12
9	69	36	-42	-81	148	-200	68	47	62	30	91	-75	76	39

Table 4. Measured (expt.) and numerical (FE) strains (με) for load cases 8 to 10. Strain gages (10 – 18) are active for these load cases.

Strain gage number	Load case 8 (glenoid)		Load case 9 (glenoid)		Load case 10 (glenoid)	
	Expt. Strain	FE strain	Expt. Strain	FE strain	Expt. strain	FE strain
10	64	144	36	110	49	94
11	-70	-53	-26	-22	-64	-66
12	-18	-4	-11	-2	-13	-2
13	-346	-110	-230	-94	-203	-104
14	821	2437	498	1574	514	1056
15	146	132	80	124	130	114
16	2*	98	4*	58	2*	16
17	-199	-100	-122	-57	-99	-49
18	6	2	2	2	5	1

* strain gage not responding to change in load.

4.3 Results

The FE model of the experimental scapula, containing 13853 elements, 18216 nodes, 678 constraint equations and 79201 active DOF has been solved using ANSYS FE software. Equivalent loads of the experiment were applied at glenoid, acromion, and scapular-spine. Transformations (rotational matrix and translation vector) relating the experiment and the FE model were calculated to obtain the location and the orientation of strain gages relative to the FE model coordinate system.

The unit vector {U}, along a particular strain gage, was calculated from the two measured points representing a strain gage. Strain tensors [S] in the global coordinate system (ε_{xx}, ε_{yy}, ε_{zz}, γ_{xy}, γ_{yz}, γ_{zx}) at a particular node, resembling most closely a strain gage location, were obtained from the FE solution. The strain value along the desired direction was calculated, using $S_i = \{U\}^T [S]\{U\}$. The strain gage measurement, obtained from the experiment, is designated as the measured (experimental) strain. The strain value computed from the FE model, corresponding to a strain gage location and orientation, is designated as the numerical (FE) strain. The experimental and the FE strains, corresponding to the applied load cases are listed in Tables 3 and 4. These results are graded according to the following criteria. A difference of sign (positive/negative) in strain values not very close to zero (greater/less than ±50 $\mu\varepsilon$) is evaluated as incorrect, a deviation of less than factor 2 is considered as good, a deviation less than factor 3 is considered as satisfactory, whereas a deviation more than factor 3 is considered as unsatisfactory result.

In order to visualise the quality of the results the measured strain ($\mu\varepsilon$) was plotted against FE strain ($\mu\varepsilon$), for all the ten load cases (Fig. 9a). The ideal line, for which measured strain is equal to numerical strain (slope = 1.0), was included in the plot to assess the quality of agreement. The type of marker indicates strain values for a particular load case. Results indicate that the measured strain is in good agreement with the FE strain (Fig. 9a). It is also observed that a lot of points are clustered in the lower range of strain values (± 250 $\mu\varepsilon$). Therefore, an exploded view (Fig. 9b), in the range of +250 $\mu\varepsilon$ and –250 $\mu\varepsilon$ has been used to compare strains in the lower range values. Based on the results (Tables 3 and 4), regression analysis of the measured and the FE strains was performed. The correlation coefficient (r), the Standard Error (SE) of the estimate, the Percentage Error (PE) and the test-statistic value of linear regression slope (b) were considered to analyse the quality of the results (Table 5). The SE of an estimate is the sum of the residuals, which is related to multiple correlation coefficient squared (r^2). Whereas, the SE of b is the deviation in the agreement of the measured and the numerical strains, which is further expressed as PE (in b). The PE is calculated as the ratio of SE of slope (b) and b. In order to test the null hypothesis H_o: b = 0, the test statistic along with the level of significance (P value) is computed for each load case. The null hypothesis H_o: b = 0, implies that there is no agreement between the measured and numerical strains. The H_o is rejected if the test statistic value exceeds the specified significance level. The statistical analysis has been primarily used to test whether a significant relationship exists between the measured and the numerical strains. The error in the intercept (a) of the linear regression is less important and was, therefore, not considered in the analysis. The deviations in the values of measured and numerical strains are explained in the following.

4.3.1 Applied load at the glenoid cavity (strain gages 1 – 9; load cases 1, 4, 5 and 7)

A comparison of the measured strain and FE strain for strain gages 1 to 9, due to an applied load at the glenoid cavity, indicates significantly high correlation (0.95 – 0.97) and low standard error (51 – 66 $\mu\varepsilon$). A mismatch in positive and negative strain was observed in the output of strain gage 8, which was located near the point of load application at the glenoid cavity.
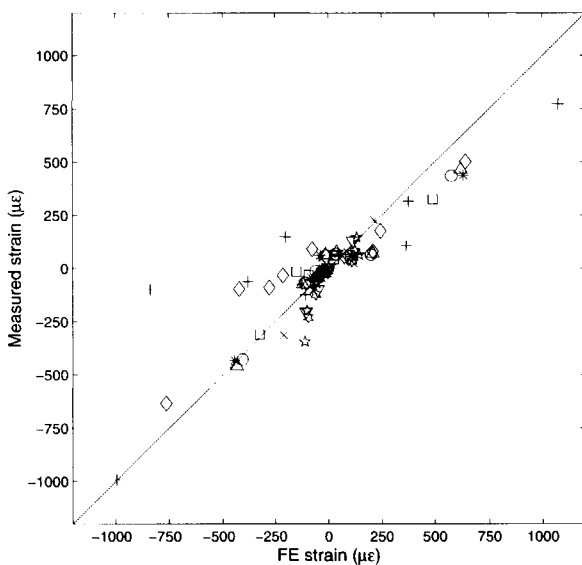
Figure 9a. Measured strain (µε) plotted against FE strain (µε) for load cases 1 – 10. Marker indicates load case.

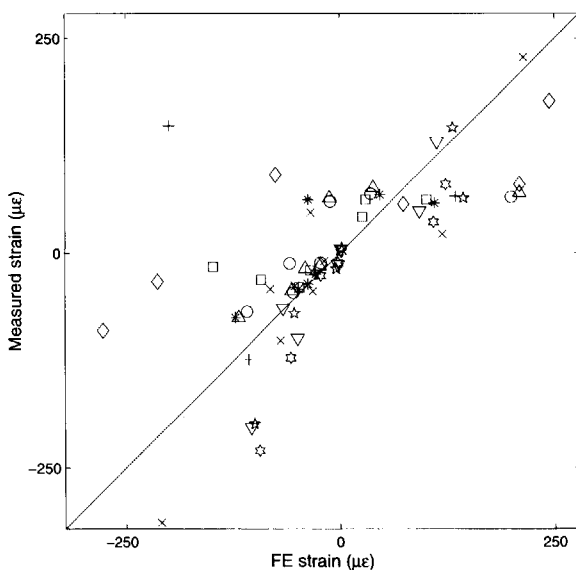**Figure 9b.** Exploded view of measured strain (µε) plotted against FE strain (µε) for load cases 1 – 10, in the range of +250 to –250 µε. Marker indicates load case.

The output of this gage was highly sensitive to small changes in the point of application of load. Strain gages located away from the area of load application exhibit more consistency in the comparison of measured and numerical strain. The behaviour of strain gages 4 and 5, located on opposite sides of the lateral border of the scapula, has important consequence. As evident from the experimental and numerical results, the outputs of gage 4 (high positive strain) and gage 5 (high negative strain) indicate bending of the lateral border due to applied compressive force at the glenoid cavity. As a result, high tensile and compressive stresses are generated in the ventral (location of gage 4) and dorsal (location of gage 5) side of the lateral border, respectively.

The results of the regression analyses, as shown in Table 5, indicate significantly high linear relationships between measured and numerical strains (PE of b = 8.81 - 10.17%; T-statistic = 9.626 - 11.348, with P = 0.0000 - 0.001). The intercept values vary between –3.47 to –9.74, and are not different from 0. Since the T-statistic value exceeds the specified significance level, the hypothesis H_o: b = 0 is rejected (Table 5). It appears, therefore, that the two variables (measured and numerical strains) do depend on each other with a confidence level more than 95%.

4.3.2 Applied load at the acromion (strain gages 1 – 9; load cases 3 and 6)

Corresponding to load cases 3 and 6, correlation coefficients of 0.87 and 0.94, and standard errors of 248 με and 105 με, were observed between the measured and the FE strains. Out of nine, the outputs of six gages were satisfactory. The load transfer, due to an applied load at the acromion, takes place predominantly along the lateral border, resulting in severe bending. This is indicated by the high strain outputs in the gages 4 (positive) and 5 (negative), both experimentally and numerically. The behaviour of the strain gages 8 and 9, (located at the base of the scapular spine and the glenoid) for load case 3, was inconsistent. A possible reason was the proximity of these gages near a region of high load, caused by application of load on top of the acromion. Although, the FE and the measured strains of gage 1 (load case 3) indicate similar signs (positive/negative), the large differences between these values indicate incorrect results. In order to obtain more meaningful equation, this data point (outlier) was omitted and new regression analysis was performed (Table 5). For load cases 3, the correlation coefficient and the standard error of the estimate are 0.93 and 197 με, respectively.

The regression analyses indicate a linear relationship between the measured and FE strains (PE of b = 13.82 - 16.12%; T-statistic = 6.20 - 7.58, with P = 0.0008 - 0.001). The intercept values for the third and the sixth load cases are 2.89 and 50.37, respectively. The T-statistic value exceeds the specified significance level and therefore, the hypothesis H_o: b = 0 is rejected (Table 5). These results indicate that the two variables (measured and FE strains) do depend on each other, with a very high confidence level.

4.3.3 Applied load at the scapular spine (strain gages 1 – 9; load case 2)

The results of the measured and FE strain, due to applied load at the scapular spine was consistent with a high correlation coefficient of 0.90 and low standard error of 64 με (Table 5). The strain gage outputs when plotted against resultant loads indicate non-linear nature particularly at higher loads. This might be due to the high reactive moments occurring at the constraints, which was caused by the high out-of-plane loading at the scapular spine. The latter was responsible for sudden changes in the gradient of the load-deflection curve of the scapula, while it was continuously loaded.

Table 5. Regression analysis of the measured and FE strains for all load cases.
([+] excluding strain gage 1 – outlier, * excluding strain gages 14 and 16)

Load case	Strain gages	Correlation coefficient (r)	Standard Error (SE) in με	Linear Regression $y = a + bx$		Standard Error (SE) of b	Percentage Error (PE) of b	T statistic (P value)
				a	b			
1	1 - 9	0.964	62.75	-6.37	0.810	0.0841	10.38	9.626 (P=0.0000)
2	1 - 9	0.906	64.40	-9.09	1.063	0.1878	17.67	5.659 (P=0.0008)
3	1 - 9[+]	0.930	197.59	2.89	0.756	0.1219	16.12	6.200 (P=0.0008)
4	1 - 9	0.974	54.30	-3.47	0.774	0.0682	8.81	11.348 (P=0.0000)
5	1 - 9	0.956	51.53	7.29	0.707	0.0821	11.61	8.602 (P=0.001)
6	1 - 9	0.944	105.87	50.37	0.685	0.0947	13.82	7.579 (P=0.001)
7	1 - 9	0.965	65.92	-9.74	0.814	0.0828	10.17	9.829 (P=0.0000)
8	9 - 18*	0.890	82.64	-61.83	1.441	0.3290	22.83	4.380 (P=0.0072)
9	9 - 18*	0.890	52.16	-48.73	1.149	0.2624	22.83	4.379 (P=0.0072)
10	9 - 18*	0.944	29.11	18.14	0.713	0.1107	15.53	6.440 (P=0.0013)

However, a comparison of the measured and predicted strains, as shown in Table 3, indicates that out of nine, the results of only two gages are unsatisfactory. The results of 7 gages are very well comparable. High strain outputs of gage 4 and 5 (tensile and compressive) indicate that a high amount of load transfer takes place along the lateral border.

The results of regression analyses indicate that the regression slope, 1.063 (SE = 0.18, PE = 17.67%) is very close to 1 and the intercept value, -9.09 is not different from 0. The hypothesis H_o: b = 0 is rejected, since the T-statistic value exceeds the specified significance level. Hence, the two variables (measured and FE strains) exhibit a strong relation between each other with a very high confidence level, for this load case.

4.3.4 Applied load at the glenoid cavity (strain gages 10 – 18; load cases 8, 9 and 10)

The strain gages 10 to 18 are located in the superior half of the scapula. In order to obtain feasible experimental validation of the FE model of the scapula, the point of application of load should be located at a reasonable distance from the strain gages. Therefore, applied loads were restricted to various locations in the glenoid cavity only. A comparison of the measured strain and the FE strain, for this second set of nine gages, indicates high correlation and low standard error (Table 5). The strain gage 16 was found to be non-responsive, as there was no change in measurement with increase in applied load; hence it was omitted from the analysis. The results of strain gage 14 should be neglected; the gage located near the constraint 3 was subject to large strain resulting from high reactive forces and moments at this constraint. Barring these two gages, the measured strain and FE strains are well comparable.

The results of the regression analyses exhibit linear relationships between the measured and FE strains. The regression slope ranges from 1.15 to 1.44, whereas the intercept ranges from –25.71 to – 61.83. These values indicate that the slope and the intercept are not significantly different from 1 and 0, respectively. However, the percentage errors in slope vary between 15.52 (T-statistic = 6.44, P = 0.0013) to 22.83 (T-statistic = 4.38, P = 0.0072), which are higher than the earlier load cases. Moreover, it may still be stated with a very high degree of confidence that the two variables (measured and FE strains) are strongly related to each other.

4.4 Discussion

The primary goal of the study is to validate a realistic 3-D FE model of the scapula using solid and shell modelling approach and material properties and thickness taken from CT-scan data. The studies of Keyak et al. (1993) and Dalstra et al. (1995), based on the femur and the pelvic bone, respectively, are significant contributions towards strain gage validations of realistic FE modelling of bone. However, in both the studies, a part of the bone was fixed in a bed of cement, which appears to be a simplified method of constraining the bone in the experiment. Hence, a new experimental set-up was required to support the bone in the mechanical testing machine as well as impose bending and deflection in almost all directions, when it is loaded. The novelty of this study lie in applying special purpose constraints, supporting links interconnected by ball joints and hinge joints, to impose bending and deflection in all directions in response to applied loads. A total number of eighteen strain gages was fixed at a variety of locations on the surface of a fresh scapula, in order to validate the proposed FE model. The scapula was loaded in a mechanical testing machine and supported at the Angulus Inferior and the lateral border by links, interconnected by ball joints and hinge joints. The loads are applied on the surface of the scapula at several locations, like glenoid cavity, acromion, and scapular spine. The loading and constraint conditions are most closely simulated in the FE model. Grading of the results and regression analysis of the measured and FE strains were performed to obtain an estimate of the quality of the FE model.

The results of the strain gages 1 to 9 and 10 to 18 were found to have a high correlation between the measured (experimental) and numerical (FE) strains, except a few mismatches or deviations (Fig. 9). It can be observed from these measured and numerical predictions, that the transfer of load takes place predominantly along the lateral border due to an applied load at the glenoid cavity, acromion and spine (Tables 3 and 4). The outputs of gage 4 (high positive strain) and gage 5 (high negative strain) indicate bending of the lateral border resulting in high tensile and compressive stresses in the ventral and dorsal side of the lateral border, respectively.

A regression analysis (Table 5) indicates strong agreement for the first set of strain gages (1 – 9), when load is applied at the glenoid. The correlation coefficient varies between 0.956 and 0.973 and SE of the estimate varies between 52 to 66 με. The percentage error (9 – 12%) in regression slope (b) is low, indicating that the two variables (measured and FE strains) strongly depend on each other. Whereas for the second set (strain gages 10 – 18, load cases 8 – 10), the variation of the correlation coefficient and the SE of the estimate was 0.890 – 0.944 and 29 – 83 με, respectively. The PE (15 – 23%) in regression slope (b) for the second set of gages is slightly higher than the PE for first set of gages. Strain gage 16 is non-responsive to change in the load and strain gage 14 is located near the large strain area of constraint 3. Therefore, these two gages are omitted from the analysis. Moreover, it appears from the statistical analyses that the agreement between the two variables (measured and FE strains) is high (Table 5). A comparison of the measured and the FE strains, for an applied load at the spine (Table 3; load case 2) and the acromion (Table 3; load cases 3 and 6), indicates that the results (per load case) of seven gages, out of nine, still are very well comparable. Results, corresponding to load cases at the acromion and the scapular spine, have also been significantly consistent (r = 0.906 – 0.944 and SE of estimate = 64 – 106 με), except a single case where the SE of the estimate is calculated as 198 με (Table 5). Considering all the contributing factors that might be responsible for the deviations between measured and FE strain, it appears, as a whole, that the FE results show high correlation with that of the experimental results.

It is difficult to obtain strain gage measurements on a fresh bone. Fixation of the strain gages on the moist, oily surface of bone involves practical problems. Further, the strain gage measurements yield data, which is an average of the real strains occurring underneath the gage. On the other hand, the accuracy of the FE strains depends on the quality of representation of the FE model as compared to the mechanical testing conditions. The FE analysis provides a continuous field of stresses and strains, and if there is a sharp gradient in these quantities, it will be virtually impossible to find a perfect correlation between the experiment and the FE results. One of the possible reasons for the mismatch in values of FE and measured strains might be due to the linear isotropic assumption of bone material properties, which is an idealisation of the reality. The magnitude of errors, whether large or small, due to these assumptions is difficult to predict. Bone, in reality, is a non-linear, viscoelastic, anisotropic material. Apart from the stress/strain gradient, another reason for the large deviations between the FE and the measured strains can arise due to errors in allocating the thickness of shell elements from the CT-scan image. This can be observed in the location of gage 1. The shell thickness at this location (medial border) is relatively thick, and therefore, the local resistance against deformation is higher. The stresses in this area are expected to be low, which is correctly indicated by the low values of measured strain. The relatively large values of FE strain as compared to the low values of measured strain, confirm the predominant influence of the thickness factor (in shell elements) in the FE analysis of stresses and strain. Therefore, a high degree of carefulness is required for allocating thickness of the shell elements from the CT-scan data to the FE model. Finally, it was also observed that the results of FE analysis were sensitive to approximations in the FE modelling of loading conditions. For example, a slight change in the location and orientation of the applied load at the glenoid leads to changes in the bending mode of the bone structures in the vicinity of the glenoid, resulting in deviations of magnitude and direction of FE strains.

There are hardly any reports available on experimental strain gage measurements on fresh scapula. Measurements of strain on the femur (Rohlmann et al., 1982; Walker et al., 1987; Keyak et al., 1993) and the pelvic bone (Jacob et al., 1976; Lionberger et al., 1985; Finlay et al., 1986; Ries et al., 1989; Dalstra et al, 1995) have been used for experimental validation of numerical models and related biomechanical evaluations. The results of this study may be compared to similar

investigations by Rohlman et al. (1982), Keyak et al. (1993) and Dalstra et al. (1995) regarding experimental validations of strain predictions by 3-D FE models of the femur and the pelvic bone. Keyak et al. (1993) reported that when measured strain (dependent variable) was plotted against FE strain (independent variable), the correlation coefficient, 0.769, the regression slope, 0.94 (SE of b = 0.19) and the intercept, -149 με were obtained for nine out of eleven rosette gages fixed on the proximal portion of the left femur. The SE of the estimate for this regression was 311 με. The output of two strain gages were omitted from the regression analysis since, one gage was not working properly, and the other gage with the largest FE strain, -4500 με, was an outlier (Keyak et al., 1993). On the other hand, the stresses calculated from the strain data of the experiment were compared to the results of FE model for eight strain rosette gages fixed on the pelvic bone (Dalstra et al. 1995). Although the numerical and experimental results (stresses) were comparable, a thorough statistical analysis on the quality of agreement of the results was missing. In contrast, high correlation coefficients (0.89 – 0.97) and low percentage error in regression slope (9 – 23%) are observed in this study (Table 5). The regression slope (b = 0.68 – 1.44, SE of b = 0.07 – 0.33) and the intercept are not significantly different from 1 and 0, respectively (Table 5). The SE of the estimate varies between 29 με and 105 με, except a single case where the value is 198 με. In view of the complicated testing procedure on a fresh scapula, the significance of high correlation coefficients, low standard errors and percentage errors in slope, as compared to similar studies (Keyak et al., 1993; Dalstra et al., 1995), strongly suggests the validity of the proposed FE model of the scapula.

In developing the present 3-D model of the scapula, our priorities have been computational time and ease of model generation with the consideration of moderate quality of mesh size. A high mesh refinement in some locations might yield better correlation but at the same time would require significant effort and substantially greater computational time. In some cases, the uncertainty in correlating strain gage locations and orientations with the FE model or the errors in the measured and the predicted strains, or both, might be the cause of the scatter in some results.

4.5 Conclusion

Considering the complicated testing procedure on a fresh sample of scapula, the high correlation coefficients and the relatively low standard errors and percentage errors in regression slope, strongly suggest that the numerical strains calculated by the FE model can be used as a valid predictor of the actual measured strain. It is therefore, concluded that the present method of generating a detailed FE model of scapula, using CT-scan measurements and combination of shell and solid elements is appropriate for scapula, since bending and membrane capabilities can be included in the model. The FE model of the scapula, using a static shoulder model of forces would be useful in the prediction of stresses and strain, realistically.

Acknowledgements

References

Dalstra, M., Huiskes, R. and van Erning, L. (1995). Development and validation of a three-dimensional finite element model of the pelvic bone. J. Biomech. Eng. 117, 272-278.

Finlay, J.B., Bourne, R.B., Landsbers, P.D. and Andreae, P. (1986). Pelvic stresses in vitro – I. malsizing of endoprostheses. J. Biomechanics, 19, 703-704.

Huiskes, R., Weinans, H., Grootenboer, H.J., Dalstra, M., Fudala, B. and Slooff, T.J. (1987). Adaptive bone-remodelling theory applied to prosthetic-design analysis. J. Biomechanics 20, 1135-1150.

Huiskes, R., Weinans, H. and Dalstra, M. (1989). Adaptive bone-remodelling and biomechanical design considerations for non-cemented total hip arthroplasty. Orthopaedics 12, 1255-1267.

Huikes, R., Weinans, H. and van Rietbergen, B. (1992). The relationship between stress shielding and bone resorption around total hip stems and the effect of flexible materials. Clin. Orthop. Rel. Res. 274, 124-134.

Huiskes, R. (1993). Stress shielding and bone resorption in THA: clinical versus computer-simulation studies. Acta Orthopaedica Belgica 59 (Suppl. 1), 118-129.

Huiskes, R. (1997). Validation of the adaptive-bone remodelling simulation models. In: Lowet, G. et al. (Eds). Bone Research in Biomechanics. IOS Press, Amsterdam, 33-48.

Jacob, H.A.C., Huggler, A.H., Dietschi, C. and Schreiber, A. (1976). Mechanical function of subchondral bone as experimentally determined on the acetabulum of the human pelvis. J. Biomechanics, 9, 625-627.

Kerner, J., Huikes, R., van Lenthe, G.H., Weinans, H., van Rietbergen, B., Engh, C.A. and Amis, A.A. (1999). Correlation between pre-operative periprosthetic bone density and post-operative bone loss in THA can be explained by strain-adaptive remodelling. J. Biomechanics 32, 695-703.

Keyak J.H., Meagher J.M., Skinner H.B. and Mote C.D. Jr. (1990). Automated three-dimensional finite element modelling of bone: a new method. J. Biomed. Eng. 12, 389-397.

Keyak J.H., Fourkas, M.G., Meagher J.M. and Skinner H.B. (1993). Validation of an automated method of three-dimensional finite element modelling of bone. J. Biomed. Eng. 15, 505-509.

Lionberger, D., Walker, P.S. and Granholm, J. (1985). Effects of prosthetic acetabular replacement on strains in the pelvis. J. Orthop. Res. 3, 372-379.

Pronk, G.M. and Van der Helm, F.C.T. (1991). The palpator, an instrument for measuring the three-dimensional positions of bony landmarks in a fast and easy way. J. Med. Eng. Tech. 15(1), 15-20.

Ries, M., Pugh, J., Au, J.C., Gurtowski, J. and Dee, R. (1989). Cortical pelvic strains with varying size hemiarthroplasty in vitro. J. Biomechanics 22, 775-780.

Rohlmann, A., Bergmann, G. and Koelbel, R. (1982). The relevance of stress computation in the femur with and without endo-prostheses. In: Gallagher RH et al., eds. Finite Elements in Biomechanics. New York: Wiley, 1982; 361-377.

Veldpaus, F.E., Woltring, H.J. and Dortmans, L.J.M.G. (1988). A least squares algorithm for equiform transformation from spatial marker coordinates. J. Biomechanics 21, 45-54.

Walker P.S., Schneeweis, D., Murphy, S. and Nelson, P. (1987). Strains and mocromotions of press-fit femoral stem prostheses. J. Biomechanics 20, 693-702.

Wright T.M. and Hayes, W.C. (1979). Strain gauge application on compact bone. J. Biomechanics 12, 471-475.

Appendix A

Mechanical testing machine	Zwick 1484, Germany
Located:	Delft University of Technology, Delft, The Netherlands.
Traverse velocity:	200 mm/min.
Rotation disk speed:	5 degrees per second.
Force transducer:	5 kN, sensitivity 2.4 N. attached to the stirred part.
Traverse transducer:	125 mm, sensitivity 0.06 mm.
Clamp:	Self griping jaw, 10 kN, attached to the stirred part.

A/D converter
Type: 12 bits.
Frequency: 50 Hz.

Strain Amplifier: KWS 3073 TF-mess verstarker, Hottinger Boldwin
                             Messtechnik, Germany

Voltage: 1 Volt.
Measured: ¼ bridge (one active gage, one dummy gage)
Connected: ½ bridge.

Formula:

$$\varepsilon \; = \; \frac{4}{k} \; \frac{S_p}{V} \; \frac{Um}{A_s} \qquad \text{(microstrain)}$$

where
$\in$ = strain (με)
k = gauge factor = 2.1
Sp = gain of strain gage used (1 or 0.2) = 0.2
V = voltage = 1 volt
Um = (value from A/D converter/2048)*10V
A_s = number of strain gauges measured in the bridge = 1
(¼ bridge used, hence A_s = 1)

Strain gauges: KFG-5-120-Cl-11L1M2R, KYOWA, Japan.
Type: General purpose gages.
Resistance: 120 Ω
Gage factor: 2.1
Gage length: 5 mm.
Gage width: 1.4 mm.
Matrix length: 9.4 mm.
Matrix width: 2.8 mm.

Strain gauge adhesive: CC-33A, KYOWA, Japan.
Temperature range: -196⁰C to + 120⁰C.

Coating: M-coat C KIT, Micro–measurement division, USA.
Type: Air drying silicone rubber, 20 minutes.

Chapter 5

Biomechanical Stress Analysis of the Scapula during Humeral Abduction

Abstract

An estimate of the stresses and strain in various parts of the scapula under normal physiological conditions is necessary for understanding the load transfer mechanism and for the development of glenoid prostheses. For this purpose, an experimentally validated, three-dimensional (3-D) Finite Element (FE) model of the scapula was used to calculate the stress distribution in the scapula during unloaded humeral abduction. Material properties of the elements are based on quantitative Computed Tomography (CT) measurements of the scapula. A musculoskeletal shoulder model calculates the muscle, ligament and joint reaction forces, during seven load cases of unloaded humeral abduction; 0 to 180 degrees, in steps of 30 degrees. The action of major muscle (m) forces (m. trapezius, m deltoideus, and m serratus anterior) and joint reaction forces (GlenoHumeral – GH, AcromioClavicular – AC, and ScapuloThoracic Gliding Plane – STGP) generates high stresses (30 – 60 MPa) in the solid bony ridges of the scapula. High tensile and compressive stresses (-30 to -58 MPa) are observed on cranial and caudal side of scapular spine, respectively, indicating bending of the scapular spine. The acromion is subject to bending, due to the pulling forces exerted by the AC-joint reaction force and the m. deltoideus, resulting in tensile and compressive stresses in the ventral medial part and dorsal lateral part. The GH-joint reaction force, a part of the force exerted by thorax-Angular Inferior (AI) joint reaction force and the m. serratus anterior are predominantly transferred along the lateral border resulting in severe bending of the lateral border. As a result high tensile (15 – 60 MPa) and compressive (-15 to -50 MPa) stresses are generated in the ventral and dorsal side of the lateral border, respectively. The glenoid is largely subject to high compressive forces by the GH-joint reaction force. High compressive stresses (-45 to -58 MPa) are transmitted at the connection of glenoid-scapular spine-infraspinous fossa. The Trigonum Spinae (TS) and the medial border are subject to bending due to the action of m. serratus anterior, inserting at AI and the reaction force at thorax-AI acting perpendicular to the plane of the scapula. The stresses (tensile and compressive) in the infraspinous fossa and supraspinous fossa are low (0.05 – 15 MPa), which indicate that the function of these structures is to act as attachment sites of large muscles rather than sharing of load. A qualitative estimate of the function of coraco-acromiale ligament was obtained, since data on geometry and material properties are still unknown. The ligament is stretched, and presumably will be under tension during humeral abduction.

Keywords: Shoulder, scapula, finite element modelling, stress analysis, ligament coraco-acromiale.

5.1 Introduction

The shoulder mechanism is an example of a very complex musculoskeletal structure, and consists of a chain of bones connecting the humerus to the trunk. The shoulder consists of scapula and clavicle and functions as a movable but stable base for the motions of the humerus. The SternoClavicular (SC-) joint connects the clavicle and sternum, and the scapula in its turn is connected to the clavicle by the AcromioClavicular (AC-) joint. Another connection between the scapula and the thorax is the ScapuloThoracic Gliding Plane (STGP), which constraints possible movements with two Degrees-Of-Freedom (DOF) and makes the system a closed chain mechanism. The humerus articulates with the scapula at the GlenoHumeral (GH) joint, which can be represented as a ball-and-socket joint. There are three extracapsular ligaments in the shoulder: the costoclavicular ligament limiting the range of motion of the SC-joint and the conoid and trapezoid ligament acting at the AC-joint. Seventeen muscles are crossing the joints of the shoulder mechanism; most of them are polyarticular, fan-shaped and have large attachment sites. In contrast to the pelvic bone, the shoulder achieves a considerable range of motion. Motions of the SC-joint and the AC-joint, which represent the motion of the shoulder, contribute to the large range of motions. The shoulder is a multifunctional joint with an infinite number of functions ranging from manipulating objects, throwing a ball and rising from a chair to lifting heavy load.

The scapula is a large, flat, triangular bone consisting of five solid bony ridges (glenoid, scapular spine, medial and lateral border, and coracoid process) and two thin, hard laminated structures – the infraspinous and supraspinous fossa. The glenoid, the scapular spine, and the lateral border originate from the infraspinous fossa. The scapula is subject to a number of muscle forces, ligament and joint reaction forces during elevation of the arm. Quantitative and qualitative estimates of all the muscles, ligaments and joint reaction forces acting on the scapula, during activities like unloaded humeral abduction, unloaded anteflexion, loaded abduction and loaded anteflexion was extensively investigated by Van der Helm (1994[a,b]).

It seems from the location, magnitude and direction of these forces that the scapula is loaded all over its structure. The primary function of the scapula is two-fold. On the one hand it offers an additional joint, so that the total rotation of the humerus with respect to the thorax can increase. On the other, it is a large bone, where the muscles have large lever arms with regard to the SC- and the AC-joint. Hence, smaller muscles will be sufficient to provide the necessary moments, which are in general larger than the moments around the GH-joint. The shape of the scapula provides large moment about SC- and AC-joint. This function is more important for the particular shape of the scapula.

The effect of load transfer across the scapula, using a detailed 3-D Finite Element (FE) model of bone has not been discussed until now. Studies, in the area of FE modelling and stress analysis of the scapula were mostly restricted to two-dimensional (2-D) models of the glenoid with or without the prosthesis (Orr et al., 1988; Friedman et al., 1992; Lacroix and Prendergast, 1997; Stone et al, 1999; Lacroix et al., 2000). These models lack the ability to describe the 3-D complicated geometry and mechanics adequately, since other important bony structures (e.g. scapula spine, medial border, lateral border, infraspinous and supraspinous fossa), joints (e.g. AC, STGP) and the effect of muscles, ligaments, and joint reaction forces were omitted. The 3-D model of Lacroix et al. (1997) and Lacroix et al. (2000) using Computed Tomography (CT) scan data was an effort in this direction. However, the quality of mesh generation (total elements: 7251 total degrees of freedom: 29415) is considered to be coarse. A simple coarse model is in itself not a problem, as long as the model is validated and the errors in the FE representation are minimum. However, neither a

validation nor the errors in FE representation was discussed (Lacroix et al., 1997; Lacroix et al., 2000), which makes it difficult to assess the accuracy of the results. The model might be able to predict certain qualitative trends, but lacks the ability to understand, in detail, the stresses induced in the individual parts of the scapula due to the action of muscle, ligaments and joint reaction forces, quantitatively. Similar to the pelvic bone structure (Dalstra, 1993; Dalstra et al., 1995), the scapula consists of a low-density, low elastic-modulus trabecular bone and is entirely covered by a layer of compact bone, representing a so-called 'sandwich structure.' However, little is known about the basic mechanics of the scapula and the load transfer mechanism, qualitatively and quantitatively.

Due to the highly complicated structure of the scapula, FE analysis is required to obtain a proper insight in the stress distributions throughout the bone. The present model was developed using a 3-D mesh, combination of shell-solid elements, with material properties and thickness extracted from CT-scan data (Chapter 3). The applied loading conditions include the effect of all muscles, ligaments, and joint reaction forces.

The purpose of this study was to evaluate and assess the stress distributions in a natural scapula during humeral abduction, using an experimentally validated 3-D FE model. New information about the qualitative behaviour of the coraco-acromiale ligament and the functional assessment of constituent structures of the scapula can be obtained from this study.

5.2 Materials and Methods

An elaborate description of the FE model of the scapula and the experimental validation has been reported in Chapter 3 and Chapter 4, respectively. A brief outline is presented here. The 3-D FE model of a right scapula was developed using a combination of solid and shell elements (2-layered shell). Inner cancellous bone regions and a part of the compact bone layer were modelled using ten-node tetrahedral solid elements. The outer cortical bone was modelled using two-layered shell elements, with 0.5 mm thickness of each layer. The contribution of the overlapping layer of shell elements within the solid elements was minimised by allocating a very low value for the Young's modulus. The Young's modulus and the Poisson's ratio of the shell elements, representing the outer cortical layer of 0.5 mm thickness, were taken as 17.5 GPa (Chapter 2) and 0.3 (Dalstra et al., 1995), respectively. The material properties of solid elements were based on Computed Tomography (CT) gray values. Using linear relationship between apparent density (ρ) and CT gray value (H), and power law relationships between Young's Modulus and apparent density (ρ), material properties were assigned to the elements (Chapters 2 and 3). The edge lengths of elements were specified between 3 – 4 mm or smaller on a side, and mesh generation was obtained using ANSYS FE software (Chapter 3). The solid elements were overlaid with shell elements so that they shared common nodes. A ventral view of the FE model is shown in Figure 1. The model contained 10921 elements, 14086 nodes, and a total number of 63435 active DOF.

5.2.1 Ligament coraco-acromiale

The ligament coraco-acromiale is connected between the cranial side of acromion and the cranial side of coracoid process. The qualitative and quantitative functions of this ligament are unknown. In order to assess the qualitative function of this ligament in the scapula, two additional beam elements were introduced in the FE model (Fig. 2). Nodes located on the cranial (top) side of acromion and coracoid process were connected to create these beam elements.
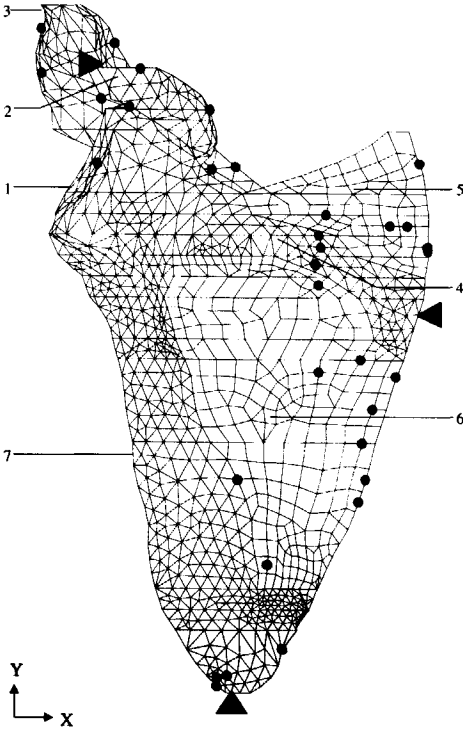
Figure 1. Finite element model of the scapula
1. Glenoid; 2. Coracoid Process; 3. Acromion;
4. Scapular Spine; 5. Supraspinous fossa;
6. Infraspinous fossa; 7. Lateral border. ●
Point of application of force; ▲ node restraint
to translate in all directions ($U_x = U_y = U_z = 0$);
◀ node restraint to translate in x- and z-
directions ($U_x = U_z = 0$); ▶ node restraint to
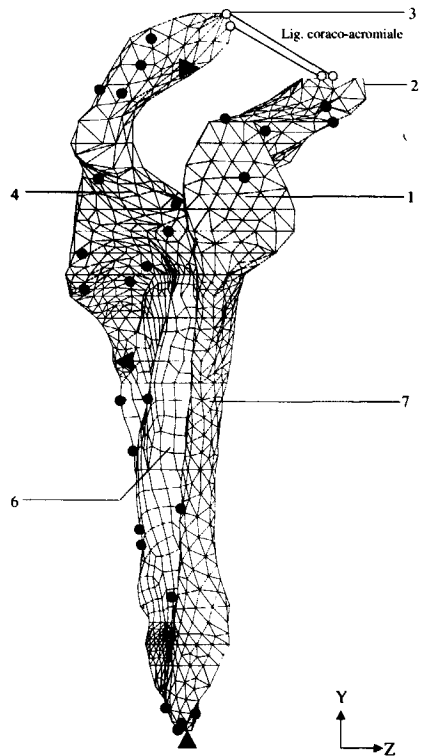translate in x-direction ($U_x = 0$).

Figure 2. A lateral view of FE model of
the scapula showing the ligament coraco-
acromiale as two beam elements formed
by connecting nodes (o); for more
explanations see Figure 1.

Reliable data on the geometry and the material properties of this ligament are also unknown. Hence, a very low value of Young's modulus, 100 MPa and unit cross sectional area and thickness were assumed, so that only the lengthening and shortening of the ligament can be calculated without affecting the load distribution of the scapula.

5.2.2 Applied loading conditions

The musculoskeletal shoulder model (Van der Helm, 1994[a,b]) and the CT images were based on the same cadaver. Geometric transformations were necessary to relate the shoulder model, to the CT image and finally to the FE model. Van der Helm and Veenbaas (1991) reported that generally more than one muscle lines of force were necessary to adequately represent the mechanical effect of muscles with large attachment sites. The location of muscles (m.) and joint reaction forces are illustrated in ventral and dorsal views in Figures 3b and 3b, respectively. Each muscle was represented by one to six elements, where each element can be considered as a single independent muscle line of force (Van der Helm and Veenbaas, 1991). During humeral abduction, the muscle elements change their length as well as orientation with respect to each other. A total number of ninety-five muscle elements were used to define all the shoulder muscles in the model. The muscle forces, the reaction forces due to the conoid ligament and the joint reaction forces (GH, AC, STGP), for seven load cases (unloaded abduction from 0 – 180 degree) were calculated from the shoulder model of forces (Van der Helm, 1994[a]). These forces were used as applied loading conditions for the FE model (Fig.1). The nearest node numbers on the surface of the FE model, corresponding to a point of force application, were computed. All the forces were applied as concentrated forces on these node numbers, since data on physiological cross-sectional area (PSCA) of the attachment sites of muscles and ligaments were not available. Additionally, constraints were applied at three nodes, located farthest from each other, to avoid rigid body motion (Figs 1 and 2). The consequences of using these constraints were checked so that they had minimum effect on the stress distribution of the scapula.

5.3 Results

The action of muscle, ligaments and joint reaction forces has considerable effect on the stresses evoked in the individual bony ridges, constituting the scapula. A schematic diagram of the major forces, applied on the scapula by m. trapezius, m. deltoideus and m. serratus anterior and the joint reactions (GH, AC and STGP) forces, are depicted in Figure 4. The distributions of principal stresses (tensile and compressive), for seven load cases, are presented in Figures 5 – 11. The force and moment analyses are presented with respect to a local co-ordinate system. The origin of the local co-ordinate system is at the thorax-TS connection, with the x-axis along the scapular spine pointing from medial to lateral (TS-AC), the y-axis is in the scapular plane defined by AC-TS-AI, pointing from caudal to cranial and z-axis from ventral to dorsal. During 90-degree humeral abduction, the forces are higher as compared to other six load cases. Therefore, the results for this load case are chosen for more detailed interpretation. A quantitative and qualitative estimate of the load transfer mechanism on individual parts of the scapula is presented in the following sections.

5.3.1 Acromion

The moments around the AC-joint are side effects of the muscle activity needed around the SC- and GH-joint, since no monoarticular muscle is crossing the joint. Moments produced by some muscles, particularly by the m. deltoideus, clavicular part, and the m. trapezius, clavicular part, are counterbalanced by the extracapsular conoid ligament, preventing the clavicle from rotating forward around its length axis (Van der Helm, 1994[a]).
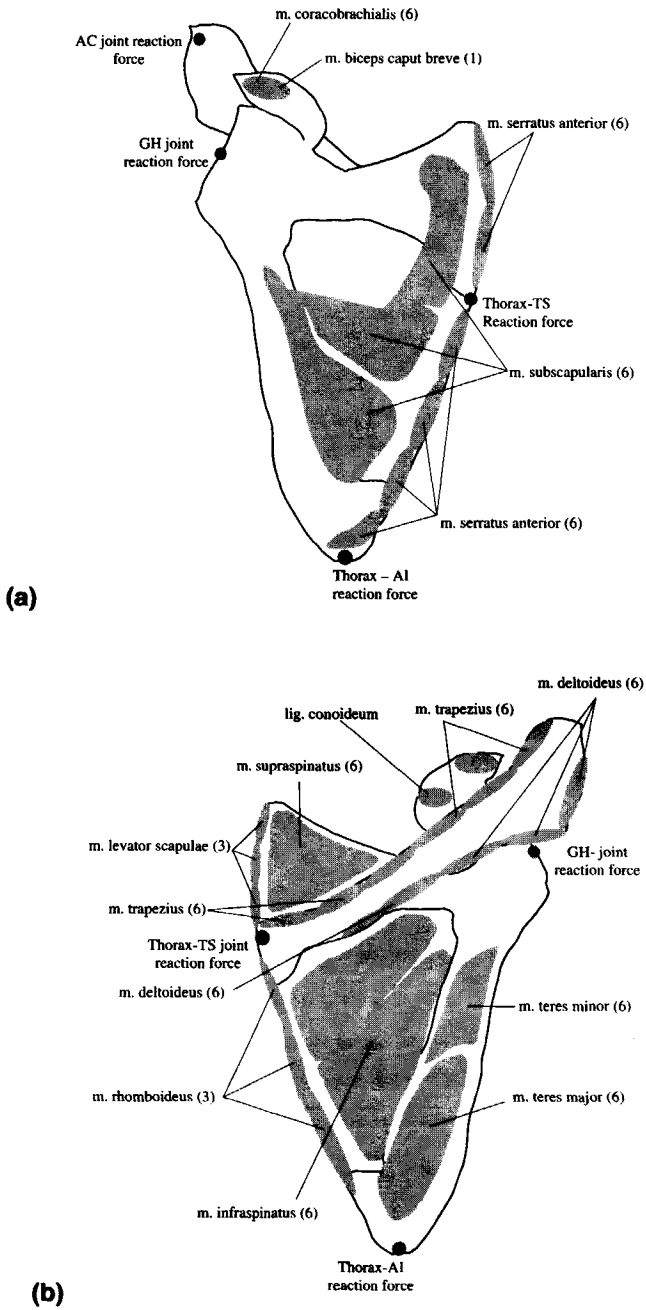
Figure 3. The locations of the muscles (m.) and the joint reaction forces in the scapula. Numbers within bracket indicate the number of muscle lines of action. (a) ventral view; (b) dorsal view.

The acromion is therefore, subject to the combined effect of the following forces, (1) the AC-joint reaction force due to the pressing of the scapula against the clavicle, (2) the m. trapezius, (3) the m. deltoideus and (4) the conoid ligament attached to the coracoid process. Without the conoid ligament, joint reaction forces are mainly directed along the longitudinal axis of the clavicle. Inclusion of the conoid ligament causes the joint reaction force to be directed downwards with respect to the fixed scapula. The combined effect of the pulling force by m. deltoideus and m. trapezius, and the AC joint reaction force, produces a bending moment around the y-axis resulting in tension in the ventral medial part and compression in the dorsal lateral part of the acromion.
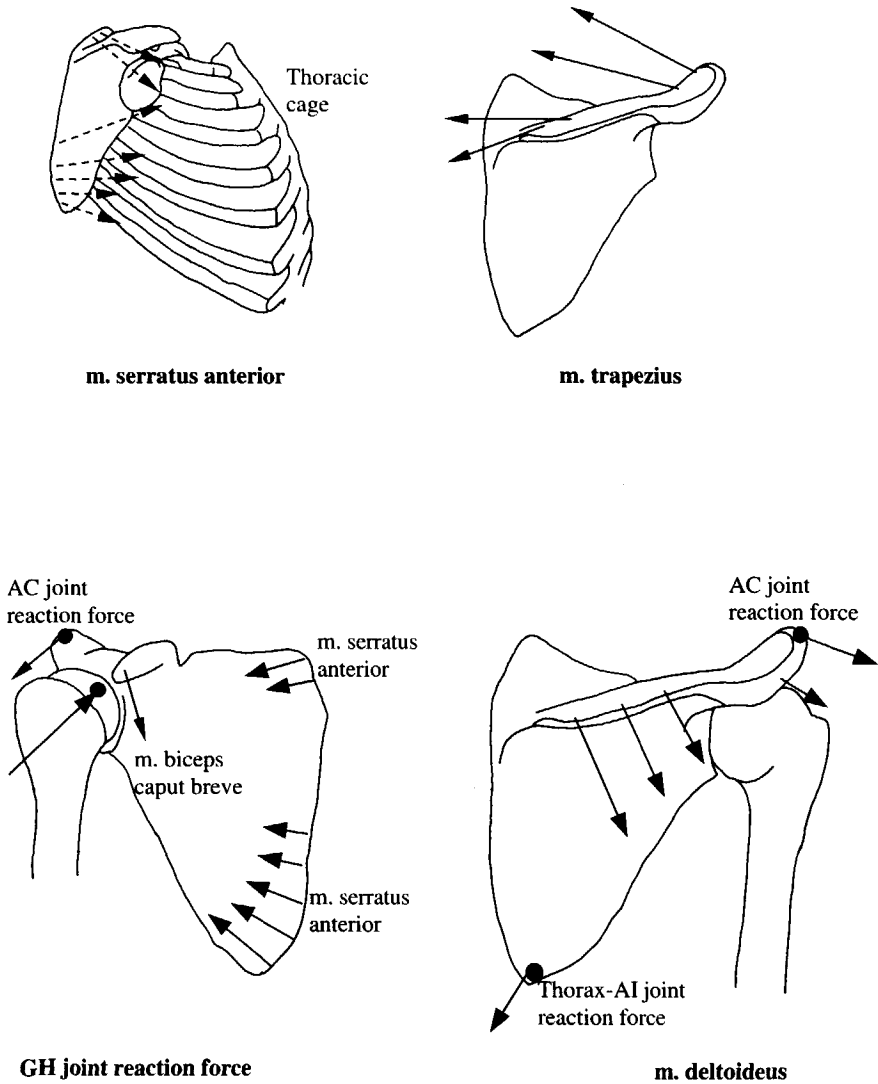
Figure 4. Schematic diagram of the major muscle and joint reaction forces.
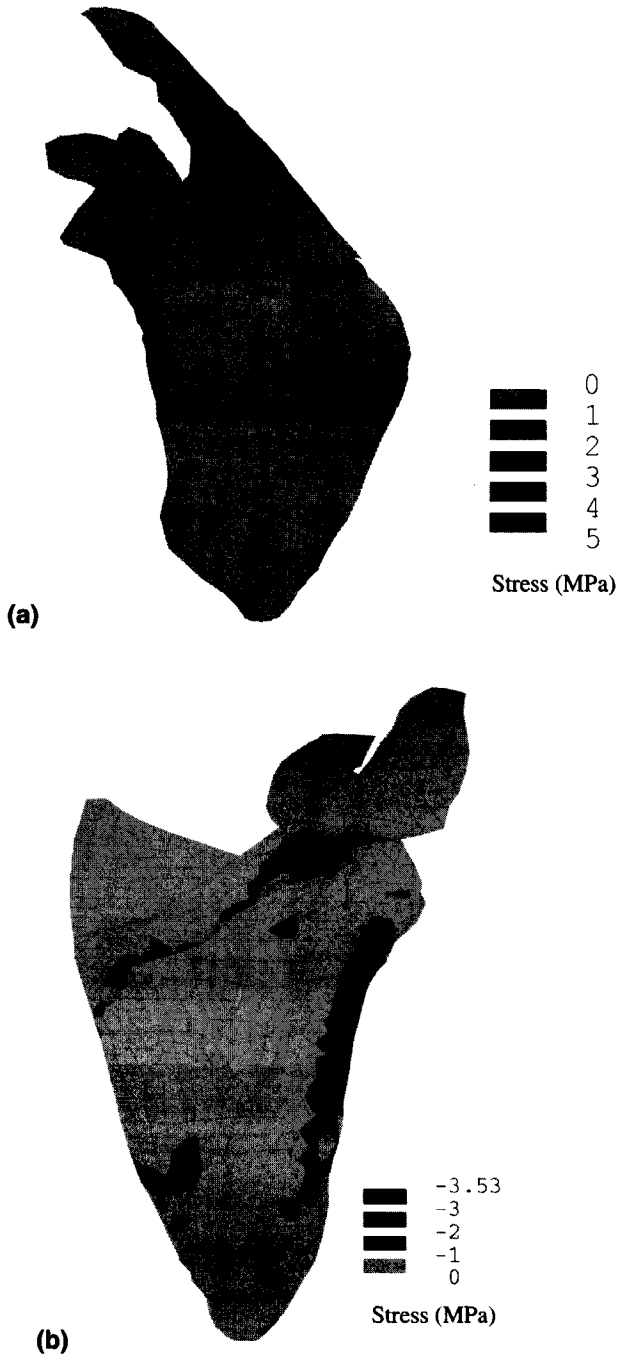
Figure 5. Principal normal stress distribution (MPa) during 0-degree humeral abduction; (a) tensile (frontal-medial view); (b) compressive (dorsal view).
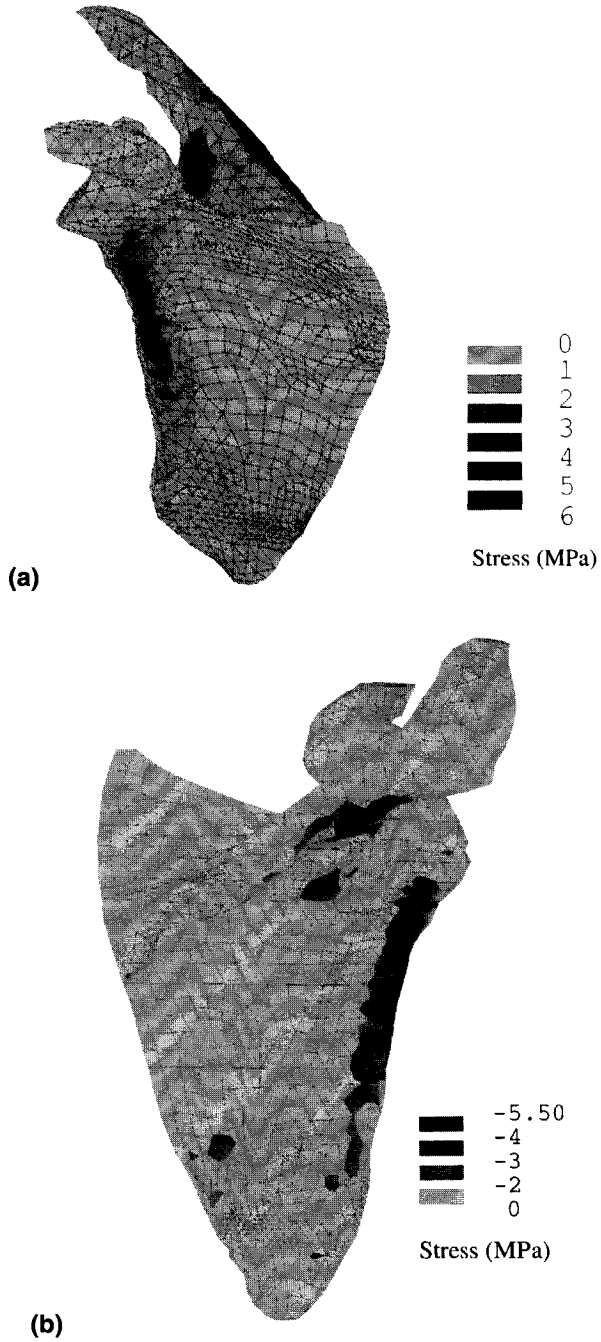
Figure 6. Principal normal stress distribution (MPa) during 30-degree humeral abduction; (a) tensile (frontal-medial view); (b) compressive (dorsal view).

5.3.2 Scapular spine

The scapular spine is one of the few solid bony structures in the scapula. A number of major muscle forces, m. trapezius and m. deltoideus, are acting on the spine (Figs 3 and 4). In the shoulder model there are six lines of forces of the m. trapezius and six lines of forces of the m. deltoideus, acting perpendicular to the spine, but in opposite directions. The scapular spine is originating normally (branching out) from the vertical (scapular) plane of the fossa and partly from the glenoid. Around 90-degree abduction, all parts of the m. trapezius become active to counteract the protracting force of m. serratus anterior. Muscle deltoideus has the largest PSCA of the muscles of the shoulder mechanism, and exerts by far the largest moments around the GH-joint. During abduction, the muscle parts in the medial side (pars medialis) are most active (Fig. 3b). The resulting force due to the action of m. trapezius and m. deltoideus leads to bending of the scapular spine. The bending effect results in high principal tensile (30 to 60 MPa) and compressive (-30 to -55 MPa) stresses in the cranial (upper) part and caudal (lower) part of the spine, respectively (Fig. 8). The action of AC-joint reaction force also adds to the bending effect of the spine.

5.3.3 Glenoid

The GH-joint behaves as a spherical joint with a rotation centre fixed with respect to the scapula and has a large range of motions. During humeral elevation, muscle forces prevent the joint from dislocation by pressing the humeral head inside the glenoid. The position and insertions of the rotator cuff muscles, as a half circle around the humeral head, enables them to point the joint reaction force in almost any direction and acts as the main stabilising muscles of the GH-joint (Van der Helm, 1994[a]).

The stresses in this region largely depend on the position and direction of the GH-joint reaction force. In the rest-position (0-degree humeral elevation), the humerus is merely hanging on the inferior rim of the glenoid cavity requiring small additional muscle force to be pressed against the glenoid cavity (Van der Helm, 1991). At higher elevation angles, the muscle force vectors required to counterbalance the external moment act perpendicular to the glenoid cavity. At lower elevation angles, the intersection point is more cranial than at higher elevation angles and is located at the anterior side of the glenoid cavity (Van der Helm, 1991). The direction and magnitude of the GH-joint reaction force during humeral abduction are listed in Table 1. Evidently, the largest reaction forces are at 90-degree abduction.

During 90-degree abduction, the point of application of GH-joint reaction force is located cranially, and at the anterior side of the glenoid cavity. The bulk of the GH-joint reaction force is carried by the glenoid and to a lesser degree by the lateral border (Fig. 8). Since, the scapular spine is partly attached to the glenoid the bending effect of the spine is partially transmitted to the glenoid. Stresses within the glenoid are largely compressive in nature. As a sandwich structure, higher stresses (20 – 50 MPa) are generated in the compact bone, whereas the relatively low stresses are (0 – 5 MPa) induced in the inner trabecular bone. Frich et al. (1997) presented average results obtained from twelve penetration tests at the three proximal levels of all ten specimens taken from the glenoid. The average strength of the glenoid at the proximal subchondral level was found to be 66.9 MPa. One millimetre underneath the subchondral plate, average strength decreased by 25% and at the 2 mm level strength decreased by 70% (Frich et al. 1997). It appears, therefore, that the stresses generated in the compact and the trabecular bones are within safe limits.
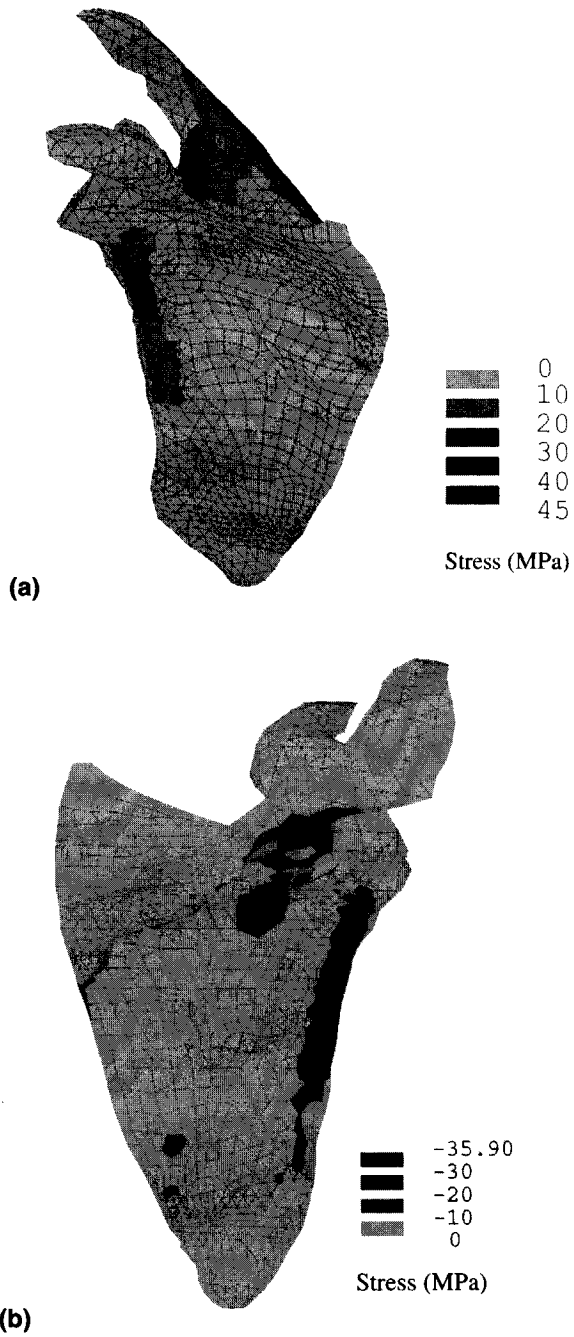
(a)

(b)

Figure 7. Principal normal stress distribution (MPa) during 60-degree humeral abduction; (a) tensile (frontal-medial view); (b) compressive (dorsal view).
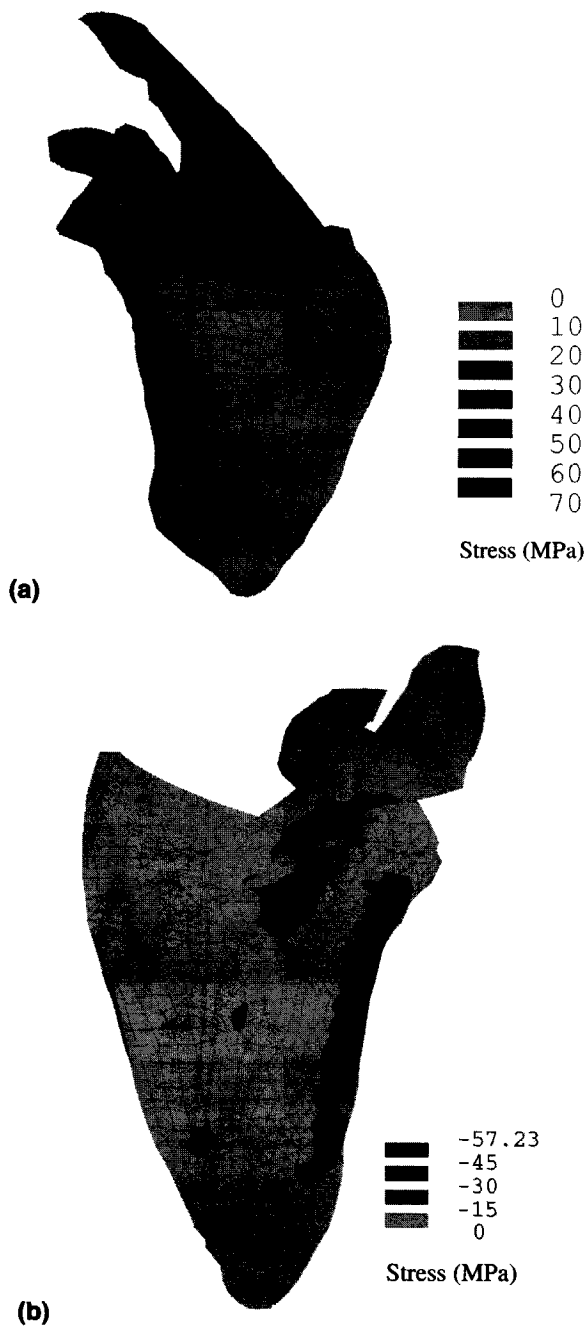
Figure 8. Principal normal stress distribution (MPa) during 90-degree humeral abduction; (a) tensile (frontal-medial view); (b) compressive (dorsal view).

Table 1. GlenoHumeral (GH) joint reaction forces during unloaded humeral elevation. Force components F_x, F_y, F_z corresponds to x, y and z directions, respectively, in the global co-ordinate system as shown in Figures 1 and 2.

Load case	Abduction angle (in degrees)	Force (in Newton)		
		F_x	F_y	F_z
1	0	-6.06	-16.41	8.07
2	30	164.46	14.03	-16.14
3	60	323.74	-36.88	-3.68
4	90	383.71	-77.28	34.62
5	120	314.03	-137.96	45.56
6	150	137.74	-134.43	11.86
7	180	39.78	-72.51	-3.73

5.3.4 Lateral border

The lateral border is loaded by the reaction force at the thorax-AI connection and the m. serratus anterior inserting at AI on one side and GH-joint reaction force on the other. The bending effect of scapular spine is partially transmitted to the lateral border, through the glenoid. The combined effect induces severe bending of the lateral border, producing high tensile stresses (15 – 60 MPa) in the ventral side (Fig. 8a) and high compressive stresses (-15 to -55 MPa) in the dorsal side (Fig. 8b). The action of muscles attached in this region, during humeral abduction is negligibly small. It may be concluded that the transfer of the high GH-joint reaction force and a part of the thorax-AI reaction force take place predominantly along the lateral border.

5.3.5 Connection of glenoid-spine-infraspinous fossa

The solid bony structures like the base of scapular spine, the glenoid and the lateral border are attached to the cranial part of the very thin, hard, laminated shell-like bone structure, the infraspinous fossa. The large bending moment is produced due to the combined action of: (1) the moment arising due to the action of m. trapezius and m. deltoideus, (2) the moment arising due to AC-joint reaction force, and (3) the moment arising due to the GH-joint reaction force. This results in the generation of very high compressive stresses (45 – 58 MPa) at the junction of glenoid, spine and infraspinous fossa, which are the highest compressive stresses in the whole scapula (Fig. 8).

5.3.6 Medial border

In the present situation, the reactive forces of the thorax on the scapula have been applied as concentrated forces, one at the Thorax-AI connection and the other at the Thorax-TS connection. In reality, however, this force is distributed along the medial border. The thorax-AI reaction force, which is acting normal to the scapular plane, has a large moment arm about the local x-axis through the scapular spine.
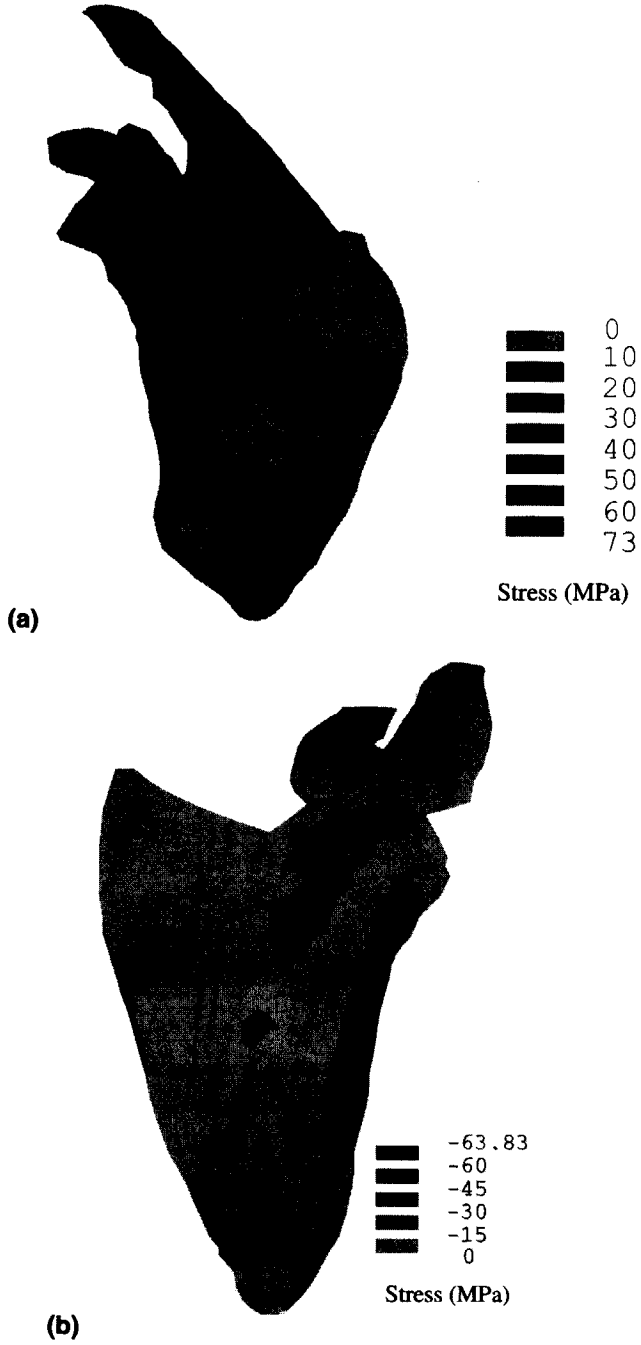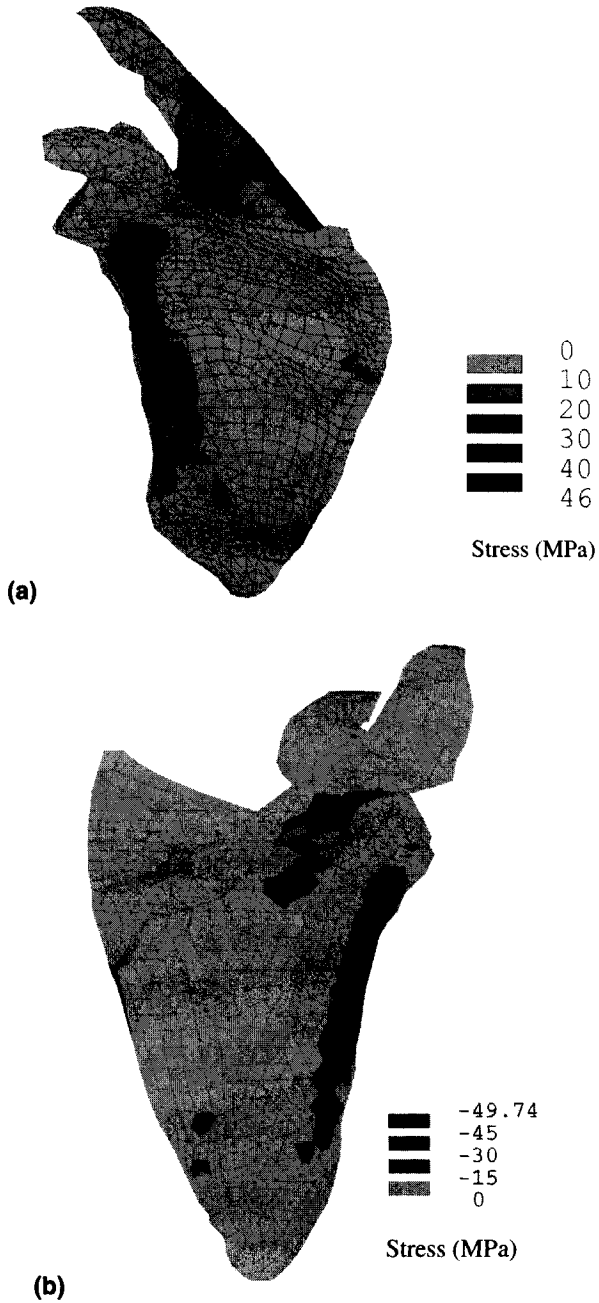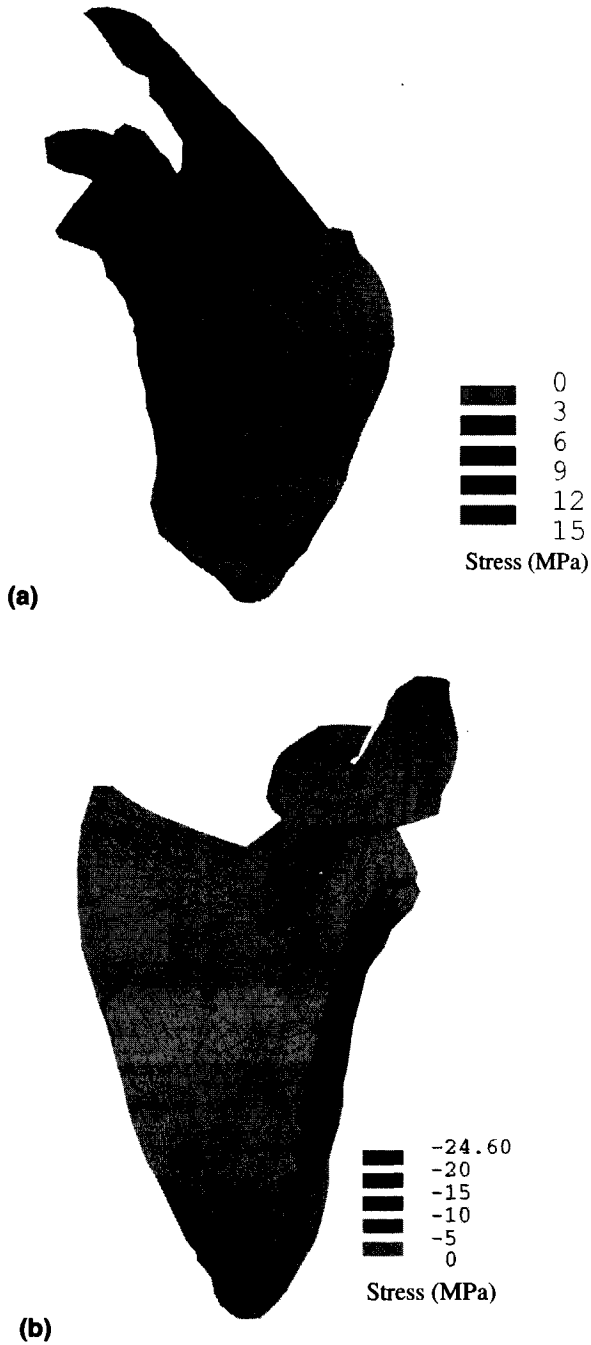
(a)

0
10
20
30
40
50
60
73

Stress (MPa)

−63.83
−60
−45
−30
−15
0

Stress (MPa)

(b)

Figure 9. Principal normal stress distribution (MPa) during 120-degree humeral abduction; (a) tensile (frontal-medial view); (b) compressive (dorsal view).

(a)

0
10
20
30
40
46

Stress (MPa)

(b)

-49.74
-45
-30
-15
0

Stress (MPa)

Figure 10. Principal normal stress distribution (MPa) during 150-degree humeral abduction; (a) tensile (frontal-medial view); (b) compressive (dorsal view).

Figure 11. Principal normal stress distribution (MPa) during 180-degree humeral abduction; (a) tensile (frontal-medial view); (b) compressive (dorsal view).

The effect of the axial moment around this axis, arising due the pulling action of m. deltoideus on the spine also contributes to the bending effect of the medial border about the local x-axis; generating tensile stresses at the ventral side and compressive stresses at the dorsal side. The stresses generated in this region are low (1 – 10 MPa), except a few locations where it varies between 15 – 30 MPa (Figs 7 – 9).

5.3.7 Trigonum Spinae

The Trigonum Spinae (TS) is located at the medial border where the scapula spine is attached to the thin infraspinous and supraspinous fossa. The lower part of m. serratus anterior, inserting at the AI, is able to produce large moments around the TS. The combined effect of two large forces, (1) m. serratus anterior, inserting at the AI, and (2) m. deltoideus, inserting at the lateral end of the scapular spine, produces high bending moments. This results in localised high stresses (45 – 60 MPa) in the TS (Figs 8a and 8b).

5.3.8 Angulus Inferior

The Angulus Inferior is always pressed to the thorax by m. serratus anterior. The reaction force at the thorax-AI connection (Fig. 4) increases with humeral abduction and is most active during 90-degree abduction, and reduces thereafter (Van der Helm, 1994[a]). The combined effect of m. serratus anterior and reaction force at the AI, generate localised stresses (15 – 30 MPa) as shown in Figure 8a. Because of the large moment arm its effect is more predominant in the lateral border than at AI.

5.3.9 Coracoid process

M. Biceps caput breve has a combined origin with m. coracobrachialis and exerts a pulling force in the caudal (tip) part of the coracoid process (Fig. 4). The muscle is active after 60-degree abduction, but it does not generate high stresses in the coracoid process.

5.3.10 Infraspinous and Supraspinous fossa

Large fan shaped muscles (m. infraspinatus, m. supraspinatus, m. subscapularis) are attached to either sides of the very thin, hard and laminated shell-like structures, known as the infraspinous fossa and the supraspinous fossa. These muscles are mostly acting parallel to the fossa. The m. infraspinatus, attached to the dorsal side of infraspinous fossa, has a small moment arm around the sagittal axis till 60-degree abduction. At higher abduction angles, the moment arm becomes negative and the muscle is inactive. The force exerted by m. supraspinatus, attached to the dorsal side of supraspinous fossa, is small. The m. subscapularis, attached to the ventral side of infraspinous and supraspinous fossa, obtains a useful moment arm to counterbalance the external moment during abduction. Its activity is moderate during humeral abduction and exerts a maximum force of 60 N during 90-degree abduction. The combined effect of these three muscles generates a relatively low level of stress (tensile and compressive), varying between 0.05 – 15 MPa in most parts of infraspinous fossa, except a few locations adjacent to the medial border and the connection with spine-glenoid, where it varies between 15 – 24 MPa (Fig. 8). In contrast, the stresses generated in the supraspinous fossa are very low (0.05 – 5 MPa). It appears, therefore, that the fossa area acts more as attachment sites of large muscles. However, low stresses do not imply that the corresponding substructure is irrelevant for the overall stiffness of the scapula.

5.3.11 Ligament coraco-acromiale

Due to the action of AC-joint reaction force and m. biceps caput breve, the interconnected nodes connected to form the ligament (beam) element are displaced away from one another (Fig. 12). This implies increase in the distances, i.e. displacement (U_i) of the nodal co-ordinates, between the connected nodes. The nodes located in the acromion are displaced in the caudal (U_y is negative), the lateral (U_x is negative) and the dorsal (U_z is negative) directions. Whereas the nodes located in the coracoid process are displaced in the cranial (U_y is positive), the medial (U_x is positive) and the ventral (U_z is positive) directions. Moreover, the nodal displacements along x- and y-directions are predominantly higher than that in the z-direction. These results indicate that the ligament is elongated, primarily in x-y plane. This increase in distance signifies separation between the acromion and coracoid process. Since nothing is known about its stress-strain characteristics and its length, it appears that the ligament is stretched, and presumably will be under tension during humeral abduction.

5.4 Discussion

Most finite element studies on scapula deal with glenoid prostheses rather than the mechanics of scapula, as a whole (Orr et al., 1988; Friedman et al., 1992; Lacroix and Prendergast, 1997, Stone et al, 1999). Using an experimentally validated FE model of the scapula, based on CT-scan data, the goal of this study was to understand the mechanics of the load transfer on the scapula due to the action of muscles, ligaments, and joint reaction forces. In order to assess the stresses and strains in the different parts of the scapula, the musculoskeletal shoulder model of forces acting on the scapula (Van der Helm, 1994[a,b]), during humeral abduction, was used as loading conditions. A realistic estimate of the stress distribution has been obtained, since the FE model and the static shoulder model of forces (Van der Helm, 1994[a,b]) were based on the same cadaver.
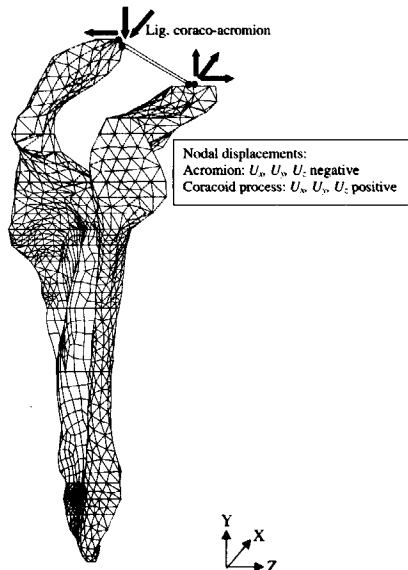
Figure 12. Directions of nodal deflections of the ligament coraco-acromiale in the FE model of the scapula (lateral view).

The morphology of bones is highly dependent on the loading. The natural adaptation and optimisation of the shape of the bone with load is generally referred to as Wolff's law (Wolff, 1892). The scapula being no exception, its complicated shape must be related to the forces acting on it and to the induced stresses within it. The results of the stress analysis indicate that the thick bony ridges are the 'pillars' of the scapula structure. The scapular spine, the lateral border, the glenoid and the acromion, support the bulk of the load. Similar idea was put forward by Anetzberger and Putz (1996). The major forces acting on the scapula include the effect of m. deltoideus, m. trapezius, m. serratus anterior, GH-joint reaction force, AC-joint reaction force, and thorax-AI reaction force and thorax-TS reaction force. These forces generate high stresses (tensile and compressive) in the scapular spine, lateral border, acromion, glenoid and at the connection of fossa-spine-glenoid.

The function of each and every bony structure, which combines to form the complex 3-D structure of the scapula, can not be precisely evaluated from this biomechanical study, since it is based on a single type of movement of the humerus, i.e. unloaded abduction. However, it can be observed from this study that the stresses in the solid bony ridges (scapular spine, lateral border, acromion, and glenoid) are substantially higher as compared to the stresses in the infraspinous and supraspinous fossa. Therefore, it seems that the function of the fossa area is to act as attachment sites of large muscles rather than sharing of load. Although this aspect is evident from this study, the shape of the scapula presumably is a compromise between many requirements. Stress analysis of the scapula using other loading conditions like, unloaded anteflexion, loaded abduction and loaded anteflexion might lead to more precise answers to the questions – why is the scapula structure so complicated and what are the function of its individual parts?

The results of the 3-D FE model of Lacroix et al. (1997) using CT-scan data can be compared with our study. The static shoulder model of forces (Van der Helm, 1994[a,b]) was used as applied loading conditions in their study, but on a different FE model of the scapula. The 3-D FE model appears to be a rather simplified approach, which does not seem to represent the geometry of the scapula accurately. If the geometry of the scapula is considered at the first place, it is virtually impossible to model the entire structure using a total number of 7251 brick elements and 29415 active DOF, unless certain simplifications were made in the structural representation. The quality of mesh generation is considered to be coarse as compared to our model (10921 elements, 14086 nodes and 63435 active DOF). The use of only solid elements for modelling fossa as well as solid bony ridges might be an inappropriate modelling approach. However, the results of our study are well supported by the qualitative results predicted by their study.

A few words must be said about the modelling artefacts. One of them is the high stress concentration in the Trigonum Spinae (TS), located at the medial border where the scapular spine is attached to the thin infraspinous fossa. This is primarily due to a combined effect of two large forces caused by the m. serratus anterior inserting at the AI, and the m. deltoideus inserting at the lateral end of spine. However, the procedure of locating the nearest node number in the FE model, corresponding to a point of application of force, resulted in a small shift of the point of application as compared to the shoulder model (Van der Helm, 1994[a]), thereby introducing an error. These shifts resulted in some residual moments (Table 3, Chapter 4) as compared to the state of moment equilibrium in the shoulder model (Van der Helm, 1994[a]). Consequently, some localised high stresses around the constraints in the Thorax-TS region were generated. The other major reason could be due to the wedge shaped structure of bone in that location, which gradually tapers to an extremely thin bone (Fig. 9). Probably, at this particular area the present model generates rather inadequate results for stresses and strains. This may be also due to the high 3-D stress distribution near this wedge shaped area, which could not be represented correctly by the two layers of shell

elements that merge to a single layer. Another modelling artefact in the medial border may be caused due to the application of concentrated joint reaction forces, one at the Thorax-AI connection and the other at the Thorax-TS connection. But in reality, the reaction forces are distributed along the medial border. In general, the muscle, ligament and joint reaction forces were applied as concentrated loads in the FE model; representation of trapezius muscle action, for example, was by six lines of forces. In reality, however, the forces should be distributed on the surface of those elements that are located in the respective physiological areas of insertion, which are yet to be investigated.

The functional aspect of the coraco-acromiale ligament was unknown, both qualitatively and quantitatively. Since the geometrical and material property data regarding this ligament are unknown, a low value of Young's modulus (100 MPa) and unit geometrical data (cross-section, thickness) were assumed at this level of the study. The lengthening and shortening of the ligament can be calculated without affecting the load distribution in the scapula. A qualitative prediction, that the ligament was under tension during humeral abduction, was obtained from this study.

5.5 Conclusions

Based on an experimentally validated realistic 3-D FE model of the scapula, using CT-scan data and the static shoulder model of forces, the effect of load transfer mechanism in the form of stress distribution can be studied. The following are the specific conclusions of this study:

(1) High stresses, tensile and compressive are observed on cranial and caudal side of scapular spine, respectively indicating bending of the spine. This is largely caused due to the combined action of pulling forces by m. trapezius and m. deltoideus and also due to moment caused by AC-joint reaction forces.

(2) The acromion is subject to bending due to the action of pulling force by m. deltoideus and AC-joint reaction force resulting in tensile and compressive stresses in the ventral-medial part and dorsal-lateral part.

(3) The most important force of the scapula, the GH-joint reaction force, and a part of the thorax-AI joint reaction force are predominantly transferred along the lateral border resulting in severe bending of the lateral border. High tensile and compressive stresses are observed in the ventral and dorsal side of the lateral border, respectively.

(4) The glenoid is largely subject to high compressive stresses due to the GH-joint reaction force. As a sandwich structure, high stresses are generated in the compact bone whereas relatively low stresses are induced in the inner trabecular bone. However, these stresses are below the strength of glenoid compact and trabecular bone.

(5) High compressive stresses are generated at the connection of glenoid-scapular spine-infraspinous fossa.

(6) The TS and the medial border are subject to bending due to action of m. serratus anterior, inserting at AI and the reaction force at thorax-AI acting normal to the scapular plane.

(7) Stresses in the infraspinous fossa and supraspinous fossa are low, which indicate that the function of these structures is to act as attachment sites of large muscles.

(8) The solid bony structures of the scapula are subject to relatively high stresses as compared to low stresses in the thin, hard, laminated fossa areas.

References

Anetzberger, H. and Putz, R. (1996). The scapula: principles of construction and stress. Acta. Anat 156, 70-80.

Dalstra, M. (1993). Biomechanical aspects of the pelvic bone and design criteria for acetabular prosthesis. Doctoral Thesis, University of Nijmegen, The Netherlands.

Dalstra, M., Huiskes, R. and van Erning, L. (1995). Development and validation of a three-dimensional finite element model of the pelvic bone. J. Biomech Eng. 117, 272-278.

Frich, L.H., Jensen, N.C., Odgaard, A., Pedersen, C.M., Søjbjerg, J.O. and Dalstra, M, (1997). Bone strength and material properties of the glenoid. J. Shoulder Elbow Surg.; 6: 97-104.

Friedman, J.R., LaBerge, M., Dooley, R.L. and O'Hara, A.L. (1992). Finite element modelling of the glenoid component: Effect of design parameters on stress distribution. J. Shoulder Elbow Surg. 1, 261-270.

Lacroix, D. and Prendergast, P.J. (1997). Stress analysis of glenoid component designs for shoulder arthroplasty. Proc. Inst. Mech. Engrs, Part H 211, 467-474.

Lacroix, D., Prendergast, P.J., Murray, R., McAlinden, S. and D'Arcy, E. (1997). The use of Quantitative Computed Tomography to generate a finite element model of the scapula. Proc. of the 14th Conf. Irish Manufacturing Committee. Ed J. Monaghan & C.G. Lyons, 257-262.

Orr, T.E., Carter, D.R. and Schurman D.J. (1988). Stress analyses of glenoid component designs, Clin Orthop. Rel. Res. 232, 217-224.

Stone, K.D., Grabowski, J.J., Cofield, R.H., Morrey, B.F. and An, K.N. (1999). Stress analysis of glenoid components in total shoulder arthroplasty. J. Shoulder Elbow Surg. 8(2), 151-158.

Van der Helm, F.C.T. and Veenbaas, R. (1991). Modelling the mechanical effect of muscles with large attachment sites: application to the shoulder mechanism. J. Biomechanics 24(12), 1151-63.

Van der Helm, F.C.T. (1991). The Shoulder Mechanism, a dynamic approach. Doctoral thesis, Delft University of Technology, The Netherlands.

Van der Helm, F.C.T. (1994[a]). Analysis of the kinematic and dynamic behaviour of the shoulder mechanism. J. Biomechanics 27, 527-550.

Van der Helm, F.C.T. (1994[b]). A finite element musculoskeletal model of the shoulder mechanism. J. Biomechanics 27, 551-569.

Wolff, J. (1892). *Das Gesetz der Transformation der Knochen.* Berlin, Hirchwild. Translated as *The Law of Bone Remodelling*, Springer-Verlag, Berlin, 1986.

Chapter 6

Stress Analysis of Cemented Glenoid Prostheses
in Total Shoulder Arthroplasty

Abstract

Glenoid component loosening is the most-frequently-encountered problem in the total shoulder arthroplasty. In order to investigate probable failure mechanisms and to analyse glenoid load transfer, a detailed three-dimensional (3-D) Finite Element (FE) model of the glenoid prosthesis was developed. Large size FE models were generated using a submodelling approach, which were based on an overall reference solution of a normal scapula model acted upon by all the muscles, ligaments and joint reaction forces. The FE submodels, one total polyethylene and the other, metal backed polyethylene, were developed using Computed Tomography (CT) data. The prosthesis and the cement layer were modelled as being rigidly connected to the underlying bone. Based on the FE stress analysis of two basic glenoid prosthesis models, the following observations were made. (1) The submodelling technique, which required a large size submodel and the use of prescribed displacements at cut-boundaries located far away from the glenoid, is very important for evaluations on glenoid component. (2) High stresses are absorbed by the glenoid component, resulting in lower stresses in the cortical and cancellous bone, as compared to that of the natural glenoid. (3) A total polyethylene design appears to provide an overall stress distribution that was closer to the natural glenoid as compared to a metal-backed design. (4) Total polyethylene design results in lower principal tensile stresses (1 – 10 MPa) in the cement, but generates higher stresses within the prosthesis as compared to a metal-backed design. (5) The metal-backed designs generate high stresses (10 – 15 MPa) in the metallic flange and add rigidity to the implant. Consequently, the tensile stresses in the underlying cement are reduced, except a few locations along the periphery where it varies between 5 – 11.5 MPa. A peak Von Mises a stress of 9.80 MPa is generated in the cement for the metal-backed design, as compared to 8.31 MPa for the total-polyethylene design. (6) The cement-bone interface is subject to higher stresses (normal: 2.51 MPa, shear: 3.41 MPa) for total polyethylene design, as compared to the polyethylene-cement interface (normal: 2.58 MPa, shear: 1.33 MPa). (7) The implant-cement interface stresses (normal: 5.92 MPa, shear: 1.22 MPa) are higher for the metal-backed design as compared to a total polyethylene design. (8) High stresses generated at the implant-cement and the cement-bone (normal: 2.86 MPa, shear: 3.55 MPa) interfaces for the metal-backed designs, or at the cement-bone interface for the total polyethylene designs, during 90-degree humeral abduction, is of high significance as far as debonding of prosthesis from cement or bone is concerned. (9) Results indicate that for total polyethylene design, the cement-bone interface adjacent to the tip of the keel seems very likely to fail (interface debonding) as compared to the superior edge of the prosthesis, since lower bond strength is offered lower density bone around the keel. (10) Whereas, in case of metal-backed design, this interface adjacent to the tip of the keel appears even more likely to fail. From biomechanical point of view the total polyethylene design, therefore, seems to be a better option. However, the fixation strength of polyethylene with cement is poor, which increases the risk of a mobile prosthesis. In contrast, the metal-backing adds rigidity to the implant, causes reduction of stresses in the polyethylene cup and in the cement, but generates higher metal-cement and cement-bone interface stresses. Preservation of a part of the subchondral bone in the superior-inferior direction might lead to an increase in the stiffness of the implanted glenoid and the lesser use of cement. In view of these contradictory design considerations, revisions in the design of the metal-backing (keel) is necessary to reduce stresses in the cement, and at the respective material interfaces before improved results in glenoid arthroplasty may be attained.

Keywords: Glenoid prosthesis, scapula, finite element analysis, submodelling, computed tomography.

6.1 Introduction

Total Shoulder Arthroplasty (TSA) is performed in the case of severe pain due to osteoarthritis, rheumatoid arthritis and fractures or dislocations with traumatic arthritis. Aseptic glenoid loosening is the most-frequently-encountered complication, threatening the TSA. Loosening is defined as the progression of radiolucent lines exceeding 1.5 mm in width or any definite change in the position of the component (Stewart and Kelly, 1997; Torchia et al., 1997; Wallace et al., 1999). Loosening may occur shortly (1 to 3 years) after surgery, though a few in numbers, probably due to peak stresses occurring within a prosthesis-cement-bone configuration (Neer et al, 1982; Cofield, 1984). Medium (3 to 10 years) to long-term (10 years or more) follow-up observations show radiographic changes that indicate loosening (Thomas et al., 1991; McCullagh, 1995; Sneppen et al., 1996; Torchia et al., 1997; Sperling et al., 1998; Skirving, 1999; Wallace et al., 1999). This may be attributed to bone remodelling caused by TSA induced changes in the stress distributions.

Clinical and radiographic investigations, mostly with the Neer I (total polyethylene glenoid), and the Neer II (metal-backed polyethylene glenoid) prostheses revealed potential complications with possible revisions and recommendations (Table 1). Wallace et al. (1999) observed radiolucent lines in thirteen (41%) of the thirty-two arthroplasties performed with cement. Sperling et al. (1998) reported long term results of Neer I TSA performed between 1976 and 1985 in thirty-six patients who were fifty years or less. Four TSA were followed by an excellent result; thirteen, a satisfactory result; and seventeen, an unsatisfactory or unsuccessful result. Radiolucent lines were observed in nineteen (59%) of the thirty-two shoulders. A shift in the position of glenoid component was seen in seven (22%) cases and revision surgery was required for two additional cases (Sperling et al., 1998). Patients who needed revision surgery were considered to be unsatisfactory results. The data from their study indicate that a shoulder arthroplasty provides marked long-term relief of pain and improvement in motion. Similar investigations (Torchia et al., 1997) were performed on seventy-nine patients with 89 replacements with an average follow-up period (FUP) of 12.2 years (range, 5 to 17 years). Seventy-five glenoid components developed bone-cement radiolucencies, and thirty-nine (44%) glenoid components had radiographic evidence of definite loosening. Glenoid loosening was associated with pain. A prospective study by Stewart and Kelly (1997) of thirty-seven Neer II total shoulder replacements, with a mean FUP of 9.5 years (7 to 13) observed radiographs showing loosening in nine out of ten glenoid components. But of these only three had significant symptoms of loosening and required revisions. Sneppen et al. (1996) reported results on 62 Neer II TSA performed on patients with rheumatoid arthritis with a mean FUP of 7.6 years (range 4.3 to 11.6 years). The results revealed proximal migration in thirty-four (55%) of the patients, and twenty-five (40%) showed progressive radiographic loosening of the glenoid component. Apart from short-term complications postoperatively, the risk of loosening is mostly a relatively late complication that is eventually followed by pronounced bone destruction related to the loose component. Short- to mid-term information (less than 10 years), by McCullagh (1995) indicated good to excellent clinical results in approximately 90% of the cases. Berms (1993) summarised experiences that several skilled surgeons have had with lucent lines. He reported that the overall failure percentage of TSA with radiolucent lines was 38.6. Boyd et al. (1990) observed that TSA produced encouraging results in terms of functional improvements (pain relief, range of motion, and patient satisfaction) in 131 patients for an average FUP of 3.8 years (range, 2 – 10.3 years). Progressive glenoid loosening was reported in 12% of total shoulder arthroplasties but no correlation with pain relief or range of motion was noted. There was evidence of high incidence of radiographic lucent lines in 74% of the fifty TSA, as reported by Barrett et al. (1987). About 36% were noted around the keel, which were more significant than those that occur under the flange.

Table 1.   Investigations with cemented glenoid prosthesis (without revision surgery).
PE - PolyEthylene; MB – Metal-Backed polyethylene; N.R. – data Not Recorded.

Author, year	Design	Follow-up period (years)	No. of shoulders	Percentage of defective glenoid component	
				Radio-lucency	*Loosen-ing*
Amstutz et al., 1981	DANA	2 – 10	56	94	4
Neer et al., 1982	Neer I (PE, MB)	2 – 8.25	194	30	0
Cofield, 1984	Neer I	2 – 6.5	73	82	21
Barrett et al., 1987	Neer I	2 – 7.5	50	74	18
Barrett et al., 1989	Neer I (PE) & Neer II (MB)	2 – 11	129	82	10
Hawkins et al., 1989	Neer I	2 – 8.6	70	Nearly all	7
Boyd et al., 1990	Neer I	2 – 10.3	131	N.R.	12
Sneppen et al., 1996	Neer II	4.3 – 11.6	62	21	40
Torchia et al., 1997	Neer I	5 – 17	89	84	82
Stewart and Kelly, 1997	Neer II	7 – 13	37	62	24
Sperling et al., 1998	Neer I	5 – 20	32	59	28
Wallace et al., 1999	Neer II (PE and MB), Cofield (PE), Global (PE)	3.8 – 7.5	32	41	25

Results of clinical and radiographic study suggest that over time bone-cement lucent line about the glenoid component slowly progress to definite loosening, indicated in most cases by shifting of the component (Torchia et al., 1997). A statistically significant relation between radiographic loosening and pain (P value = 0.0001) was obtained by Torchia et al. (1997). The cause of some cement-bone radiolucencies, in particular those seen in early post-operative radiographs, was attributed to poor cementing technique (Neer et al., 1982; Wilde et al., 1984; Barrett et al., 1987; Kelly et al., 1987). The appearance of radiolucent lines around the prosthesis keel increased over time. These findings imply that the reasons for bone-cement radiolucencies and associated glenoid component loosening are multi-factorial. Design of the implant, surgical technique, limitations in quantity and quality of bone available for fixation, tissue reaction to particulate debris, rotator cuff deficiency with glenohumeral instability, and high patient activity levels were proposed as potential causes of glenoid loosening (Boyd et al., 1990; Wilde et al., 1984; Barrett et al., 1987; Kelly et al., 1987).

TSA is a technically difficult procedure, with higher requirements and perhaps a greater potential for errors and complications as compared to other commonly performed arthroplasties, like the hip and the knee. From an anatomic point of view, the small volume of bone available for fixation of the implant in the glenoid is a limiting factor in TSA (Cofield, 1984). Computed Tomography (CT) scans of sections through the glenoid cavity of a normal healthy person reveal that the cancellous bone has a higher density anteriorly and posteriorly than centrally (Müller-Gerbl et al., 1992; Anglin et al., 1996[a]). Fukuda et al. (1988) in a biomechanical analysis of stability and fixation strength remarked that the fixation strength of the glenoid component was lowest for the Neer I (total polyethylene design). In general, all metal-backed glenoid components appeared to have sufficient fixation strength against normal shoulder joint forces. The strength of porous spongy bone is low, which adds to the complication of fixation of the prosthesis in the glenoid. Hence, it becomes a real challenge to design a glenoid prosthesis that can withstand repetitive stresses as well as maintain secure fixation during normal movements.

Since the introduction of the Neer prosthesis in the 1970s several designs, closely resembling the Neer prosthesis, were developed (Amstutz et al., 1981; Cofield, 1984; Amstutz et al., 1988). The glenoid prosthesis consists of an Ultra High Molecular Weight PolyEthylene (UHMWPE) cup with a keel to anchor inside the scapula (Fig. 1). The designs of these components differ mainly in the radius of curvature of the cup and the shape of the keel. An increased radius of curvature of the glenoid as compared to their corresponding humeral head would allow translation during movement, but at the same time might increase the contact stresses due to point loading. Metal backing of these polyethylene components and the use of bone-ingrowth surfaces are also available. The Biomodular (Biomet Inc., Warsaw, Indiana) glenoid component design, which is frequently used in TSA, was chosen for this study. The glenoid component is available in a polyethylene version, with or without metal backing (Fig. 1). It consists of a centrally located tapered keel, which is symmetric with respect to the frontal plane. The humeral component coated with porous bone-ingrowth material can be press fitted. Fixation of the glenoid component within bone is achieved by the use of cement (polymethylmethacrylate: PMMA) layer of approximate thickness of 2 to 2.5 mm.

Stress analysis is required for implant evaluations. It helps in design, failure prediction and improvement of a prosthesis. Mechanical failure depends on the stresses generated in a material with regard to its strength. The interfaces of different materials are often the weakest link in the prosthesis-cement-bone configuration. Interface debonding might lead to gross loosening. The generation of polyethylene wear particle may be accelerated in a few individuals, although it is uncommon as compared to the lower limb prostheses. Studies on stress analysis of glenoid components are few and were mostly restricted to two-dimensional (2-D) FE models (Rohlmann et al., 1984, Orr et al., 1988, Friedman et al., 1992; Lacroix and Prendergast, 1997; Stone et al, 1999). A three-dimensional (3-D) FE study was restricted to the glenoid area only, with constraints applied at four nodes not far from the glenoid region to avoid rigid body motions (Lacroix et al., 2000). Results of these analyses suggest certain qualitative trends in stress distribution of the bone-prosthesis configuration. But, the 2-D simplification of the 3-D glenoid structure can lead to a loss of the structure's mechanical integrity (Stone et al., 1999). This loss of integrity of the circumferential structure, for 2-D or truncated 3-D models, along with the out-of-plane forces will induce large modelling errors and consequently have a crucial impact on the results. Therefore, in order to understand the mechanical factors responsible for the probable failure mechanisms, a realistic 3-D FE model of the glenoid prosthesis is required (Stone et al., 1999). Following the studies on the hip prostheses (Weinans et al., 1991) and the acetabular prostheses (Dalstra et al., 1995), a 3-D FE model of the glenoid prosthesis was developed using CT-scans and realistic loading conditions.

Table 2. Mechanical properties of implant materials and cement.

Material	Elastic Modulus (MPa)	Poisson's ratio
Ultra High Molecular Weight Polyethylene (UHMWPE)	1174	0.40
Cobalt-chromium-molybdenum alloy	234500	0.30
Cement (PMMA)	2200	0.34

The purpose of this study is to analyse two basic designs of cemented glenoid prosthesis, one total polyethylene and the other metal-backed polyethylene, in order to investigate some mechanical factors related to the common failure mechanisms of an implant. A comparative analysis of these two basic models can reveal the biomechanical factors regarding choice of a particular prosthesis and might lead to design considerations for improved glenoid prosthesis.

6.2 Materials and Methods

6.2.1 Finite element model of a cemented glenoid prosthesis

A 3-D FE model of a glenoid (right scapula) was developed using CT-scan data. The outer geometry of the bone was reconstructed by connecting cubic B-splines through keypoints that were generated from CT-slices. The glenoid component was generated using ANSYS FE software and was placed within the glenoid bone. For metal-backed design, a thin metal tray of 1 mm thickness, used in practice, was applied. The keel and the tray are made of cobalt-chromium- molybdenum alloy. Following the surgical technique, a cement layer of 2 – 2.5 mm thickness, underlying the glenoid component was included and the prosthesis was modelled as completely embedded in the cement layer. A perfect bond was assumed at all the interfaces of the materials, constituting the configuration.

A combination of shell and solid elements was used to build a realistic bone model. The inner volume of the cancellous bone and the prosthesis was filled with 3-D ten-node tetrahedral solid elements. The element edge lengths, varying between 1 – 3 mm, were specified and mesh generation was obtained utilising ANSYS FE software. The hard cortical outer shell was modelled as eight-node quadrilateral two-layered shell elements, with 0.5 mm thickness of each layer (Chapter 3). A FE representation of the glenoid component and prosthesis-cement construction is shown in Figures 2a and 2b, respectively. A FE model of the glenoid with prosthesis is shown in Figure 3b. The FE model of the total polyethylene glenoid prosthesis contained 11660 elements, 15532 nodes and a total number of 56871 active DOF. Whereas, for metal-backed design additional shell elements were used to represent the thin metallic tray. The FE model contained 12053 elements, 15532 nodes and a total number of 59175 active DOF.

Bone was assumed to be a linear isotropic material. The material properties of bone elements were extracted from CT-scan image of a dry scapula (Chapters 2 and 3). The mechanical properties of the glenoid component are listed in Table 2.
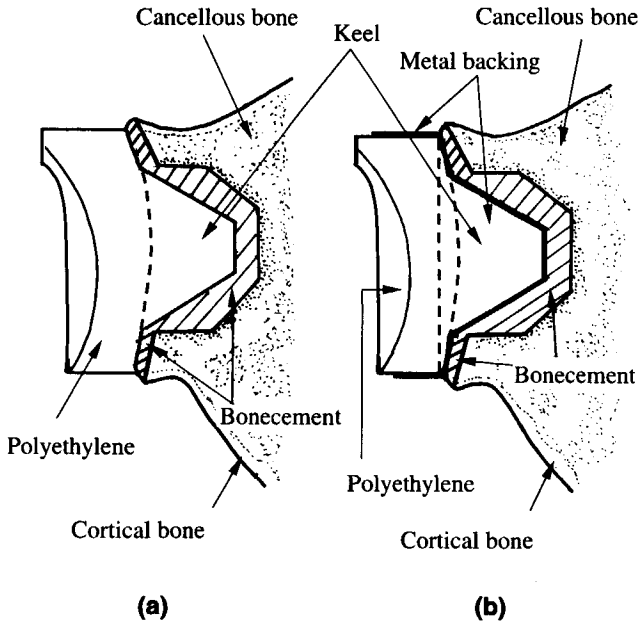
Figure 1. Glenoid component designs in total shoulder replacement. (a) Total polyethylene component; (b) Metal-backed polyethylene component.
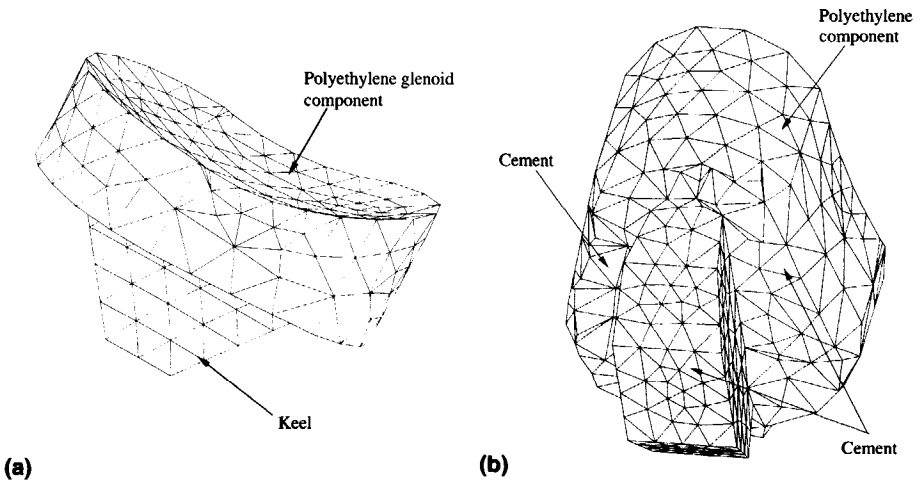

Figure 2. Finite element (FE) model of the glenoid prosthesis. (a) FE model of glenoid component; (b) FE model of prosthesis-cement configuration.

6.2.2 Submodelling technique and applied loading conditions

The overall model of the natural scapula, which served as the reference solution included the effect of all muscles, ligaments and joint reaction forces during humeral abduction (Chapter 5). The elastic behaviour of the overall model can be effectively imposed on a submodel with the prosthesis. The objective of using a submodel of glenoid prosthesis, with a fine mesh in the domain of inclusion of the prosthesis, was to focus our investigation in the domain of inclusion of the prosthesis with regard to the failure mechanisms. The effect of the forces acting on bony structures connected to the glenoid on the stresses generated in the glenoid with the prosthesis cannot be neglected. In order to fulfil these two major considerations, a link between the submodel and the overall model was called for. Therefore, the elastic behaviour of the overall model of the natural scapula, as a whole, needed to be included in the analysis. Any other form of approximate boundary conditions, applying constraints at locations far away from the region of interest to restrain rigid body motion, was considered to be inappropriate and would lead to doubtful results. A complete FE model of the scapula with glenoid prosthesis can be an alternative option. The numerical requirements for the generation and solving of a refined global FE model, however, are much larger. Comparing the submodel with the glenoid prosthesis and the overall model, the major areas of differences were:

(a) Change in the geometry and material properties in the domain of inclusion of the prosthesis, leading to change in the stiffness of the glenoid and consequently stresses and strain generated within the bone-prosthesis configuration.

(b) Change in the load application point. The perturbation due to change of load application point at locations far away from the prosthesis is small as compared to the overall scapula model (Fig. 3).
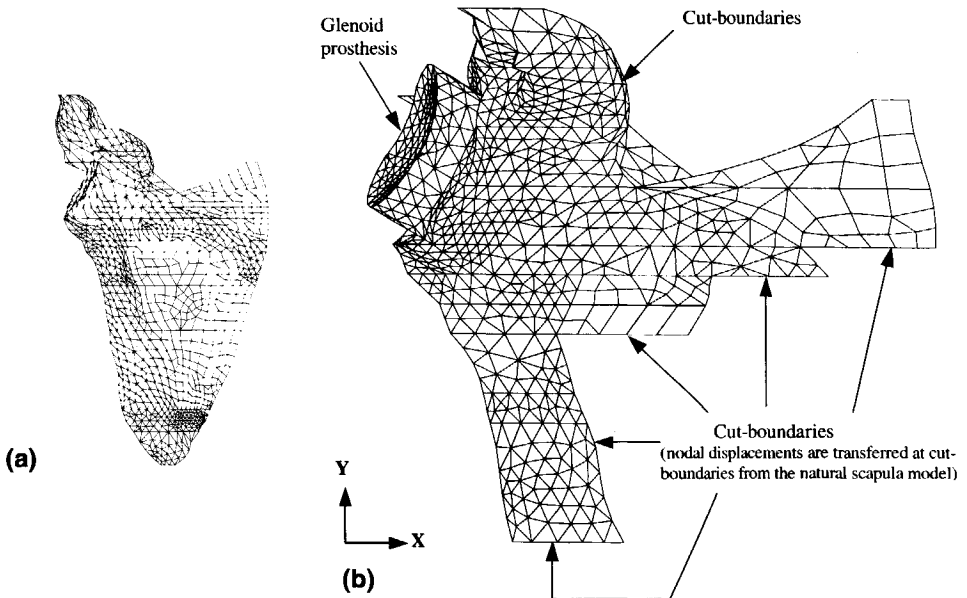
Figure 3. Proposed submodel: (a) natural scapula model, and (b) submodel with the prosthesis.

A link between the submodel with a prosthesis and the overall model can be established by transferring the displacements (at nodes) from the overall model at the cut-boundary to the submodel (Fig. 3). The location of the cut-boundary should be sufficiently far away from the region of interest, i.e. the glenoid, so that the effect on the stress distribution due to the inclusion of prosthesis was assumed to be damped out. If the inclusion is small as compared to the dimensions of the entire body, then it can be assumed that, sufficiently far from the inclusion, the differences between the two solutions (displacements) become zero. However, it may be recalled that due to a change in the load application point the effect might not damp out. The cut-boundaries were chosen at locations far away from the prosthesis, so that the deviations in stress distribution at the cut-boundary between the overall and the sub-model, due localised change in the point of application of load were minimal.

The location of the cut-boundary is of crucial importance and will have predominant influence on the results. The dimension of the cut-boundary (or interface) was not assumed to be small as compared to the overall dimension of the scapula and should be located far away from the prosthesis, as shown in the FE model (Fig. 3). This procedure called for a large size of the submodel. The validity of the submodelling technique was checked by comparing the stress distribution at the cut-boundaries of the submodel with those of the overall reference solution. The overall stress distribution of both the implanted models was found to be comparable to that of the natural scapula model. However, deviations in stress distributions were observed in the domain of inclusion of the prosthesis (Chapter 5).

The non-zero values of displacements at the nodes located along a cut-boundary, for each load step, were obtained from the results of the overall model (Chapter 5). These displacements were prescribed on the nodes located along the bottom (lateral border), the right (infraspinous and supraspinous fossa) and the posterior (scapular spine) cut-boundaries in the submodel with the prosthesis (Fig. 3b). In order to determine the DOF values at a cut-boundary node, the ANSYS program first projected a node of the submodel onto the nearest element in the overall model. The DOF values of this projected point were then interpolated using element shape function. These DOF values were assigned to the corresponding node. In order to reduce complications involving interpolation of DOF values, an exactly similar mesh as compared to the overall model, was generated for the submodel at the cut-boundaries. This method was useful for obtaining the rotational DOF values of shell elements. The solid elements were selected to obtain translational DOF values of cut-boundary nodes. Whereas the shell elements were selected to obtain translational and rotational DOF values of cut-boundary nodes, belonging to the shell elements. The translational DOF values of nodes, located along the shell-solid cut-boundary, were found to be equal for both the cases of element selection. This technique would lead to results in the domain of the inclusion. An alternative method, specifying equivalent nodal loads (equivalent load method) at the cut-boundary can be adapted using the submodelling approach. The displacement method, however, as compared to the equivalent load method was easier to implement in the ANSYS FE software.

A static musculoskeletal model of the shoulder was used to calculate the loading conditions of the scapula (Van der Helm, 1994[a,b]). The dominant force acting on the glenoid is the GlenoHumeral (GH) joint reaction force. The point of application as well as magnitude and direction of this reaction force varies with the change in abduction angle of the arm. Berms (1993) observed that the resultant GH-joint reaction force (F) moves from inferior to superior and then to the centre of the glenoid cavity, which has been termed as the "rocking horse" effect and may be responsible for the high rate of glenoid lucent lines in the TSA. Typical values of the force, corresponding to angular abduction of the arm, are presented in Table 3.

Table 3. Glenohumeral (GH) joint reaction forces corresponding to humeral abduction angles (Van der Helm, 1994[a]). Force directions, Fx, Fy, Fz corresponds to x, y and z directions (Fig. 3b).

Load case	Abduction angle (in degree)	Force (in Newton)			
		Fx	Fy	Fz	F (resultant)
2	30	164.46	14.03	-16.14	165.84
3	60	323.74	-36.88	-3.68	325.85
4	90	383.71	-77.28	34.62	392.95
5	120	314.03	-137.96	45.56	346.01
6	150	137.74	-134.43	11.86	192.83
7	180	39.78	-72.51	-3.73	82.79

The GH-joint reaction force was distributed on the articulating surface of the glenoid component. The contact area was estimated according to the Hertz theory of elastic contact for non-conforming surfaces in contact (Hertz, 1882). Based on this theory, expressions were derived, which are useful in practical problems to calculate the radius (a) of the contact circle. The GH reaction force was distributed on the face of those elements, which were geometrically equal to the contact area. The following calculation was based on the total load, the principal radii of curvature (R_i) of the surfaces in contact and the elastic constants (modulus of elasticity, E and Poisson's ratio, μ) of two bodies in contact. The radius (a) of the contact area (A) can be calculated using the relative radius of curvature (R) and the relative modulus of elasticity (E^*). The relative radius of curvature was related to the principal radii of curvature (R_1 and R_2) of bodies in contact and is given by,

$$\frac{1}{R} = \frac{1}{R_1} - \frac{1}{R_2} \tag{6.1}$$

where R_1 = the principal radius of curvature of the humeral component = 20 mm
         R_2 = the principal radius of curvature of the glenoid component = 30 mm

Since the distributed load acting on the second body was equal to that on the first, the relative modulus of elasticity (E^*) may be written as,

$$\frac{1}{E^*} = \frac{1-\mu_1^2}{E_1} + \frac{1-\mu_2^2}{E_2} \tag{6.2}$$

where E^* = the relative modulus of elasticity
         E_1 = Young's modulus of the humeral component (Co-Cr-Mo alloy)
         μ_1 = Poisson's ratio of the humeral component
         E_2 = Young's modulus of the glenoid component (UHMWPE)
         μ_2 = Poisson's ratio of the glenoid component.

Substituting the values in the Eqs (6.1) and (6.2) we obtain, R = 60 mm and E^* = 1390 MPa. In practical problems, it is convenient to use the Eqs (6.1) and (6.2) in combination with the total load (*F*) to calculate the radius (*a*) of the contact circle,

$$a = \left(\frac{3FR}{4E^*} \right)^{1/3} \tag{6.3}$$

The area (*A*) of the contact circle is given by, $\qquad A = \pi a^2$ $\qquad$ (6.4)

The distributed load as proposed by Hertz, exerted between two frictionless elastic solids of revolution in contact, is given by

$$p(r) = p_o \left\{ 1 - (r/a)^2 \right\}^{1/2} \tag{6.5}$$

where *r* is the radial distance.

The total load (*F*), compressing the solids is related to the pressure by

$$F = \int_0^a p(r) 2\pi r \, \mathrm{d}r = \frac{2}{3} p_o \pi a^2 \tag{6.6}$$

Hence, the maximum pressure p_o is 3/2 times the mean pressure p_m.

In practical problems, it is convenient to determine the total load (F) in combination with the Eqs (6.6) and (6.4):

$$p_o = \frac{3F}{2\pi a^2} = \frac{3}{2} p_m = \left(\frac{6FE^{*2}}{\pi^3 R^2} \right)^{1/3} \tag{6.7}$$

Considering the dimensions of the bodies laterally (*a*, *R*) and in depth (*l*), it may be recalled that the calculations of the dimensions of the contact surface must be so related that it was consistent with the assumptions of the Hertz theory, which may be summarised as follows:
(i)   The surfaces are continuous and non-conforming: $a << R$; (R is calculated as 60 mm)
(ii)   The strains are small.
(iii)   Each solid can be considered as an elastic half-space: $a << R_{1,2}$; $a << l$;
(iv)   There is no friction at the contact surfaces.

The load can be distributed on the contact area as, (i) uniform pressure, or (ii) Hertz pressure. According to the Hertz theory, the pressure distribution should be parabolic. This implies that the pressure is maximum (p_o) at the centre of the contact circle and minimum (equal to zero) at the periphery (radial distance = *a*), according to the Eq. (6.7). The present FE mesh, with element edge length varying between 2 – 3 mm, was unsuitable for implementation of a parabolic distribution. Implementation of a parabolic distribution for better estimation of contact stresses calls for far too finer mesh size, which will further increase the existing large size submodel. The solution of such a large size FE model, however, was hindered by software and hardware limitations. Moreover, the GH joint is a "non-weight-bearing" joint as compared the lower limbs (Mansat et al., 1998).

Table 4. Dimensions of contact area and load distribution corresponding to load cases.
(* During 0-degree abduction the humeral component merely hangs from the tip of the glenoid component (inferior side). The reaction force and the contact dimensions are small as compared to the other load cases. Therefore, the GH force is applied as a concentrated force for this load case.)

Load case	Abduction angle (in degree)	Total force (F) in N	Radius of contact circle (a) in mm. Eq. (6.3)	Area of contact circle (A) in mm^2 Eq. (6.4)	Mean pressure (p_m) in N/ mm^2
2	30	165.84	1.751	9.632	17.218
3	60	325.85	2.193	15.108	21.567
4	90	392.95	2.334	17.114	22.960
5	120	346.01	2.237	15.721	22.0091
6	150	192.83	1.841	10.647	18.111
7	180	82.79	1.389	6.061	13.658

A joint reaction force less than the body weight is generated during 90-degree abduction of the arm (Table 4). Whereas, joint reaction force of about two to four times the body weight are generated at the hip or the knee during walking (Frankel and Nordin, 1980). The effect of contact stresses was therefore, less relevant in glenoid components. In order to apply approximate loading conditions, the distributed loads were normally taken into account using work equivalent loads so that the parabolic distribution was represented by a uniformly distributed pressure (p_m). According to the calculations presented in Table 4, the GH reaction force for each load case was totally distributed on the face of those elements that are geometrically equal to the contact area. Based on this simplified uniform load distribution on a coarse mesh, an average value of stresses in the polyethylene cup can be obtained. Higher stresses would be generated at the subsurface if a parabolic distribution with maximum pressure ($p_o = 1.5\ p_m$) is applied on the glenoid component.

6.3 Results

6.3.1 Interpretation of the results with relevance to failure scenarios

The failure scenarios for total hip arthroplasty, introduced by Huiskes (1993), are useful to analyse failure mechanisms of other reconstructed joints like the TSA. These reconstructions (implants) may fail at various locations within the structure. The likelihood of mechanical failure depends on the stresses induced in a material versus the strength of that material. The repetitive nature of the external loads generates high stresses in the materials and at the interfaces. As a result, mechanical damage, in the form of micro-cracks, is gradually accumulated in the cement and at its interface. These micro-cracks reduce the strength of the cement and its bonds with an implant and bone, eventually causing failure. Lee et al. (1977) reported tensile strength of surgical simplex bone cement by testing cylindrical specimens in diametrical compression. They reported mean failure

strength of 25 MPa. Saha and Pal (1984) indicated that, usually hand mixed cement fails under tensile stress of 25 MPa.

The interfaces between different materials are often the weakest links within the bone-prosthesis configuration, leading to debonding (interface disruption). The interface stresses were calculated at an interface node using the normal and shear stress components. The normal stress (σ_n) and the shear stress (τ) were calculated using these stresses components at any nodal point and the unit normal vector (direction cosines) to any inclined plane through this point. This method ensures equilibrium of stresses at the material interface.

The Hoffman's failure criterion (Hoffman, 1967) was used in this study to evaluate the probability of bone-prosthesis interface failure. It accounts for the multi-axial stresses in failure initiation and the gradually changing interface bone density and strength. Although experimental validations in support of the Hoffman's criterion are very few (Stone et al., 1983; Kaplan et al., 1985), it has been used to evaluate cement-bone interface failure for cemented prosthesis, and prosthesis-bone interface failure for uncemented prosthesis. It works reasonably well for trabecular bone (Stone et al., 1983; Kaplan et al., 1985), and the Hoffman number can only provide for qualitative estimates on a relative basis (Huiskes and van Rietbergen, 1995). The prosthesis-cement interface failure, however, cannot be assessed using this criterion. Weinans et al. (1993) incorporated this failure (debonding) criterion in a FE model simulating the process of implant-bone disruption. At each interface nodal point, a Hoffman number (*FL*) can be determined from the normal and shear stresses, using

$$FL = \frac{1}{S_t S_c}\sigma_n^2 + \left(\frac{1}{S_t} - \frac{1}{S_c}\right)\sigma_n + \frac{1}{S_s^2}\tau^2 \qquad (6.8)$$

with S_t and S_c being the uniaxial interface tensile and compressive strengths, respectively, and S_s the interface shear strength (Huiskes and Van Rietbergen, 1995). The interface strength was related to the density of bone and was assumed to be determined by density (ρ) of bone adjacent to the interface, according to

$$S_t = 14.5\,\rho^{1.71}, \qquad S_c = 32.4\,\rho^{1.85}, \qquad S_s = 21.6\,\rho^{1.65} \qquad (6.9)$$

These relationships between the density and the strength were derived from Kaplan et al. (1985) and Stone et al. (1983), who determined the static strength of trabecular for a range of bone densities. As a first step towards experimental validation, Hoffman's 3-D isotropic failure criterion was applied to the multi-axial testing data, along with data from uniaxial compression tests, indicating a compressive strength approximately three times the tensile strength (Stone et al., 1983). Bovine trabecular bone specimens were tested in multi-axial mode, using special devices that permitted in plane stress condition with specified ratios of normal to shear stress, ranging from 0 (pure shear) to +1.00. In continuation to this study, Kaplan et al. (1985) measured ultimate strengths in tension and compression for two groups of twenty-four trabecular bone specimens. It was concluded that the strength was related to the local apparent density by a power-law function. The measurements of this study (Kaplan et al., 1985) suggested that the tensile strength of trabecular bone was significantly less than the compressive strength, thus supporting similar predictions by Stone et al. (1983) based on extrapolation of shear strength data using Hoffman's 3-D isotropic failure criterion. The use of interface strength data, given by Eq. (6.9), in the Hoffman's failure

criterion (Eq. 6.8) is an attempt to account for the microstructure of bone. The state of local interface stress can be substituted in the Eq. (6.8) to obtain a value, termed as the Hoffman number (*FL*). The value of *FL* represents whether a point on the interface is less likely, more likely or very likely to fail. For *FL* less than 1, no interface failure is expected; for *FL* greater than 1, failure is expected. Although it was used to evaluate the probability of interface disruption (Huiskes and Van Rietbergen, 1995), the *FL* cannot be designated as probability in true sense; the value of probability cannot exceed unity. This failure criterion can be described by an ellipsoid for 3-D, or an ellipse for 2-D cases. A combination of normal and shear values outside the ellipse provokes a failure of the bond.

In case of a stronger bond between cement with intermedullary cancellous bone, the strength of the interface may be taken as S_t = 5.5 MPa, S_c = 2.5 MPa and S_s = 8.0 MPa (Krause et al., 1982). Mann et al. (1999) reported that the strength of cement-bone interface was significantly higher when loaded in shear (2.25 MPa) than that loaded in tension (1.35 MPa). The cement-bone test specimens were fabricated from six fresh-frozen human proximal femurs (mean age 58, range 25-77). Their study, however, was limited only to tensile or shear loading without consideration of mixed mode loading. Hence, these data may lead to doubtful evaluations on the interface failure criterion. The actual state of stress at the cement-bone interface consists of a combination of tensile and shear stresses. The data obtained from their study indicated that the cement-bone interfaces with equal amounts of tensile and shear stress was more likely to fail under tensile loading. Moreover, for a particular value of the shear stress, *FL* is higher for tensile stresses as compared to compressive ones. A high value of *FL* indicates a high risk of failure of the interface. Hence, a combination of shear and tension appears to be more harmful to the interfacial bond than shear in combination with compression. The tensile strength of the prosthesis-cement interface was reported to be 8 MPa (Keller et al., 1980), whereas the shear strength was 6 MPa (Barb et al., 1982; Arroyo and Stark, 1987; Stone et al., 1989). Therefore, the tensile and the shear stresses produced at the prosthesis-cement and at the cement-bone interfaces are potential threats to the TSA. The gross loosening of the implant may be due to the prosthesis-cement or the cement-bone interface loosening, failure (cracking) in the cement due to excessive stress, relative motions between the materials, and due to bone resorption induced by adverse bone remodelling.

The generation of polyethylene wear particle has been identified as an additional mode of failure, even though it is uncommon as compared to lower limb prostheses. Estimates of the stresses in the polyethylene are relevant, since these stresses would induce polyethylene wear. The failure strength of polyethylene varies between 18 – 25 MPa, depending on processing and sterilisation (Young, 1991; Greer et al. 1995; Windau and Mackin, 1996). The wear debris produces particulate reactions by macrophages, osteolysis, soft-tissue interposition, and finally gross loosening. This study, however, does not account for realistic estimates of contact stresses in the polyethylene. Hence, a careful study on contact stresses, with a finer mesh size as compared to the present study, is required to analyse the wear and wear-debris-formation problem (Wirth and Rockwood, 1994).

It might be summarised that the design of the implant is better, if stresses in the cement mantle and in the polyethylene are reduced. The multi-axial stresses (tensile/compression and shear) generated at the material interfaces should not be high so as to evoke interface failure. The deviations in stress distribution, due to the insertion of the implant, should be minimised as compared to that prevailing in case of natural bone. The stress components, evaluated in Table 5, serve as criteria for judgement.

6.3.2 Total polyethylene glenoid component

The cement mantle has often been considered as the potential area of high stresses. Presumably, it is the most likely material from which the initiation of crack propagation occurs in the glenoid arthroplasty. The location of high Von Mises stresses vary between the upper and lower part of the cement mantle, due to the change in location of the GH reaction force (30- to 180-degree abduction), as shown in Figure 4 (a - f). Relatively higher stresses are observed in the cement layer immediately below the glenoid component and adjacent to the tip of the keel, indicating probable areas of failures. The GH joint reaction force varies between 350 to 400 N, during 60- to 120-degree abduction of the arm, which generates tensile stresses in the cement varying between $1 - 10$ MPa. During 90-degree abduction, there is a tendency of the glenoid component along with the keel to bend in the superior-inferior direction. This puts the superior part of the keel and the cement into higher tensile stresses ($1 - 3$ MPa) as compared to the inferior part (Fig. 5). In some locations the stresses vary between 3 to 4 MPa. Moreover, relatively higher tensile stresses ($4 - 10$ MPa) are evoked at locations adjacent to the tip of the keel (Fig. 5). The maximum values of compressive and Von Mises stresses generated in the cement mantle are -9.37 MPa and 8.31 MPa, respectively. These results indicate that the stresses in the cement are far below its failure strength.

The interface stresses, normal (σ_n) and shear (τ) stresses, at the prosthesis-cement and the cement-bone boundaries are the most important parameter to prevent initial mechanical failure of the interface and to provide primary stability to the implant-bone configuration. The cement-bone interface is subject to higher stresses ($\sigma_n = 2.51$ MPa, $\tau = 3.41$ MPa) as compared to the prosthesis-cement interface stresses ($\sigma_n = 2.58$ MPa, $\tau = 1.33$ MPa). The peak cement-bone interface stresses are generated at the interface adjacent to the tip of the keel (Fig. 4c), whereas the peak prosthesis-cement interface stresses are generated around the superior edge of the prosthesis. The cement-bone interface around the superior edge of the prosthesis is subject to lower stresses ($\sigma_n = 1.14$ MPa, $\tau = 1.24$ MPa) as compared to the area adjacent to the tip of the keel. However, the actual failure of a cement-bone interface depends on the strength of the interface bond.

The strength of the interface bond, given by the Eq. (6.9), depends on the density (ρ) of cancellous bone elements adjacent to the cement-bone interface. The range of bone densities of these bone elements varies between 0.35 to 0.50 g cm^{-3}; the superior regions having higher density values as compared to the central region where the keel is inserted. A similar regional density distribution was reported by Batte et al. (1996), who conducted an indentation study on five normal cadaveric glenoids. They found the superior regions to be the strongest with anterior-posterior trends varying at three different depths. Müller-Gerbl et al. (1992) found a greater glenoid subchondral density anteriorly and posteriorly in young people whereas the greatest density was central in elderly people. Following these data, we obtain a range of interface strength data varying between $S_t = 2.408$ MPa, $S_c = 4.646$ MPa, $S_s = 3.821$ MPa for $\rho = 0.35$ g cm^{-3} (glenoid central) and $S_t = 4.43$ MPa, $S_c = 8.89$ MPa, $S_s = 6.88$ MPa for $\rho = 0.50$ g cm^{-3} (glenoid superior). On the one hand, using the higher strength data for a multi-axial interface stress condition ($\sigma_n = 1.14$ MPa, $\tau = 1.24$ MPa) around the superior edge of the implant, the maximal Hoffman number (*FL*) is calculated as 0.19. On the other hand, using the lower strength data for a multi-axial cement-bone interface stress ($\sigma_n = 2.51$ MPa, $\tau = 3.41$ MPa) the *FL* is calculated as 1.86. These results indicate that the cement-bone interface in the superior region is more secure against interface failure. The interface adjacent to the tip of keel is very likely to fail, even at moderate load, as compared to the superior edge of the prosthesis. Considering the prosthesis-cement interface strength ($S_t = 8$ MPa, $S_s = 8$ MPa) and the peak value of normal ($\sigma_n = 2.58$ MPa) and shear ($\tau = 1.33$ MPa) it appears, however, that the implant-cement interface is secure against failure.
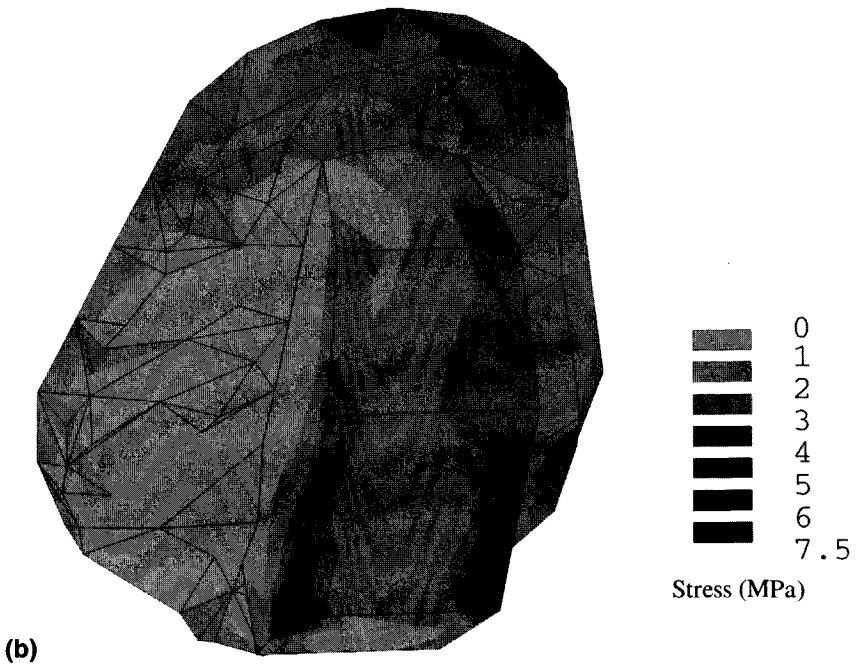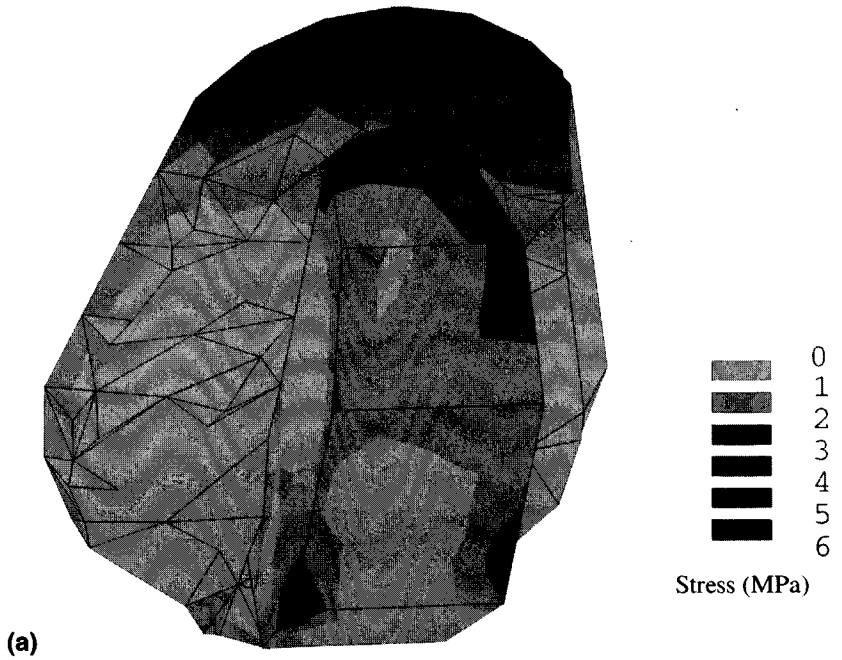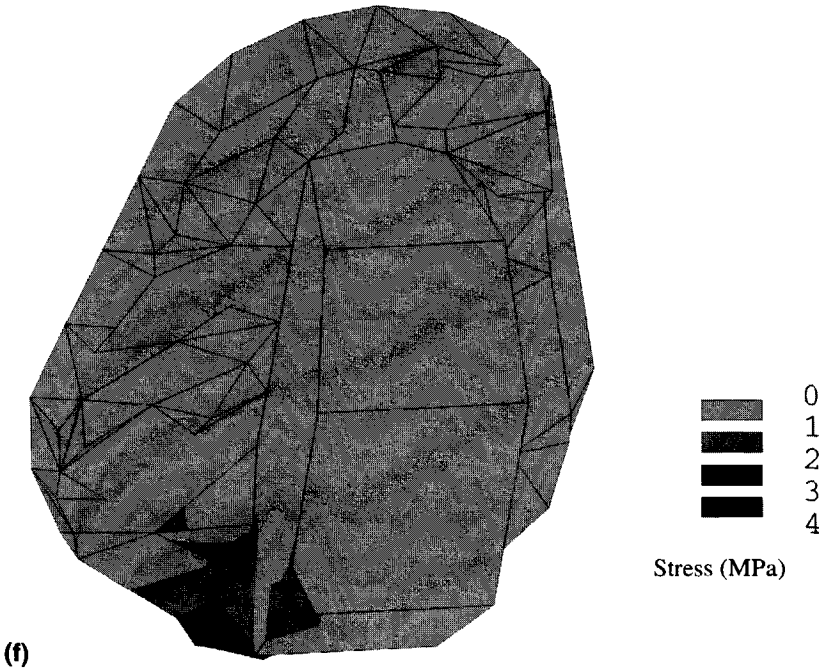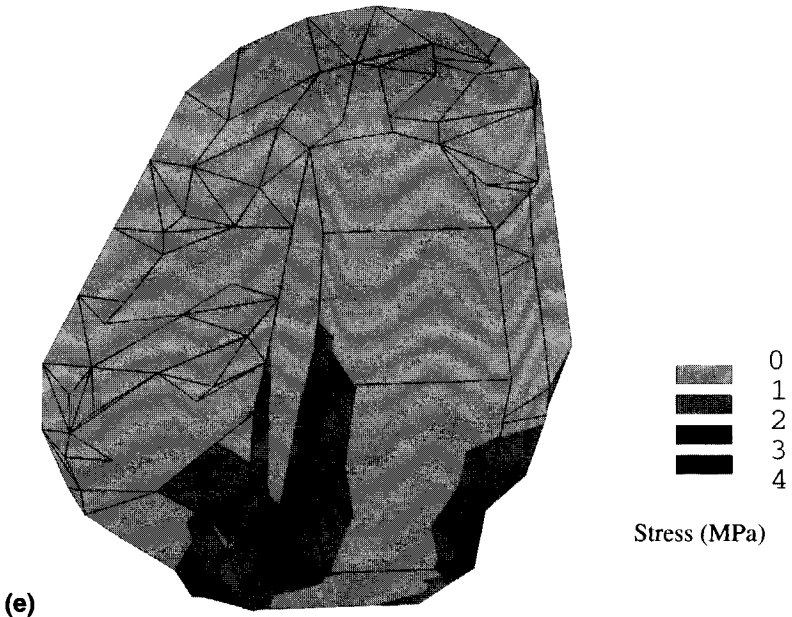
Figures 4a – b. Von Mises stress distribution (MPa) in the cement mantle for total polyethylene design; medial view. (a) 30-degree abduction; (b) 60-degree abduction.

(c)

Stress (MPa)

(d)
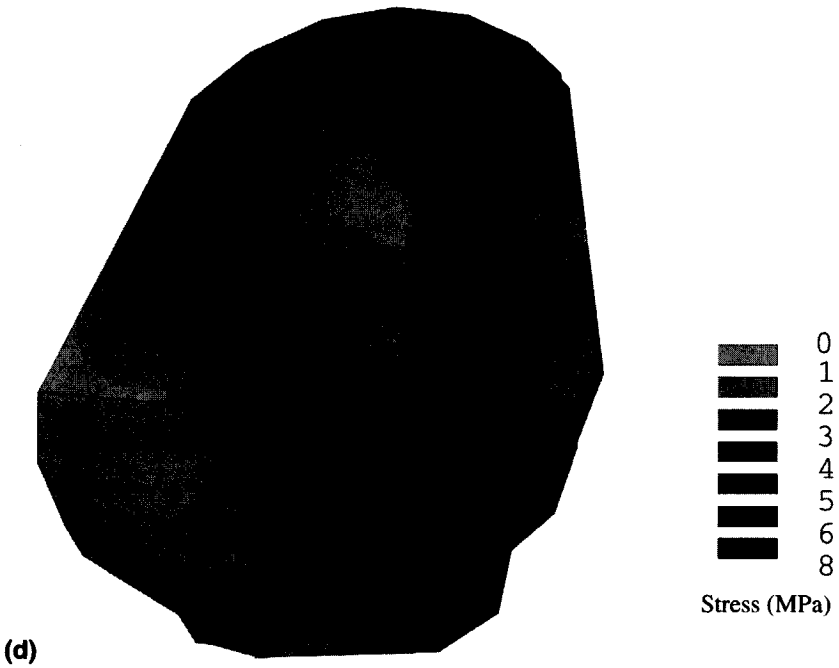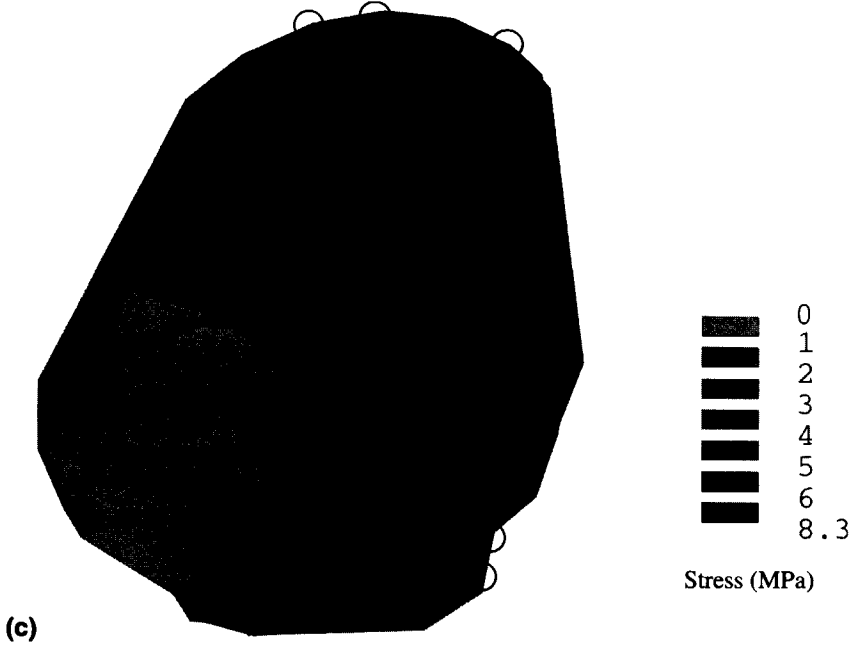
Figures 4c – d. Von Mises stress distribution (MPa) in the cement mantle for total polyethylene design; medial view. (c) 90-degree abduction; (d) 120-degree abduction.
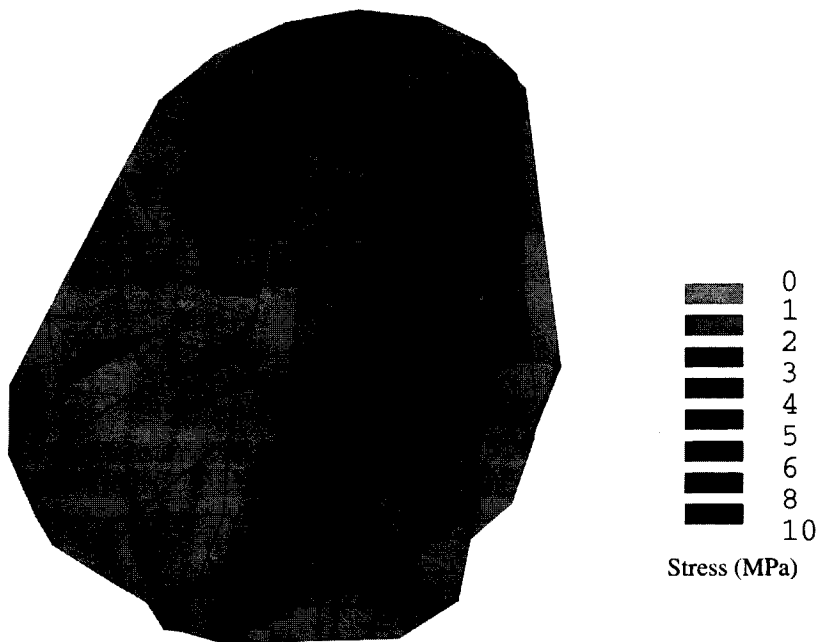O   : Location of high interface stress, indicating probable debonding.

Figures 4e – f. Von Mises stress distribution (MPa) in the cement mantle for total polyethylene design; medial view. (e) 150-degree abduction; (f) 180-degree abduction.

Figure 5. Principal tensile stress (MPa) distribution in the cement mantle for total polyethylene design, during 90-degree abduction (load case 4).
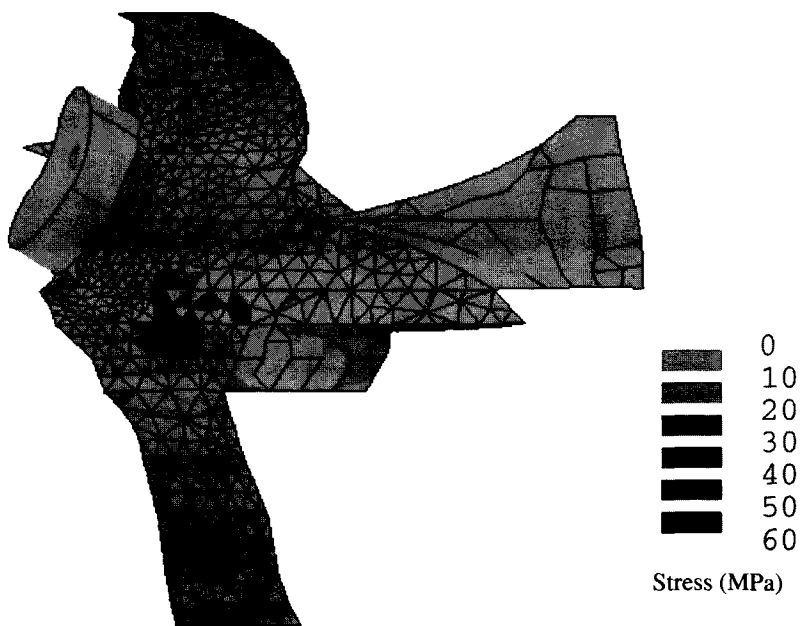
Figures 6. Von-Mises stresses (MPa) in the implanted (total polyethylene) glenoid during 90-degree abduction: frontal view.
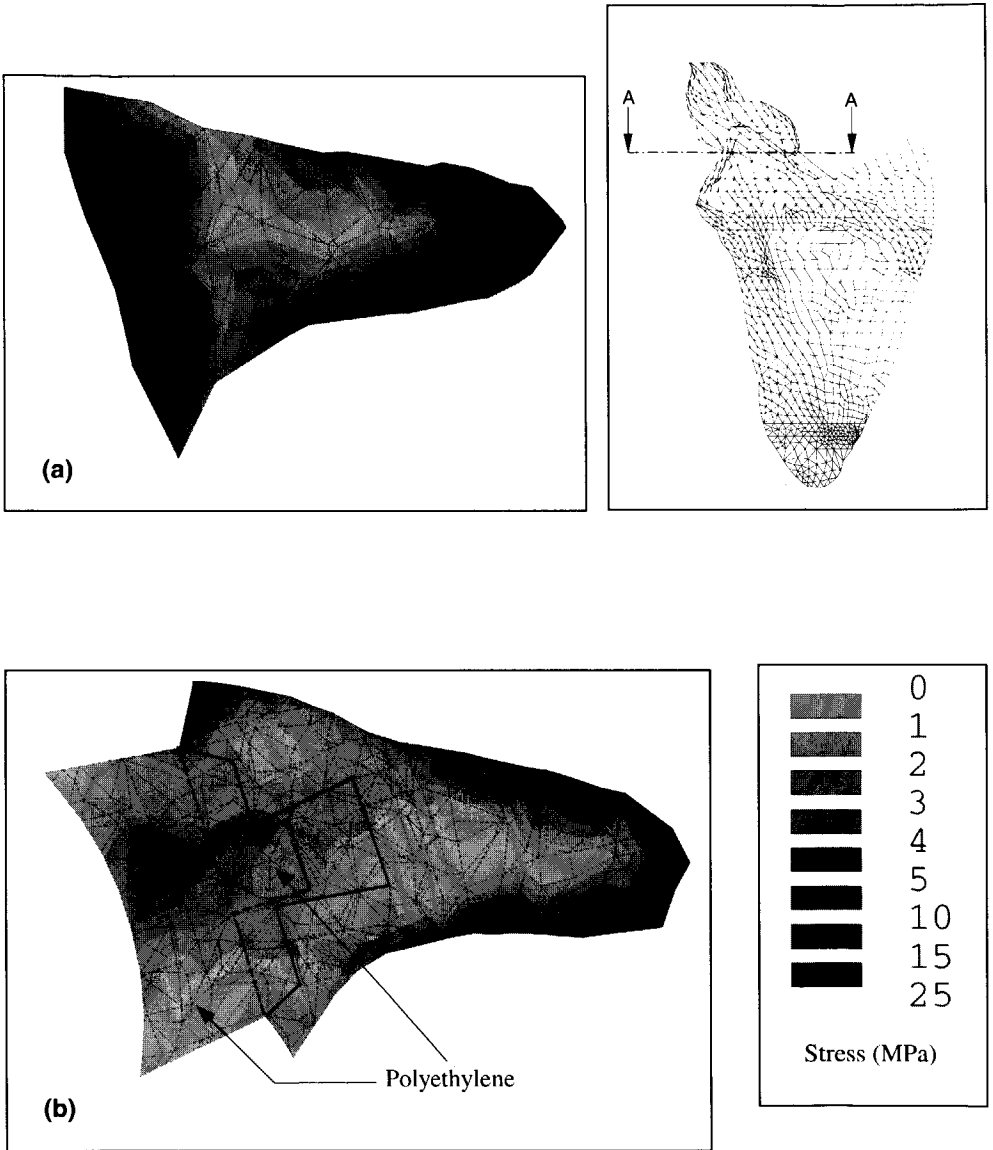
Figure 7. A sectional (A-A) view of the Von-Mises stress (MPa) distribution for (a) natural scapula model, and (b) total-polyethylene design in the glenoid prosthesis-bone model, during 90-degree abduction;

————— : prosthesis-bone or cement-bone boundary.

------ : polyethylene-cement boundary.

Table 5. Maximum values of stress components (in MPa) in PolyEthylene (PE) cup, metal-backing, cement mantle and their respective interfaces.

Stress components (MPa)	Metal-backed PE	Total PE
Von Mises stress in PE cup	14.03	15.10
Normal stress, cement (ten.)	11.51	9.98
Normal stress, cement (comp.)	-10.15	-9.37
Von Mises stress in cement	9.80	8.31
Normal stress, prosthesis-cement (ten.)	5.92	2.58
Shear stress, prosthesis-cement	1.22	1.33
Normal stress, cement-bone (ten.)	2.86	2.51
Shear stress, cement-bone	3.55	3.41

The consequences of the implantation on the stresses induced in the trabecular and cortical bone are also important. High stresses are mostly transmitted by the polyethylene component and are partially transferred to the underlying bone, thereby preserving the stress level in the bone similar to that of the natural scapula. A maximum Von Mises stress of 15 MPa is generated in the polyethylene. A sectional view of the Von-Mises stresses in the glenoid, as indicated in Figure 7, reveals that the stresses in the trabecular bone underlying the prosthesis, is slightly lower (0.05 to 3 MPa) as compared to that of the natural scapula (0.05 to 4 MPa). The distribution of Von Mises stresses (10 – 60 MPa) in the cortical bone are also reduced as compared to that of the natural glenoid, due to the inclusion of the prosthesis (Fig. 6). These results indicate that bone remodelling, if any, would not be a serious threat to the TSA as compared to the hip arthroplasty.

6.3.3 Metal-backed polyethylene component

The distribution of Von Mises stresses in the cement mantle, varying between 1 – 9.80 MPa during humeral abduction (30 – 180 degree), for the metal backed glenoid component are illustrated in Figure 8 (a – f). The tensile stresses (1 – 2 MPa) in the cement mantle, largely, are reduced as compared to the total polyethylene component, except a few locations along the periphery where it varies between 2 to 5 MPa. Higher tensile stresses (5 – 11.5 MPa) are evoked at locations adjacent to the tip of the keel during 90-degree abduction (Fig. 9). The maximum value of compressive stress induced in the cement is −10.15 MPa. These results indicate that the stresses generated in the cement mantle are well below its failure strength.

The implant-cement interface is subject to higher normal (5.92 MPa) stresses, but lower shear (1.22 MPa) stresses as compared to the total polyethylene prosthesis. Presumably, the failure (interface debonding) of the implant might occur at the prosthesis-cement interface, although the cement-bone interface stresses ($\sigma_n = 2.86$ MPa, $\tau = 3.55$ MPa) adjacent to the tip of the keel are also crucially high. But the actual failure of an interface depends on the interface bond strength.
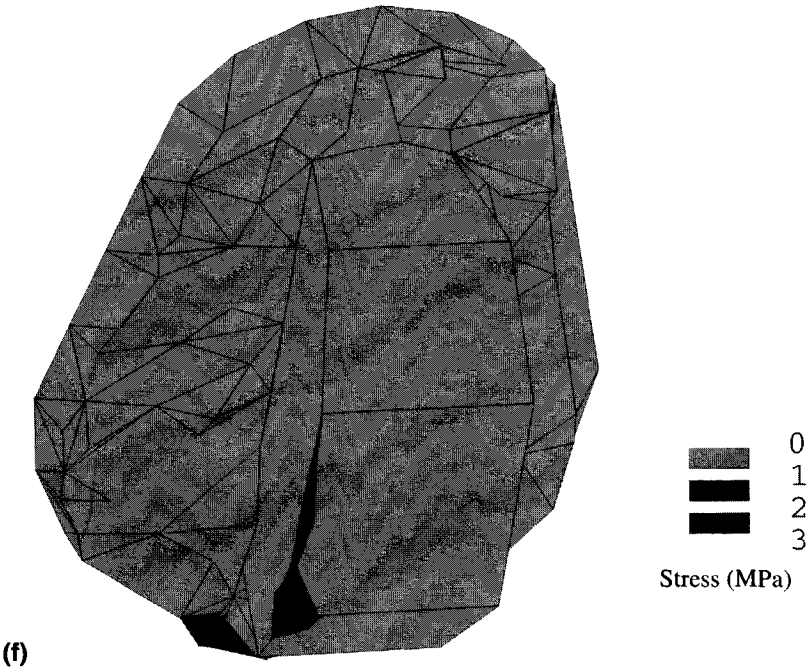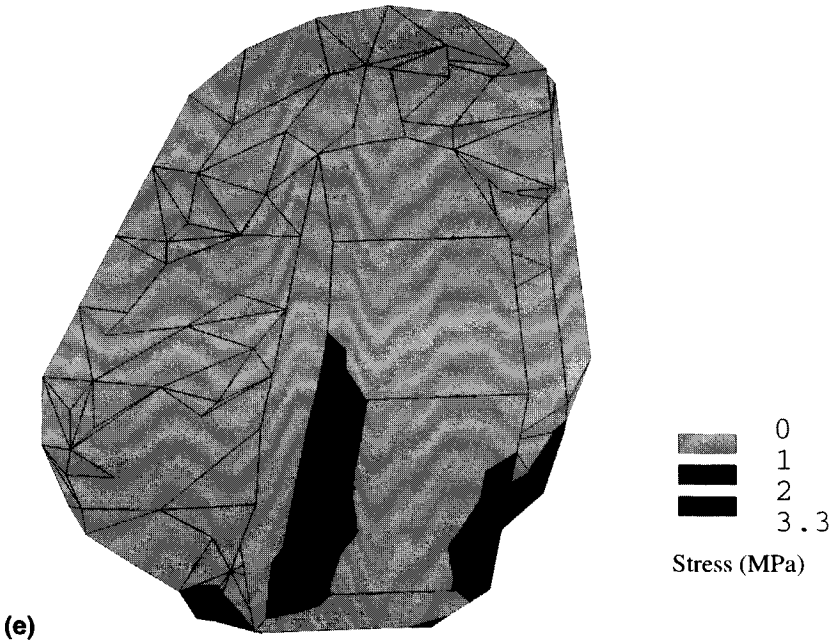
(a)

Stress (MPa)
0
1
2
3
4.6

(b)

Stress (MPa)
0
1
2
3
4
5
6
8.8
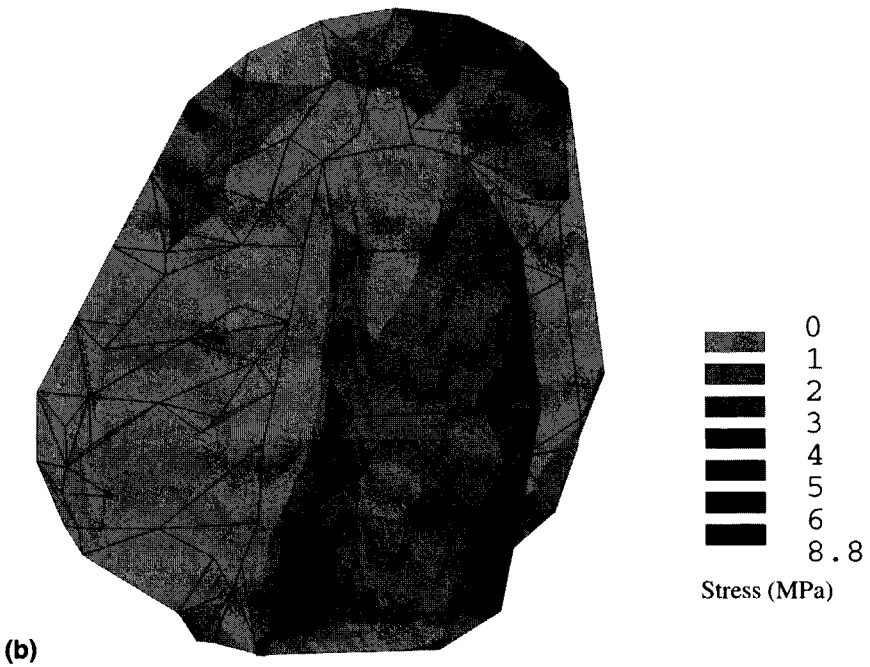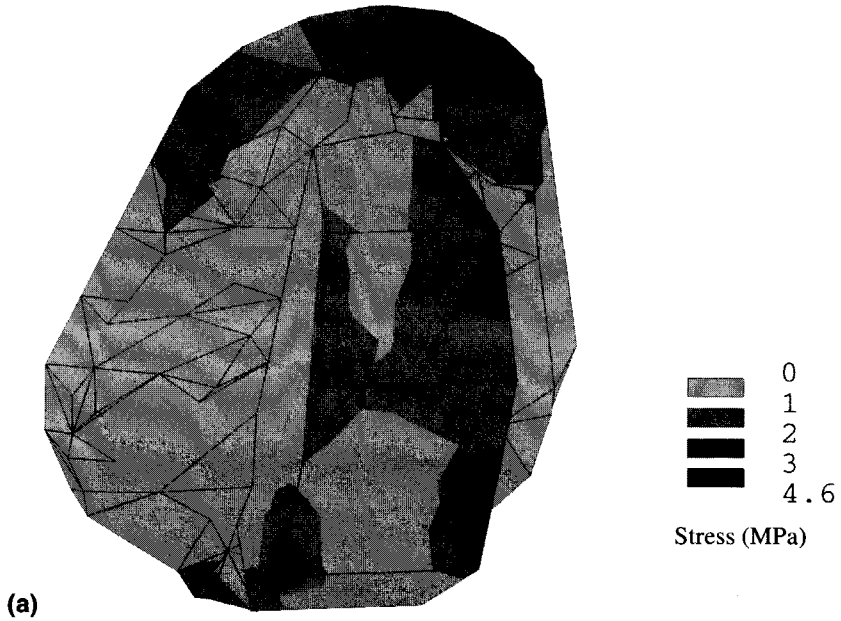
Figures 8a – b. Von Mises stress distribution (MPa) in the cement mantle for metal-backed design; medial view. (a) 30-degree abduction; (b) 60-degree abduction.

(c)

(d)
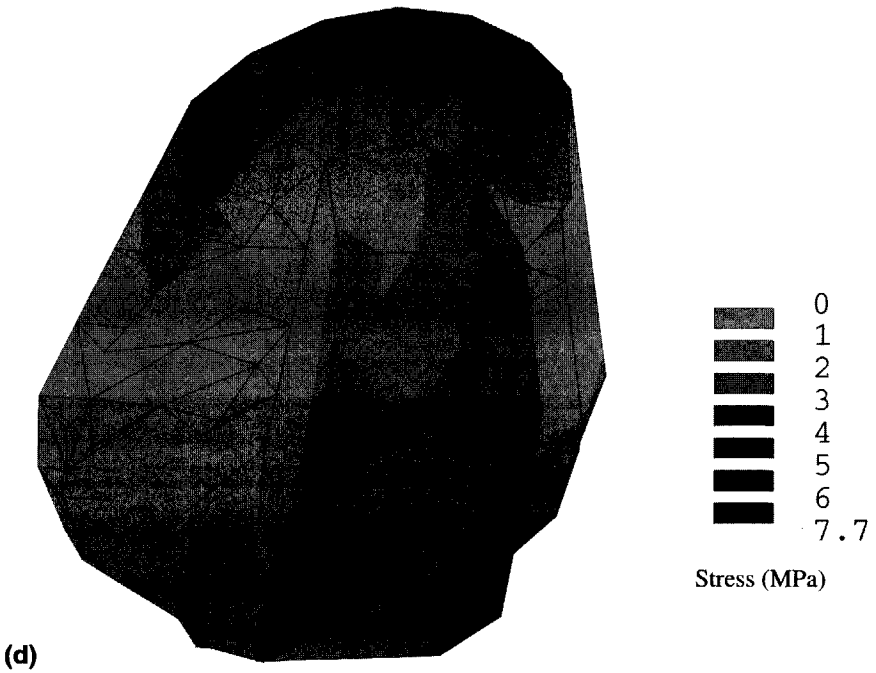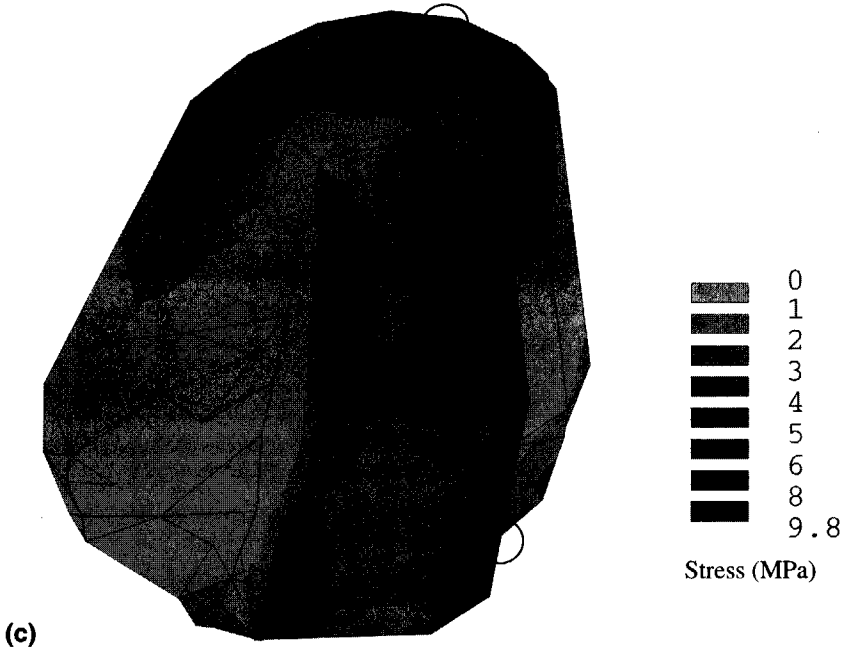
Figures 8c – d. Von Mises stress distribution (MPa) in the cement mantle for metal-backed design; medial view. (c) 90-degree abduction; (d) 120-degree abduction.

O : Location of high interface stress, indicating probable debonding.

Figures 8e – f. Von Mises stress distribution (MPa) in the cement mantle for metal-backed design; medial view. (e) 160-degree abduction; (f) 180-degree abduction.

Considering similar observations on density distribution of cancellous bone elements adjacent to the cement-bone interface, as reported in Section (6.3.2), the *FL* can be calculated for two different regions. For higher strength (S_t = 4.43 MPa, S_c = 8.98 MPa, S_s = 6.88 MPa for ρ = 0.5 g cm^{-3}) of cancellous bone in the superior side and for the peak multi-axial stresses (σ_n = 3.39 MPa, τ = 0.43 MPa) in this region, the *FL* is calculated as 0.68. Whereas, for lower strength (S_t = 2.408 MPa, S_c = 4.646 MPa, S_s = 3.821 MPa for ρ = 0.35 g cm^{-3}) of cancellous bone in the glenoid central region and for the peak multi-axial stresses (σ_n = 2.86 MPa, τ = 3.55 MPa), the *FL* is calculated as 2.16. These results indicate that the cement-bone interface adjacent to the tip of the keel is very likely to fail, even at moderate load (Fig. 8c). Considering the prosthesis-cement interface strength (S_t = 8 MPa, S_s = 8 MPa) and the peak value of multi-axial stresses (σ_n = 5.92 MPa, τ = 1.22 MPa) it appears, however, that the metal-cement interface is secure against interface failure.

The influence of the metal-backed glenoid component on the bone is not entirely different from that of the total polyethylene component. The metal-backing adds rigidity to the implant and therefore, facilitates reduction of stresses in the polyethylene and in the cement. Using a thin metal-backing, a maximum Von Mises stress of 14 MPa is generated in the polyethylene cup. The metal-backing and the metallic keel in the glenoid component carries the bulk of the stresses (Von Mises), ranging from 1 to 20 MPa. Higher Von Mises stresses, ranging between 10 and 20 MPa, are observed in the metallic flange underlying the polyethylene cup. The metal-backing leads to tensile stresses (1 – 15 MPa) in the metallic flange, indicating bending of the metallic flange. The stresses in the underlying trabecular bone are lower (0.05 – 2 MPa) than that of the total polyethylene design (0.05 – 3 MPa), as indicated in Figure 10. Moreover, the high cement-bone interface stresses, at locations adjacent to the tip of the keel might lead to interface failure.
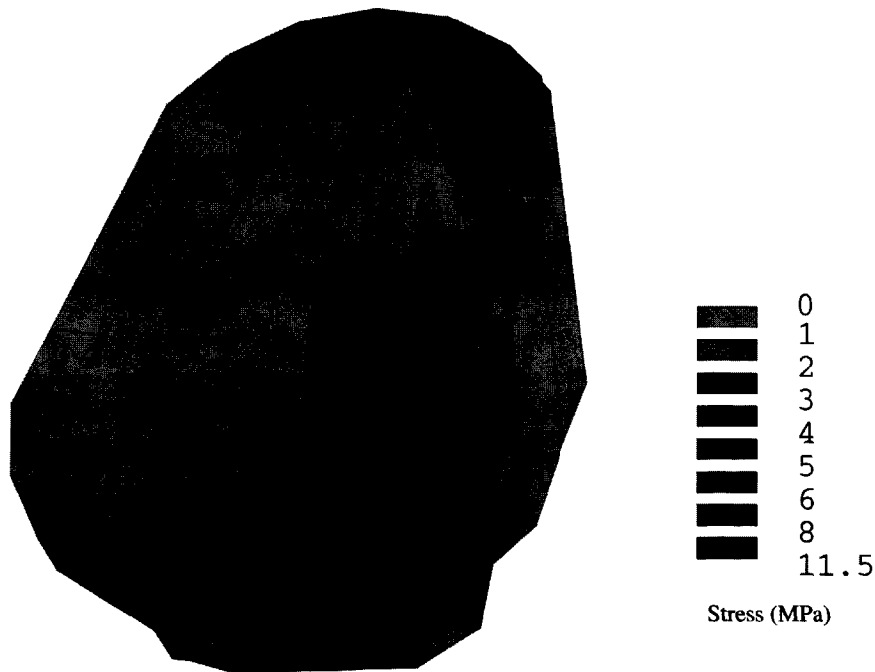

Stress (MPa)

Figure 9. Principal tensile stress in the cement mantle of metal-backed design during 90-degree abduction (load case 4).
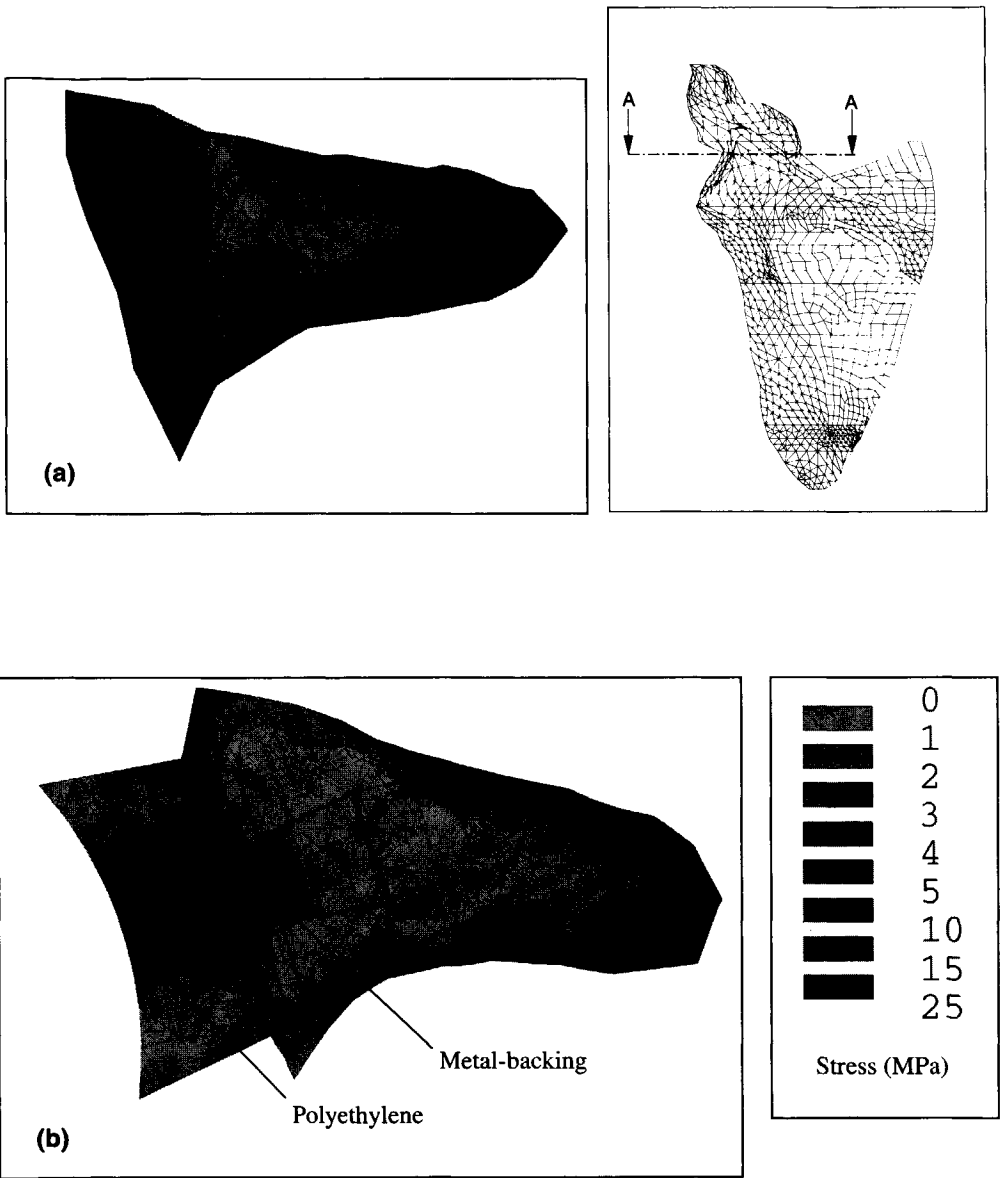
Figure 10. A sectional (A-A) view of the Von-Mises stress (MPa) distribution for (a) natural scapula model, and (b) the metal-backed design in the glenoid prosthesis-bone model, during 90-degree abduction;

    ————   : prosthesis-bone or cement-bone boundary.

    — — — .   : metal-cement boundary.

6.4 Discussion

The study is directed towards investigating some biomechanical factors related to the loosening of cemented glenoid prosthesis, using a detailed 3-D FE model of the glenoid prosthesis. Quantitative results of this study cannot be compared with other studies, since Friedman et al., 1992 did not report quantitative results and Orr et al. (1988) did not account for the cement layer. These studies were focussed on the influence of the glenoid component on the surrounding bone, which are more relevant to bone remodelling and long-term failure phenomena. According to our study, the principal stresses generated in the cement are higher than the 2-D and the 3-D analysis of Lacroix and Prendergast (1997) and Lacroix et al. (2000), respectively. The 3-D FE analysis, moreover, was not based on a submodelling approach. Four nodes in the middle of the fossa region were fixed to avoid rigid body motions, resulting in a total reactive force of 118 N at these constraints. It may be recalled that the results of these analyses were unrealistic, since they were sensitive to the major assumptions.

It may be argued in the first place about the necessity of the submodelling approach. The structure of the scapula and the loading conditions call for the submodelling approach, so that the elastic behaviour of the overall model can be included in the analysis. The submodels of the glenoid prostheses are based on an experimentally validated 3-D FE model of a natural scapula, which includes the effect of all the muscle, ligament and joint reaction forces. The stresses in this region largely depend on the position and direction of the GH-joint reaction force. The effect of muscles, ligaments and joint reaction forces on the bony structures connected to the glenoid, however, would have considerable influence on the stress distribution of the submodel with glenoid prosthesis. Considering these aspects, it may be concluded that the need of the submodelling technique would lead to realistic evaluations of stresses and strain. A large size of the submodel and the use of prescribed displacements at cut-boundaries located far away from the glenoid would have predominant influence on the results. Any other form of approximate boundary conditions, applying constraints at locations far away from the region of interest to restrain rigid body motion, is inappropriate and would lead to doubtful evaluations (Lacroix et al., 2000). The results of this study, therefore, seem to be more accurate in predictions of stresses in the bone-prosthesis configuration and the underlying trabecular bone, quantitatively and qualitatively. Stress distributions should be interpreted meticulously, as we probably are dealing with singularities. It should also be noted that the stresses in the low-density, open-cell trabecular bone structure are observed macroscopically, which will differ for a micro-mechanical model. These assumptions in macroscopic modelling approach would therefore, lead to stresses that will differ from the microscopically calculated stresses in the individual trabeculae (Van Rietbergen et al., 1995).

The method employed in this study has a number of limitations. Only one particular keel shape was considered. As compared to the hip prosthesis, different stem shapes are known to generate different interface stress patterns (Huiskes, 1990). Hence, the shape will affect the evolution of the interface failure (debonding) process. The keel was assumed to be fully bonded to the cement mantle. Bone geometry and density distribution was based on CT-scan data of one representative scapula. The mechanical properties of bone are assumed to be isotropic and to remain constant with time. Whereas, in reality, bone is anisotropic. These assumptions are idealisations of the reality. Hence, the study is conceptual in nature and the results predict certain qualitative trends.

In order to compare the deviations in stress distribution due to implantation accurately, the overall FE model of the natural scapula and the submodel with prosthesis should have exactly similar mesh. The procedure would ensure similarity in location and in material properties of the

bone element for both the models and would therefore, lead to comparison of stresses, quantitatively and accurately. Although a finer mesh was used for the bone-prosthesis submodel as compared to the natural scapula model, the changes in stress distribution can be observed at locations in the vicinity of the prosthesis. It appears, by and large, that the total-polyethylene and the metal-backed designs seem to preserve the physiological stress distributions in the cancellous bone as prevailing in case of the natural glenoid without prosthesis. However, a total polyethylene design appears to provide a more physiological environment than a metal-backed design in the cancellous bone underlying the prosthesis, indicating lesser possibility of abnormal bone remodelling.

The cement mantle, for total polyethylene design is subject to lower tensile (1 – 10 MPa) stresses as compared to the metal-backed design (tensile: 1 – 11.5 MPa). Considering the overall stress distribution, it appears, however, that the stresses in the cement mantle for metal-backed design are largely reduced as compared to the total polyethylene design, except a few locations along the periphery and the area adjacent to the tip of the keel. Cement is strong in compression, but weak in tension. The failure strength (tensile) of cement has been reported to be 25 MPa (Lee et al., 1977; Saha and Pal, 1984). The Neer II prosthesis, a metal-backed polyethylene component, was introduced in 1984 with the objective of more uniform distribution of load from the glenoid cavity to the cement layer and the surrounding bone. The modulus of elasticity of metal is very high as compared to other materials in the configuration and therefore, the metal-backing adds rigidity of the implant. This study shows that the load is transferred from the polyethylene cup to the metal, which eventually carries the bulk of the load and generates lower stresses in the underlying material. As a result, stresses in the cement layer below the glenoid component are reduced. Stresses in the polyethylene are also reduced (by 8%) as compared to the total polyethylene design. But these reductions are minor, since a thin (1 mm) metallic flange has been used in this model. A thicker metal backing would result in higher reduction of stresses in the polyethylene cup; thereby reducing the chances of polyethylene wear particle formation. This behaviour would apply for any stiff material used in the prosthesis design. Whereas, for the total polyethylene implant the reinforcement function is offered only by the cement layer. The stresses in the cement layer immediately below the polyethylene component are increased, although it is well below the failure strength. The load passing through the comparatively less stiff total polyethylene component is absorbed by the deformation of the polyethylene cup and the keel allowing more uniform transfer of load to the underlying cement and bone. The peak stress (15 MPa) within the polyethylene cup is high and is close to the yield strength of the material, increasing the risk of polyethylene wear particle formation. Higher stress would be generated during normal activity like standing up from a chair, which produces a GH contact force of 1300 N (Anglin et al., 1996[b]).

Stress distribution is lower at the prosthesis-cement interface than at the cement-bone interface for the total polyethylene design. Clinical and radiographic studies reported that loosening of the glenoid component appeared at the cement-bone interface (Cofield, 1984; Barrett et al., 1987; Berms, 1993; Torchia et al., 1997). Our results agree to the idea that the glenoid component loosening might be due to the stresses at the cement-bone interface. In case of metal-backed design, the cement-bone interface stresses adjacent to the tip of the keel is higher than the stresses around the superior edge of the prosthesis (Table 5). On the other hand, the metal-cement interface stresses are higher than the cement-bone interface stresses. This result is comparable to similar behaviour in the cemented femoral hip components, where debonding occurred mainly at the prosthesis-cement interface (Harrigan and Harris, 1991). In view of the strength properties (tensile: 8 MPa, shear: 6 MPa), higher metal-cement interface stresses might be generated during normal activity like standing up from a chair, which produces a GH contact force of 1300 N (Anglin et al., 1996[b]).

The cement-bone interface adjacent to the tip of the keel, for total polyethylene design, seems more likely to fail (*FL = 1.86*) as compared to the superior edge of the prosthesis (*FL = 0.19*). Whereas, for metal-backed design, this interface adjacent to the tip of the keel is more likely to fail (*FL = 2.16*) as compared to the superior edge of the prosthesis (*FL = 0.68*). Hence, the actual failure of an interface depends on the bone density and the bone strength of the interface bond, which is higher in the superior side of the glenoid than in the central region. Moreover, it appears that the cement-bone interface for the metal-backed design is more vulnerable to interface failure. At higher loads, debonding at the cement-bone interface might be simultaneously initiated around the superior edge and the area adjacent to the tip of the keel. This result is well supported by radiographic study of Torchia et al., (1997). They presented a comprehensive study on radiographic evaluation of cemented Neer glenoid components, with regard to earlier studies (Table 1). It was observed that the percentage of cement-bone radiolucent lines in any area of the glenoid component, excluding the keel, remained constant (84%). The percentage of radiolucent lines, however, increased around the keel (from 42% to 76%), as did the percentage of components (from 10 to 38%) that shifted in position (Torchia et al., 1997). Probably, the most important parameter to prevent initial mechanical interface failure ('primary stability') is the quality (strength) of the interface bond. This factor is represented in the failure criterion, which is dependent, in reality, on the precision of the surgical procedure, the quality of the bone stock and the penetration of the bone cement for cemented implants (Krause et al., 1982) or the amount of bone ingrowth into the uncemented implants.

The role of the subchondral bone might be crucial in the design of the implant. The value of the Young's modulus of the subchondral bone varies between 0.186 to 2.1 GPa and is approximately equal to that of cement. The subchondral bone, with a higher density as compared to the trabecular bone offers higher interface bond strength. During surgery, this bone is usually removed and replaced by cement. The higher stresses evoked at the cement-bone interface coupled with the lower interface strength of the trabecular bone might lead to interface failure. Further, the amount of bone stock available in the glenoid is small as compared to other bones. Removal of the subchondral bone and replacing it by cement would mean a substantial loss in the structural stiffness of the whole glenoid. In absence of the subchondral bone, the cement layer offers the reinforcement function, since its modulus of elasticity is higher than the polyethylene component. This would eventually result in an increase in stresses in the cement. Therefore, a part of the subchondral bone in the superior-inferior side should be preserved to strengthen the structure of the glenoid, as a whole. From the point-of-view of surgical considerations, using a very thin layer of cement in between the glenoid component (total-polyethylene) and the subchondral bone might be required for secured primary fixation. This would also eliminate direct polyethylene-bone contact.

6.5 Conclusions

Using a detailed 3-D FE model of glenoid prosthesis based on CT-scan data and physiological loading conditions the following conclusions can be made.
(1) A large size of the submodel and the use of prescribed displacements at cut-boundaries located far away from the glenoid would have considerable influence on the results.
(2) A total polyethylene design appears to provide a more physiological stress distributions than a metal backed design in the cancellous bone regions underlying the prosthesis.
(3) Higher prosthesis-cement interface stresses (normal and shear) are generated for the metal-backed design as compared to the total polyethylene design. However, for metal-backed implants, the cement-bone interface is subject to higher shear but lower normal stresses.

These high stresses, due to a moderate GH joint reaction force of 400 N (unloaded abduction, 90-degree), are of high significance as far as debonding and eventual loosening of the prosthesis is concerned.

(4) For total polyethylene design, the cement-bone interface adjacent to the tip of the keel seems very likely to fail as compared to the superior edge of the prosthesis. Whereas, in case of metal-backed design, this interface adjacent to the tip of the keel appears even more likely to fail as compared to the non-backed design.

(5) A part of the subchondral bone might be preserved to strengthen the stiffness of the implanted glenoid, as a whole. A thin layer of cement could be used in between the implant and subchondral bone for secured primary fixation.

(6) With some revisions in the design of metal-backing (keel and flange), the metal-backed prosthesis might offer better prospects in glenoid arthroplasty.

Acknowledgement

References

Amstutz, H.C., Sew Hoy, A.L. and Clarke, I.C. (1981). UCLA Anatomic total shoulder arthroplasty. Clin. Orthop. Rel. Res., 155, 7-20.

Amstutz, H.C., Thomas, B.J., Kabo, M.J., Jinnah, R.H. and Dorey, F.J. (1988). The DANA total shoulder arthroplasty. J. Bone Joint Surg. 70A, 1174-1182.

Anglin, C., Tolhurst, P., Wyss, U.P. and Pichora, D.R. (1996[a]). Mechanical properties of glenoid cancellous bone. Proc. 1st Conf. of the International Shoulder Group, Delft University of Technology, Delft, 13-18.

Anglin, C., Wyss, U.P. and Pichora, D.R. (1996[b]). Glenohumeral contact forces during five activities of daily living. Proc. 1st Conf. of the Int. Shoulder Group, Delft, The Netherlands.

Arroyo, N.A. and Stark, C.F. (1987). The effect of textures, surface finish and precoating on the strength of bone cement/stem interfaces. Proc. 13th Soc. Biomat., New York, 218.

Barb, W., Park, J.B., Kenner, G.H. and Recum, A.F. (1982). Intermedullary fixation of artificial hip joints with bone cement-precoated implants. Interfacial strengths. J. Biomed. Mat. Res. 16, 447-458.

Barrett, W.P., Franklin, J.L., Jackins, S.E., Wyss, C.R. and Matsen, F.A. III (1987). Total shoulder arthroplasty. J. Bone Joint Surg. 69-A (6), 865-872.

Barrett, W.P., Thornhill, T.S., Thomas, W.H., Gebhart, E.M. and Sledge, C.B. (1989). Non-constrained total shoulder arthroplasty for patients with polyarticular rheumatoid arthritis. J. Arthroplasty 4 (1), 91-96.

Batte, S.W.P., Cordy, M.E., Lee, T.Y., King, G.J.W., Johnson, J.A., and Chess, D.G. (1996). Cancellous bone properties of the glenoid: correlation of quantitative CT and mechanical strength. Trans. Orthop. Res. Soc. 21, 707.

Berms, J. (1993). The glenoid component in total shoulder arthroplasty. J. Shoulder Elbow Surg. 2, 47-54.

Boyd, A.D., Thomas, W.H., Scott, R.D., Sledge, C.D. and Thornhill, T.S. (1990). Total shoulder arthroplasty versus hemiarthroplasty. J. Arthroplasty 5 (4), 329-336.

Cofield, R.H. (1984). Total shoulder arthroplasty with Neer prosthesis. J. Bone Joint Surg. 66-A (6), 899-906.

Dalstra, M., Huiskes, R. and van Erning, L. (1995). Development and validation of a three-dimensional finite element model of the pelvic bone. J. Biomech. Eng. 117, 272-278.

Frankel, V.H. and Nordin, M. (1980). Basic biomechanics of the skeletal system. Philadelphia: Leo and Febiger.

Friedman, J.R., LaBerge, M., Dooley, R.L. and O'Hara, A.L. (1992). Finite element modelling of the glenoid component: Effect of design parameters on stress distribution. J. Shoulder Elbow Surg. 1, 261-270.

Fukuda, K., Chen, C.M., Cofield, R.H. and Chao, E.Y. (1988). Biomechanical analysis of stability and fixation strength of total shoulder prostheses. Orthopaedics 11(1), 141-149.

Greer, K.W., Hamilton, J.V. and Cheal, E.J. (1995). Polyethylene wear in orthopaedics. In: Wise, D.L. (Eds.) Encyclopaedic Handbook of Biomaterials and Bioengineering, Part B: Applications, 1 (21), 613-638. Marcel Dekker Inc., New York.

Harrigan, T.P. and Harris, W.H. (1991). A three-dimensional non-linear finite element study of the effect cement prosthesis debonding in cemented femoral total hip components. J. Biomechanics 24, 1047-1058.

Hawkins, R.J., Bell, R.H. and Jallay, B. (1989). Total shoulder arthroplasty. Clin. Orthop. Rel. Res. 242, 188-194.

Hertz, H. (1882). Über die Berührung fester elastischer Körper (On the contact of elastic solids). J. Reine und angewandte Mathematik, 92, 156 – 171. (For English translation see Miscellaneous Papers by H. Hertz, Eds. Jones and Schoott, London: Macmillan, 1896.)

Hoffman, O. (1967). The brittle strength of orthotropic material. J. Comp. Mat. 1, 200-206.

Huiskes, R. (1990). Comparative stress patterns in cemented total hip arthroplasty. Orthop. Rel. Sci.1, 93-108.

Huiskes, R. (1993). Failed innovation in total hip replacement. Acta Orthop. Scand. 64, 699-716.

Huiskes, R and Van Rietbergen, B. (1995). Preclinical testing of total hip stems. The effects of coating placement. Clin. Orthop. Rel. Res. 319, 64-76.

Kaplan, S.J., Hayes, W.C. and Stone, J.L. (1985). Tensile strength of bovine trabecular bone. J. Biomechanics 18, 723-727.

Keller, J.C., Lautenschlager, E.P., Marshall, G.W. and Meyer, P.R. (1980). Factors affecting surgical alloy/bone cement interface adhesion. J. Biomed. Mat. Res. 14, 639-651.

Kelly, I.G., Foster, R.S., and Fisher, W.D. (1987). Neer total shoulder replacement in rheumatoid arthritis. J. Bone Joint Surg. 69B, 723-726.

Krause, W.R., Krug, W., Eng, B. and Miller, J. (1982). Strength of cement-bone interface. Clin. Orthop. Rel. Res. 163, 290-299.

Lacroix, D. and Prendergast, P.J. (1997). Stress analysis of glenoid component designs for shoulder arthroplasty. Proc. Inst. Mech. Engrs, Part H 211, 467-474.

Lacriox, D., Murphy, L.A. and Prendergast, P.J. (2000). Three-dimensional finite element analysis of glenoid replacement prosthesis; a comparison of keeled and pegged anchorage systems. J. Biomech Engg. 122, 430-436.

Lee, A.J.C, Ling, R.S.M. and Vangala, S.S. (1977). The mechanical properties of bone cements. J. Medical Engg. & Tech, May 1977, 137-140.

Mann, K.A, Werner, F.W. and Ayers, D.C. (1999). Mechanical strength of the cement-bone interface is greater in shear than in tension. J. Biomechanics 32, 1251-1254.

Mansat, P., Barea, C., Hobatho, M-C., Darmana, R. and Mansat, M. (1998). Anatomic variation of the mechanical properties of the glenoid. J. Shoulder Elbow Surg. 7, 109-115.

McCullagh, P.J.J. (1995). Biomechanics and design of shoulder arthroplasty. Proc. Instn. Mech. Engrs, Part H 209, 207-213.

Müller-Gerbl, M., Putz, R. and Kenn, R. (1992). Demonstration of subchondral bone density patterns by three-dimensional CT Osteoabsorptiometry as a nonevasive method for in vivo assessment of individual long-term stresses in joints. J. Bone and Mineral Res. 7, Supl. 2, S411 - S418.

Neer, C.S. II, Watson, K.C., Stanton, F.J. (1982). Recent experiences in total shoulder replacement. J. Bone Joint Surg. 64A. 319-337.

Orr, T.E., Carter, D.R. and Schurman, D.J. (1988). Stress analyses of glenoid component designs, Clin. Orthop. Rel. Res. 212, 217-224.

Rohlmann, A., Mößner, U. and Bergmann, G. (1984). Finite element analysis at the scapula after shoulder joint replacement. Proc. 4th Europ. Soc. of Biomech., Davos, Switzerland.

Saha, S. and Pal, S. (1984). Mechanical properties of bone cement. J. Biomed. Mat. Res. 18(4), 435-462.

Sneppen, O., Fruensgaard, S., Johannsen, H.V., Olsen, B.S., Sojbjerg, J.O. and Andersen, N.H. (1996). Total shoulder replacement in rheumatoid arthritis: proximal migration and loosening. J. Shoulder Elbow Surg. 5(1), 47-52.

Sperling, J.W., Cofield, R.H. and Rowland, C.M. (1998). Neer hemiarthroplasty and Neer total shoulder arthroplasty in patients fifty years old or less. Long-term results. J. Bone Joint Surg. 80-A (4), 464-473.

Stewart, M.P. and Kelly, I.G. (1997). Total shoulder replacement in rheumatoid disease: 7-to 13-year follow-up of 37 joints. J. Bone Joint Surg. 79-B (1), 68-72.

Skirving, A.P (1999). Total shoulder arthroplasty – current problems and possible solutions. J. Orthop. Sc. 4(1), 42-53.

Stone, J.L., Beaupré, G.S. and Hayes, W.C. (1983). Multiaxial strength characteristics of trabecular bone. J. Biomechanics 16, 743-752.

Stone, M.H., Wilkinson, R. and Stother, I.G. (1989). Some factors affecting the strength of the cement-metal interface. J. Bone Jt. Surg. 71-B, 217-221.

Stone, K.D., Grabowski, J.J., Cofield, R.H., Morrey, B.F. and An, K.N. (1999). Stress analysis of glenoid components in total shoulder arthroplasty. J. Shoulder Elbow Surg. 8(2), 151-158.

Torchia, M.E., Cofield, R.H. and Settergren, C.R. (1997). Total shoulder arthroplasty with Neer prosthesis: long-term results. J. Shoulder Elbow Surg. 6(6), 495-505.

Thomas, B.J., Amstutz, H.C. and Cracchiolo, A. (1991). Shoulder arthroplasty for rheumatoid arthritis. Clin. Orthop. Rel. Res. 265, 125-128.

Van der Helm, F.C.T. (1994a). Analysis of the kinematic and dynamic behaviour of the shoulder mechanism. J. Biomechanics 27, 527-550.

Van der Helm, F.C.T. (1994b). A finite element musculoskeletal model of the shoulder mechanism. J. Biomechanics 27, 551-569.

Van Rietbergen, B., Weinans, H., Huiskes, R., and Odgaard, A. (1995). A new method to determine trabecular bone elastic properties and loading using micromechanical finite element models. J. Biomechanics 28, 69-81.

Wallace, A.L., Phillips, R.L., MacDougal, G.A., Walsh, W.R. and Sonnabend, D.H. (1999). Resurfacing of the glenoid in total shoulder arthroplasty. A comparison, at a mean of five years, of prostheses inserted with and without cement. J. Bone Joint Surg. 81-A (4), 510-518.

Weinans, H., Huiskes, R. and Grootenboer, H.J. (1991). Trends of mechanical consequences and modelling of a fibrous around femoral hip prostheses. J. Biomechanics 23, 991-1000.

Weinans, H., Huiskes, R. and Grootenboer, H.J. (1993). Quantitative analysis of bone reactions to relative motions at implant-bone interface. J. Biomechanics 26, 1271-1282.

Wilde, A.H., Borden, L.S. and Berms, J.J. (1984). Experiences with the Neer total shoulder replacement. In: Bateman, J.E.and Welsh R.P. (Eds.). Surgery of the shoulder. St. Louis: CV Mosby, 224-228.

Windau, J.E. and Mackin, T.J. (1996). The effects of processing and sterilisation on UHMWPE. Trans. 5th World Biomaterials Congress, Toronto, 1996.

Wirth, M.A. and Rockwood, C.A. (1994). Complications of shoulder arthroplasty. Clin. Orthop. Rel. Res. 307, 47-69.

Young, R.J. (1991). Introduction to polymers, Chapman and Hall, New York.

Chapter 7

The Possibilities of Uncemented Glenoid Prosthesis –
a Finite Element Study

Abstract

Fixation of glenoid prosthesis by the use of polymethylmethacrylate (PMMA) has been one of the major problems in total shoulder arthroplasty (TSA) and has been reported to be less reliable. The purpose of this study is to investigate some biomechanical factors related uncemented glenoid component with regard to potential failure mechanisms as indicated by the clinical observations. A three-dimensional (3-D) finite element (FE) model of an uncemented prosthesis based on Computed Tomography (CT) data and realistic loading conditions (humeral abduction) have been used for the purpose. The FE model is generated using submodelling approach, which is based on an overall reference solution of a complete scapula model acted upon by all the muscles, ligaments and joint reaction forces. The uncemented prosthesis consists of a polyethylene cup with a metal-backing. The prosthesis is assumed to be fully bonded to the bone and to the polyethylene cup. A comparison of the uncemented glenoid design with two basic models of cemented prosthesis, the total-polyethylene and the metal-backed was made. The nature of the stresses generated in the uncemented prosthesis is mostly compressive. During the initial phase of humeral abduction (30 – 90 degrees) high Von Mises stresses (20 – 107 MPa) are generated in the superior side of the metal-backing. Stresses are reduced (100 – 15 MPa) during the later half of abduction (120 – 180 degree) when the load moves from superior to central location of the glenoid cavity. A thicker metal-backing has been used to reduce excessive stresses in the polyethylene and to achieve better fixation with cement or bone. Addition of metal-backing increases the stiffness of the prosthesis thereby resulting in reduction of stresses in the polyethylene cup by 17 – 20% as compared to the cemented designs. This may imply less polyethylene wear. However, a stiffer configuration also means that the underlying cement (if present) is subject to higher tensile stresses. In case of uncemented design, the stresses in the underlying bone is relatively low (0.05 – 2 MPa) as compared to the natural glenoid (0.05 – 4 MPa). Stress-shielding can be observed in the trabecular bone underlying the prosthesis, which might lead to adverse bone remodelling and possible risk of failure. Using Hoffman failure criterion, it has been evaluated that the implant-bone interface is secure against interface failure at moderate loads, although the implant-bone (metal-bone) interface around the superior edge of the prosthesis is subject to high stresses (normal: 11.85 MPa, shear: 6.67 MPa) as compared to the cemented prosthesis. The subchondral bone, with a higher density as compared to the trabecular bone, offers higher interface bond strength. Whereas, in case of cemented designs the cement-bone interface, appears more likely to fail either at locations adjacent to the keel or at locations around the superior edge of the prosthesis. The peak polyethylene-metal interface is also subject to high stresses (normal: 4.76 MPa, shear: 1.62 MPa). These results indicate probable separation of the prosthesis from the bone or separation of the polyethylene cup from the metal-backing at higher loads. In view of the high implant-bone interface stresses, it seems that reducing the thickness of metal-backing and ensuring a high interface bond strength with tissue-ingrowth surfaces is required to improve the uncemented prosthesis.

Keywords: Uncemented glenoid prosthesis, submodelling, finite element analysis, computed tomography.

7.1 Introduction

The use of polymethylmethacrylate (PMMA) for fixation of glenoid prosthesis has been one of the major problems in the Total Shoulder Arthroplasty (TSA). The use of PMMA has been reported to be less reliable (cracking and eventual loosening), particularly in the presence of instability or massive tear of rotator cuff (Barrett et al., 1987; Franklin et al., 1988; Weiss et al., 1990). In some reports, both the total-polyethylene and the metal-backed polyethylene components, implanted with cement, demonstrated radiographic lucent lines at the cement-bone interface (Amstutz et al., 1988; Cofield and Daly, 1992). Even with modern cementing techniques, the progression of radiolucent lines was observed in at least 20 percent cases and was associated with pain and decreased functional capabilities (Cofield, 1983; Cofield, 1984; Norris and Lachiewicz, 1996).

Early reports of fixation of glenoid tissue-ingrowth components without cement noted a low prevalence of loosening (McElwain et al., 1987; Weiss et al., 1990; Cofield, 1994). Wallace et al. (1999) retrospectively reviewed clinically evident loosening of glenoid components inserted with cement and without cement in 58 shoulders (32 with cement and 26 without cement), performed by the same surgeon between four and seven years after operation. The glenoid prosthesis, a Cofield metal-backed glenoid component, was inserted without cement in patients with a mean follow-up period (FUP) of 4.7 years (range 4 – 5.4 years), postoperatively. They observed radiolucent lines in thirteen (41%) of the 32 arthroplasties performed with cement as compared to six (22%) of the 26 arthroplasties performed without cement. Separation of the polyethylene cup from the metal-backing was reported in two cases (Wallace et al., 1999). The proportion of implants classified as probably loose was approximately three times greater in the group in which cement had been used (Wallace et al., 1999). The results of their study indicate that, despite higher rate of early complications, fixation of glenoid component without cement provides an outcome that is comparable to fixation with cement in terms of relief of pain, subjective functional capacity, range of motion, and effect on general health.

Cofield (1994), in his review on uncemented TSA remarked that, despite number of complications the results of uncemented glenoid prosthesis were very similar to those reported for TSA using a cemented glenoid component. One of the several features, used in the merit analysis of the TSA, was the "striking" lack of radiographic changes at the implant-bone interface (Cofield, 1994). Radiolucent changes were displayed in only six (3%) out of 180 operations; and one component had shifted in position. This seems dramatically less than the frequency of radiographic changes seen around cemented glenoid components interface (Cofield, 1994). The special feature of glenoid component inserted without cement was the apparent slightly increased frequency of high-density polyethylene that can be associated with displacement of the polyethylene from the metal tray (Cofield, 1994). This occurred in 3 out of 180 shoulders and was located without exception on the posterior side of the glenoid component. In two additional shoulders, the polyethylene insert displaced from the metal tray at 4 and 21 months, without significant wear being present (Cofield, 1994). A summary of the radiographic and clinical investigations with uncemented glenoid prosthesis is presented in Table 1.

The clinical and radiographic results of cemented glenoid component has been threatened by high incidence of progressive radiolucent lines at the cement-bone interface, in particular the prosthesis keel portion (Berms, 1993; Torchia et al., 1997). These radiographic changes were present in 33 – 50% or more of the patients (Berms, 1993; Torchia et al., 1997). These observations lead to the conclusion that other designs of glenoid components must be pursued or alternative methods of fixation must be considered (Cofield, 1994).

Table 1. Investigations with uncemented glenoid prosthesis (upgraded from Cofield, 1994).

Author, year	Design	Fixation	No. of shoulders	Number of defective glenoid component	
				Radio-lucency	*Loosen-ing*
Bayley and Kessel, 1982	Kessel	Pressfit	33	0	0
McElwain and English, 1987	English-Macnab	Tissue-ingrowth	13	1	1
Copeland, 1990		Pressfit	20	0	0
Roper et al., 1990	Roper-Day	Pressfit	13	1	1
Weiss et al., 1990	English-Macnab	Tissue-ingrowth	9	1	0
Brostrom et al., 1992	Kessel	Pressfit	23	13	2
Cofield and Daly, 1992	Cofield	Tissue-ingrowth	31	3	1
Cofield, 1994	Cofield	Tissue-ingrowth	180	6	4
Wallace et al., 1999	Cofield	Tissue-ingrowth	26	6	2

The problem of progressive radiographic changes, the long term efficacy of cement, and the need for revision of cemented glenoid components have prompted the development of implants with porous surfaces that would induce bone-ingrowth to achieve secure fixation of implant and bone. Insertion without cement, of a glenoid component with tissue-ingrowth capability is not entirely a new concept. But the technique is yet to gain wide acceptance. Clinical and radiographic observations, though a few, have given encouraging results regarding testing of uncemented glenoid components. But, in order to reveal the biomechanical factors involved in the design of the prosthesis and to develop a better understanding of the load transfer and probable failure mechanisms, a three-dimensional (3-D) Finite Element (FE) analysis of the glenoid component is necessary. To our knowledge, Orr et al. (1988) was the only one who reported a two-dimensional (2-D) stress analysis of several uncemented glenoid component designs. The results of the 2-D analysis can suggest certain qualitative trends in stress distribution. But, the 2-D simplification of the 3-D glenoid structure can lead to a loss of the structure's mechanical integrity (Stone et al., 1999). This loss of the circumferential cortical structure along with the out-of-plane forces will have crucial impact on the results. Therefore, a realistic 3-D FE model of the glenoid component is required for biomechanical evaluations on uncemented glenoid component.

Design variations in uncemented glenoid prosthesis are few, most of them consists of, in principle, a polyethylene cup with a metal-backing with tissue-ingrowth capability. Interestingly, one of the earliest forms of TSA possessed tissue-ingrowth at the glenoid and humeral component (McElwain and English, 1987). The Kessel prosthesis with pressfit design, the Cofield metal-backed

design with tissue-ingrowth capability, and the Bio-modular porous coated glenoid components (Biomet Inc, Warsaw, Indiana) were developed and continued to be used. Only selected patients, having good bone stock were recommended for use of these porous coated uncemented prostheses. In our study, we used the experimental design prosthesis of ESKA Implants GmbH & Co., Germany, in order to develop a 3-D FE model of glenoid and implant. The prosthesis consists of a 5 mm thick polyethylene cup and a circular metal backing (cobalt-chromium-molybdenum) of 5mm thickness. A centrally placed hollow cylindrical keel (or post) together with two fins (plates) attached on it in the superior and inferior side, are integrated with the circular metal backing. A schematic diagram of the configuration and a 3-D FE model of the prosthesis are illustrated in Figures 1a and 1b, respectively.

The purpose of this study is to investigate the biomechanical aspects of uncemented glenoid component. The study is intended towards understanding the glenoid load transfer mechanism and to observe whether the clinical observations regarding failure can be explained with a better understanding of the stress analysis. A comparison of the uncemented glenoid design and two basic models of cemented prosthesis, total-polyethylene and metal-backed has also been studied.

7.2 Materials and Methods

7.2.1 Finite element model of uncemented glenoid prosthesis

A 3-D FE model of glenoid (right scapula) was developed using Computed Tomography (CT) scan data. The outer geometry of the bone was reconstructed by connecting cubic B-splines through keypoints that were generated from CT-scan data. Elements were generated within a volume of bone that was formed based on outer boundaries of closed contours of CT-scan data. The hemispherical uncemented prosthesis was positioned in the glenoid and elements were generated in different materials constituting the prosthesis. As compared to the cemented glenoid components, a part of the subchondral bone was retained and used in the bone-prosthesis configuration, in order to increase the structural stiffness of the glenoid, as a whole. In this study, the prosthesis was assumed to be fully bonded to the bone and at the polyethylene-metal interface.

A combination of shell and solid elements, similar to Chapter 6, was used to build a realistic bone model. The inner volume of cancellous bone and the prosthesis were filled with 3-D ten-node tetrahedral solid elements. The element sizes, varying between 2 – 3 mm or less on a side, were specified and mesh generation was obtained utilising ANSYS FE software. The hard cortical outer shell was modelled as eight-node quadrilateral 2-layered shell elements, with 0.5mm thickness of each layer (Chapter 3). The first layer, embedded in the solid element zone, was to keep the reference plane along the interface outer cortical shell and the underlying compact bone whereas the second layer, represented the outer cortex. The solid elements were overlaid with shell elements so that they shared common nodes. A FE model of the glenoid with prosthesis is shown in Figure 2.

Bone was assumed to be a linear isotropic material in this study. The elastic moduli of bone elements were extracted from CT-scan image (Chapters 2 and 3). The elastic modulus of the topmost (outermost) cortical shell layer of 0.5 mm thickness, were taken as 17500 MPa (Chapter 2). The lower shell layer of 0.5 mm thickness, embedded (or overlapping) in the solid element zone was allocated a very low value, 0.0001 MPa, so as to minimise its contribution in the FE analysis. The Poisson's ratio of the trabecular and cortical bone is assumed to be 0.3 (Dalstra et al., 1995). The mechanical properties of the uncemented glenoid component are listed in Table 2.
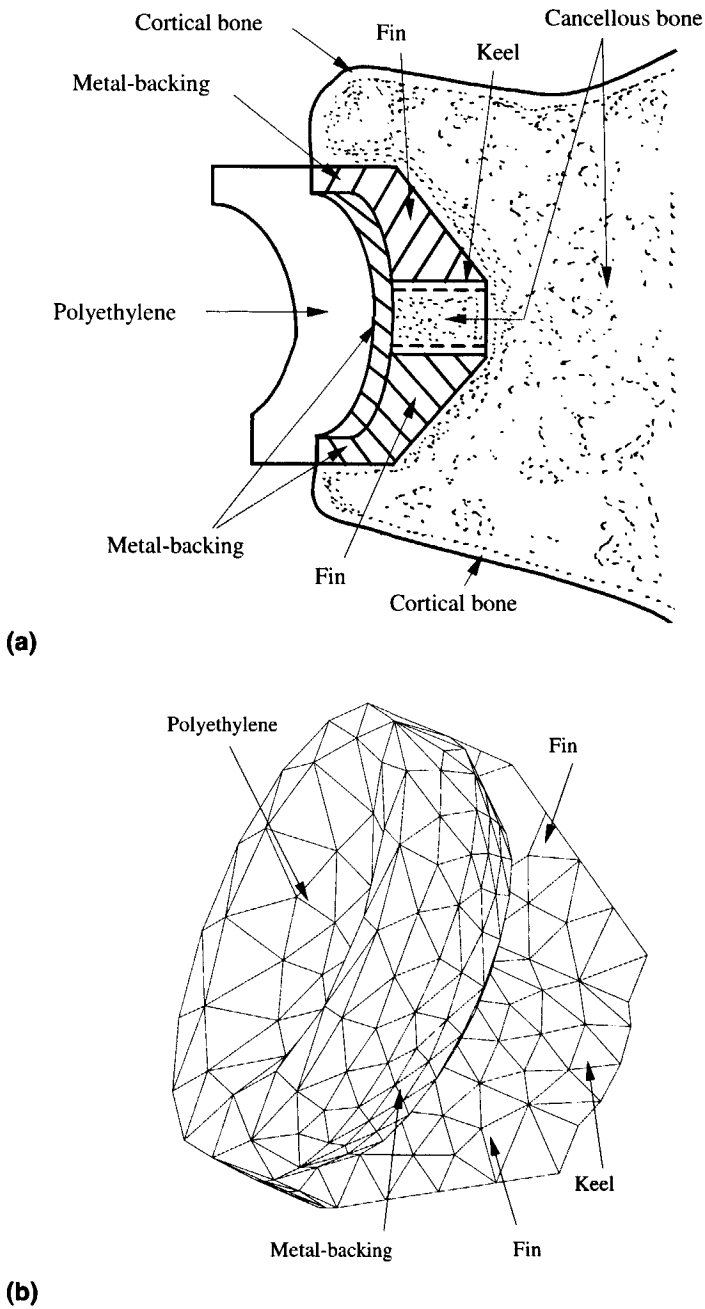
(a)

(b)

Figure 1. The uncemented glenoid prosthesis (experimental design of ESKA Implants GmbH & Co., Germany); (a) a schematic diagram of the implanted glenoid cavity, (b) a frontal view of the FE model of the uncemented prosthesis.

Table 2. Mechanical properties of implant materials.

Material	Elastic Modulus (MPa)	Poisson's ratio
Ultra High Molecular Weight Polyethylene (UHMWPE)	1174	0.40
Cobalt-chromium-molybdenum alloy	234500	0.30

7.2.2 Submodelling technique and applied loading conditions

The overall model of the natural scapula, which served as the reference solution included the effect of all muscles, ligaments and joint reaction forces during humeral abduction. The elastic behaviour of the overall model should be effectively imposed on the submodel with the prosthesis. The method of applying approximate boundary conditions, on a submodel of a glenoid prosthesis, based on an overall reference solution of the natural scapula has been discussed extensively in Chapter 6, Section (6.2.2). A brief outline is presented here.

A link between the submodel and the overall scapula model can be established by transferring the nodal displacements from the overall model at the cut-boundary to the submodel (Fig. 2). If the inclusion was small as compared to the dimensions of the entire body, then it can be assumed that sufficiently far from the inclusion the differences between the two solutions (displacements) become zero.
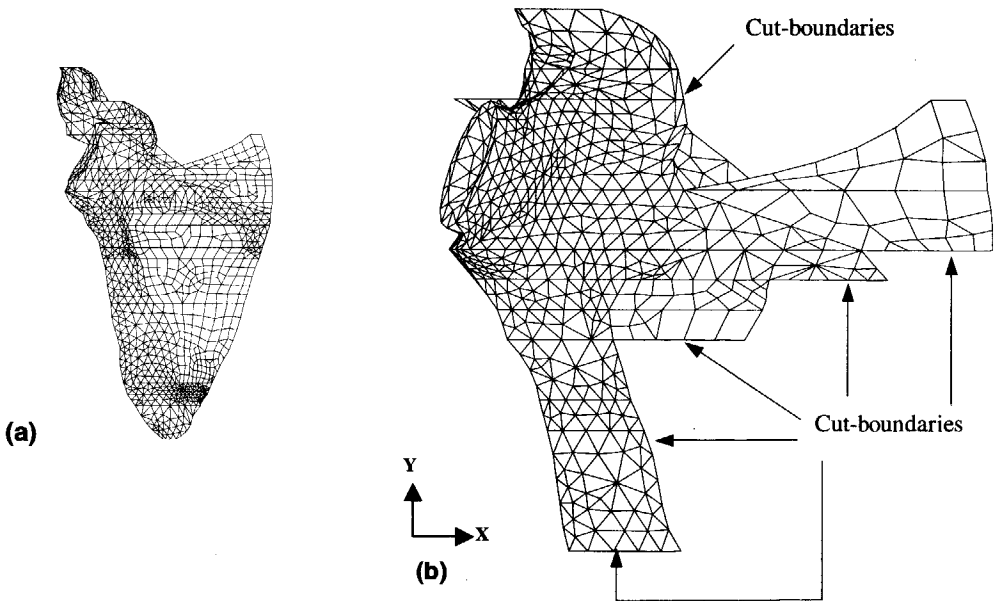
Figure 2. The proposed submodelling technique; (a) the overall natural scapula model without the prosthesis, and (b) the submodel with inclusion of the prosthesis.

Table 3. Dimensions of contact area and load distribution corresponding to load cases.
(* During 0-degree abduction the humeral component merely hangs from the tip of the glenoid component (inferior side). The reaction force and the contact dimensions are also small as compared to the other load cases. Therefore, the GH force is applied as a concentrated force for this load case.)

Load case	Abduction angle (in degree)	Total force (F) in N	Radius of contact circle (a) in mm.	Area of contact circle (A) in mm^2	Mean pressure (p_m) in N/mm^2
2	30	165.84	2.08	13.54	12.24
3	60	325.85	2.60	21.24	15.34
4	90	392.95	2.76	24.05	16.33
5	120	346.01	2.65	22.09	15.66
6	150	192.83	2.18	14.97	12.88
7	180	82.79	1.65	8.55	9.72

The location of the cut-boundary is of crucial importance and will have predominant influence on the results. The cut-boundary location should be sufficiently far away from the region of interest, i.e. the glenoid, so that the effect of inclusion of the prosthesis was damped out. Due to a change in the load application point, the effect might not damp out. However, the cut-boundaries were chosen at locations far away from the prosthesis, so that the localised change in the point of application of load had minimum effect on the stress distribution at these cut-boundaries. The procedure of choosing the cut-boundaries resulted in a large size of the submodel. The non-zero values of displacements at the nodes located along a cut-boundary, for each load step, were obtained from the results of the overall model (Chapter 5). These displacements were prescribed on the nodes located along the bottom (lateral border), the right (infraspinous and supraspinous fossa) and the posterior (scapular spine) cut-boundaries in the submodel with the prosthesis (Fig. 2b). In case of nodes belonging to solid elements only translational displacements were prescribed. Whereas, translational and rotational displacements were prescribed for nodes located along the shell-solid boundary. This technique will lead to results in the domain of the inclusion. The GlenoHumeral (GH) joint reaction force and the muscle forces acting on the closed boundaries of the coracoid process were used as the applied forces on the submodel.

The FE model of the uncemented glenoid prosthesis contained 11465 elements, 15024 nodes and a total number of 57534 active DOF. A frontal view of the model is presented in Figure 2b. The stress distributions at the cut-boundaries of the submodel were comparable to that of the overall model of the natural scapula, which serves as a validation for the sub-modelling technique. However, notable deviations in the stress distribution were observed in the vicinity of the prosthesis.

A static musculoskeletal model of the shoulder was used to calculate the loading conditions of the scapula (Van der Helm, 1994). The musculoskeletal model and the CT images were based on the same scapula. The dominant force acting on the glenoid is the GH- joint reaction force.

The point of application as well as magnitude and direction of this reaction force varies with the change in abduction angle of the arm. Berms (1993) observed that the resultant GH- joint reaction force moved from inferior to superior and then to the centre of the glenoid cavity, which has been termed as the "rocking horse" effect. The magnitude and direction of the force, corresponding to angular abduction of the arm, are presented in Table 3.

The GH joint reaction force was assumed to be distributed on the articulating surface of the glenoid component. Similar to Chapter 6, the contact area can be calculated according to the Hertz theory of elastic contact for non-conforming surfaces in contact (Hertz, 1882). Based on this theory, expressions were derived, which are useful in practical problems to calculate the radius (a) of the contact circle. The calculation was based on the principal radii of curvature ($R_1 = 25$ mm, $R_2 = 20$ mm) of surfaces in contact, the total load (F), and the elastic constants (E and μ) of the two bodies in contact (Section 6.2.2).

The load can be distributed on the contact area (A) as, (i) uniform pressure, or (ii) Hertz pressure. Ideally, the distribution of load should be parabolic in nature, based on the Hertz theory. However, the present FE mesh was considered to be unsuitable for implementation of the parabolic load distribution in the FE model to estimate contact stresses, realistically. Implementation of the parabolic pressure load required far too finer mesh size, which will further increase the size of existing large-size submodel. The solution of such a large size FE model, however, was hindered by software and hardware limitations. Moreover, the GH joint is a "non-weight-bearing" joint as compared the lower limbs (Mansat et al., 1998). A joint reaction force of about two to four times the body weight is generated at the hip or the knee during walking (Frankel and Nordin, 1980). Whereas, a GH-joint reaction force less than the body weight is generated during 90-degree abduction of the arm (Table 3). The effect of contact stresses and related polyethylene wear was therefore, less relevant in glenoid components as indicted by Cofield (1994). In order to apply approximate loading conditions, the distributed loads were normally taken into account using work equivalent loads so that the parabolic distribution was represented by an equivalent uniformly distributed pressure (p_m). The GH reaction force for each load case was totally distributed on the face of those elements that were geometrically equal to the contact area, following the calculations presented in Table 4. Based on this simplified load distribution, an average value of stresses in the polyethylene cup was obtained. However, higher stresses would be generated if a parabolic pressure distribution, with maximum pressure $p_o = 1.5\ p_m$, had been applied on the glenoid component.

7.2.3 General design considerations with relevance to failure scenarios

The interfaces of different materials are often the weakest links within the bone-prosthesis configuration, leading to debonding (interface disruption). The interface stresses are calculated at the interface nodes using the normal stress components σ_x, σ_y, σ_z and the three shearing stresses $\tau_{xy} = \tau_{yx}$, $\tau_{xz} = \tau_{zx}$, $\tau_{yz} = \tau_{zy}$. The normal stress (σ_n) and the shear stress (τ) can be calculated using these components of stresses at any nodal point and the unit normal vector (direction cosines) to any inclined plane through this point. This method ensures compatibility of the interface stresses.

In order to determine where along the cement-bone local debonding might occur, quantitatively, a multi-axial Hoffman's failure criterion (Hoffman, 1967) has been used. Weinans et al. (1993) incorporated this failure (debonding) criterion in a FE model simulating the process of implant-bone disruption.

At each interface nodal point, a Hoffman number (*FL*) can be determined from the normal and shear stresses, using

$$FL = \frac{1}{S_t S_c} \sigma_n^2 + \left(\frac{1}{S_t} - \frac{1}{S_c} \right) \sigma_n + \frac{1}{S_s^2} \tau^2 \qquad (7.1)$$

with S_t and S_c being the uniaxial interface tensile and compressive strengths, respectively, and S_s the interface shear strength (Huiskes and Van Rietbergen, 1995). The interface strength is related to the density of the bone and is assumed to be determined by the density (ρ) of the bone adjacent to the interface, according to

$$S_t = 14.5 \, \rho^{1.71}, \qquad S_c = 32.4 \, \rho^{1.85}, \qquad S_s = 21.6 \, \rho^{1.65} \qquad (7.2)$$

These relations between density and strength have been derived from Kaplan et al. (1985) and Stone et al. (1983), who determined the static strength of trabecular for a range of bone densities. The state of local interface stress can be substituted in Eq. (7.1) to obtain a value, termed as the Hoffman number (*FL*). The value of *FL* represents the chances of interface failure. For *FL* less than 1, no interface failure is expected; for *FL* greater than 1, failure is expected. This failure criterion can be described by an ellipsoid for 3-D, or an ellipse for 2-D cases. A combination of interface normal and shear values outside the ellipse provokes a failure of the bond.

7.3 Results

The emphasis of this study lies on evaluating the stress distributions in the uncemented prosthesis and the underlying bone. Stress distributions in the domain of the prosthesis must be interpreted very carefully, as we probably are dealing with singularities. The stresses generated are mostly compressive, which means that the prosthesis is pushed inside the glenoid cavity. Based on the numerical predictions, a comparison of stress distributions between uncemented and cemented designs has been presented to evaluate the differences in designs and to identify the key factors in the design of improved glenoid prosthesis.

7.3.1 Stresses in the uncemented prosthesis

The high stiffness of the thick (5 mm) metal backing, as compared to other materials (polyethylene, and bone) of the implant, is the obvious cause for making the implant more rigid. The variation in the stress distribution (Von Mises) in the metallic component due to the "rocking horse" effect of the applied GH-joint reaction force (Berms, 1993) is illustrated in Figure 3 (a – e), which corresponds to unloaded humeral abduction from 30- to 180- degree. During 30- to 90-degree humeral abduction the stresses, varying between 20 to 107 MPa, appear to be concentrated in the superior part, in and around the junction of the fin and the circular metal-backing (Figs 3a, 3b, 3c). However, when the point of application of force moves from superior to a more central position (120-degree abduction), these stresses (30 – 70 MPa) are reduced and appear to be more uniformly distributed. During higher abduction (150 degree) of the arm, the stresses varying between 30 to 100 MPa are concentrated in the inferior part, in and around the junction of the fin and the circular metal-backing, (Figs 3d, 3e). The peak stress decreases from 100 to 15 MPa with further increase in abduction from 150- to 180-degree.
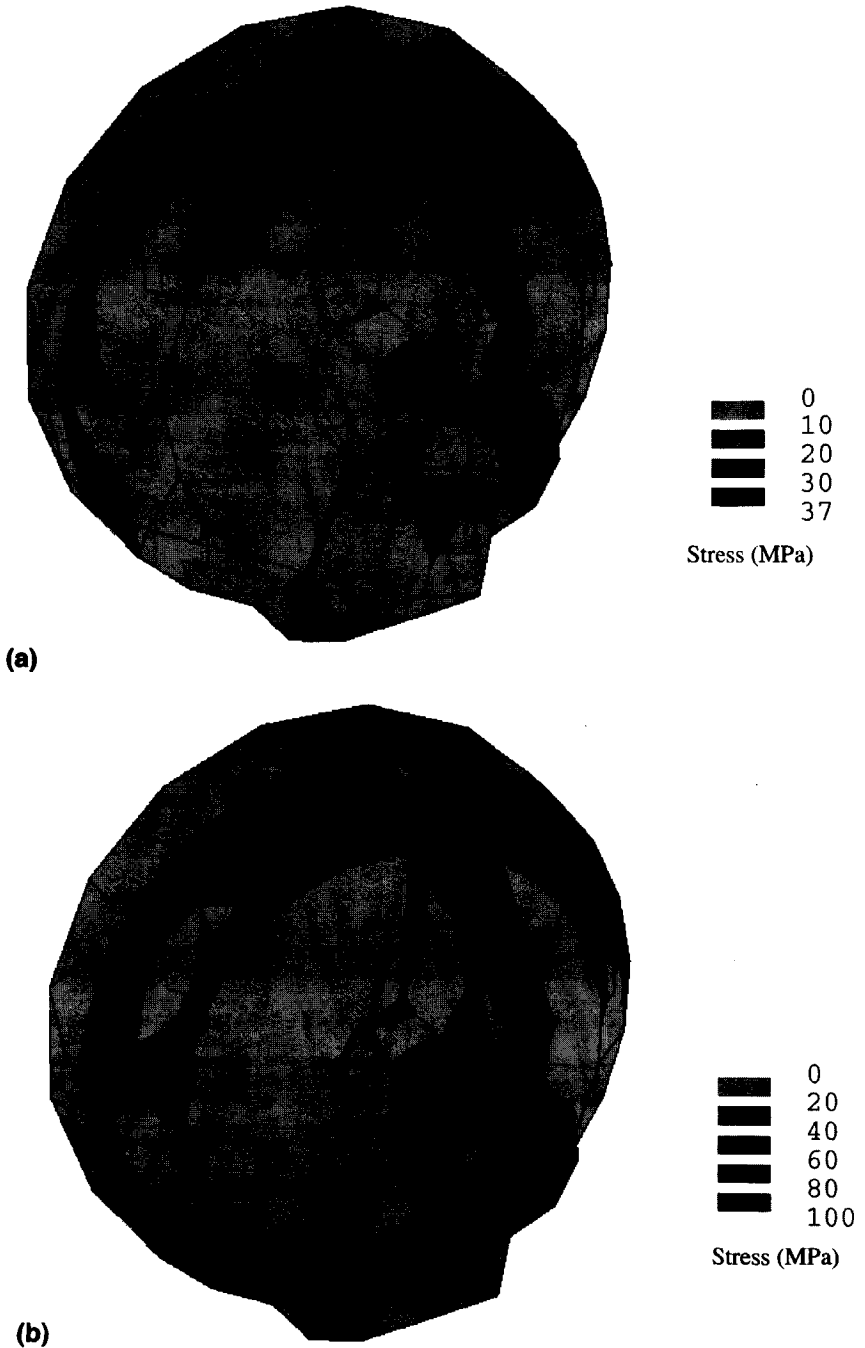
Figures 3a –b. Von Mises stress distribution (MPa) in the prosthesis; frontal view.
(a) 30-degree abduction; (b) 60-degree abduction.

Stress (MPa)

(c)

Stress (MPa)

(d)
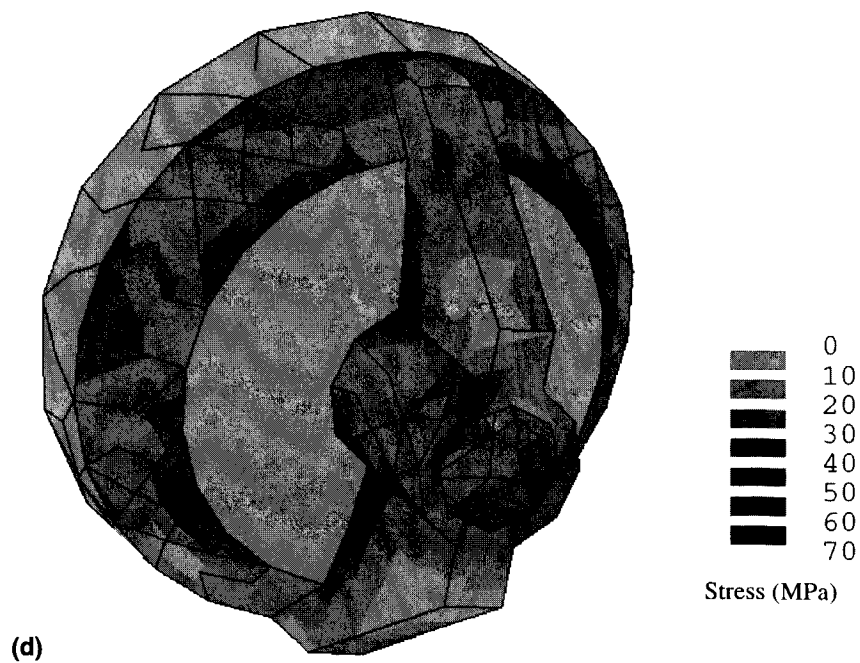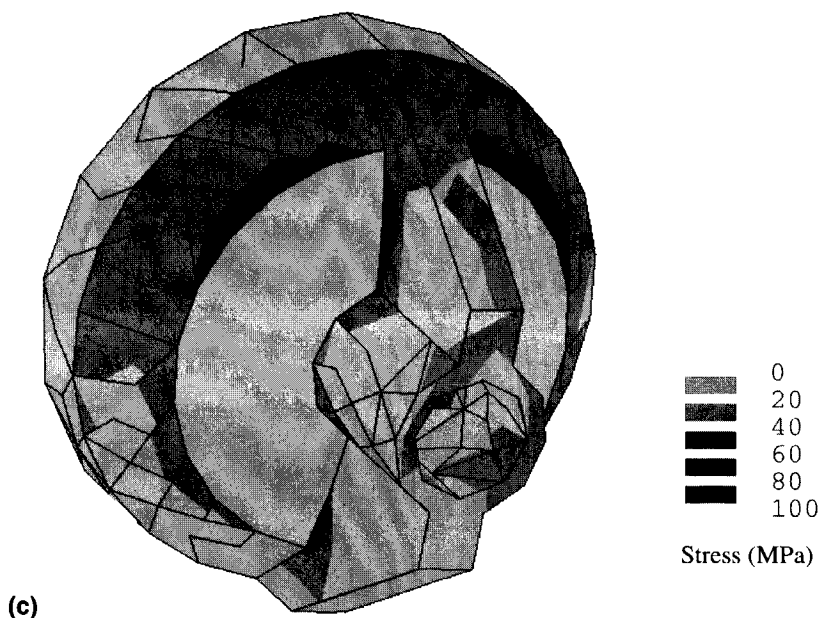
Figures 3c – d. Von Mises stress distribution (MPa) in the prosthesis; frontal view. (c) 90-degree abduction; (d) 120-degree abduction.

(e)

0
20
40
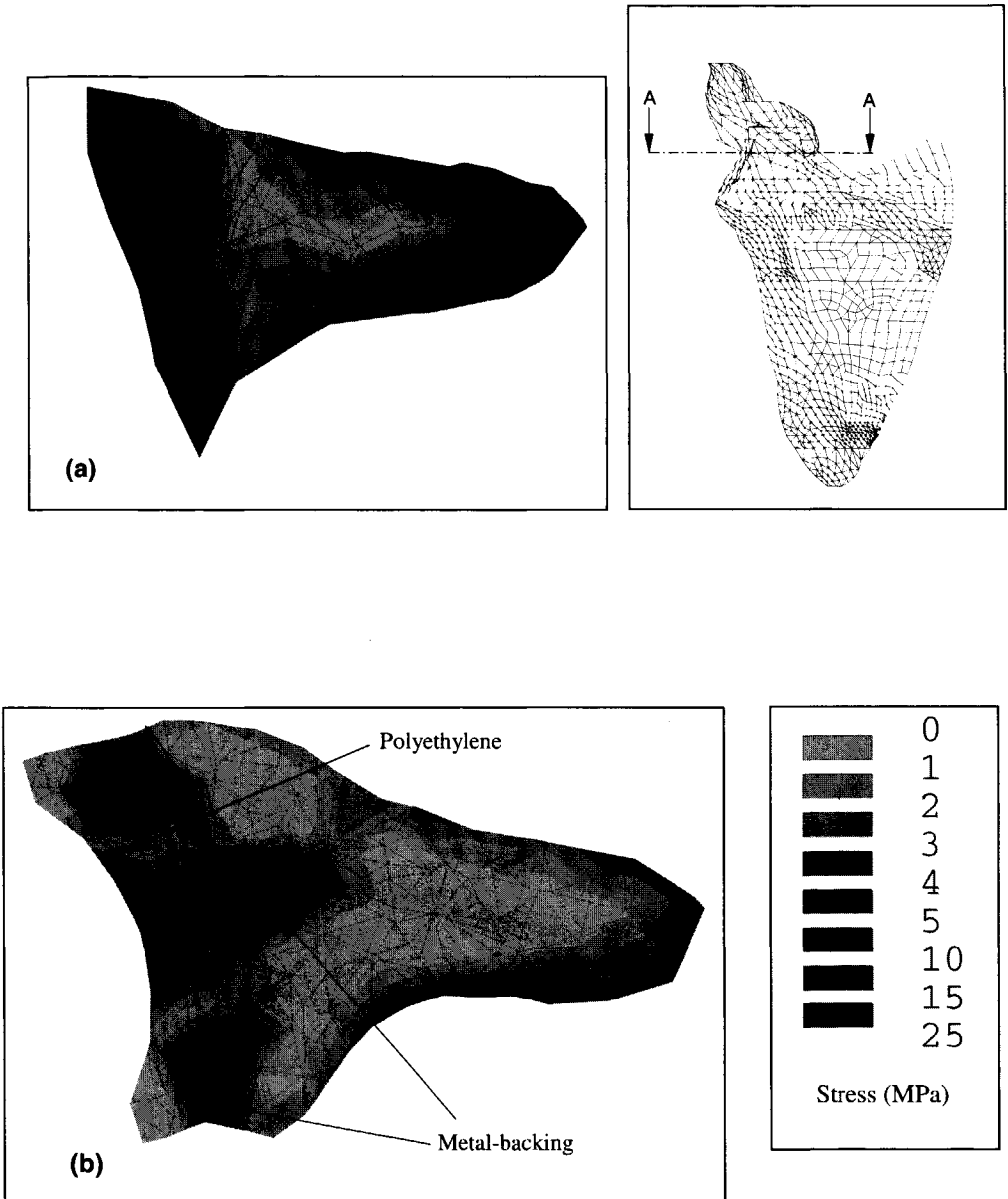60
80
100

Stress (MPa)

(f)

0
5
10
15
20

Stress (MPa)

Figures 3e – f. Von Mises stress distribution (MPa) in the prosthesis; frontal view; (e) 150-degree abduction; (f) 180-degree abduction.

Figure 4. A sectional (A-A) view of the Von-Mises stress (MPa) distribution for (a) natural scapula model, and (b) the metal backed uncemented glenoid prosthesis-bone model, during 90-degree abduction; ———— : implant-bone boundary.

The consequences of implantation on the stresses induced in the trabecular and cortical bone are important for the survival of the prosthesis. During humeral abduction, the Von Mises stresses (10 – 50 MPa) in the cortical bone are reduced as compared to that of the natural glenoid, due to the insertion of the prosthesis. The thick metal-backing adds rigidity to the implant and therefore, causes reduction in stresses in the polyethylene and the underlying bone. The combined effect of a thick (5 mm) metal-backing (Fig. 1) on a 5 mm thick polyethylene cup results in lower stresses (1 – 12 MPa) in the polyethylene cup. Hence, the risk of wear and wear-particle-debris formation is reduced. The metal backing in the glenoid component, consisting of the flange, the fins and the keel carries the bulk of the stresses (Von Mises), ranging between 20 and 50 MPa (Fig. 3c). The metal-backing leads to tensile stresses (10 to 40 MPa) in the metallic flange, indicating bending of the flange. In order to observe the stress distribution in the cancellous bone during 90-degree abduction, a sectional view through the glenoid is shown in Figure 4, as a representative case. A lateral view of stress distribution in the underlying bone is also presented in Figure 5. These results indicate that the stresses in the underlying trabecular bone are relatively low (0.05 to 2 MPa) as compared to the natural glenoid without prosthesis (0.05 to 4 MPa), as indicated in Figures 4 and 5. Additionally, it can be observed that the metal-backing results in stress transfer to the cortical bone, leaving the underlying trabecular bone at a relatively low stress level.

7.3.2 Interface stress assessment

The interfaces are often the mechanically weakest zones in a prosthesis-bone configuration. The stresses in the immediate vicinity of the prosthesis-bone configuration are of crucial importance when evaluating the design of the implant. The Hoffman failure criterion was used to evaluate the probability of prosthesis-bone interface failure (debonding).
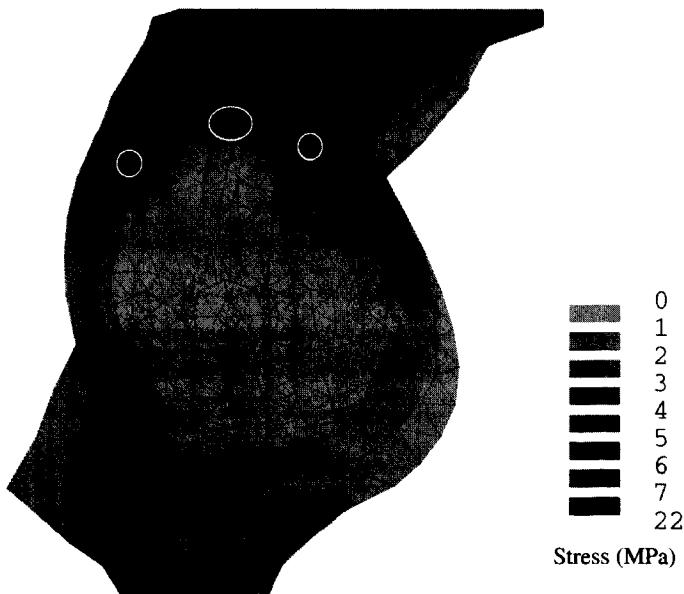
Figures 5. Von Mises stress distribution (MPa) in the bone during 90-degree abduction, in the vicinity of the prosthesis; a lateral view.
O : Location of high interface stress, indicating probable debonding.

It appears that the metal-bone interface, at superior edge of the prosthesis, is subject to high normal (σ_n) and shear (τ) stresses ($\sigma_n = 11.85$ MPa, $\tau = 6.67$ MPa). Whereas, this interface in the glenoid central region (adjacent to the fin), is subject to lower stresses ($\sigma_n = 1.73$ MPa, $\tau = 1.61$ MPa).

The metal-polyethylene interface is also subject to high normal stress (4.76 MPa), but low shear stress (1.62 MPa). Obviously, the high stresses induced at the prosthesis-bone interface are likely to cause mechanical failure, but does not necessarily indicate a failure or debonding. The survival of the prosthesis will largely depend on the strength of interface layers, the quality of underlying bone and the fixation technique.

A part of the subchondral bone has been retained in case of uncemented glenoid components as compared to the cemented implants, where it is replaced by cement. The density of the bone elements around the superior edge of the prosthesis, adjacent to the interface of peak stress, varies between $1 - 1.2$ g cm^{-3}. Therefore, these bone elements offer higher strength at the interface as compared to cancellous bone elements, with lower density range between $0.35 - 0.5$ g cm^{-3}, located in the glenoid posterior and central regions (adjacent to flange, fin and keel).

Similar regional density distribution was reported by Batte et al. (1996), who conducted an indentation study on five normal cadaveric glenoids. They found the superior regions to be the strongest with anterior-posterior trends varying at three different depths. Müller-Gerbl et al. (1992) found a greater glenoid subchondral density anteriorly and posteriorly in young people whereas the greatest density was central in elderly people. Following these data, we obtain a range of interface strength data (using Eq. 7.2) varying between $S_t = 14.50$ MPa, $S_c = 32.40$ MPa, $S_s = 21.60$ MPa for $\rho = 1.0$ g cm^{-3} (glenoid superior) and $S_t = 2.408$ MPa, $S_c = 4.646$ MPa, $S_s = 3.821$ MPa for $\rho = 0.35$ g cm^{-3} (glenoid central). On the one hand, using the higher strength data for a peak implant-bone interface stress ($\sigma_n = 11.85$ MPa, $\tau = 6.67$ MPa), around the superior edge of the implant, the maximal Hoffman number (FL) is calculated as 0.84. On the other hand, using the lower strength data in the glenoid central region and a multi-axial cement-bone interface stress ($\sigma_n = 1.73$ MPa, $\tau = 1.61$ MPa), the FL is calculated as 0.79. Considering an interface strength of $S_t = 4.43$ MPa, $S_c = 8.98$ MPa, $S_s = 6.88$ MPa for $\rho = 0.5$ g cm^{-3} in the glenoid posterior region and a peak implant-bone stress condition ($\sigma_n = 0.15$ MPa, $\tau = 2.37$ MPa), the FL is calculated as 0.14. These results indicate that the implant-bone interface is secure against interface failure, during moderate loading conditions.

7.3.3 Uncemented versus cemented glenoid prosthesis

The stress distribution in different components of the cemented and the uncemented glenoid prosthesis and the consequences of implantation on the underlying bone strongly depends on whether the implants are metal-backed or not. A summary of the maximum values of various stress components is presented in Table 4. The metal-backing is a material of high stiffness as compared to other materials (bone and cement) in the configuration and therefore, offers the reinforcement function to the polyethylene cup. This leads to reduction in the deformation of the cup and the stresses within it. The peak stresses in the polyethylene cup of the uncemented metal-backed design are reduced in the range of $17 - 20\%$ as compared to that of the cemented metal-backed and the total polyethylene designs. Although our comparison is based on different designs of metal-backing, for the uncemented and the cemented implants, it can still be observed that stresses in the polyethylene cup of the relatively thinner metal-backed design are also reduced when cement is used (8%), but these reductions are less as compared to the thicker metal-backed non-cemented cup (20%).

Table 4. A comparison of the maximum values of stress components (in MPa) in the PolyEthylene (PE), cement mantle and at various material interfaces in the uncemented (metal-backed PE) and the cemented prostheses (total PE and metal-backed PE).

Stress components (MPa)	Uncemented	Cemented	
	Metal-backed PE	Metal-backed PE	Total PE
Von Mises stress in PE cup	11.92	14.03	15.10
Normal stress, cement (ten.)	-	11.51	9.98
Normal stress, cement (comp.)	-	-10.15	-9.37
Von Mises stress in cement	-	9.80	8.31
Normal stress, implant-cement (ten.)	-	5.92	2.58
Shear stress, implant-cement	-	1.22	1.33
Normal stress, implant-bone (ten.)	11.85	2.86	2.51
Shear stress, implant-bone	6.67	3.55	3.41

The stresses evoked at the interfaces of different materials are of vital importance when comparing the design of prostheses. At the implant-bone interface, cemented designs generate considerably lower stresses (normal and shear) as compared to the uncemented designs. Between the two cemented designs, peak normal (2.51 MPa) and shear (3.41 MPa) stresses at the implant-bone interface are observed to be higher than the implant-cement interface stresses (σ_n = 2.58 MPa, τ = 1.33 MPa) for the non-backed designs. Whereas, the metal-backing results in higher implant-cement interface stresses (σ_n = 5.92 MPa, τ = 1.22 MPa). The cement-bone interface is also subject to higher stresses (σ_n = 2.86 MPa, τ = 3.55 MPa). Results indicate that for the total polyethylene design, the cement-bone interface adjacent to the tip of the keel seems more likely to fail *(FL = 1.86)* as compared to the superior edge of the prosthesis *(FL = 0.19)*. In case of metal-backed design, also the interface adjacent to the tip of the keel is more likely to fail *(FL = 2.16)* as compared to the superior edge *(FL = 0.68)* of the prosthesis. The metal-cement interface stresses are also high, which may induce failure at higher loads. It appears that the cement-bone interface for the metal backed design is more vulnerable to interface failure (debonding). In contrast, the implant-bone interface for uncemented design appears less probable to fail than the cemented design *(FL = 0.84 vs. Fl = 2.16)*, although the stresses are significantly higher than that in the cemented designs. Therefore, the actual failure of an interface depends on the bone density and the bone strength of the interface bond, which is higher in the superior side of the glenoid than the central region.

The uncemented design results in higher transfer of stresses to the cortical bone. The stresses in underlying cancellous bone are lower (0.05 – 2 MPa) as compared to the cemented designs (0.05 – 3 MPa). On the one hand, using cement in combination with a thin metal-backing results in higher tensile stresses (11.5 MPa) in the cement mantle, as well as higher cement-bone (σ_n = 2.86 MPa, τ = 3.55 MPa) and prosthesis-cement (σ_n = 5.92 MPa, τ = 1.22 MPa) interface stresses. On the other

hand, using a thicker metal-backing for uncemented prosthesis generates higher implant-bone interface stresses (σ_n = 11.85 MPa, τ = 6.67 MPa).

7.4 Discussion

This study is aimed at biomechanical investigations, using FE technique, regarding the possibilities of uncemented prosthesis in the TSA. Using a detailed 3-D FE model of an implanted glenoid, generated from CT-scan data and using realistic GH- joint reaction force, it might be possible to understand the glenoid load transfer mechanism and to observe whether the clinical observations regarding failure can be explained with a stress analysis. However, the method employed in this study has a number of limitations. Only one particular design of uncemented prosthesis was considered. Different designs are known to generate different interface stress patterns (Huiskes, 1990), consequently affecting the evolution of the interface failure (debonding) process. The prosthesis is assumed to be fully bonded to the underlying bone. Whereas, in reality, there might be debonding or relative motions at the interfaces of various materials in due course of time. The present mesh was not fine enough to simulate the parabolic pressure distribution and was therefore, unsuitable for an accurate estimation of contact stresses in the polyethylene cup. Bone geometry and density distribution were based on CT-scan data of one 'representative' scapula. The mechanical properties of bone were assumed to be linear, isotropic and to remain constant with time. Whereas, in reality, bone is anisotropic and is subject to continuous remodelling. In our study, the open-cell trabecular bone and compact bone structures were both modelled as solid elements and assumed to have uniform density and modulus of elasticity throughout the element. These assumptions in macroscopic modelling approach would therefore lead to stresses that will differ from the microscopically calculated stresses in the trabeculae (Van Rietbergen et al., 1995).
These assumptions are obviously a schematic representation of reality. Stress distributions should be interpreted meticulously, as we probably are dealing with singularities. Therefore, the study is conceptual in nature and the results, which predict certain qualitative trends, should be interpreted within these limitations.

The metal-backing has a crucial influence in the various design concepts evaluated in this study. The use of metal-backing offers rigidity to the component. The stresses in the polyethylene cup strongly depend on the stiffness of the prosthesis. Both for the cemented and the uncemented implants a qualitative comparison of the stresses generated in the polyethylene can be obtained. It appears that the metal-backing results in stress reductions in the polyethylene. But these reductions depend on the thickness and the shape of the metal-backing. On the one hand, the stresses in the polyethylene cup for the cemented total-polyethylene component is 20 percent higher than the uncemented metal-backed one, which may increase the risk of polyethylene wear. On the other, a thicker (5 mm) metal-backing, as used in case of uncemented design, however, results in higher metal-bone (σ_n = 11.85 MPa, τ = 6.67 MPa) and polyethylene-metal (σ_n = 4.76 MPa, τ = 1.62 MPa) interface stresses. Obviously, these high interface stresses indicate possibility of interface disruption; separation of the prosthesis from bone or separation of the polyethylene cup from metal-backing. However, this does not necessarily mean that the interface failure (debonding) will occur.

The failure of an interface actually depends on its strength in shear and tension, which is obviously higher for metal-bone and metal-cement connection than polyethylene-bone or polyethylene-cement connection (Fukuda et al., 1988). A large variety of fixation techniques are used for uncemented implants (e.g. hydroxyapatite-coated, porous-coated, threaded cups, fixation with pegs and screws). Although the Hoffman failure criterion was used in this study to evaluate the probability of prosthesis-bone interface failure, in true sense it cannot be designated as probability

since its value cannot be larger than unity. It works reasonably well for trabecular bone (Stone et al., 1983; Kaplan et al., 1985), but has not been tested for bones between hydroxyapatite and bone (Huiskes and van Rietbergen, 1995). However, it does account for the multi-axial stress condition in failure initiation and also the gradually changing interface bone density and strength. Huiskes and van Rietbergen, 1995, remarked that the Hoffman number could only provide for qualitative estimates on a relative basis. If the interface fails, it will be attributable to fatigue, not static load. Additionally, the bond between hydroxyapatite and metal may be the weak link, rather than the bond between hydroxyapatite and bone.

The results on interface stresses indicate that the implant-bone boundary is secure against failure, at a moderate load. At the implant-bone interface, the uncemented design generates considerably higher stresses (normal and shear) as compared to the cemented design. However, the cement-bone interface *(FL = 2.16 and 1.86* for total PE and metal-backed PE, respectively) appears more likely to fail as compared to the implant-bone interface for uncemented design appears less probable to fail *(FL = 0.84),* although the stresses are substantially higher in case of the uncemented design. This is mainly due to the presence of a part of the subchondral bone in the superior region. The subchondral bone with higher density offers higher interface bond strength as compared to the trabecular bone in case of cemented designs. Between the two variations in the design of cemented glenoid prosthesis, the presence of cement has least influence on the stress levels in the polyethylene. The Young's modulus of cement (2.2 GPa) is approximately equal to compact bone (1.8 - 2.0 GPa) or in some cases subchondral bone (Dalstra et al., 1993). A thicker layer of subchondral bone can be considered to be equivalent to a cement mantle. The choice of fixation method, with or without cement, depends not only on the biomechanical factors but also on the quantity and quality of bone as well as the effective preparation of the subchondral bone. The use of uncemented prosthesis may lead to good results in many cases of osteoarthritis and post-traumatic arthritis. The use of cement, however, might be preferable in cases of rheumatoid arthritis, where bone deficiency and poor bone quality could have consequential influence in the arthroplasty.

A stiffer cup, with a thick metal-backing, will generate high stresses within it and will tend to transfer the stresses to the cortical bone and partially to the underlying cement or bone as the case may be. In order to compare the TSA induced changes in stress distribution, accurately, the overall FE model of a natural scapula and a submodel with prosthesis should have exactly similar mesh. The procedure would ensure similarity in location and material properties of bone elements of natural and implanted models and would eventually lead to comparison of stresses, quantitatively and accurately. Although a finer mesh has been used for the bone-prosthesis submodel as compared to whole scapula model, the changes in the stress distribution can be observed at locations in the domain of inclusion of the prosthesis. The differences in stress distribution as indicated in Figure 4, between the glenoid with or without the component can be regarded as a 'representative' case. It appears that the Von Mises stress distribution in the cancellous bone is low for the uncemented design, varying between 0.5 – 2 MPa as compared to higher stresses (0.5 – 4 MPa) generated in cemented designs. Higher stresses are generated in the metal and particularly at the metal-polyethylene and metal-bone interfaces. Obviously, these higher stresses are more likely to cause mechanical failure at the material interfaces. Consequently, the bone receives an insufficient amount of stress or strain, which hinders the bone remodelling activity. The phenomenon is commonly known as "stress shielding", which may reduce the bone mineral content significantly, eventually leading to local resorption of the bone near the implant. Although strong conclusions cannot be drawn based on one representative case, yet the indications of bone resorption are apparent. This might lead to focal osteolysis, which has been observed adjacent to the collar of the screw and the central column of the tissue-ingrowth glenoid components inserted without cement (Cofield, 1994;

Wallace et al., 1999). Stress analysis of an acetabular prosthesis (Dalstra, 1993) indicated similar results, which can be related to clinical investigations indicating extensive osteolysis behind the cup for acetabular prosthesis in combination with metal backing while the cement-bone interface remained intact (Pierson and Harris, 1993).

The presence of metal-backing in the glenoid component generates high stresses within it and also at its interfaces, because it is highly stiff material as compared to the polyethylene and the cement. This result is well supported by similar behaviour not only in glenoid prostheses (Orr et al., 1988; Friedman et al., 1992; Lacroix and Prendergast, 1997, Stone et al., 1999) but also in cemented acetabular prosthesis (Dalstra et al., 1993) and in cemented femoral total hip components (Weinans et al., 1991), where debonding occurs mainly at the prosthesis-cement interface (Harrigan and Harris, 1991). The high stresses generated in the metal facilitate reduction of the stresses in the underlying trabecular bone, causing a change in the mechanical environment inside the glenoid. This would eventually cause adverse bone remodelling. The actual effect of the bone remodelling in this sensitive area, whether apposition (addition) or resorption (removal), requires further investigation. On the one hand, the stress transfer to the cortical bone is improved by the addition of metal backing. On the other, a metal keel, if securely bonded to the surrounding bone causes stress shielding in the cancellous bone under the component (Orr et al., 1988). A hollow cylindrical central keel, as used in our model, is beneficial as compared to a solid keel from surgical and anatomical viewpoints. It would be relatively easier for the surgeon to insert the rigid metal into the meagre volume of bone in the glenoid. The fins attached on either sides of the central keel and the circular metal-backing acts like stiffener plates in the configuration and add rigidity to the prosthesis in the superior-inferior direction against the rocking horse effect of the GH joint reaction force. In view of the high stress concentrations at the junction of the fins and circular metal-backing, revisions in the design of fins might lead to better stress distribution in the underlying trabecular bone. A thicker polyethylene cup (7 mm), with a thinner circular metal-backing (3 mm) would result in lower peak stresses in the polyethylene and reduction of the weight of the prosthesis.

The results of this study are well supported by clinical and radiographic studies with this type of glenoid component (Cofield, 1994; Wallace et al., 1999). These studies report that the nature of complications is somewhat different from those reported for cemented version. The glenoid component inserted without cement, therefore, appears to be a reasonable alternative to fixation with cement. It should be, however, be understood that the problems associated with the prothesis-bone interface and their long term implications are yet to be solved and new problems such as, separation of polyethylene component from the metal tray and the occurrence of accelerated polyethylene wear, even though it is uncommon, have been introduced.

7.5 Conclusions

(1) High stresses are evoked during humeral abduction in the superior and inferior locations of the prosthesis, in and around the junction of the fin and the circular metal-backing.
(2) Stresses in the polyethylene component are reduced for uncemented prosthesis as compared to the cemented ones, which may imply less polyethylene wear. Increasing the stiffness of the cup, by adding metal-backing decreases the stresses in the polyethylene liner.
(3) The implant-bone interface, for the uncemented prosthesis is subject to higher stresses (normal and shear) as compared to the cemented prostheses. However, the implant-bone interface appears less probable to fail at moderate loads, since higher interface bond strength is offered by higher bone density.

(4) The cancellous bone, underlying the uncemented prosthesis is subject to lower stresses as compared to cemented glenoid components. This might eventually lead to adverse bone remodelling and local resorption behind the prosthesis.

(5) It seems that a high fixation strength at the implant-bone interface for primary stability is required in order to achieve better possibilities with the uncemented prosthesis. Once the initial fixation is secured at the implant-bone interface using tissue-ingrowth or porous coated surfaces and the quality of glenoid bone is not poor, it appears, that the uncemented prosthesis can offer better results as compared to the cemented components in long-term perspective.

Acknowledgement

References

Amstutz, H.C., Thomas, B.J., Kabo, M.J., Jinnah, R.H. and Dorey, F.J. (1988). The DANA total shoulder arthroplasty. J. Bone Joint Surg. 70A, 1174-1182.

Bayley, J.I.L., Kessel, L. (1982). The Kessel Total Shoulder Replacement. In: Bayley, I. and Kessel, L. (eds), Shoulder Surgery. 160-164. New York, Springer-Verlag,

Barrett, W.P., Franklin, J.L., Jackins, S.E., Wyss, C.R. and Matsen, F.A. (1987). Total shoulder arthroplasty. J Bone Joint Surg. 69-A (6), 865-872.

Batte, S.W.P., Cordy, M.E., Lee, T.Y., King, G.J.W., Johnson, J.A., and Chess, D.G. (1996). Cancellous bone properties of the glenoid: correlation of quantitative CT and mechanical strength. Trans. Orthop. Res. Soc. 21, 707.

Berms, J. (1993). The glenoid component in total shoulder arthroplasty. J. Shoulder Elbow Surg. 2, 47-54.

Brostrom, L-A., Wallensten, R., Olsson, E., Anderson, D. (1992). The Kessel prosthesis in total shoulder arthroplasty. Clin. Orthop. Rel. Res. 277, 155.

Cofield, R.H. (1983). Unconstrained total shoulder prosthesis. Clin. Orthop. Rel. Res. 173, 97-108.

Cofield, R.H. (1984). Total shoulder arthroplasty with Neer prosthesis. J. Bone Joint Surg. 66-A(6), 899-906.

Cofield, R.H. and Daly, P.J (1992). Total shoulder arthroplasty with a tissue-ingrowth glenoid component. J. Shoulder Elbow Surg. 1, 77-85.

Cofield, R.H. (1994). Uncemented total shoulder arthroplasty. Clin. Orthop. Rel. Res. 307, 86-93.

Copeland, S. (1990). Cementless total shoulder replacement. In Post. M, Morrey, B.F., Hawkins, R.J. (eds). Survey of the shoulder. 289-297. St. Louis, Mosby Year Book,

Dalstra, M. (1993). Biomechanical aspects of the pelvic bone and design criteria for acetabular prosthesis. Doctoral Thesis, University of Nijmegen, The Netherlands.

Dalstra, M., Huiskes, R. and van Erning, L. (1995). Development and validation of a three-dimensional finite element model of the pelvic bone. J. Biomech. Eng. 117, 272-278.

Friedman, J.R., LaBerge, M., Dooley, R.L. and O'Hara, A.L. (1992). Finite element modelling of the glenoid component: Effect of design parameters on stress distribution. J. Shoulder Elbow Surg. 1, 261-270.

Franklin, J.L., Barrett, W.P., Jackins, S.E. and Matsen, F.A. (1988). Glenoid loosening in total shoulder arthroplasty. Association with rotator cuff deficiency. J. Arthroplasty 3, 39-46.

Fukuda, K., Chen, C.M., Cofield, R.H. and Chao, E.Y. (1988). Biomechanical analysis of stability and fixation strength of total shoulder prostheses. Orthopaedics 11(1), 141-149.

Harrigan, T.P. and Harris, W.H. (1991). A three-dimensional non-linear finite element study of the effect cement prosthesis debonding in cemented femoral total hip components. J. Biomechanics 24, 1047-1058.

Hoffman, O. (1967). The brittle strength of orthotropic material. J. Comp. Mat. 1, 200-206.

Hertz, H. (1882). Über die Berührung fester elastischer Körper (On the contact of elastic solids). J. reine und angewandte Mathematik, 92, 156-171. (For English translation see Miscellaneous Papers by H. Hertz, Eds. Jones and Schoott, London: Macmillan, 1896.)

Huiskes, R. (1990). Comparative stress patterns in cemented total hip arthroplasty. Orthop. Rel. Sci.1, 93-108.

Huiskes, R and van Rietbergen, B. (1995). Preclinical testing of total hip stems. The effects of coating placement. Clin. Orthop. Rel. Res. 319, 64-76.

Kaplan, S.J., Hayes, W.C. and Stone, J.L. (1985). Tensile strength of bovine trabecular bone. J. Biomechanics 18, 723-727.

Lacroix, D. and Prendergast, P.J. (1997). Stress analysis of glenoid component designs for shoulder arthroplasty. Proc. Inst. Mech. Engrs, Part H 211, 467-474.

Lacriox, D., Murphy, L.A. and Prendergast, P.J. (2000). Three-dimensional finite element analysis of glenoid replacement prosthesis; a comparison of keeled and pegged anchorage systems. J. Biomech Engg. 122, 430-436.

Mansat, P., Barea, C., Hobatho, M-C., Darmana, R. and Mansat, M. (1998). Anatomic variation of the mechanical properties of the glenoid. J. Shoulder Elbow Surg. 7, 109-115.

McElwain, J.P. and English, E. (1987). The early results of porous-coated total shoulder arthroplasty. Clin. Orthop. Rel. Res. 218, 217-224.

Müller-Gerbl, M., Putz, R. and Kenn, R. (1992). Demonstration of subchondral bone density patterns by three-dimensional CT Osteoabsorptiometry as a nonevasive method for in vivo assessment of individual long-term stresses in joints. J. Bone and Mineral Res. 7, Supl. 2, S411 - S418.

Norris, B.L. and Lachiewicz, P.F. (1996). Modern cement technique and the survivorship of total shoulder arthroplasty. Clin. Orthop. Rel. Res. 328, 76-85.

Orr, T.E., Carter, D.R. and Schurman, D.J. (1988). Stress analyses of glenoid component designs, Clin. Orthop. Rel. Res. 212, 217-224.

Pierson, J.L., Harris, W.H. (1993). Extensive osteolysis behind an acetabular component that was well fixed with cement – a case report. J. Bone Joint Surg., 75-A, 268-271.

Roper, B.A., Paterson, J.M.H. and Day, W.H. (1990). The Roper-Day total shoulder replacement. J. Bone Joint Surg. 72-B, 694.

Sneppen, O., Fruensgaard, S., Johannsen, H.V., Olsen, B.S., Sojbjerg, J.O. and Andersen, N.H. (1996). Total shoulder replacement in rheumatoid arthritis: proximal migration and loosening. J. Shoulder Elbow Surg. 5(1), 47-52.

Sperling, J.W., Cofield, R.H. and Rowland, C.M. (1998). Neer hemiarthroplasty and Neer total shoulder arthroplasty in patients fifty years old or less. Long-term results. J. Bone Joint Surg. 80-A (4), 464-473.

Stewart, M.P. and Kelly, I.G. (1997). Total shoulder replacement in rheumatoid disease: 7-to 13-year follow-up of 37 joints. J. Bone Joint Surg. 79-B (1), 68-72.

Stone, J.L., Beaupré, G.S. and Hayes, W.C. (1983). Multiaxial strength characteristics of trabecular bone. J. Biomechanics 16, 743-752.

Stone, K.D., Grabowski, J.J., Cofield, R.H., Morrey, B.F. and An, K.N. (1999). Stress analysis of glenoid components in total shoulder arthroplasty. J. Shoulder Elbow Surg. 8(2), 151-158.

Torchia, M.E., Cofield, R.H. and Settergren, C.R. (1997). Total shoulder arthroplasty with Neer prosthesis: long-term results. J. Shoulder Elbow Surg. 6(6), 495-505.

Van der Helm, F.C.T. (1994). A finite element musculoskeletal model of the shoulder mechanism. J. Biomechanics 27, 551-569.

Van Rietbergen, B., Weinans, H., Huiskes, R., and Odgaard, A. (1995). A new method to determine trabecular bone elastic properties and loading using micromechanical finite element models. J. Biomechanics 28, 69-81.

Wallace, A.L., Phillips, R.L., MacDougal, G.A., Walsh, W.R. and Sonnabend, D.H. (1999). Resurfacing of the glenoid in total shoulder arthroplasty. A comparison, at a mean of five years, of prostheses inserted with and without cement. J Bone Joint Surg. 81-A (4), 510-518.

Weinans, H., Huiskes, R. and Grootenboer, H.J. (1991). Trends of mechanical consequences and modelling of a fibrous around femoral hip prostheses. J. Biomechanics 23, 991-1000.

Weinans, H., Huiskes, R. and Grootenboer, H.J. (1993). Quantitative analysis of bone reactions to relative motions at implant-bone interface. J. Biomechanics 26, 1271-1282.

Weiss, A.-P.C., Adams, M.A., Moore, J.R. and Weiland, A.J. (1990). Unconstrained shoulder arthroplasty. A five-year follow-up study. Clin. Orthop. Rel. Res. 257, 86-90.

Wirth, M.A. and Rockwood, C.A. (1994). Complications of shoulder arthroplasty. Clin. Orthop. Rel. Res. 307, 47-69.

Chapter 8

Conclusions

8.1 Introduction

Total Shoulder Arthroplasty (TSA) is a surgical procedure that involves the reconstruction of the GlenoHumeral (GH-) joint by inserting the humeral and the glenoid component in the humerus and the scapula, respectively. The primary objective of the TSA is to relieve pain and to restore the large range of motion. But in reality, the results are not at all encouraging and are far from the normal range of motions of the scapula. Since the introduction of Neer Prostheses in 1974, clinical and radiographic feedback reveals glenoid component loosening as the most-frequently-occurring problem in the TSA. The precise relationship between the cause and the effect, regarding aseptic loosening of the glenoid prostheses and the extent to which the mechanical factors play a role in this process, however, are not clearly understood yet. The design of the implant, the choice of materials and the technique of fixation to the bone certainly require a detailed biomechanical investigation.

Stress analysis is required for implant evaluations. Studies on three-dimensional (3-D) stress analyses of glenoid prostheses are very few and are inadequate to evaluate the design of the implant. The motivation of this study is to understand the load transfer mechanism and to investigate some mechanical factors related to loosening and subsequent failure of the glenoid prostheses. The primary goal of the study was to improve fixation and to obtain a proper insight in the stresses and strains generated in the bone and in the glenoid component. Cement (PMMA) is widely used for primary fixation of the prosthesis to the bone. The uncemented designs with tissue-ingrowth materials, however, have also been used in specific cases. Realistic 3-D FE models of the glenoid prostheses (cemented and uncemented) have been analysed to understand the glenoid load transfer, potential failure criteria and to suggest measures for improved glenoid prostheses. The failure of a prosthesis may be due to the excessive stresses induced in the materials and at various material interfaces as compared to the strength of the materials and their interfaces, and due to the effect of bone remodelling. In this study only some failure criteria have been studied using the initial FE stress analyses during humeral abduction to suggest measures for better glenoid prostheses.

In order to understand how the loading is being transferred to the various parts of the scapula adequately, a 3-D FE stress distribution of a scapula was obtained. Unfortunately, there has been a scarcity of these studies in recent times. A major part of the study, though a sub-goal, was directed towards the development, the analysis and the experimental validation of a realistic 3-D FE model of the scapula, which can predict stresses and strain, during abduction of the arm.

8.2 Significance

The relationships between the elastic modulus and apparent density of scapular trabecular bone were based on only limited number of testing data (n = 25) and they represented an average value of the elastic modulus. The presence of anisotropy in the trabecular bone can be observed, but was not actually determined due to lack of information on trabecular orientation. The effect of anisotropy might lead to some minor deviations in the stress values in the trabecular bone as compared to the 'effective isotropic tissue modulus', used in this study. More accurate information on the anisotropy of trabecular bone is required, which can be obtained using micro-models of trabecular bone.

The studies, leading to the thesis, started about 6-years ago when computation time was generally considered as a major factor in the generation and solving of FE models of bones. The emphasis of the study lies on the development and analysis of a 3-D FE model of the scapula and its further use in the development of submodels with the glenoid prostheses. Within the limitations of image processing and FE modelling software, we have aimed at an accurate representation of the scapular geometry, using a 3-D mesh, a combination of solid and shell elements with material properties and thickness taken from Computed Tomography (CT) scan data. The static shoulder model of forces (Van der Helm, 1994) and the FE model were based on the same cadaver. This shoulder model of forces, which included the effect of all muscles (m.), ligaments, and joint reaction forces, during humeral abduction were used as applied loading conditions.

With the rapid and enormous development of hardware and software in recent times, the computational time has reduced to a minor problem. However, computational time is still an important factor in optimisation procedures, where numerous calculations need to be carried out. FE simulations on bone remodelling and consideration of non-linear material properties of bone requires substantial computational time also. The proposed 3-D FE model would be useful in studying the stress distributions in the scapula during other activities like loaded abduction, unloaded and loaded anteflexion and can be utilised in related clinical investigation. In developing the present 3-D model of the scapula, our priorities were computational time and the ease of model generation with a moderate quality of mesh size. Although convergence in results was achieved for this mesh size, a higher mesh refinement might yield better quantitative results. Consequently, this would require significant effort and greater computational time.

Model validation is important in order to trust the results. A fresh cadaveric scapula with eighteen strain gages fixed at various locations and orientations was loaded in a mechanical testing machine and supported at three locations by linkage mechanisms. The present study suggests a new experimental set-up towards strain gage validation of 3-D FE models of bone. The novelty of this study lies in applying special purpose constraints, supporting links interconnected by ball joints, to allow for bending and deflection in all directions in response to applied loads. Loads were applied on the surface of the scapula at a variety of locations, like the glenoid cavity, acromion, and scapular spine. Results indicated a good agreement between the measured strain of the experiment and the numerical strain of the FE model. High correlation coefficients, low standard errors and percentage errors in regression slope were observed between the measured and FE strain. In view of the complicated testing procedure on a fresh sample of scapula, the significance of high correlation coefficients and relatively low standard errors, as compared to similar studies (Keyak et al., 1993; Dalstra et al., 1995), strongly suggests that the numerical strains calculated by the FE model can be used as a valid predictor of the measured strains.

Most FE studies on the scapula deal with the glenoid prosthesis rather than the load transfer mechanism of the scapula, as a whole. The static shoulder model of forces, during unloaded humeral abduction, were used as applied loading conditions for the FE model (Chapter 3) to study the stress distribution in a natural scapula. The natural adaptation and optimisation of the shape of the bone with load is generally referred to as Wolff's law (Wolff, 1892). The scapula being no exception, its complicated shape must be related to the forces acting on it and to the induced stresses within it. Results indicate that the thick bony ridges – lateral border, scapular spine and acromion, support the bulk of the load. High tensile and compressive stresses were generated on the opposite sides of the scapular spine and the lateral border, indicating bending of these structures. Stresses in the infraspinous and supraspinous fossa were low, which might indicate that the function of these structures is to act as attachment sites of large muscles. Since the geometrical and material property

data about the ligament coraco-acromiale were unknown, a low value of Young's modulus and unit geometrical data (cross-section, thickness) were assumed at this level of the study. Using beam elements, only the lengthening and shortening of the ligament can be calculated without affecting the load distribution in the scapula. A qualitative prediction was obtained from this study, which indicates that the ligament is stretched, and presumably will be under tension during abduction.

A few words must be said about the modelling artefacts. The procedure of locating the nearest node number in the FE model, for each point of application of force, resulted in a small shift of the point of application as compared to the shoulder model (Van der Helm, 1994). These shifts introduce an error in the form of residual moments as compared to the state of moment equilibrium in the shoulder model; thereby generating localised stresses around the constraints. Another modelling artefact in the medial border was caused due to the application of concentrated forces, one at the Thorax-Angulus Inferior (AI) connection and the other at the Thorax-Trigonum Spinae (TS) connection. But in reality, the reaction forces are distributed along the medial border. In general, the muscle, ligament and joint reaction forces were applied as concentrated loads in the model; representation of the trapezius muscle action, for example, was by six lines of forces. In reality, however, the forces should be distributed on the surfaces of those elements that are located in the respective anatomical areas of insertion, which remains to be investigated.

The mechanical consequences and biomechanical failure scenarios, as discussed in Section (1.5.1), of inserting glenoid prostheses (cemented and uncemented) was assessed using 3-D FE sub-models of the glenoid. The FE models was generated using a submodelling technique, which was based on an overall reference solution of a complete scapula model acted upon by all the muscles, ligaments and joint reaction forces. The objective of using a submodel of glenoid prosthesis, with a fine mesh in the domain of inclusion of the prosthesis, was to focus our investigation in the vicinity of the prosthesis. On the other hand, the elastic behaviour of the overall model of the natural scapula, as a whole, was needed to be included in the analysis. Therefore, a large size of the submodel and the use of prescribed displacements along the cut-boundaries were required to effectively impose the elastic behaviour of the overall model on the submodel with prosthesis. Any other form of approximate boundary conditions, like applying constraints at locations far away from the region of interest to restrain rigid body motion, was considered to be inappropriate and would lead to doubtful results as used in the study of Lacroix et al. (2000).

The tensile stresses evoked in the cement are very important as far as its failure is concerned. The cement mantle, for total polyethylene design was subject to lower tensile (1 – 10 MPa) stresses as compared to the metal-backed design (tensile: 1 – 11.5 MPa). Stresses in the cement mantle, for both the designs, were well below its failure strength. Considering the overall stress distribution, it appears, however, that the stresses in the cement for metal-backed design were largely reduced as compared to the total polyethylene design, except a few locations along the periphery and the area adjacent to the tip of the keel. This study showed that the load was transferred from the polyethylene cup to the metal, which eventually carried the bulk of the load and generated lower stresses in the underlying material. As a result, stresses in the cement layer below the glenoid component were reduced. Stresses in the polyethylene (metal-backed design) were also reduced (by 8%) as compared to the total polyethylene design. But these reductions were minor, since a thin (1 mm) metallic flange was used in this model. Whereas, for the total polyethylene implant the reinforcement function was offered only by the cement layer. The stresses in the cement immediately below the polyethylene component were increased, although it was well below the failure strength. Higher stress would be generated during normal activity like standing up from a chair, which produces a GH contact force of 1300 N (Anglin et al., 1996).

The interfaces of different materials are often the weakest link in the bone-prosthesis configuration. The actual failure of an interface not only depends on the multiaxial stresses (normal and shear) at the interface but also on the interface bond strength. The Hoffman failure criterion was used in this study to evaluate bone-prosthesis interface failure. It works reasonably well for trabecular bone (Stone et al., 1983; Kaplan et al., 1985), and the Hoffman number (*FL*) can provide for qualitative estimates on a relative basis (Huiskes and van Rietbergen, 1995). The criterion, however, has not been tested for bonds between hydroxyapetite and bone. Although, the Hoffman's failure theory had less support in experimental validation (Stone et al., 1983; Kaplan et al., 1985), it accounts for the multiaxial stress condition in failure initiation and also gradually changing interface bone density and strength. As a first step towards an experimental validation, Hoffman's 3-D isotropic failure criterion was applied to the multiaxial testing data of bovine trabecular bone specimens, along with data from uniaxial compression tests that indicated a compressive strength approximately three times the tensile strength (Stone et al., 1983). The direct measurements of ultimate strengths in tension and compression of trabecular bone specimens in the study by Kaplan et al. (1985) suggested that the tensile strength of trabecular bone was significantly less than the compressive strength. These results supported similar predictions by Stone et al. (1983) based on extrapolation of shear strength data, using Hoffman's 3-D isotropic failure criterion. It appears that the lack of experimental validation on this failure criterion is mainly due to practical problems involving measurement of multiaxial strength of trabecular bone or cement-bone specimens. The testing methodology, such as the shape of specimen, the design of testing device, the fixation technique of specimen to the testing device would have important consequences on measurement of strength data that may be further used to validate the failure theory. Efforts should also be directed to measure the multiaxial strength of trabecular bone or cement-bone specimens in various orientations to account for the directional strength characteristics.

In case of total polyethylene design, the cement-bone interface adjacent to the tip of the keel seemed more likely to fail (*FL = 1.86*) as compared to the superior edge of the prosthesis (*FL = 0.19*), although the stresses around the superior edge were not significantly lower. The cement-bone interface, for metal-backed design, adjacent to the tip of the keel is more likely to fail (*FL = 2.16*) as compared to the superior edge of the prosthesis (*FL = 0.68*). Hence, the actual failure of an interface depends on the bone density and the interface bond strength, which was higher in the superior side of the glenoid than in the central region.

Between the two cemented designs, it appears that the cement-bone interface for the metal-backed design was more vulnerable to interface failure (debonding). At higher loads, debonding at the cement-bone interface might be simultaneously initiated around the superior edge and the area adjacent to the tip of the keel. From a biomechanical point of view, it appears that the cemented total polyethylene design is a better option, since it provides an overall stress distribution that was closer to the natural glenoid as compared to a metal-backed design. Moreover, the fixation strength of polyethylene with cement had been reported to be poor as compared to a metal-backed design, which increases the risk of a mobile prosthesis. Since the fixation strength with cement was higher as compared to the total polyethylene design (Fukuda et al., 1988), using the metal-backing also reduces the risk of a mobile prosthesis. On the contrary, the use of a thicker metal backing might lead to stress shielding, as compared to a total polyethylene implant, thereby increasing the risk of adverse bone remodelling and bone resorption. The thicker the metal-backing, the higher the metal-cement or the metal-bone (if cement is absent) interface stresses. In view of these contradictory design considerations, it appears that both the designs are vulnerable to gross loosening and failure, in some way or the other. Hence, the need for optimisation is realised. The objective of optimisation in the design would be to reduce the high stresses in the cement and at the cement-bone or at the

metal-cement interfaces. Probably, the most important parameter to prevent an initial mechanical interface failure ('primary stability') is the quality (strength) of the interface bond. This factor is represented in the failure criterion, which is dependent, in reality, on the precision of the surgical procedure, the quality of the bone stock and the penetration of the bone cement for cemented implants (Krause et al., 1982), or the amount of bone-ingrowth into the uncemented implants.

The problems of progressive radiographic changes, the long-term efficacy of cement, and the need for revisions in the cemented glenoid components have prompted the development of glenoid components with tissue-ingrowth surfaces. FE stress analysis of an uncemented glenoid component revealed that a thicker metal-backing resulted in reduction of stresses in the polyethylene as compared to the cemented designs, which may imply less polyethylene wear at the contact surface. Moreover, high stresses were generated in the metal-backing leaving the underlying bone at a relatively low stress level as compared to the natural glenoid. Stress-shielding was observed in the trabecular bone underlying the prosthesis, which might lead to adverse bone remodelling and possible risk of failure. Using the Hoffman failure criterion, it was evaluated that the implant-bone interface was secure against interface failure at moderate loads, although the implant-bone (metal-bone) interface around the superior edge of the prosthesis was subject to high stresses. The subchondral bone with a higher density as compared to the trabecular bone offered higher interface bond strength, thereby reducing the possibilities of bone-prosthesis interface failure. Whereas, in case of cemented designs the cement-bone interface, was very likely to fail at locations adjacent to the tip of the keel. At higher loads, debonding might also be initiated at the interface around the superior edge of the prosthesis. The high stresses at the polyethylene-metal interface indicated the possibility of separation of the polyethylene cup from the metal-backing at higher loads.

Finally, the significance of the stress analyses on the design of glenoid prostheses is of vital importance. The same high stress concentrations, which were observed at the superior edge of the cement mantle for cemented metal-backed implants, were seen in the subchondral bone for uncemented metal-backed implants. For cemented cups, the objective for optimisation would be to reduce the high stresses in the cement mantle as well as the polyethylene cup. Whereas for the uncemented cups, the objective for optimisation would be more uniform load transfer to the underlying bone and to reduce the high metal-bone interface stresses. For cemented implants, it might be practical to apply more stiffeners in the superior side by locally increasing the thickness of the polyethylene or the cement layer. Another option could be to place the prosthesis in such a position, so that the GH-joint reaction force during the initial phase of the abduction is distributed more centrally. The superior side of the prosthesis might be placed at a slightly more laterally inclined position in the frontal plane so that the articulating surface is more erect as compared to that prevailing in the natural glenoid. Removal of the subchondral bone and replacing it by cement would mean a greater loss in the structural stiffness of the whole glenoid and at same time increase stresses in the cement. Preserving a part of the subchondral bone in the superior-inferior side would strengthen the structure of the glenoid as a whole. On the other, the subchondral bone with a higher density as compared to the trabecular bone offered higher interface bond strength. From the surgical considerations, using a very thin layer of cement might be required for primary fixation. This would also eliminate direct polyethylene-bone contact.

Clinical and radiographic studies reported that the glenoid component inserted without cement appears to be a reasonable alternative to fixation with cement (Cofield, 1994; Wallace et al, 1999). The results of our study indicated similar trends. Moreover, the choice of fixation method, with or without cement, depends not only on the biomechanical factors but also on the quantity and quality of bone and the effective preparation of subchondral bone. The metal-backing is mostly favoured for

fixation of the implant to the bone to avoid direct polyethylene-bone contact. It should, however, be understood that the problems associated with the prosthesis-bone interface stresses and its long-term consequences are yet to be solved and new problems such as, separation of modular parts of the glenoid component have been introduced (Wallace et al., 1999).

8.3 Unsolved problems and recommendations for future research

The 3-D FE model using CT-scan data and stress analysis of the scapula is one of the very few publications in this area. The FE model, which was experimentally validated, can serve as a platform for further investigations corresponding to various loading conditions and for comparing the deviations in stress distribution, if any, due to TSA induced changes. Until now, only a few studies on the biomechanical aspects of the scapula and the glenoid prosthesis has been reported as compared to the enormous amount of studies in the area of lower limbs like pelvic, femur, tibia bones. Economic reasons, as well as higher demand of lower limb prostheses, might be the major reasons behind it. Therefore, the scope of future research in this area is open, far and wide.

The present FE model was based on certain simplifications regarding the description of bone. Bone was assumed to be a linear, isotropic material. Whereas, in reality, bone is anisotropic and is subject to continuous remodelling. These assumptions were idealisations of the reality. With the availability of efficient image processing and FE software, more sophistication can be added to the FE model. More accurate descriptions on the anisotropy of glenoid cancellous bone can be performed by using micro-models of trabecular bone. A refined model of the trabecular bone not only leads to a better description of the material properties (anisotropy, continuum), but it could also give us more information about the actual remodelling signal on a micro-structural level. Simulation of viscoelastic properties could be another step ahead. The area of origin and insertion of the muscles should be estimated so that the forces can be distributed on the surface of scapula, more realistically. This would lead to a better estimation of the stress distribution in the natural scapula.

During the last twenty-years, there has not been a major development in the design of glenoid prosthesis. Although many designs evolved in the market, the most-frequently-occurring-problem of glenoid component loosening continued to threaten the TSA. The variations in the design of the glenoid prostheses are not very large, most of them closely resembling the Neer I, Neer II and Cofield prostheses. The less number of investigations on stresses and strain in the implanted configuration as well as the natural bone is one of the main reasons behind it. Modifications of several parameters – e.g. polyethylene and metal-backed thickness, cement thickness, conformity, material properties of implant, position and orientation of the prosthesis in the glenoid cavity – can be analysed. The effect on the cement stresses and at the material interfaces due to changes in these parameters would be useful for the design of improved glenoid prosthesis. A revision in the design of the keel should be undertaken, in view of the high stresses induced by it in the cement mantle and at the interface. Alternative designs of uncemented metal-backed glenoid prosthesis, with tissue-ingrowth surfaces should be investigated. Quantitative analysis on the aspect of bone ingrowth would be very useful for the assessment of bone-prosthesis fixation. A refined mesh will be required in the polyethylene component to obtain an accurate representation of the contact stresses, which are relevant in the context of polyethylene-wear-particle formation. The possibilities of loosening in the uncemented design, in long-term perspective, are lesser as compared to the cemented designs, once the initial phase of fixation with bone is achieved. Similar to the situation of a dental implant, a small volume of bone in the glenoid is available for fixation of the prosthesis. Preservation of the bone in this area and adapting some key features in the design of uncemented dental implants might lead to better prospects in the design of glenoid prostheses.

In this study, a perfect bond (idealised condition) was assumed at the material interfaces. However, in order to simulate more realistic condition, the effect of coefficient of friction on the interface stresses is required. The debonding process can be simulated by iterative FE solution using the gap elements and the variation in coefficient of friction (Verdonschot, 1995). The stress distributions at various stages of the debonding process can be obtained from iterative FE simulations. The gap elements at the interfaces can be activated or deactivated and subsequently, the effect on stress distributions can be compared. These investigations will eventually lead to more in-depth observations on the cement debonding process. Micro FE models, using micro CT-scan data, could be developed to analyse micro-motions and the debonding phenomena at various interfaces of the glenoid prostheses. The study on debonding could be correlated to experimental studies, in which the scapula with the glenoid prosthesis could be subject to cyclic loading, until loosening of the component appears. Finally, adaptive bone remodelling simulations with FE models could predict long-term complications in the TSA.

References

Anglin, C., Wyss, U.P. and Pichora, D.R. (1996). Glenohumeral contact forces during five activities of daily living. Proc. 1st Conf. of the Int. Shoulder Group, Delft, The Netherlands.

Cofield, R.H. (1994). Uncemented total shoulder arthroplasty. Clin. Orthop. Rel. Res. 307, 86-93.

Dalstra, M., Huiskes, R. and van Erning, L. (1995). Development and validation of a three-dimensional finite element model of the pelvic bone. J. Biomech Eng. 117, 272-278.

Fukuda, K., Chen, C.M., Cofield, R.H. and Chao, E.Y. (1988). Biomechanical analysis of stability and fixation strength of total shoulder prostheses. Orthopaedics 11(1), 141-149.

Huiskes, R and Van Rietbergen, B. (1995). Preclinical testing of total hip stems. The effects of coating placement. Clin. Orthop. Rel. Res. 319, 64-76.

Kaplan, S.J., Hayes, W.C. and Stone, J.L. (1985). Tensile strength of bovine trabecular bone. J. Biomechanics 18, 723-727.

Keyak J.H., Fourkas, M.G., Meagher J.M. and Skinner H.B. (1993). Validation of an automated method of three-dimensional finite element modelling of bone. J. Biomed. Eng., 15, 505-509.

Krause, W.R., Krug, W., Eng, B. and Miller, J. (1982). Strength of cement-bone interface. Clin. Orthop. 163, 290-299.

Lacriox, D., Murphy, L.A. and Prendergast, P.J. (2000). Three-dimensional finite element analysis of glenoid replacement prosthesis; a comparison of keeled and pegged anchorage systems. J. Biomech Engg. 122, 430-436.

Stone, J.L., Beaupré, G.S. and Hayes, W.C. (1983). Multiaxial strength characteristics of trabecular bone. J. Biomechanics 16, 743-752.

Van der Helm, F.C.T. (1994). Analysis of the kinematic and dynamic behaviour of the shoulder mechanism. J. Biomechanics 27, 527-550.

Verdonschot, N. (1995). Biomechanical failure scenarios for cemented total hip replacement. Doctoral Thesis. University of Nijmegen, The Netherlands.

Wallace, A.L., Phillips, R.L., MacDougal, G.A., Walsh, W.R. and Sonnabend, D.H. (1999). Resurfacing of the glenoid in total shoulder arthroplasty. A comparison, at a mean of five years, of prostheses inserted with and without cement. J Bone Joint Surg. 81-A (4), 510-518.

Wolff, J. (1892). Das Gesetz der Transformation der Knochen. Berlin, Hirchwild. Translated as The law of Bone Remodeling, Springer-Verlag, Berlin, 1986.
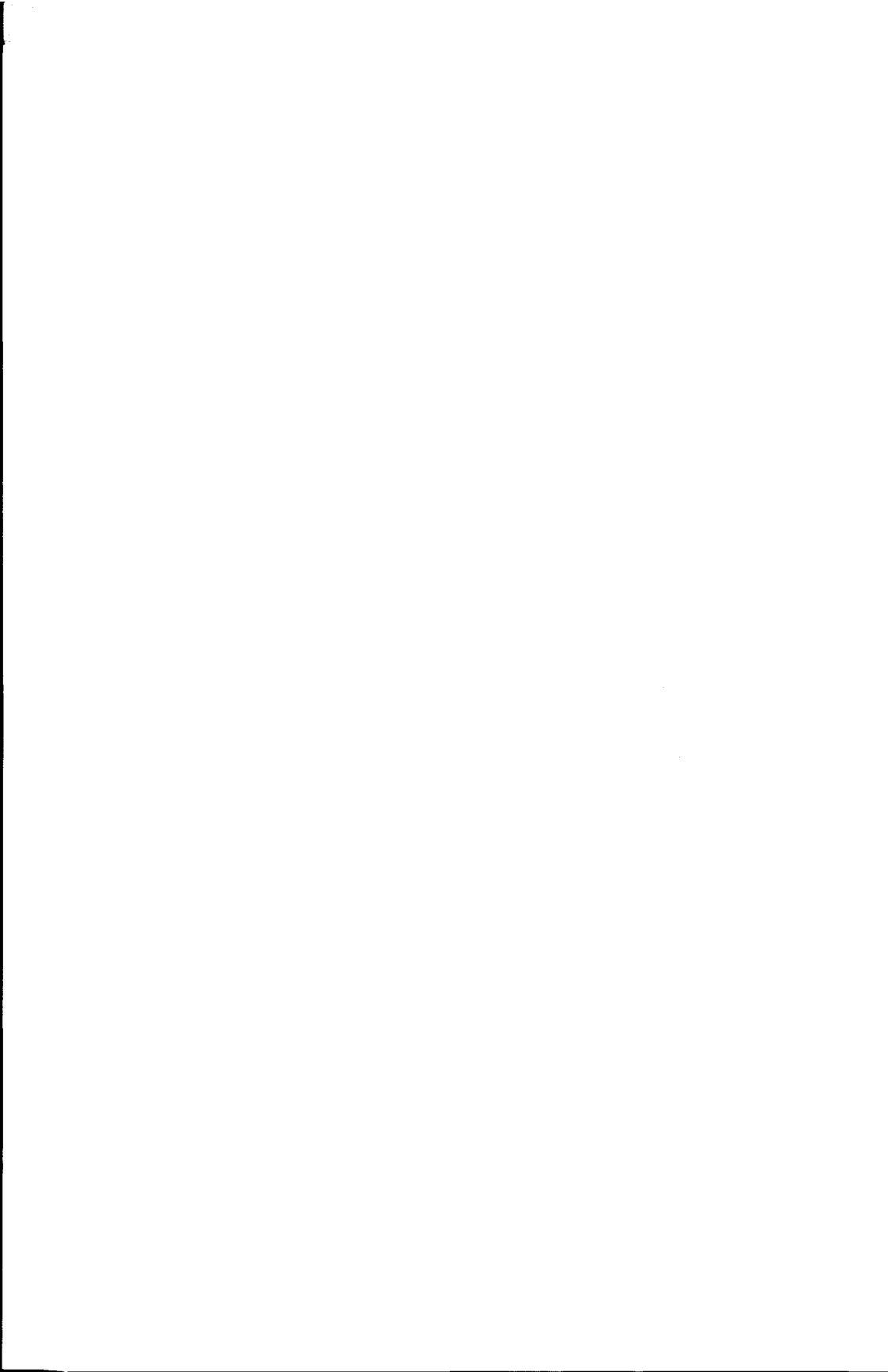
Summary

Total Shoulder Arthroplasty (TSA) is a surgical procedure that involves the reconstruction of the glenohumeral joint, by inserting a humeral and a glenoid component in the humerus and the scapula, respectively. Over the last two decades, clinical and radiographic feedback reveals glenoid component loosening as the most-frequently-occurring problem in the TSA. Therefore, the present study is intended towards investigating some biomechanical factors responsible for loosening of the glenoid component. The precise relationship between the cause and the effect, regarding aseptic loosening of the glenoid component and the extent to which the mechanical factors play a role in this process, however, are not clearly understood yet. Analysis of the failure criteria, with the help of three-dimensional (3-D) Finite Element (FE) models of glenoid prosthesis configuration, might suggest measures for improvement in the design of the prostheses. Before analysing a prosthetic joint, a 3-D FE model of the natural scapula based on Computed Tomography (CT) scan data is required for assessing the stress distribution in a scapula during normal physiological movements of the arm. Therefore, the 3-D FE stress analysis of a normal scapula is an important sub-goal. Although computer models and experimental methods have been used, the emphasis of this study lies on the development, validation and use of the 3-D FE model of a scapula.

Mechanical properties of scapular trabecular bone were assumed to be a linear isotropic material and were similar to those of other trabecular bone of different anatomical regions. In Chapter 2, an attempt has been made to relate quantitatively CT gray values in Hounsfield Units with apparent density (ρ), and apparent density with elastic modulus (E). A linear regression, generalised for all CT-scan slices defining the whole scapula was derived from two reference points (one no-bone condition, i.e. air, another cortical bone). Based on structural and analytical models of trabecular bone, power law relations were fitted for two ranges of apparent density. Powers of 2 and 3 ($E \sim \rho^2$, $E \sim \rho^3$) have been used for open cell structure and closed cell structure, respectively. The transition from open to closed structure was assumed to occur at an apparent density of 350 kg m^{-3}. The theoretical relationships were fitted to experimental data of glenoid cancellous bone specimens.

The scapula is one of the most complex bones of the human body, due to its irregular geometry, and loading conditions. In some FE models, mostly two-dimensional and restricted to the glenoid area, these aspects have been simplified to a great extent, resulting in stress patterns that are far from reality. The objective of Chapter 3 is to develop a more realistic 3-D FE model of the scapula, which can predict stresses and strains accurately. The shell elements were used to represent a part of the compact bone layer (i.e. the outer cortical layer) and the very thin and rather flat part of the scapula – infraspinous and supraspinous fossa, respectively. The solid elements were used to model the remaining part of the compact bone and the trabecular bone. The geometry of the scapula, the material properties of elements in the FE model, and thickness of shell elements, were obtained from CT-scan data. The method of generating the FE model results in proper element shapes without distortion. The shell-solid modelling technique not only eliminated the generation of distorted elements with abnormal aspect ratio but also caused substantial reduction in the computational time. The applied loading conditions were obtained from the static shoulder model of forces. High stresses (20 – 60 MPa) were observed in the solid bony ridges, like the lateral border, the scapular spine, and the acromion and at the connection of spine-glenoid-fossa. Numerical results indicate that the stresses in the high-density compact bone were substantially higher as compared to stresses in the low-density trabecular bone.

The quality of a FE model and its accuracy of predicted stresses and strains depend on the quality of representation of the FE model as compared to the actual conditions (normal bone or a

bone with implant). A thorough experimental validation with strain gage measurements on a fresh bone has always been considered as a better tool to assess the quality of FE predictions. In Chapter 5, a fresh cadaveric scapula with eighteen strain gages attached at various locations and orientations, was loaded in a mechanical testing machine and supported at three locations by linkage mechanisms, interconnected by ball joints. The objective of using these support conditions was to allow for bending and deflection of the scapula in almost all directions, in response to applied loads at various locations. A detailed FE model of the tested scapula was developed, similar to the procedure in Chapter 3. The loading and the support conditions in the experiment were simulated and applied on this FE model. The experimentally measured strains were compared with the numerical (FE) strains for several load cases to validate the proposed modelling approach. Results indicated a good agreement between the experimental and the numerically obtained strains. Considering the complicated testing procedure on a fresh sample of scapula, the high correlation coefficients (0.89 – 0.97), low of standard errors (29 – 105 microstrain) and low percentage errors in the regression slope (9 – 23%), strongly suggest that the numerically calculated strains by the FE model can be used as a valid predictor of the actual measured strains.

In Chapter 5, the stress distribution in various parts of the scapula during unloaded humeral abduction was obtained. For this purpose, the 3-D FE model of the scapula (Chapter 3) was used in combination with the static shoulder model of forces. The action of major muscle (m) forces (m. trapezius, m deltoideus, and m serrratus anterior) and joint reaction forces (GlenoHumeral – GH, AcromioClavicular – AC, and ScapuloThoracic Gliding Plane – STGP) generated high stresses in the solid bony ridges of the scapula. High tensile and compressive stresses were observed on the cranial and the caudal side of the scapular spine, respectively, indicating bending of the scapular spine. The GH-joint reaction force, a part of the force exerted by thorax-Angular Inferior (AI) joint reaction force and the m. serratus anterior were predominantly transferred along the lateral border causing high tensile and compressive stresses in the ventral and dorsal side of the lateral border, respectively. The glenoid was largely subject to high compressive forces by GH-joint reaction force. High compressive stresses were transmitted at the connection of glenoid-scapular spine-infraspinous fossa. The Trigonum Spinae (TS) and the medial border were subject to bending, due to the action of m. serratus anterior, inserting at AI and the reaction force at thorax-AI acting perpendicular to the plane of the scapula. Stresses in the infraspinous and supraspinous fossa were low (0.06 – 15 MPa), which might indicate that the function of these structures is to act as attachment sites of large muscles. From this analysis, it appeared that the ligament coraco-acromiale was under tension during abduction of the arm.

In order to analyse some mechanical factors associated with the probable failure mechanisms, 3-D FE submodels based on CT-scan data, one total polyethylene and the other, metal backed polyethylene, were used (Chapter 6). The FE model was generated using submodelling approach, which was based on an overall reference solution of a complete scapula model acted upon by all the muscles, ligaments and joint reaction forces. The results of FE stress analysis indicated that a total polyethylene design generated lower tensile stresses (1 – 3.6 MPa) in the cement as compared to higher tensile stresses (1 – 5.23 MPa) for metal-backed design. However, the metal-backed designs generated lower Von Mises stresses (6.72 MPa) in the cement than to that for the total polyethylene design (7.25 MPa). The prosthesis-cement interface stresses (normal: 5.96 MPa, shear: 2.05 MPa) were higher than the cement-bone (normal: 4.52 MPa, shear: 1.52 MPa) interfaces for the metal-backed design. Whereas, for total polyethylene design, the cement-bone interface stresses (normal: 3.64 MPa, shear: 2.66 MPa) were higher than the polyethylene-cement interface (normal: 1.23 MPa, shear: 2.09 MPa). Results indicated that for total polyethylene design, the cement-bone interface adjacent to the tip of the keel seemed very likely to fail (interface debonding) as compared to the superior edge of the prosthesis, although the stresses were higher around the superior edge.

Whereas, for metal-backed design, this interface around the superior edge of the prosthesis appeared more likely to fail as compared to the area adjacent to the tip of the keel. From biomechanical point of view, the total polyethylene therefore, appeared to be a better option. Moreover, the fixation strength of polyethylene with cement has been reported to be poor as compared to metal-backed designs, which increases the risk of a mobile prosthesis. In contrast, the metal-backing adds rigidity to the implant, causes reduction in the stresses in polyethylene cup and possesses higher fixation strength with cement. Therefore, it may be concluded that both the designs were vulnerable to loosening and failure, in some way or the other.

The use of cement for fixation of glenoid prosthesis has been one of the major problems in TSA and has been reported to be less reliable. Using a 3-D FE stress analysis of an uncemented prosthesis, the purpose of the study was to assess the stress distribution in various materials and at their respective interfaces and to observe to what extent the mechanical factors play a role in potential failure mechanisms (Chapter 7). Results indicated that the Von Mises stresses in the thick metal-backing varied between 16 – 70 MPa. A comparison with two cemented designs indicated that the metal-backing has been used to reduce excessive stresses in the polyethylene cup, increasing the stiffness of the cup and to achieve better fixation with cement or bone. However, a stiffer configuration also means that the cement mantle (if present), in general, would be subject to lower Von Mises stresses, but higher stresses at the periphery. When cement is absent, stress-shielding was observed in the underlying bone surrounding the prosthesis, which might lead to adverse bone remodelling. Results indicated that the implant-bone interface was secure against interface failure at moderate loads, although the implant-bone (metal-bone) interface around the superior edge of the prosthesis was subject to high stresses (normal: 5.97 MPa, shear: 6.44 MPa) as compared to the cemented prosthesis. The subchondral bone, with a higher density as compared to the trabecular bone, offers higher interface bond strength. The peak polyethylene-metal interface was also subject to high stresses (normal: 5.89 MPa, shear: 1.92 MPa). These results indicated probable separation of the prosthesis from the bone or separation of the polyethylene cup from the metal at higher loads. In view of the high implant-bone interface stresses, it seemed that reducing the thickness of metal-backing and ensuring a high interface bond strength was required to achieve better prospects with the uncemented prosthesis.

The 3-D FE stress analysis of the scapula, using CT-scan data, was one of the very few publications in this area. The model, which was experimentally validated, can serve as a platform for future investigations corresponding to other loading conditions and for comparing the deviations in stress distribution, if any, due to TSA induced changes. Until now, only a few studies on biomechanical aspects of the scapula and the glenoid prosthesis have been reported, as compared to the enormous amount of studies in the area of lower limbs like pelvic, femur, tibia bones. Economic reasons, as well as higher demand of prostheses for the lower limb, might be the major reasons behind it. Therefore, the scope of future research in this area is open, far and wide.

Curriculum vitae

On the first day of September, 1967, I was born in the city of Calcutta in India. I studied at the Patha Bhavan School, in Calcutta during my secondary and higher-secondary courses. I passed the Secondary Examination in the year 1983 and the Higher Secondary Examination in the year 1985. From 1985 until 1989, I studied Mechanical Engineering at the Bengal Engineering College, Calcutta University. After my graduation, I completed one year industrial training during 1989-90. In 1990, I joined the Jadavpur University, Calcutta for my Master's degree in Mechanical Engineering. I developed a keen interest in biomechanics research during my Masters dissertation. Thereafter in 1992, I joined as a Lecturer in the Jadavpur University at the School of Bio-Science and Engineering. During the later half of 1994, an opportunity to pursue Ph.D. research at the Delft University of Technology, The Netherlands, was offered to me, which I gladly accepted. The doctoral research project on stress analysis of the scapula and design considerations of glenoid prosthesis lasted from September, 1994 until September, 2001. Presently, I am teaching as an Assistant Professor at the Department of Applied Mechanics, Bengal Engineering College (Deemed University), Calcutta, India.

Sanjay Gupta

Office address: Department of Applied Mechanics
Bengal Engineering College (Deemed University)
Howrah 711 103, West Bengal, India.
Tel.: +91-33- 668 4561/62/63
Fax: +91-33- 668 4564, 2916
Email: sgupta@appmech.becs.ac.in
sguptabec@hotmail.com

Home address: AD 270, Sector 1
Salt Lake, Calcutta 700 064
West Bengal, India.
Tel.: +91-33- 334 4887.

List of Publication

International Journal

(1) Gupta S., Van der Helm F.C.T., De Wijn J.R., Spoor C.W. "Relationships between computed tomography gray values, apparent bone density and bone stiffness for human scapula." *Submitted to Journal of Shoulder and Elbow Surgery.*

(2) Gupta S., Kaptein B.L., Van der Helm F.C.T., Van Keulen A. "Three-dimensional finite element modelling of human scapula using computed tomography." *Submitted to Journal of Biomechanical Engineering (ASME).*

(3) Gupta S., Van der Helm F.C.T., Sterk J.C., Van Keulen A., Kaptein B.L. "Experimental Validation of Three-dimensional Finite Element Modelling of the Scapula." *Submitted to Journal of Biomechanical Engineering (ASME).*

(4) Gupta S. and Van der Helm F.C.T. "Biomechanical stress analysis of the scapula during humeral abduction." *Submitted to Clinical Biomechanics (Elsevier Science).*

(5) Gupta S., Van der Helm F.C.T., Van Keulen A. "Stress Analysis of Cemented Glenoid Prostheses in Total Shoulder Arthroplasty." *Submitted to Journal of Biomechanical Engineering (ASME).*

(6) Gupta S., Van der Helm F.C.T., Van Keulen A. "The possibilities of uncemented glenoid prosthesis – a finite element study." *Submitted to Clinical Biomechanics (Elsevier Science).*

International Conference

(1) Gupta S., Van der Helm F.C.T., Spoor C.W., Kaptein B.L. Three-dimensional finite element analysis of human scapula using computer tomography. Proceedings of XVth Congress of the International Society of Biomechanics, July 2-6, 1995, Jyvaskyla, Finland.

(2) Gupta S. and Kaptein B.L., Modelling and analysis of artificial shoulder joint using computer aided design system. Proceedings of International Conference of CAD, CAM, Robotics and Factories of Future, December 17-20, 1996, Narosa (Publ.), New Delhi, India.

(3) Gupta S., Van der Helm F.C.T., Kaptein B.L., Van Keulen F., Spoor C.W., Sterk J.C. Experimental validation of three-dimensional finite element modelling of human scapula, Proceedings of XVIIth Congress of International Society of Biomechanics, August 8-13, 1999, Calgary, Canada.

(4) Gupta S. and Van der Helm F.C.T. "Stress analysis of the scapula during abduction." Clinical Biomechanics, Vol. 15, 2000. (Proceeding of 2nd Conference of the International Shoulder Group, August 15-16, 1999, Calgary, Canada)

(5) Gupta S., Van der Helm F.C.T. and Van Keulen F. "Stress analysis of cemented and uncemented glenoid prostheses." 12th Conference of the European Society of Biomechanics, August 27-30, 2000, Trinity College, Dublin, Ireland.